

AD-A015 892

DESIGN, CONSTRUCTION AND TESTING OF A PULSED HIGH
ENERGY INDUCTIVE SUPERCONDUCTING ENERGY STORAGE SYSTEM

E. J. Lucas, et al

Magnetic Corporation of America

Prepared for:

Air Force Aero-Propulsion Laboratory

September 1975

DISTRIBUTED BY:

NTIS

National Technical Information Service
U. S. DEPARTMENT OF COMMERCE

AFAPL-TR-75-60

296101

AD A013000

DESIGN, CONSTRUCTION AND TESTING OF A PULSED HIGH
ENERGY INDUCTIVE SUPERCONDUCTING ENERGY STORAGE SYSTEM

Magnetic Corporation of America
179 Bear Hill Road
Waltham, Massachusetts 02154

September 1975

Technical Report AFAPL-TR-75-60

Final Report for Period 1 April 1971 - 4 April 1975

Approved for public release; distribution unlimited.

Air Force Aero-Propulsion Laboratory
Air Force Wright Aeronautical Laboratories
Air Force Systems Command
Wright-Patterson Air Force Base, Ohio 45433

Pres. No. 1-1
NATIONAL TECHNICAL
INFORMATION SERVICE
U.S. Department of Commerce
Springfield, VA 22151

NOTICE

When Government drawings, specifications, or other data are used for any purpose other than in connection with a definitely related Government procurement operation, the United States Government thereby incurs no responsibility nor any obligation whatsoever; and the fact that the government may have formulated, furnished, or in any way supplied the said drawings, specifications, or other data, is not to be regarded by implication or otherwise as in any manner licensing the holder or any other person or corporation, or conveying any rights or permission to manufacture, use, or sell any patented invention that may in any way be related thereto.

This final report was submitted by Magnetic Corporation of America, under Contract F33615-71-C-1454. The effort was sponsored by the Air Force Aero Propulsion Laboratory, Air Force Systems Command, Wright-Patterson AFB, Ohio under Project 3145, task 314501, Work Unit 31453201 with Jerrell M. Turner/AFAPL/POD-1 as Project Engineer. Edward J. Lucas of Magnetic Corporation of America was technically responsible for the work.

The report describes work performed during the period April 1971 to April 1975 by E.J. Lucas, W.F.B. Punchard, P.M.G. Margosian, R.J. Thome, R.J. Camille, Z.J.J. Stekly, R.J. Powers and P.W. Dippolito, all of Magnetic Corporation of America.

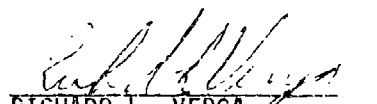
The report summarizes work carried out under Phase I of the contract during the period April 1971 to April 1972, a detailed description of which is given in Technical Report AFAPL-TR-72-38, Volumes I, II and III (Magnetic Corporation of America report number MCAD-26), and describes in detail work conducted Phases II and III of the contract during the period May 1972 to April 1975.

This report has been reviewed by the Information Office, (ASD/OIP) and is releasable to the National Technical Information Service (NTIS). At NTIS, it will be available to the general public, including foreign nations.

This technical report has been reviewed and is approved for publication.


JERRELL M. TURNER, GS-13
Project Engineer

FOR THE COMMANDER


RICHARD L. VERGA
Technical Area Manager
Power Conditioning
Power Distribution Branch

A

Copies of this report should not be returned unless return is required by security considerations, contractual obligations, or notice on a specific document.

Unclassified

SECURITY CLASSIFICATION OF THIS PAGE (When Data Entered)

REPORT DOCUMENTATION PAGE		READ INSTRUCTIONS BEFORE COMPLETING FORM
1. REPORT NUMBER AFAPL-TR-75-60	2. GOVT ACCESSION NO.	3. RECIPIENT'S CATALOG NUMBER
4. TITLE (and Subtitle) DESIGN, CONSTRUCTION AND TESTING OF A PULSED HIGH ENERGY INDUCTIVE SUPERCONDUCTING ENERGY STORAGE SYSTEM		5. TYPE OF REPORT & PERIOD COVERED Final Report for Period 1 April 1971 - 4 April 1975
7. AUTHOR(s) E. J. Lucas, W. F. B. Punchard, P. M. G. Margosian et al		6. PERFORMING ORG. REPORT NUMBER MCA-TR-WP10-2
9. PERFORMING ORGANIZATION NAME AND ADDRESS Magnetic Corporation of America 179 Bear Hill Road Waltham, Massachusetts 02154		8. CONTRACT OR GRANT NUMBER(s) F33615-71-C-1454
11. CONTROLLING OFFICE NAME AND ADDRESS Air Force Aero-Propulsion Laboratory, Air Force Wright Aeronautical Laboratories, Air Force Systems Command, Wright-Patterson Air Force Base, Ohio 45433		10. PROGRAM ELEMENT, PROJECT, TASK AREA & WORK UNIT NUMBERS Program Element 62203F Proj. 3145, Task Area 314532 Work Unit 31453201
14. MONITORING AGENCY NAME & ADDRESS (if different from Controlling Office)		12. REPORT DATE September 1975
		13. NUMBER OF PAGES 291
		15. SECURITY CLASS. (of this report) Unclassified
		15a. DECLASSIFICATION DOWNGRADING SCHEDULE
16. DISTRIBUTION STATEMENT (of this Report) Approved for public release; distribution unlimited.		
17. DISTRIBUTION STATEMENT (of the Abstract entered in Block 20, if different from Report)		
18. SUPPLEMENTARY NOTES		
19. KEY WORDS (Continue on reverse side if necessary and identify by block number) superconducting magnet; superconducting wire; inductive energy storage; non-conducting dewar; current switch; superconductor energy losses		
20. ABSTRACT (Continue on reverse side if necessary and identify by block number) Major problems associated with inductive energy storage systems operated at high repetition rates include: breaking high currents in inductive circuits; developing a low loss superconductor and from it building a coil which remains superconducting during the rapid charge period; and building a low heat leak non-conducting dewar. Theoretical analyses concerning conductor energy losses, transient heating effects, electrical circuits, and switch actuation, were conducted. To confirm these analyses experiments were conducted on model non-conducting dewars		

DD FORM 1 JAN 73 1473

EDITION OF 1 NOV 65 IS OBSOLETE

Unclassified

SECURITY CLASSIFICATION OF THIS PAGE (When Data Entered)

Unclassified

SECURITY CLASSIFICATION OF THIS PAGE(When Data Entered)

and 1 and 7 kJ stored energy model coils using a pneumatically actuated vacuum interrupter. A model non-conducting dewar held liquid helium with acceptable heat leaks and outgassing rates; a 1 kJ coil operated for an indefinite period at a repetition rate of five pulses per second at 0.89 of the critical current at charge and discharge times of the order of 0.17 s and 0.2 ms respectively and at a peak current density in the conductor of 77×10^7 A/m²; the switch was cycled 7,000 times at five pulses per second and 3,000 times at one pulse per second without deterioration. A non-conducting dewar to contain a 100 kJ coil was built and the system was tested using a hydraulically actuated vacuum interrupter. Measured dewar heat leaks and energy losses agreed, within experimental error and the limitations of the models, with the theoretical predictions. The coil withstood a voltage of 50 kV applied across its terminals. A series of 5 kJ 400 μ s pulses was obtained at 200 pulses per second using a helium blast switch. Feasibility of building non-conducting dewars, of rapidly pulsing superconducting coils, and of predicting energy losses was demonstrated. Further theoretical and experimental work should be conducted to establish the operational limits of the 100 kJ coil when repetitively pulsed, to determine the range of applicability of the helium blast switch, and to refine the energy loss analyses.

TABLE OF CONTENTS

SECTION		PAGE
I	INTRODUCTION	1
II	100 kJ COIL SYSTEM DESIGN	9
	1. INTRODUCTION	9
	2. SWITCHING AND CONTROL CIRCUITRY	11
	a. Charging and Switching	11
	b. Arc Quench Circuit	19
	c. Timing Controls and Interlocks	19
	3. NON-CONDUCTING DEWAR	27
	a. Introduction	27
	b. Thermal Insulation	30
	c. Non-Conducting Materials Investigation	32
	d. Model Non-Conducting Dewars	32
	e. 100 kJ Coil Non-Conducting Dewar Design	39
	f. 100 kJ Coil Non-Conducting Dewar Testing and Experimental Results	51
	g. Conceptual Light Weight Non-Conducting Dewar	55
	h. Summary and Conclusions	58
	4. VAPOR COOLED CURRENT LEADS	58
	a. Introduction	58
	b. Cryogenic Aspects of Current Lead Design	59
	c. High Voltage Aspects of Current Lead Design	66
	d. Experimental Program for Testing the Current Leads	73
	e. Summary and Conclusions	78
	5. 100 kJ COIL DESIGN	78
	a. Introduction	78
	b. Optimization of Coil for Minimum System Weight	80
	c. Effect of Transient Heating on Coil Performance	87
	d. Conductor Selection	94
	e. Model Coils	99
	f. 100 kJ Coil Electrical and Magnetic Design Aspects	100
	g. 100 kJ Coil High Voltage Design Aspects	113
	h. 100 kJ Coil Mechanical Design Aspects	115
	i. Summary and Conclusions	121
III	COIL EVALUATION PROGRAM	129
	1. INTRODUCTION	129
	2. LIMITS OF PERFORMANCE	129
	a. 1 kJ Coil Evaluation Tests	129
	b. 7 kJ Coil Evaluation Tests	140
	c. 100 kJ Coil Evaluation Tests	140

TABLE OF CONTENTS (Continued)

SECTION	PAGE
III COIL EVALUATION PROGRAM (Continued)	
3. THEORY OF LOSSES IN PULSED COILS	150
a. Formulae Used to Predict Losses in Superconductors	150
b. Models Concerning the State of the Superconductor in a Coil	156
4. LOSS MEASUREMENT METHODS	160
a. Introduction	160
b. Helium Boiloff Method	161
c. Electronic Method	162
5. LOSS MEASUREMENTS MADE USING THE 1 kJ COIL	173
6. LOSS MEASUREMENTS MADE USING THE 7 kJ COIL	180
a. Introduction	180
b. Boiloff Measurements	180
c. Inductive Effects of the Metal Dewar with Respect to the Electronic Method	182
d. Energy Losses in the Metallic Dewar	194
e. Electronic Loss Measurements on the 7 kJ Coil	195
f. Summary and Conclusions	204
7. LOSS MEASUREMENTS MADE USING THE 100 kJ COIL	206
a. Introduction	206
b. Preliminary Measurements	206
c. Electronic Loss Measurements on the 100 kJ Coil	216
d. Summary and Interpretation	223
8. MULTIPLE PULSE TESTS	225
a. Philosophy	225
b. Design and Testing of Electric Circuit and of Switch for Pulsed Operation	227
c. Suggested Future Work	227
REFERENCES	235

APPENDICES

APPENDIX	PAGE
I PREDICTED LOSSES IN SUPERCONDUCTORS	237
II DERIVATION OF RELATIONSHIP BETWEEN HYSTERESIS LOOP AND LOSS DURING CYCLE	263
III EFFECT OF PHASE SHIFT AND DRIFT VOLTAGE ON LOSS LOOP MEASUREMENT	267
IV NON-INDUCTIVE CURRENT SHUNT	269

TABLE OF CONTENTS (Concluded)

APPENDIX		PAGE
V	HIGH RESOLUTION VOLTAGE DIVIDER	271
VI	ELECTRIC CIRCUIT MODEL FOR DEWAR LOSSES	273
VII	PREDICTED LOSS VOLTAGE FOR THE 7 kJ COIL DUE TO MAGNETIZATION LOSSES	275
VIII	DESIGN OF RELAXATION OSCILLATOR TO PRODUCE A SERIES OF PULSES FROM AN ENERGY STORAGE COIL	277
IX	DESIGN OF ARC QUENCH CIRCUIT FOR HELIUM SWITCHES	279

LIST OF ILLUSTRATIONS

FIGURE		PAGE
1	Schematic of inductive energy storage system	10
2	Hydraulic circuit	14
3	Detail of vacuum interrupter, hydraulic actuator and backup contactor	16
4	Actual switching times for vacuum interrupter driven by the hydraulic system using the Moog 35 Servovalve	17
5	Electric circuit used for measurement of opening and closing times of the vacuum interrupter	18
6	Overall schematic of electrical system for 100 kJ coil	20
7	Overall view of experimental setup	21
8	Schematic of arc quench circuit and counterpulse current	22
9	Experimental arrangement for testing the arc quench circuit	23
10	Detailed photograph showing battery, arc quench inductor, spark gap, spark gap actuator, hydraulic actuator for vacuum interrupter, and backup contactor	24
11	Closeup of resistor bank and parallel capacitors	25
12	Timing diagram for operation of 100 kJ coil	26
13	Control panel schematic - high voltage controls	28
14	Control panel schematic-switching for operation of experiment	29
15	Thermal conductivity of Micro-Cel T-4 insulation as a function of pressure	31
16	Model fiberglass helium container used for determining the suitability of various non-conducting materials	35
17	Schematic of model fiberglass dewar in a steel test chamber	36
18	Experimental setup to evaluate helium permeability rate of fiberglass	37
19	Experimental apparatus used for evaluating various model non-conducting dewars	38
20	Schematic of non-conducting dewar for the 100 kJ coil	45

LIST OF ILLUSTRATIONS (Continued)

FIGURE		PAGE
21	Inner shell of dewar for 100 kJ coil (photograph)	47
22	Outer shell of dewar for 100 kJ coil (photograph)	48
23	Experimental set-up used for evaluating the non-conducting dewar performance	52
24	Conceptual light weight dewar	56
25	Boil off data in several sets of vapor cooled current leads	60
26	Predicted boil off due to vapor cooled leads in the 100 kJ coil system vs. current through the leads	62
27	Schematic of vapor cooled current lead for 100 kJ energy storage coil	63
28	Effect of additional helium boiloff on design current for vapor cooled leads	64
29	Normalized total boil off vs. excess boil off for configurations with leads operating, leads not operating, and leads removed	65
30	Uniform field strength breakdown voltage of helium gas at one atmosphere and various temperatures vs. electrode separation	67
31	Electric field concentration factor for equal parallel cylinders	69
32	Schematic of non-conducting dewar showing arrangement of current leads	70
33	Breakdown electric field strength of helium gas at one atmosphere for various temperatures vs. electrode separation	71
34	Maximum field strength for current leads and electrostatic shields vs. voltage across coil terminals	72
35	Schematic illustrating experiment to measure breakdown properties of current lead configuration using a full-scale model	74
36	Schematic of circuit used for high voltage ringing experiments	76
37	High voltage ringing test on the 100 kJ coil at 50 kV	77
38	High voltage ringing test on the 100 kJ coil at 63.3 kV	79

LIST OF ILLUSTRATIONS (Continued)

FIGURE		PAGE
39	Temperature rise in hottest part of the winding bundle as a function of time after beginning of pulse	89
40	Temperature decay during the interpulse period in the hottest part of the winding bundle	90
41	Heat transfer characteristics of boiling helium I for a well-ventilated vertical plate	92
42	Peak nucleate boiling heat flux characteristics for narrow vertical channels in liquid helium	93
43	Braid consisting of 48 strands of 4.5×10^{-3} inch diameter superconducting wire	96
44	Braid consisting of 3 x 48 strands of 4.5×10^{-3} inch diameter superconducting wire	97
45	Schematic illustrating the dimensions of the 1 kJ energy storage coils	101
46	Photograph of the 1 kJ energy storage coil	102
47	Photograph showing detail of windings of the 1 kJ energy storage coil	103
48	H-I characteristic and load lines for the 1 kJ energy storage coil	105
49	Schematic illustrating the dimensions of the 7 kJ energy storage coil	106
50	Photograph of 7 kJ coil during winding	107
51	Photograph of 7 kJ coil after winding	108
52	H-I characteristic and load lines for the 100 kJ energy storage coil	112
53	100 kJ coil inter-braid voltage vs. coil terminal voltage	114
54	Electric field strength in interlayer insulation vs. coil terminal voltage	116
55	Dielectric strength of kapton H film vs. temperature	117
56	Breakdown strength of liquid helium and transformer oil for two 2.65 cm diameter spheres	118
57	Average hoop stress at coil median plane as a function of coil current	120

LIST OF ILLUSTRATIONS (Continued)

FIGURE		PAGE
58	Strength of E glass fibers as a function of temperature	122
59	Coil form and flanges used for construction of the 100 kJ energy storage coil	123
60	Schematic showing cross section of windings illustrating the construction technique	124
61	Schematic illustrating dimensions of 100 kJ energy storage coil	125
62	100 kJ energy storage coil with current leads, supports and dewar neck plug	126
63	Schematic showing assembly of coil, current leads and dewar	127
64	Current during charge of pulsed 1 kJ model energy storage coil constructed with braided single core conductor	132
65	Train of pulses at a repetition rate of 1/second, 1 kJ coil	133
66	Voltage across resistive load during discharge of the 1 kJ coil at a repetition rate of 1 pulse per second	134
67	Current during charge of a pulsed 1 kJ energy storage coil when operated at a repetition rate of 5 pulses per second	135
68	Pulse train of duration about 15 seconds depicting current during charge of a pulsed 1 kJ energy storage coil when operated at a repetition rate of 5 pulses per second	136
69	Voltage across the resistive load when the energy storage coil was repetitively charged and discharged at a rate of 5 pulses per second	137
70	Pulse train showing current during charge of 1 kJ coil when repetitively pulsed at a rate of 5 pulses per second and a quench after about 16 seconds	139
71	General view of apparatus used during the testing and evaluation of the 1 kJ model coils	142
72	Dewar containing 1 kJ model coil, and dump resistor	142
73	Overall schematic of electrical system for 100 kJ coil	147
74	Photograph of top of dewar, power leads for 100 kJ coil, and resistor bank used for switching tests	148
75	Discharge of the 100 kJ coil into a 0.6 Ω load	149

LIST OF ILLUSTRATIONS (Continued)

FIGURE		PAGE
76	Distribution of conductor length with field strength in the 1 kJ coil	157
77	Distribution of conductor length with field strength in the 7 kJ coil	158
78	Schematic of loss measurement device circuit	164
79	Block diagram of loss measurement circuit	165
80	Schematic of non inductive current shunt	167
81	Voltage divider	170
82	Final version of integrator used for loss loop measurements	171
83	Schematic of low speed experiment for loss loop measurements	174
84	Comparison of predicted and measured losses due to eddy currents in dewar walls	176
85	Comparison of measured losses (as a function of discharge time) due to the 1 kJ coil with the theoretical losses as predicted according to various models	178
86	Comparison of measured losses (as a function of discharge time) due to the 1 kJ coil with theoretical losses assuming certain modifications to the previously derived theory	179
87	Sketch of 7 kJ coil with sense coil added	181
88	Comparison of measured losses for the 7 kJ coil (as a function of discharge time) with theoretical losses as predicted according to various models	183
89	Various experimental arrangements for measuring inductances and losses of the 7 kJ coil	184
90	Self inductance of 7 kJ coil at room temperature	185
91	Self inductance of sense coil on 7 kJ coil at room temperature	186
92	Mutual inductance between 7 kJ coil and sense coil at room temperature	187
93	Self inductance of 7 kJ coil at 77 K	188
94	Self inductance of sense coil on 7 kJ coil at 77 K	189
95	Mutual inductance between 7 kJ coil and sense coil at 77 K	190

LIST OF ILLUSTRATIONS (Continued)

FIGURE		PAGE
96	Self inductance of 7 kJ coil at 4.2 K	191
97	Self inductance of sense coil on 7 kJ coil at 4.2 K	192
98	Mutual inductance between 7 kJ coil and sense coil at 4.2 K	193
99	Equivalent loss resistance of 7 kJ coil at room temperature	196
100	Equivalent loss resistance of 7 kJ coil at 77 K	197
101	Equivalent loss resistance of 7 kJ coil in a metallic dewar at 4.2 K	198
102	Schematic of model for dewar loss circuit	199
103	Predicted loss voltage caused by dewar for 7 kJ coil	200
104	Predicted loss voltage caused by superconductor for 7 kJ coil	201
105	Schematic of low speed loss measurement circuit	202
106	Loss loop for 7 kJ coil	203
107	Energy dissipated in a charge-discharge cycle vs. coil stored energy for 7 kJ coil	205
108	Self inductance of 100 kJ coil at room temperature	207
109	Self inductance of sense coil for 100 kJ coil at room temperature	208
110	Mutual inductance between 100 kJ coil and sense coil at room temperature	209
111	Self inductance of 100 kJ coil at 77 K	210
112	Self inductance of sense coil for 100 kJ coil at 77 K	211
113	Mutual inductance between 100 kJ coil and sense coil at 77 K	212
114	Self inductance of 100 kJ coil at 4.2 K	213
115	Self inductance of sense coil for 100 kJ coil at 4.2 K	214
116	Mutual inductance between 100 kJ coil and sense coil at 4.2 K	215
117	Equivalent loss resistance for 100 kJ coil at room temperature	217

LIST OF ILLUSTRATIONS (Continued)

FIGURE		PAGE
118	Equivalent loss resistance for 100 kJ coil at 77 K	218
119	Equivalent loss resistance for 100 kJ coil at 4.2 K	219
120	Loss loop for 100 kJ coil during ringing test	220
121	Energy dissipated in a charge-discharge cycle vs. coil stored energy for 100 kJ coil	221
122	Energy dissipated in a charge-discharge cycle vs. coil current for 100 kJ coil	222
123	Energy dissipated in a charge-discharge cycle vs. coil stored energy for 100 kJ coil showing loss trend lines as a function of frequency	224
124	Circuit used to extract train of pulses from 100 kJ coil with helium switch	228
125	Schematics of helium blast switch and of overall circuit for higher repetition rate operation	229
126	Photograph of helium switch	230
127	Pulses extracted from 100 kJ coil with helium switch	231
128	Single pulse of current to 0.2 ohm load delivered by helium switch	232
129	Single pulse of current through the helium switch	233
130	Schematic illustrating the non-linear electric field-current density characteristic for the critical state model of a superconductor	238
131	Schematic showing a layer of rectangular superconductor immersed in a background field, B , which is parallel to the layer	239
132	Schematic illustrating the shielding currents induced on the surfaces of a superconductor immersed in a field which rises from zero to B .	240
133	Schematic illustrating a typical $B - j_c$ curve for a superconductor	242
134	Schematic illustrating the field penetration profiles and critical current density distributions in a flat slab of superconductor as the field is raised from zero to the critical field	243

LIST OF ILLUSTRATIONS (Continued)

FIGURE		PAGE
135	Schematic showing the $B - j_c$ curve for a typical superconductor and the $B - j_t$ load line for a conductor carrying a transport current	246
136	Schematic showing the profiles of flux density, current density and electric field across a slab of superconductor carrying a transport current and subjected to a background field proportional to the transport current	247
137	Model used for calculating the local power dissipation $p(x)$ in a rectangular slab of superconductor carrying a transport current density	249
138	Schematic illustrating the model used for calculating the power dissipation in a wire of circular cross section carrying a transport current	254
139	Schematic illustrating the model used to calculate the energy loss in a coil carrying a transport current	257

LIST OF TABLES

TABLE		PAGE
I	Specification sheet for vacuum interrupter	12
II	Specifications for hydraulic actuator and power supply	15
III	Comparison of properties of fiberglass and stainless steel	33
IV	Comparison of properties of hand laid up polyester/ fiberglass and epoxy/fiberglass made by an autoclave process	40
V	Summary of tests on model dewars	41
VI	Specifications for the non-conducting dewar	44
VII	Components of 100 kJ coil non-conducting dewar	46
VIII	Comparison of predicted and measured cryogen usage in 100 kJ non-conducting dewar	49
IX	Summary of tests on 100 kJ coil dewar	53
X	Specifications for the flight system non-conducting dewar	57
XI	Effective resistance of helium and foam at 50 kV	75
XII	Coil and system weights for a 100 kJ coil system	85
XIII	Range of mission constraints used in the parametric study to determine system weights	86
XIV	Specifications of the 1 kJ energy storage coil	104
XV	Specifications of the 7 kJ energy storage coil	109
XVI	Specifications of the 100 kJ energy storage coil	111
XVII	Summary of 1 kJ coil performance (single core conductor)	141
XVIII	Summary of 7 kJ coil performance	143
XIX	Summary of tests performed with 100 kJ coil	144
XX	Energy loss formulae	155
XXI	Simple energy loss models	159

LIST OF TABLES (Concluded)

TABLE		PAGE
XXI.	Component requirements for accurate loss measurement	166
XXIII	Current shunt characteristics	168
XXIV	Data sheet on AD-523L operational amplifier	172

SECTION I

INTRODUCTION

This program was divided into three phases. The purpose of Phase I was to expose and overcome the major problems associated with the effective use of superconducting coils in pulsed inductive energy storage systems operating at high pulse repetition rates and, after having done so, to produce (1) a detailed design for an experimental 100 kJ stored energy system capable of being operated at a repetition rate of five pulses per second and (2) a conceptual design for a lightweight airborne system with similar performance.

Phase II consisted of building the 100 kJ experimental system, and Phase III consisted of testing and evaluating it.

Phase I was carried out during the period 1 April 1971 to 17 April 1972 and consisted of complementary analytical and experimental studies. The work carried out during this phase is described in detail in Technical Report AFAPL-TR-72-38, Volumes I, II, and III, December, 1972, but for the convenience of the reader is summarized below.

The analytical studies were divided into the following specific tasks:

(1) A parametric study was made for each of the systems A through E specified in the work statement of the subject contract plus 360 other systems ranging in energy storage capabilities from 10,000 joules to 10,000,000 joules, with output pulses ranging in duration from 10 microseconds to 400 microseconds, and with total numbers of pulses ranging from 300 to 30,000 pulses. In each case, the system was optimized for the minimum overall weight.

(2) A study was made of the requirements for the superconductor to be used in each of the systems studied. In this study, special cognizance was taken of the thermal environment in which the conductor would be operating. The losses for conductors of various sizes and configurations were calculated. A determination was then made of the present day availability of these conductors. Only those conductors that could be fabricated with present-day technology were utilized in the designs presented in this report.

(3) An investigation was made of the requirements for both the main and auxiliary circuit switching elements for the 100,000 joule systems. A survey was then made of the current availability of components to meet these requirements. This survey resulted in the selection of a linearly actuated high vacuum switch for the main circuit and a mercury ignitron for the arc quench circuit. Several different available components were found that were suitable for use in several of the different circuit configurations considered. The mercury ignitron was selected only because of its proven reliability when used in the arc quench circuits of an experimental system built and tested during this first phase of the program.

In addition to the switches mentioned above, a study was made of alternative methods of switching the main circuit. This study resulted in the conceptual design of a rotary actuated switch that makes use of the magnetic

field of the energy storage coil to help extinguish the arc and decrease the switch losses.

(4) An analysis was made of the losses that could be expected in the power leads connecting the coil to the external circuits and in the walls of a metallic dewar, should such be used in the system.

The experimental studies were divided into the following specific tasks:

(1) An evaluation was made of likely candidates for materials suitable for the construction of a non-conducting dewar. Tests were made to determine tensile, compressive and shear properties of various structural materials and epoxy cements. Based on the results of these tests, a model vacuum shell was built and tested. The shell exhibited sufficient strength to withstand the external pressure loading encountered in vacuum applications. Vacuum outgassing rates and helium diffusion rates were measured and found to be satisfactory. Three model dewars were built and tested at room and cryogenic temperatures. Based on these tests, a hand laid up polyester fiberglass laminate was selected for the room temperature outer container of the dewar, and an epoxy fiberglass laminate, similar to G10, made by a high pressure, high temperature laying up technique was selected for the inner helium temperature container of the dewar.

(2) Evaluation tests were made on conductors deemed suitable for use in pulsed systems. Two basic conductors were considered. Both were niobium titanium copper composite superconducting wires having a diameter of 4.5×10^{-3} inch. One had a single filament of niobium titanium with a copper to superconductor ratio of 1.4 to 1, and the other had 121 filaments of niobium titanium with a copper to superconductor ratio of 3 to 1. Flattened tubular braids consisting of 48 wires were made from each of these conductors.

Two 1 kJ nominal stored energy coils were built, one from each of the braids described above. They were pulsed repetitively at a repetition rate of five pulses per second. During these pulsed tests, measurements were made of the energy dissipation in the windings caused by the changing magnetic fields.

A 7 kJ nominal stored energy coil was built from the braid composed of single core conductor. This was also successfully tested under pulsed conditions.

(3) Tests were made on a smaller model of the high vacuum switch selected for use in the 100 kJ system. This switch was operated at a rate of five pulses per second for over 7,000 cycles and at one pulse per second for over 3,000 cycles. During this period, no deterioration was noted in the switch performance.

The results of the analytical studies and the experiments conducted on model dewars and coils during Phase I of this program indicated that:

- (1) energy storage coils could be built which would operate at repetition rates of up to five pulses per second at high fractions of the coil critical current,

- (2) dewars, which would have acceptable heat leaks, outgasing rates, and helium diffusion rates, could be built from non-conducting materials, and
- (3) vacuum interrupters could operate reliably at high repetition rates for some thousands of cycles without deterioration in performance.

It also demonstrated the validity of designing coils of larger size from data generated by carefully designed and tested smaller coils.

Based on the results of the Phase I studies, designs for an experimental 100 kJ stored energy system and a conceptual lightweight flight system were produced.

This report describes details of the construction and evaluation of the 10 kJ energy storage system, but sufficient information concerning the work carried out during Phase I of the program is given to provide a logical sequence of events from the program's inception to the testing of the 100 kJ coil system. The work was carried out during the period May 1972 to April 1975.

The report is divided into two technical sections, together with a number of appendices. Section II deals with the design of the system; and Section III, with the evaluation of the coil.

The system can be divided into four major subsystems: (1) the switching and control circuitry, (2) the non-conducting dewar, (3) the vapor-cooled leads, and (4) the 100 kJ coil. A subsection is devoted to each of these items.

The electrical circuitry is described in Section II-2, Switching and Control Circuitry. The requirements were to charge the coil to 2,000 A, to interrupt the current and allow the coil to discharge at a variety of discharge rates and discharge voltages, and to provide protection against various types of equipment failures or operational errors. A mechanical timer was used to control the charge time of the coil when powered by a set of submarine batteries. At the end of the charge time, the control circuitry commanded the hydraulically powered vacuum interrupter to open. As it opened, it mechanically tripped a microswitch which fired a spark gap and activated the arc quench circuit, thereby forcing a current zero in the vacuum switch and extinguishing the arc. A contactor acted as a back-up circuit breaker in the event that the vacuum interrupter failed to break the current. The coil discharged into a resistor bank consisting of a number of high power carbon resistors whose resistance could be varied to suit the requirements of the experiment.

The non-conducting dewar is described in Section II-3, Non-Conducting Dewar. This section begins with an explanation of why a dewar made of non-conducting materials is necessary in a pulsed system and continues with the rationale behind the choice of a vacuum space containing powdered insulation as opposed to a cryogenic radiation shield. It goes on to summarize the results of the non-conducting materials investigation (including the tests on model dewars) carried out during Phase I of this program and gives the reasons which led to the choice of an outer shell consisting of hand laid up polyester

fiberglass and an inner shell consisting of an epoxy fiberglass laminate made by an autoclave process.

A description of the 100 kJ coil non-conducting dewar is given next, together with a detailed exposition of the predicted performance. This is followed by details of tests performed on the dewar and a comparison between the predicted performance and the experimental results. The agreement between the predicted and the measured performance confirms the validity of the design techniques.

Finally, a summary of the conceptual lightweight non-conducting dewar is given.

The vapor-cooled leads are described in Section II-4, Vapor-Cooled Current Leads. The section begins with an explanation of the necessity of vapor-cooled leads as a means of minimizing the heat leak into the dewar and a description of the compromises which must be made when using vapor-cooled leads in an experimental pulsed system. The following two subsections deal with cryogenic and high voltage design aspects, respectively.

In the cryogenic aspects subsection, an explanation of the principles involved is given together with a summary of the results of an analysis conducted during Phase I of the program concerning the effect of additional boil-off (e.g., due to coil losses) on the lead design. The subsection concludes with a description of the leads actually constructed for the 100 kJ coil and their predicted boil-off as a function of coil current.

The high voltage design aspects subsection describes the problems of operating current leads in an environment of helium gas which has very poor breakdown characteristics and goes on to deal with the measures taken to ensure that breakdown between leads does not occur. It was concluded that in the low temperature region of the leads towards the liquid helium surface breakdown would not occur. However, in the warm region near to the lid of the dewar where the leads pass through the open-cell-foam neck plug, firm conclusions could not be drawn because of the lack of data concerning the properties of helium-permeated foam. It was, therefore, decided to do an experiment with a full-scale model of the leads and foam in the region of the dewar lid. This experiment is described. It was found that no breakdown occurred at inter-lead potentials of 50 kV (the maximum voltage available with the existing power supply). Later experiments on the leads in the 100 kJ coil system indicated that breakdown occurred at a voltage greater than 50 kV and less than 63 kV, consistent with the results of the experiments made on the model.

The design of the 100 kJ coil is described in Section II-5, 100 kJ Coil Design. The section begins with an explanation of the design compromises which must be considered in designing and building a lightweight superconducting energy storage coil capable of being pulsed rapidly with short discharge times. Next are described the influences of various parameters on the system weight, and an explanation is given of why a low field, large bore coil gives a minimum weight system. The influence of wire size on system weight is dealt with in detail, and examples of the variation of the system weight with wire size are given.

Next follows an extensive summary of the results of analyses carried out during Phase I of the program, concerning the effects of transient heating on coil performance. It is concluded that the cooling channels are ventilated well enough that they will not choke with helium gas but that under certain circumstances (operation at high fractions of the critical current for long pulse train lengths) the conductor may not cool sufficiently between pulses, and that this might lead to the coil going normal. This effect was observed in tests on one of the model coils.

The following subsection considers the conductor requirements in light of the preceding analyses and concludes that the best conductor configuration is one which is a braid (which has a large cooled surface to conductor volume ratio) consisting of individually insulated conductors with as small a diameter as practically possible (to minimize the heat generation per unit volume of conductor when operated under transient field conditions). The section concludes with summaries of analyses carried out during Phase I concerning the implications of breakage of individual strands within the braid on coil performance.

Details of the construction of the two 1 kJ nominal stored energy model coils and of the 7 kJ nominal stored energy model coil are described in the next subsection.

The final three subsections describe electrical and magnetic aspects, high voltage aspects, and mechanical aspects of the 100 kJ coil design, respectively. The reasons are given for selecting two braids, each containing 144 strands wound in parallel for the conductor; for supporting each layer of windings individually with epoxy/glass structure; and for choosing kapton H film interlayer electrical insulation.

Section III, Coil Evaluation Program, describes the experiments carried out on the model coils and on the 100 kJ coil.

The series of pulsed tests on the model coils, which consisted of charging the coils to various fractions of the critical current in about 0.2 s and discharging in times between 4 ms and 0.2 ms at repetition rates of one and five pulses per second, are described in Section III-2, Limits of Performance. These tests, as indicated above, confirmed the validity of the analyses concerning the effect of transient heating within the windings. The 1 kJ nominal stored energy coil made from the single core conductor could be operated at a repetition rate of five pulses per second at a charge time of 0.167 s and a discharge time of 4 ms with an inter-pulse time of 25 ms to 0.89 of the coil critical current for pulse train lengths in excess of one minute without quenching. Also described in this section are the tests conducted on the 100 kJ coil.

Section III-3, Theory of Losses in Pulsed Coils, describes the various losses which may be present in a superconducting coil when operated in a pulsed mode and gives expressions whereby the magnitude of these losses may be calculated. Appendix I, Predicted Losses in Superconductors, gives the derivation of some of these formulae.

Section III-4, Loss Measurement Methods, describes two techniques by which these losses may be measured. The first, the helium boil-off method, consists of measuring with a gas meter the quantity of helium boiled off during a train of pulses. After allowance has been made for heat input from sources other than from within the coil windings, the quantity of boil-off gas can be related to the heat generation during a charge/discharge cycle of the coil. This method was used to measure the energy losses on the 1 kJ and 7 kJ model coils. The second method is an electronic method which involves integrating the voltage across the coil terminals and displaying it against coil current as a hysteresis loop. The area of the loop so formed is proportional to the energy dissipated during a charge/discharge cycle. Appendix II, Theory of the Loss Loop, gives a mathematical derivation of the theory of this technique. The description of this electronic technique includes a discussion of the specifications of the components of the circuit necessary to ensure an accurate result. Appendix III, Effect of Phase Shift and Drift Voltage on Loss Loop Measurement, derives an expression for the error introduced due to integrator voltage drift and phase shift. The analyses result in performance requirements for the integrator, the voltage divider, and the current shunt. The designs of the current shunt and the voltage divider are shown to be compatible with these requirements in Appendix IV, Non-Inductive Current Shunt, and Appendix V, High Resolution Voltage Divider, respectively.

Section III-5, Loss Measurements Made Using the 1 kJ Coil, describes experiments conducted to measure losses by the helium boil-off method. The influence of eddy currents in the dewar walls is discussed. The measured losses are compared with the theoretical losses, and an explanation is given of modifications to the loss model which would give closer agreement between the theoretical results and the experimental results.

Section III-6, Loss Measurements Made Using the 7 kJ Coil, describes the results of loss measurements made using the boil-off method and compares them with the theoretical losses. It also describes loss measurements made using the electronic method. Since the 7 kJ coil was contained in a metallic dewar, induced currents in the walls of the dewar influenced the hysteresis loop obtained from the coil. To quantify this effect, measurements of the self-inductances of the energy storage coil and the sense coil and of their mutual inductance were made over a range of frequencies at various temperatures. It was found that to avoid changes in mutual inductance due to the influence of the dewar, experiments would have to be run at frequencies less than 10 Hz.

A model for the coupling between the dewar and the 7 kJ coil at low frequencies (less than 10 Hz) was formulated, and the coupling equations are presented in Appendix VI, Electric Circuit Model for Dewar Losses. The contribution to the loss voltage due to the dewar as a function of frequency was calculated from this and compared with the predicted loss voltage due to the coil (derived in Appendix VII, Predicted Loss Voltage for 7 kJ Coil Due to Magnetization Losses). This comparison allowed a frequency regime to be identified in which the voltage due to the coil predominated. This frequency was about 0.1 Hz. Loss loop measurements were, therefore, made at a frequency of about 0.1 Hz (charge and discharge times of about two to three seconds) and at currents ranging from 150 A to 700 A.

Where they overlapped, the results of the energy loss measurements made by the boil-off method and by the electronic method were in reasonable agree-

ment. Explanations are given in terms of the theoretical model to explain differences between the experimental and theoretical losses.

Section III-7, Loss Measurements Made Using the 100 kJ Coil, describes loss measurements made on the 100 kJ coil by means of the electronic apparatus. As with the 7 kJ coil, inductances were measured at various temperatures over a range of frequencies to find the range over which they remained constant and therefore over which the electronic loss measurement technique would be usable. It was found that this range extended from dc to about 2.5 kHz. A series of loss measurements were made using the electronic technique at various coil currents and frequencies by allowing the coil to ring with various capacitors. A cross check was obtained by observing the rate of decay of the current oscillations. Agreement between the losses measured by the two methods was within experimental error. The section closes with a comparison between the theoretically predicted losses and the experimentally measured losses and an explanation of the differences between them.

Section III-8, Multiple Pulse Tests, describes a technique for extracting a series of pulses at very high repetition rates (~ 200 Hz). In this technique, the energy storage coil acts as an energy reservoir, which slowly runs down and feeds an intermediate energy storage capacitor. The coil stores enough energy for the whole pulse train and the capacitor enough energy for one pulse. There is a switch across the capacitor which is open while the coil is charging the capacitor. The switch consists of a tube made from an insulator connected at one end to a helium cylinder and with two electrodes at the other end. The electrodes are attached to the terminals of the intermediate energy storage capacitor, and the load is in one leg of the circuit. When the capacitor is charged to a preset voltage determined by the electrode spacing, the helium gas flowing from the cylinder past the electrodes breaks down, allowing the capacitor to discharge through the load. The arc is extinguished by means of a self-excited arc quench circuit across the helium switch, and the capacitor begins to charge from the coil again. Using this device, a series of 2.5 kJ pulses were obtained at a repetition rate of about 200 Hz. Appendix VIII, Design of Relaxation Oscillator to Produce a Series of Pulses from an Energy Storage Coil, describes the design of this circuit; and Appendix IX, Design of Arc Quench Circuit for Helium Switches, describes the design of the arc quench circuit.

In summary, the work carried out under this program demonstrated the feasibility of:

- (1) operating superconductive energy storage coils at rapid repetition rates to high fractions of the critical current.
- (2) building non-conducting dewars with properties entirely acceptable for use in rapidly pulsed cryogenic systems.
- (3) operating vacuum interrupters at rates of five pulses per second for thousands of cycles.
- (4) obtaining pulse trains at repetition rates of about 200 pulses per second by electronic means.

- (5) building vapor-cooled leads capable of operation at voltages in excess of 50 kV in a warm helium gas environment.
- (6) designing large dewars and coils by means of data obtained from small models.
- (7) predicting coil and dewar performance from theoretical analyses.

SECTION II

100 kJ COIL SYSTEM DESIGN

1. INTRODUCTION

This section of the report is devoted to a description of the design details of a superconducting coil energy storage system capable of storing up to 100 kJ and being pulsed at rates up to 5 pps. The objectives of this part of the program were to design a system that could be built and operated to yield information on the techniques that would be utilized to construct light weight superconducting coil systems capable of being repetitively charged and discharged at rapid rates.

The major elements of the system that are considered in this section are: the switching and control circuits; the dewar; the leads connecting the coil to the power supply and loads; and the superconducting coil itself. Figure 1 is a simplified schematic of the system that was built and tested. As shown the system consists of: a power supply in the form of a battery bank; a superconducting coil housed in a dewar; a room temperature switch used to apply battery voltage to the coil terminals when the coil is energized; a circuit consisting of a charged capacitor, tuning coil and switch used to extinguish the arc in the room temperature switch when it is opened at the end of the coil charging period; a load consisting of linear resistors used to absorb the coil energy; and a capacitor used to limit the rise time of the voltage wave when the coil energy is released to the load.

The circuit operates in the following fashion. First the capacitor in the arc quench circuit is charged to a predetermined voltage. Next the room temperature switch is closed allowing the coil to take on current from the battery bank. When the coil is charged to the desired level the room temperature switch is opened and an arc drawn across its contacts. When these contacts are fully opened, the switch (a triggered spark gap) in the arc quench circuit is closed allowing the capacitor in this circuit to discharge through the path formed by the arcing contacts of the room temperature switch. The discharge current from the arc quench capacitor flows in opposition to the battery bank current, forcing the current through the room temperature switch to zero thus extinguishing the arc across the room temperature switch contacts. The energy stored in the arc quench capacitor and the resonant frequency of this capacitor with the tuning coil connected in series with it are such that the voltage across the room temperature switch terminals is held below the restriking potential for a time long enough to allow the switch to regain its full dielectric strength. The energy stored in the coil is then discharged into the load.

The design described in this section is for a system that would be used as a test bed to gather data for use in designing future systems. The data of primary interest were: the losses sustained in the coil during pulsing; the voltage limits placed on the discharge pulse by the coil, leads and dewar construction; and the helium losses that the system would sustain during standby.

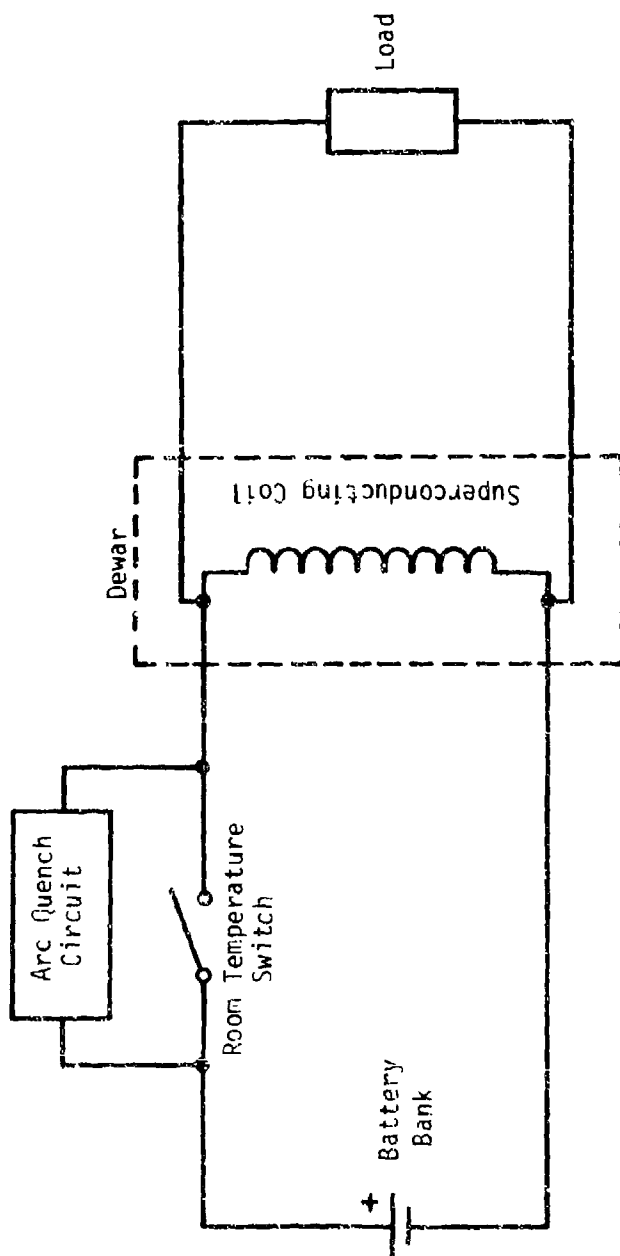


Figure 1 Schematic of Inductive Energy Storage System

2. SWITCHING AND CONTROL CIRCUITRY

The basic tasks to be accomplished by the electrical control system for the 100 kJ coil are (1) to charge the coil to at least 2,000 Amps (100 kJ), (2) to interrupt the charging circuit reliably in order to allow the coil to discharge at a variety of rates and voltages, (3) to provide protection against various types of possible equipment failures or operational errors. In addition, it is necessary that the system be capable of operation at the rate of 5 pulses per second, or at least be readily adaptable to this mode of operation.

a. Charging and Switching

The power supply selected for charging the 100 kJ coil consisted of a set of submarine batteries. For the initial (single shot) tests of the 100 kJ coil, it was decided to use a set of six of these 2-volt cells in order to form a 12-volt power supply with a very high (greater than 20,000 amp.) current capacity. Given such a 12-volt power supply, the charging rate for the 100 kJ coil (52 millihenries) is about 240 amps per second. This relatively slow charging rate makes possible the use of a simple mechanical timer to control the experiment and the use of a standard heavy duty contactor to provide a secondary means of interrupting the charging circuit should the primary (fast acting) device fail to operate. An additional safety feature was provided by the selection of conductor (3/0 electrical cable) such that the total electrical resistance of the charging circuit is about 3.7 milliohms, thus allowing a maximum system (short circuit) current of 3,250 amps; this ultimate system current is close to the predicted quench current for the 100 kJ coil.

As has been previously described(1), the primary switching arrangement for this system consists of a commercially available vacuum interrupter (Table I) that is driven by a hydraulic actuator whose schematic is given in Figure 2 and whose design has already been reported(1); the specifications are given in Table II. This vacuum interrupter fulfills the system requirements for high current capacity, high standoff voltage capability, very rapid recovery from arcs, and mechanical ruggedness. A photograph of the vacuum interrupter, hydraulic actuator assembly is given in Figure 3.

The opening and closing times of the vacuum interrupter were measured for a moderate range of hydraulic pressures (Figure 4) by means of the electrical circuit given in Figure 5. From these measurements it was concluded that adequate switching speeds for single shot operation were available at a hydraulic pressure of 1,000 psi; this operating point was selected for all the experiments that are reported herein to minimize the likelihood of oil leaks in the hydraulic system and to minimize the noise generated by the hydraulic pump. At a hydraulic pressure of 1,000 psi, the opening and closing times for the vacuum interrupter are about 40 milliseconds.

A secondary switching system consisting of a commercially available contactor (GE# IC2800, Y108 B109G) was installed to provide a second

Table I

SPECIFICATIONS
GENERAL ELECTRIC POWER/VAC VACUUM INTERRUPTERS
MODELS PV-03G & PV-03H

PV-03G-12-15A18 (3 Stud Mounting) Order No. 0186L0739P021, Outline Dwg. 086600573

PV-03H-12-15A18 (4 Stud Mounting) Order No. 0186L0739P022, Outline Dwg. 086600591

3 ϕ Rating, Symmetrical Basis

Rated maximum line to line voltage	15.5 kV, rms
Rated frequency	50/60 Hertz
Rated voltage range factor (K)	1.3
Low frequency withstand	50 kV, rms
Impulse withstand, full wave	110 kV, crest
Rated continuous current	
35° rise over 40° ambient	1200 amperes, rms
Generated heat loss at 1200 amps	22 watts
65° rise over 40° ambient (with heat sinks)	2000 amperes, rms
Generated heat loss at 2000 amps	60 watts
Rated short circuit current (at rated maximum voltage)	18,000 amperes, rms
Maximum interrupting Capability	23,000 amperes, rms
Maximum asymmetry factor (s)	1.3
Rated maximum voltage divided by "K"	12 kV, rms
3 second current carrying capability	23,000 amperes, rms
Momentary, close & latch capability	
with 400 pounds contact force	40,000 amperes, rms
with 850 pounds contact force	60,000 amperes, rms
Capacitance switching current, maximum	600 amperes, rms

Mechanical Data

Interrupter weight	24 pounds
Moving contact weight	3.70 pounds
Contact force due to atmosphere	25 to 45 pounds
Added force required for momentary	
40,000 amperes	400 pounds
60,000 amperes	850 pounds

Mechanism Requirements

Contact Stroke	0.75 inches
Opening speed (average to 9/16" gap)	6.5 to 7.5 ft/s
Overtravel, maximum	0.25 inches
Closing speed (average 1st 1/4" travel)	2.5 to 3.5 ft/s
Contact bounce duration, maximum	0.002 s

Table I (Continued)

Typical Interrupting Life

Contact erosion limit	0.125 inch
Mechanical life	10,000 unit operations
Shelf life (estimated)	20 years

<u>3 ϕ Breaker Series</u>		<u>3 ϕ Recloser Series</u>	
<u>*Unit Operations</u>	<u>Current Amps, Rms</u>	<u>*Unit Operations</u>	<u>Current Amps, Rms</u>
4	23,000	48	16,000
10	19,000	120	8,800
18	16,000	144	3,200

*Plus 5,000 unit operations at 2,000 amperes

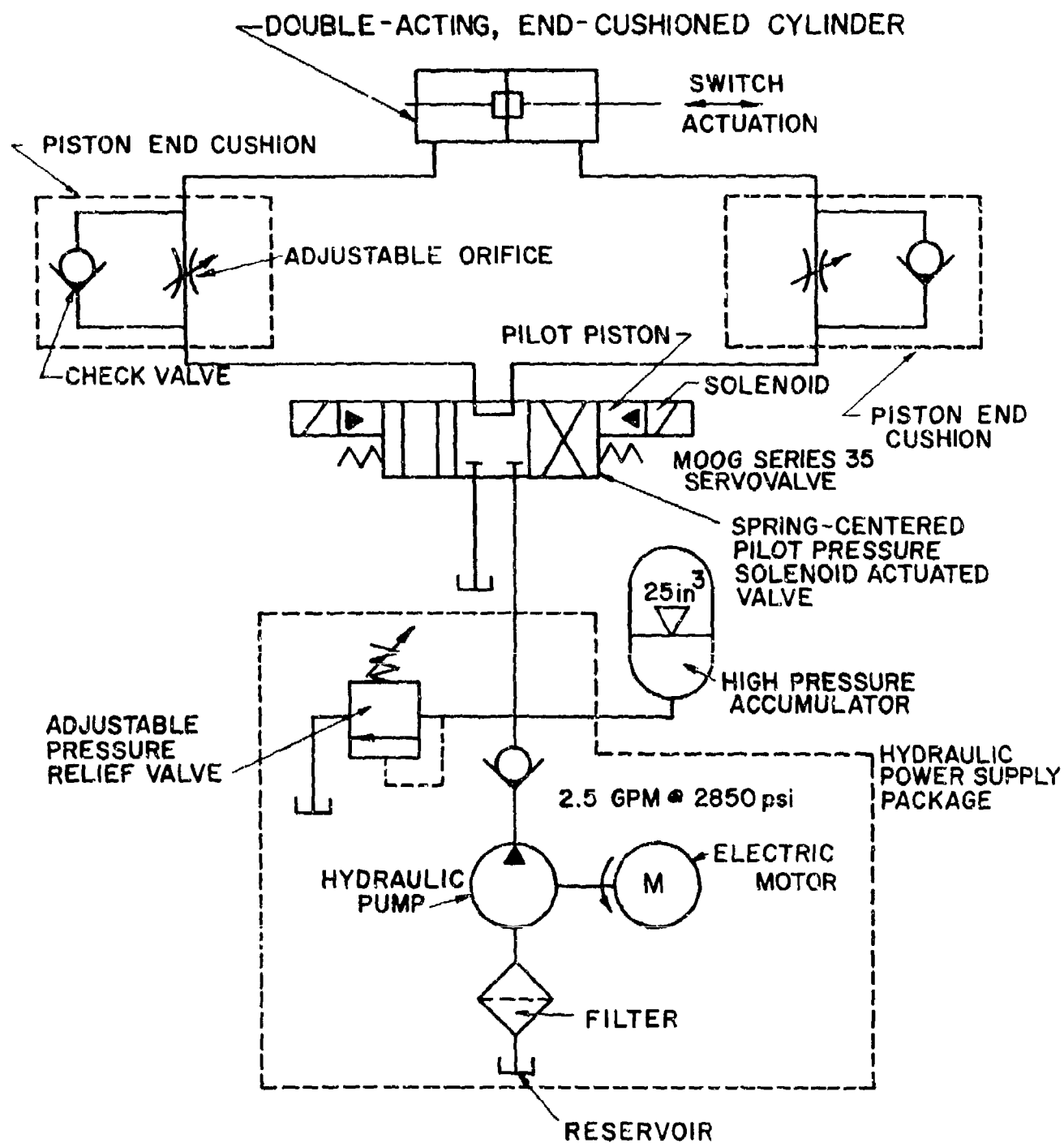


Figure 2 Hydraulic Circuit

Table II

SPECIFICATIONS FOR HYDRAULIC ACTUATOR

Overall Size	24" x 12" x 17" high
Weight (less hydraulic power supply)	44 pounds
Actuator stroke	0.8 inches
Actuator operating pressure	2,850 psi
Hydraulic fluid flow rate	2.5 gpm
Piston area	0.6 sq. inch
Closing time	8 milliseconds
Opening time	8 milliseconds

SPECIFICATIONS FOR HYDRAULIC POWER SUPPLY

Maximum output pressure	3,000 psi
Maximum flow rate	5 gpm
Drive motor	5 hp 220V, 3 ϕ
Reservoir volume	10 gallons
Pump type	Pressure compensated Variable displacement



Figure 3

Detail of vacuum interrupter (bottom), hydraulic actuator and backup contactor (top). Noninductive shunt is in oil bath at right.

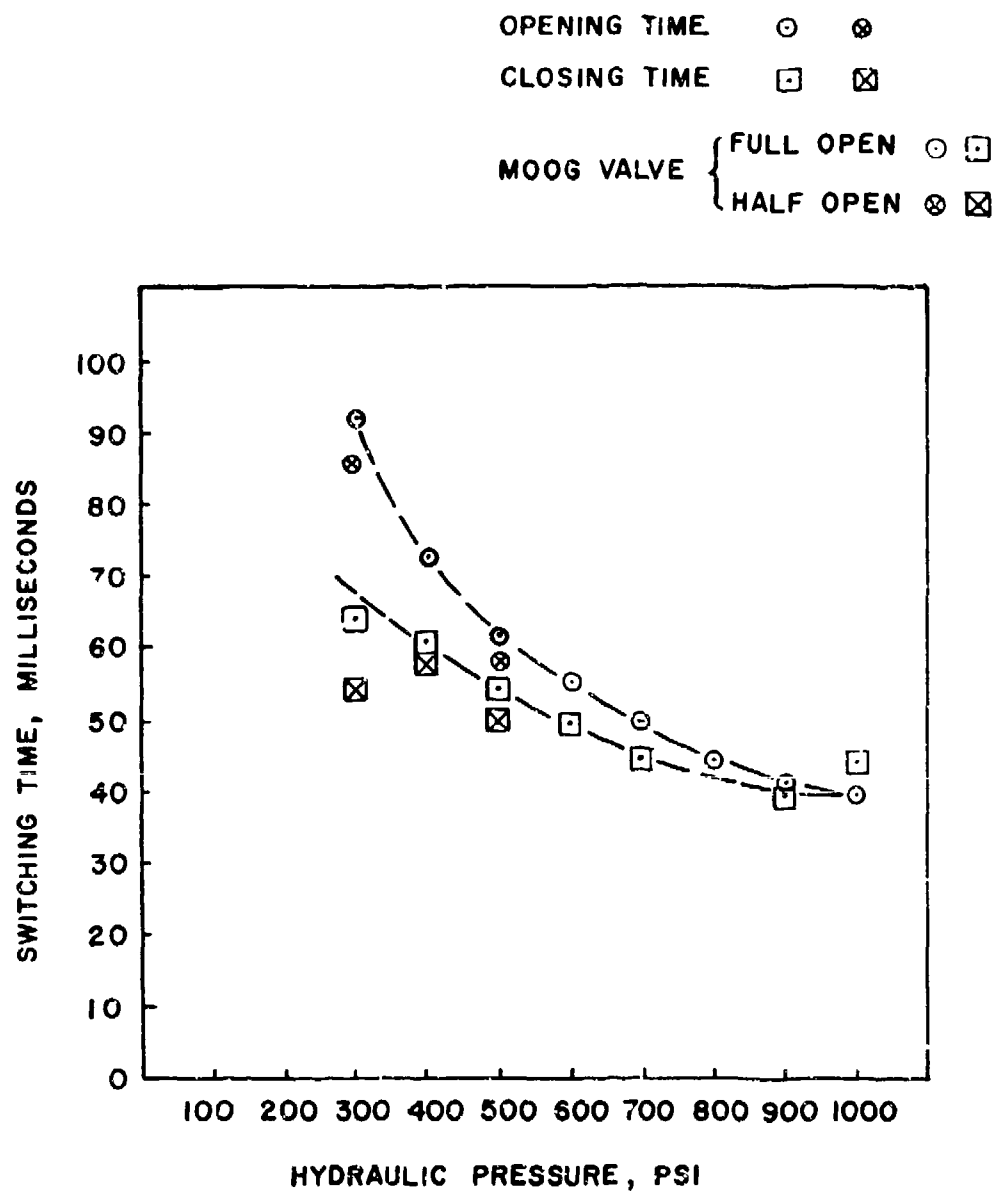


Figure 4 Actual switching times for vacuum interrupter driven by the hydraulic system using the Moog 35 Servovalve.

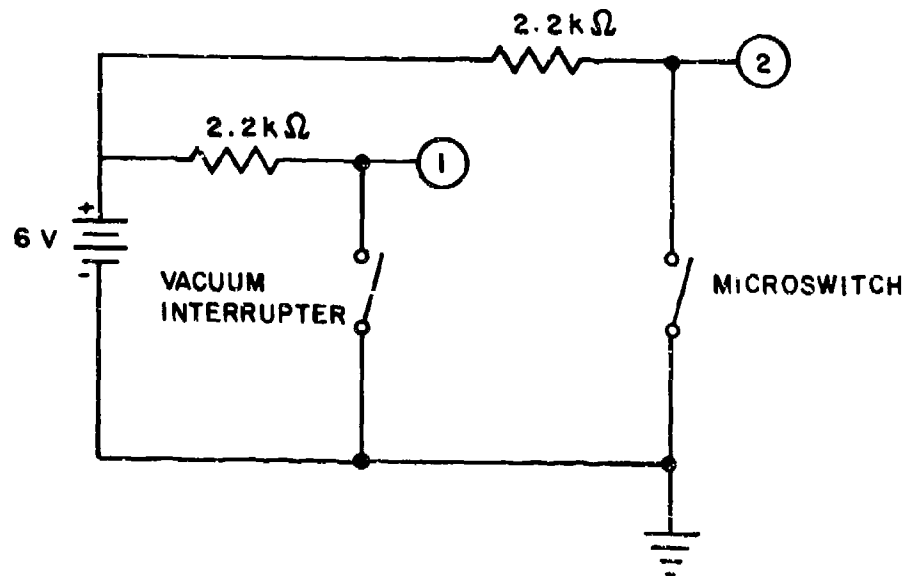


Figure 5 Electric circuit used for measurement of open and closing times of the vacuum interrupter. To measure opening time, trigger an oscilloscope from (1) and observe (2). To measure closing time, trigger from (2) and observe (1).

means of breaking the charging circuit should the vacuum interrupter fail to operate. In practice, both the vacuum interrupter and the backup contactor were commanded to open simultaneously; under normal conditions the vacuum interrupter opened the charging circuit (in 40 milliseconds) long before the opening of the contactor (250 milliseconds). With this arrangement, if the vacuum interrupter should fail to open, then the coil would be charged to a current that was at most 60 amps greater than the desired value before the backup contactor opened. An overall system schematic is given in Figure 6; a photograph showing the location of the contactor and resistor bank is given in Figure 7.

b. Arc Quench Circuit

For the vacuum interrupter to break the charging circuit reliably, it is necessary that some external means be provided to prevent arcing across the switch. In normal operation, the vacuum interrupter was opened, then the arc was extinguished by means of an external circuit whose function was to force the switch current to zero for sufficient time to allow recovery. The arc quench circuit that was selected is a simple series resonant circuit that is connected across the vacuum interrupter as shown in Figure 8; the component values are given in the arc quench circuit test setup shown in Figure 9. This circuit was tested over a current range of 640 amps to 2,750 amps, the full range required for operation of both the 7 kJ coil and the 100 kJ coil. The principle of operation is that when the spark gap (EG&G #GP-22B or EG&G #GP-12B) is fired, the capacitor discharges into the inductor through the switch, reducing the net switch current for the first half cycle (Figure 8). If the capacitor has been charged to the correct initial voltage, then the ringing current (capacitor voltage divided by circuit surge impedance, $\sqrt{L/C}$, which is about 10 ohms in this case) will cancel the switch current for a quarter of a cycle ($t \approx \sqrt{LC}$), allowing the switch to recover its blocking state. For the components selected, the current is held near zero for about 25 microseconds. An advantage of a simple ringing circuit over a circuit that provides a more carefully shaped pulse(1) for this arc quench application is that if the arc fails to extinguish on the first half cycle because of too high an initial voltage on the capacitor, then it may be extinguished one cycle later; in other words, the slowly decaying oscillating current in this circuit provides several opportunities for extinguishing the arc. An additional capacitor is placed across the load resistor (Figure 6) to limit the rate of rise of voltage across the vacuum interrupter thus increasing its likelihood of turning off. A photograph of the arc quench circuit is given in Figure 10 (the spark gap is in an oil bath; a spare spark gap is shown in the foreground) and a closeup of the resistor bank and its parallel capacitors is given in Figure 11.

c. Timing, Controls, and Interlocks

A mechanical control system was selected for single shot operation of the 100 kJ coil because of its simplicity and ruggedness. The sequence of required operations is shown in Figure 12. The automatic operations were controlled by a mechanical timer. As indicated in the

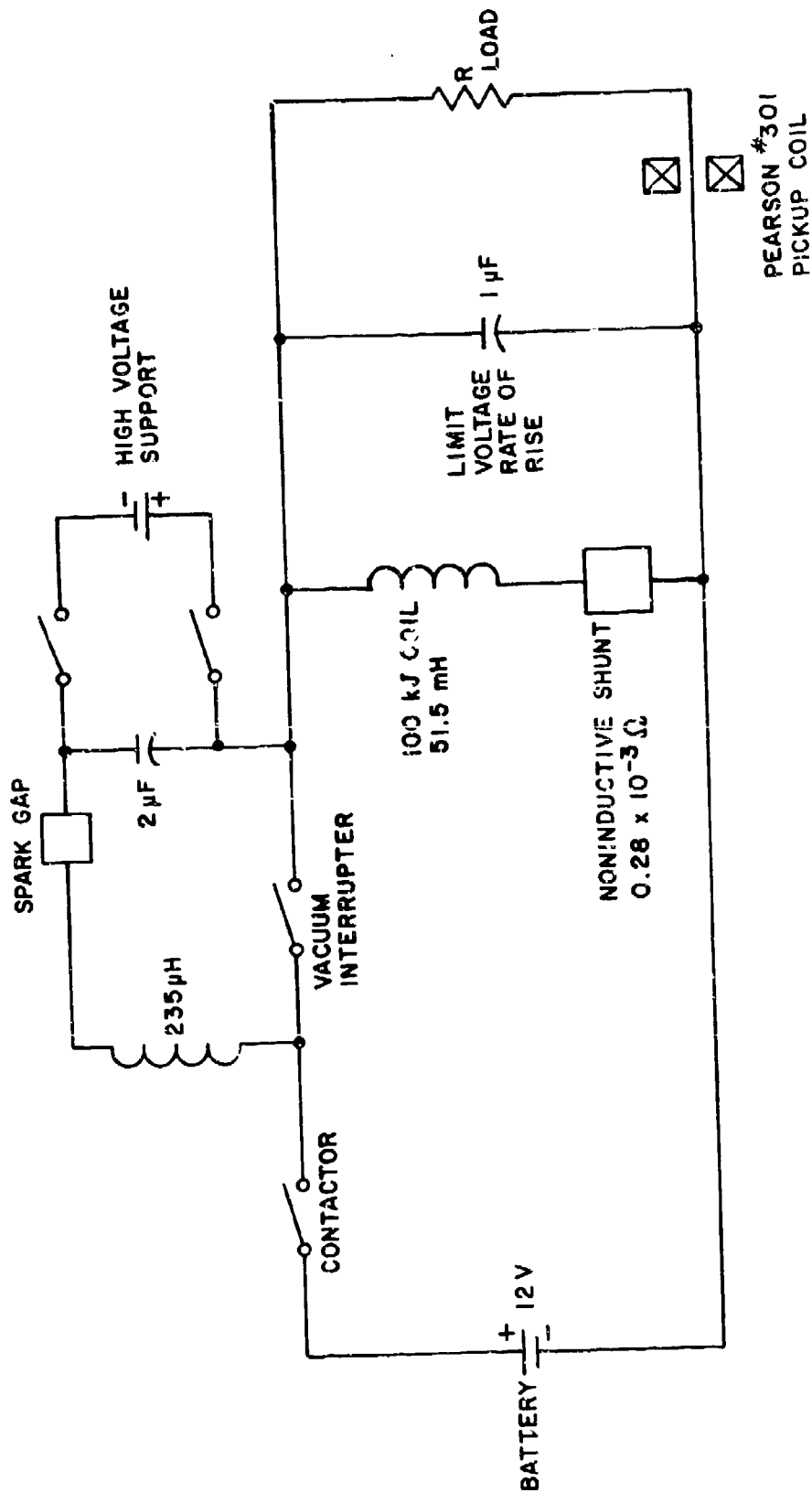


Figure 6: Overall Schematic of Electrical System for 100 kJ Coil

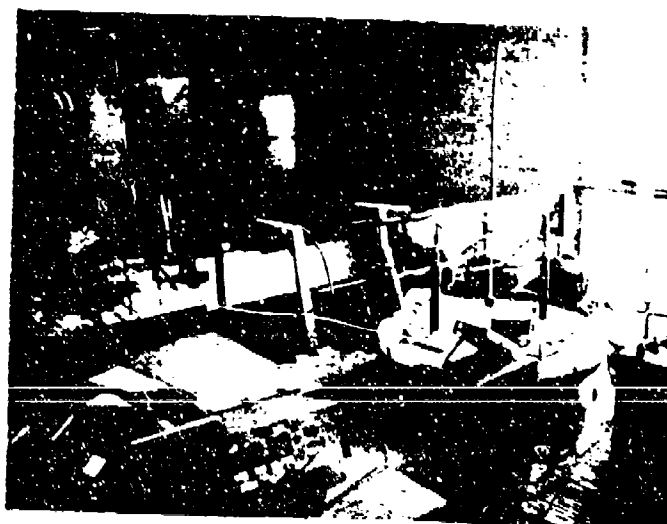


Figure 7 Overall view of experimental setup showing top of dewar for a 100 kJ coil, backup contactor, integrator, and oscilloscope.

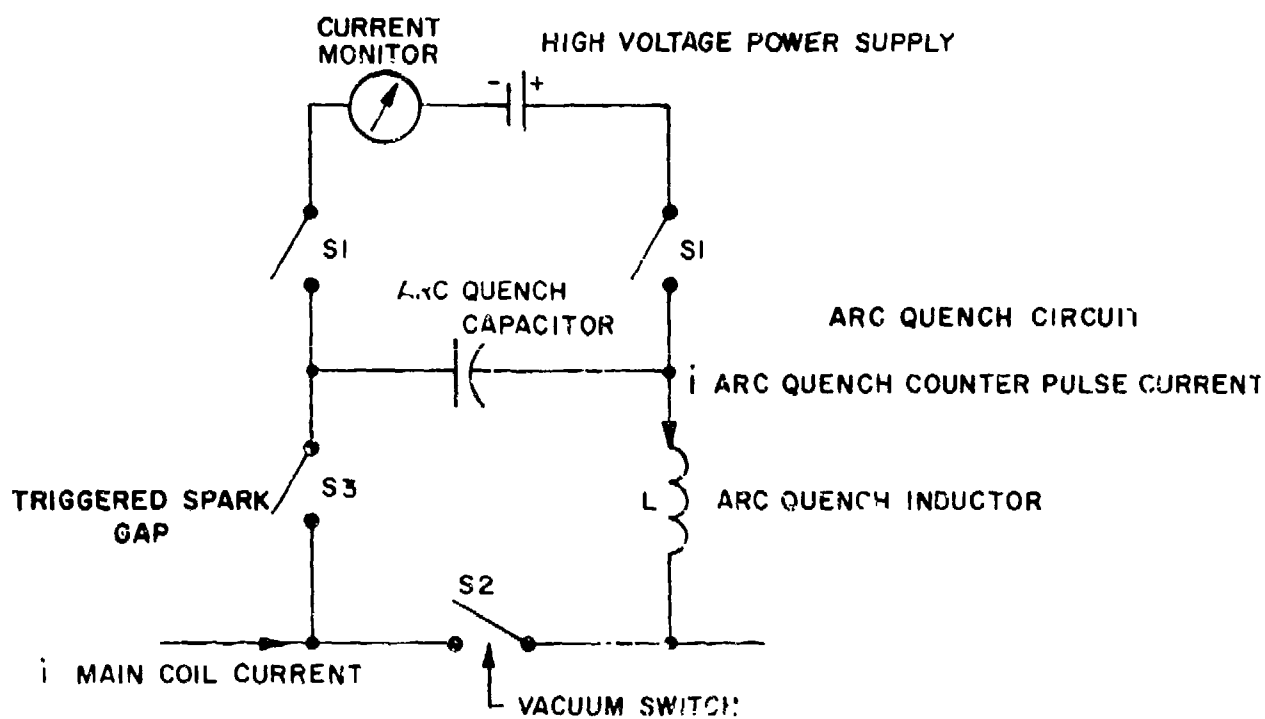
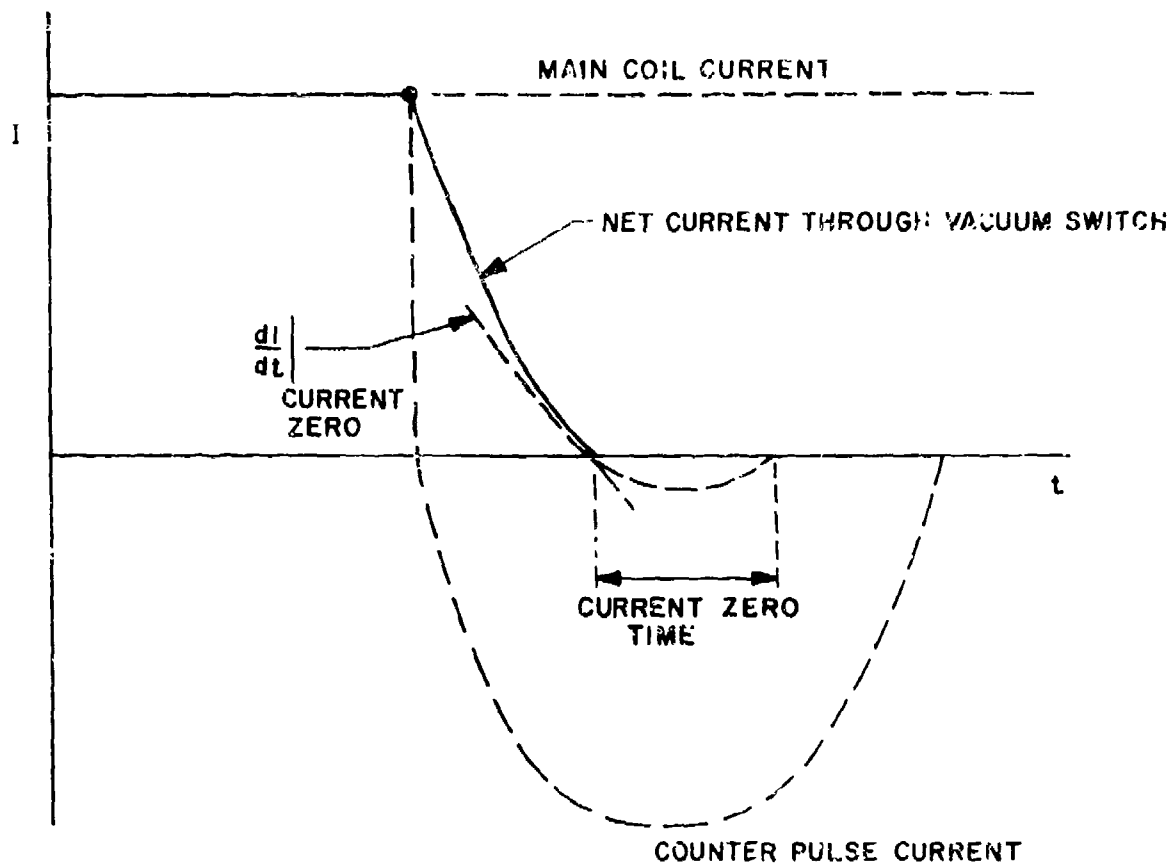


Figure 8 Schematic of Arc Quench Circuit and Counter Pulse Current.

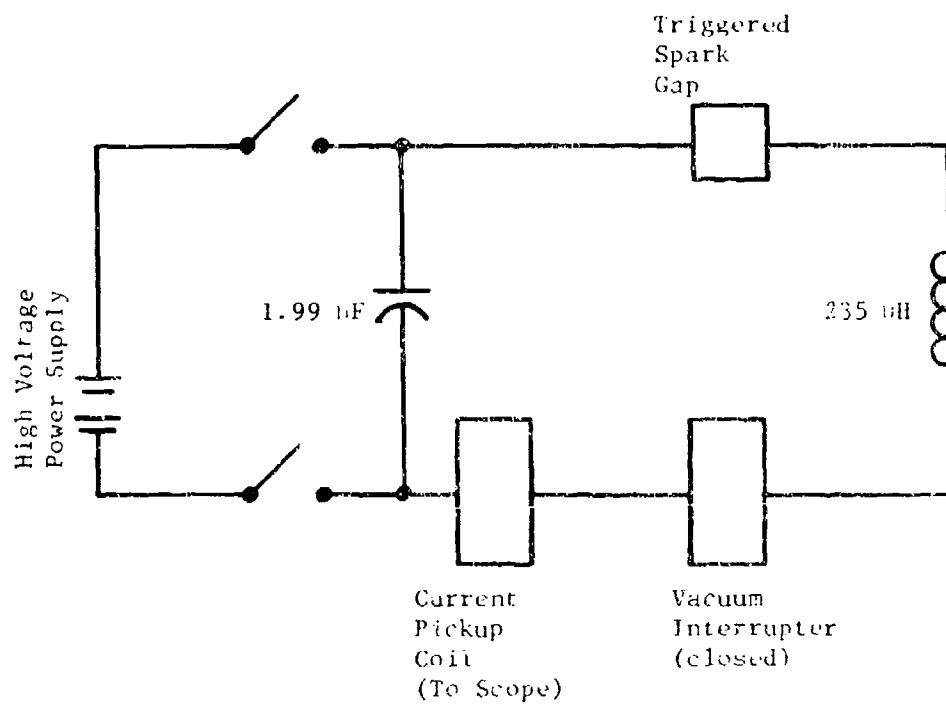


Figure 9 Experimental arrangement for testing the arc quench circuit.

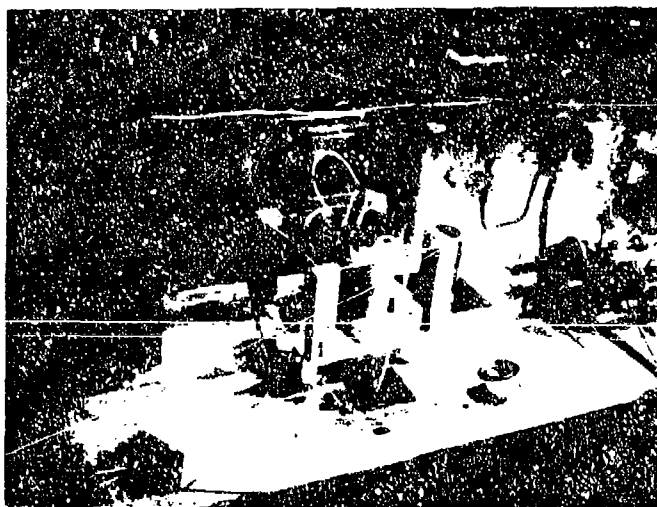


Figure 10

Detailed photograph showing battery (background), arc quench inductor, spark gap (in oil bath), spark gap actuator, hydraulic actuator for vacuum interrupter, and backup contactor.

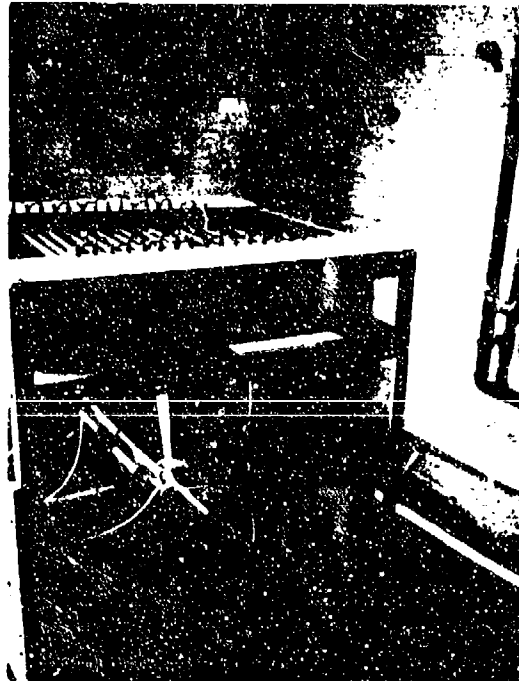


Figure 11 Closeup of resistor bank and parallel capacitors (total of 1 μ F at 60 kV).

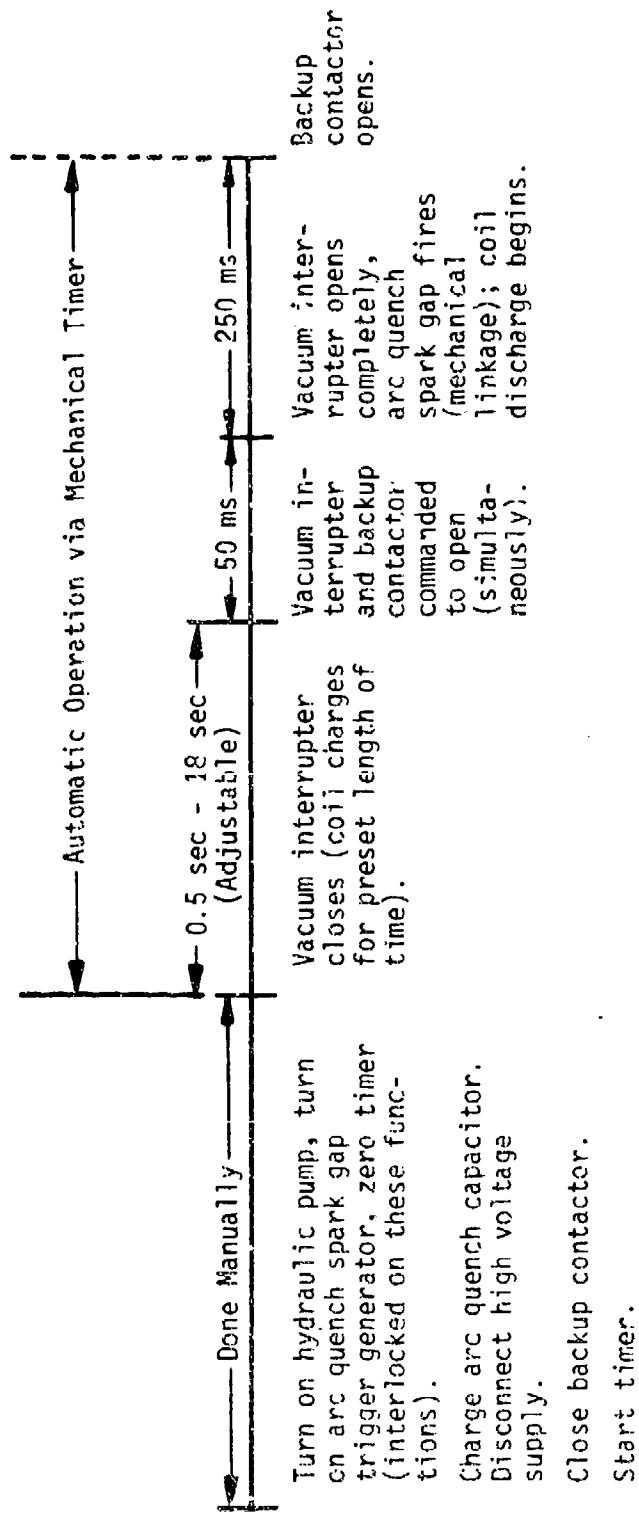


Figure 12 Timing diagram for operation of 100 kJ coil.

figure, interlocks are provided on several of the manual operations in order to minimize the chances of serious operational errors. It should be noted that the spark gap that controls the arc quench circuit is tripped by a microswitch that is activated by a linen phenolic rod attached to the plunger of the vacuum interrupter; this mechanical linkage together with an interlock on the power switch for the spark gap triggering unit ensured proper timing of the arc quench pulse. The actual implementation of the manual controls, interlocks, etc., was accomplished by means of a system of switches and relays that are connected as shown in Figures 13 and 14. This experimental arrangement proved adequate for all the experiments that were undertaken.

3. NON-CONDUCTING DEWAR DESIGN

a. Introduction

In inductive energy storage systems of necessity there are time varying magnetic fields. Furthermore, in systems which use cryogenic or superconducting magnets the magnet must be in a container which will maintain the cryogenic environment. This container will therefore be subjected to the time varying magnetic field unless the container is shielded in some way. This shielding could be achieved by making the energy storage coil in a toroidal geometry. However, studies (2) have indicated that toroidal systems are considerably heavier than solenoidal systems having similar operating specifications. Since weight is at a premium in this project, toroidal systems could not be used and efforts were directed to minimizing the weight of a solenoidal system.

It has been previously shown (2) that non-conducting dewars significantly reduce system weight. This saving comes from two sources. Firstly, non-metallic materials having higher strength to weight ratios than metals can be used thereby reducing the weight of the dewar. Secondly, the effects of electrical coupling between the energy storage coil and the dewar walls are eliminated. In a metallic dewar the time varying magnetic field induces eddy currents in the dewar walls. The energy which is dissipated in the walls is removed from the system by boiling off cryogen. Clearly this increases the overall system weight since additional cryogen must be carried on a mission to allow for this energy dissipation.

The technology of non-conducting dewars is not well developed and the purpose of this part of the program was to advance the state of the art of non-conducting dewar design to a point where a dewar large enough to contain the 100 kJ energy storage coil could be reliably built.

The development program was divided into three phases: non-conducting materials investigation (1); model dewar design, fabrication and testing; and full size dewar design, fabrication and testing. Each of these three phases will be dealt with in more detail below.

The non-conducting dewar eventually designed for the 100 kJ energy storage coil represents an intermediate stage in the development of a

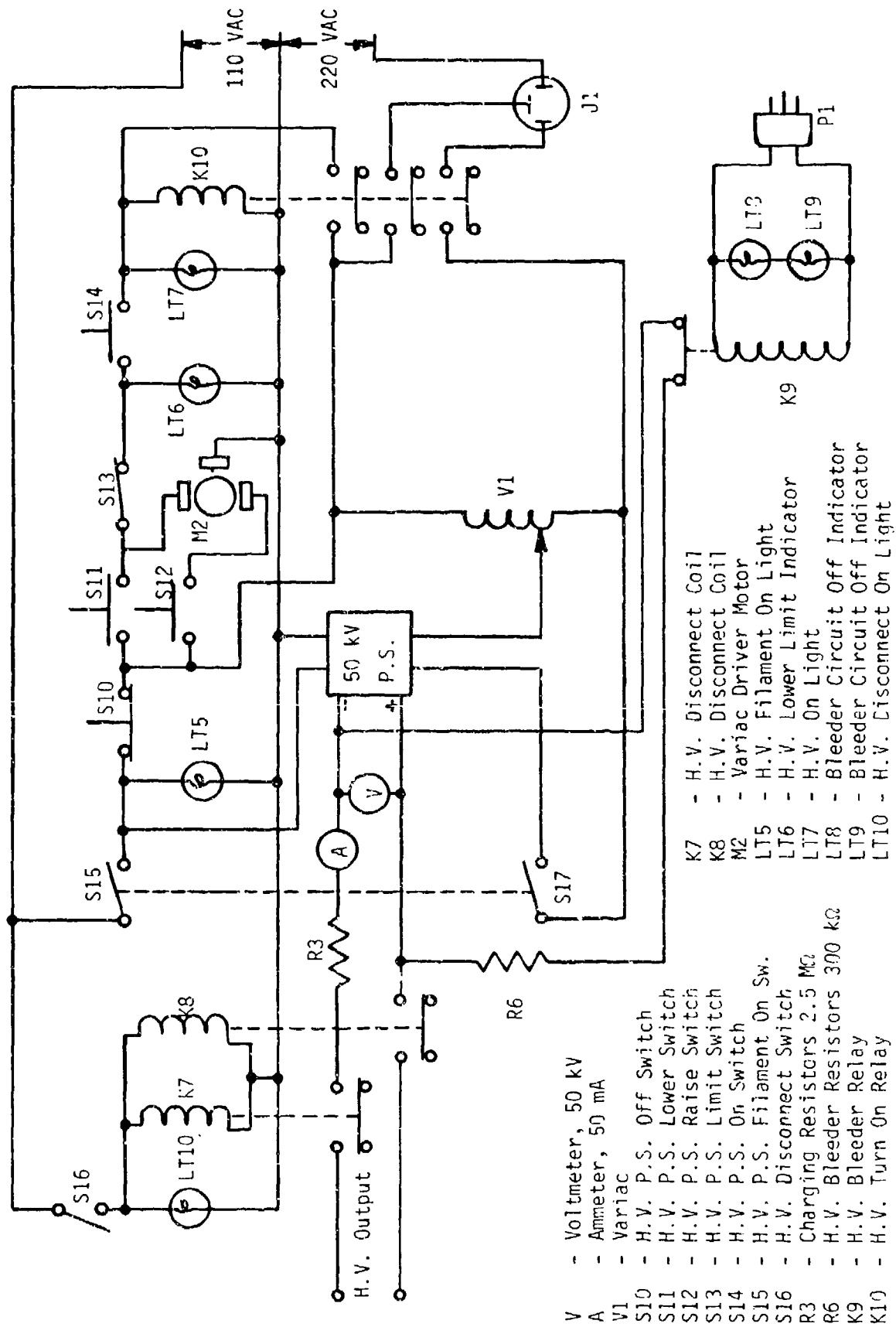
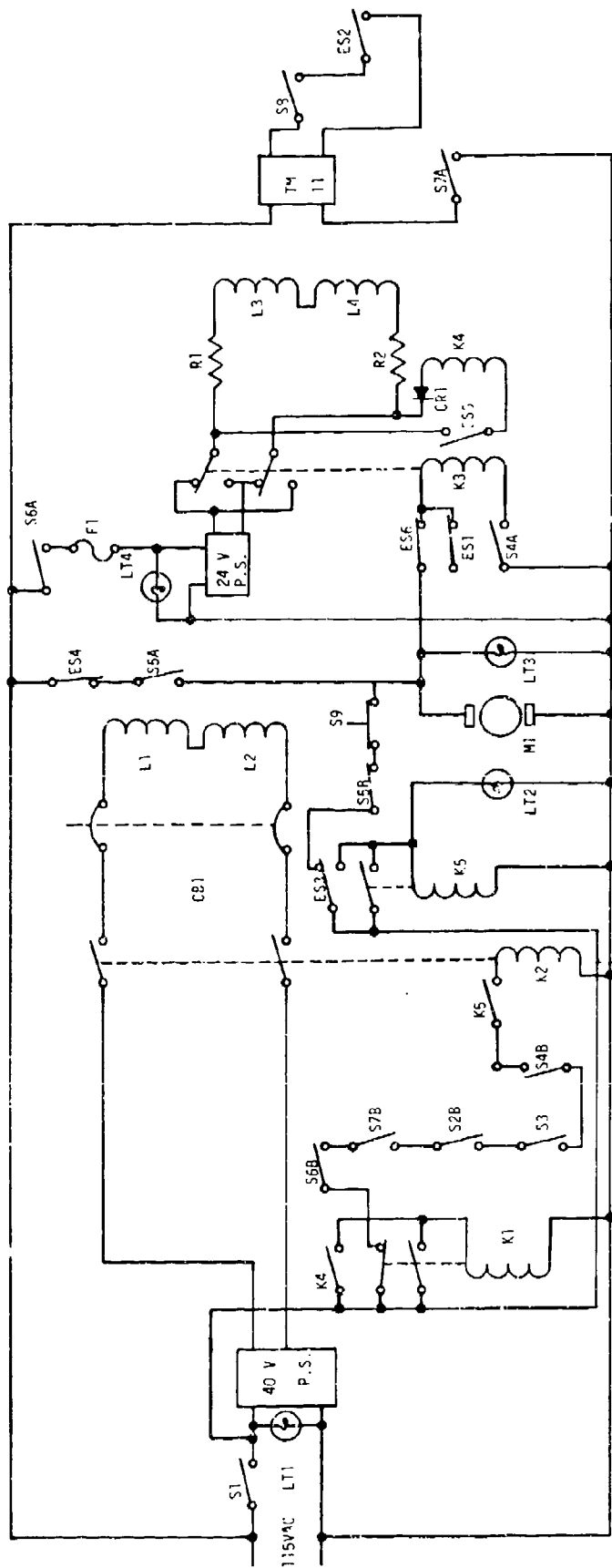
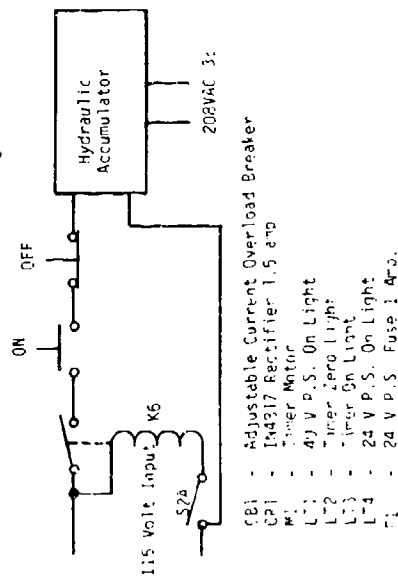


figure 13 Control panel schematic - high voltage controls.



- ES1 - Vacuum Switch Timer Switch
 ES2 - Arm Trigger Micro Switch
 ES3 - Timer Zero Switch
 ES4 - Timer Off Switch
 ES5 - Arm 24 V Relay Car Operated Contactor 044
 ES6 - Vacuum Switch Timer Switch
 K1 - Contactor Off Latching Relay
 K2 - Contactor On Relay
 K3 - 24 V Reversing Relay
 K4 - Contactor Opening Relay
 K5 - Timer Zero Interlock Relay
 K6 - Remote Power Relay
 L1 & L2 Contactor Coils
 L3 & L4 Moog Valve Coils

- S1 - Contactor P.S. On Switch
 S2A - Hydraulic Power On Switch
 S2B - Hydraulic Power Interlock Switch
 S3 - Contactor On Relay
 S4A - Vacuum Switch Emergency Off Switch
 S4B - Vacuum Switch Interlock Switch
 S5A - Timer On Switch
 S5B - Timer Interlock Switch
 S6A - 24 Volt P.S. On Switch
 S6B - 24 Volt P.S. Interlock Switch
 S7A - Trigger Module On Switch
 S7B - Trigger Module Interlock Switch
 S8 - Trigger Module Firing Switch
 S9 - Timer Zero Pushbutton
 R1 & R2 Current Limiting Resistors 500 ..



Control panel schematic - switching for operation of experiment.

Figure 14

light weight dewar suitable for airborne use. The emphasis in this design was on producing a thoroughly reliable dewar by using design procedures which would be applicable to the development of a light weight dewar but which did not in this case result in a minimum weight design. However, in addition to the three phase program outlined above, a light weight dewar design suitable for airborne use was produced (1). This design was based on the results of a parametric study carried out to arrive at a minimum overall weight system.

b. Thermal Insulation

In designing the dewar, consideration was given to the three basic types of cryogenic insulation: multiple radiation shields of aluminum foil and spacer or aluminized mylar, expanded polyurethane or polystyrene foam, and evacuated powder. In general, the foamed insulations have higher thermal conductivity than either powder or multilayer insulation. In addition, the high thermal contraction coefficient of the foams makes it undesirable as an insulation between two vessels. It was concluded that the most effective insulation for the light weight dewar would be multilayer insulation operating in a vacuum of better than 0.01 μ Hg of mercury. However, for the laboratory dewar where space and weight are not prime requisites, it was concluded that evacuated powder insulation would be entirely satisfactory and would result in a lower overall cost. The dewar was therefore designed with a 12-inch vacuum space all around the inner vessel to provide sufficient space to accommodate the desired quantity of powder insulation.

Micro-Cel T-4, a synthetic calcium silicate, was selected as the powder insulation most suitable for the application. It is a high efficiency cryogenic insulation which is a finely divided powder having free flow characteristics. It can be poured directly into the vacuum jacket through any suitable port such as the evacuation tube in the adaptor flange. Figure 15 shows a curve of overall thermal conductivity versus interstitial vacuum pressure for the powder. It can be seen that to reach its full potential (thermal conductivity equal to 5 μ W/cmK) the interstitial vacuum pressure must be below about 2 μ Hg. However, if the vacuum pressure is an order of magnitude higher (20 μ Hg), the thermal conductivity is only a factor of two higher (10 μ W/cmK) so that in this range the effective thermal conductivity is insensitive to pressure.

Thus one goal of the experimental program was to achieve a vacuum pressure of less than 2 μ Hg with powder insulation in the system and less than 0.01 μ Hg without powder insulation in the system. The former objective was easily achieved during testing the full size dewar and the latter objective was closely approached (0.02 μ Hg at 77 K) in the tests on the model dewars. It was expected that because of the cryopumping which occurs at 4.2 K the goal of 0.01 μ Hg would be surpassed in a system containing liquid helium.

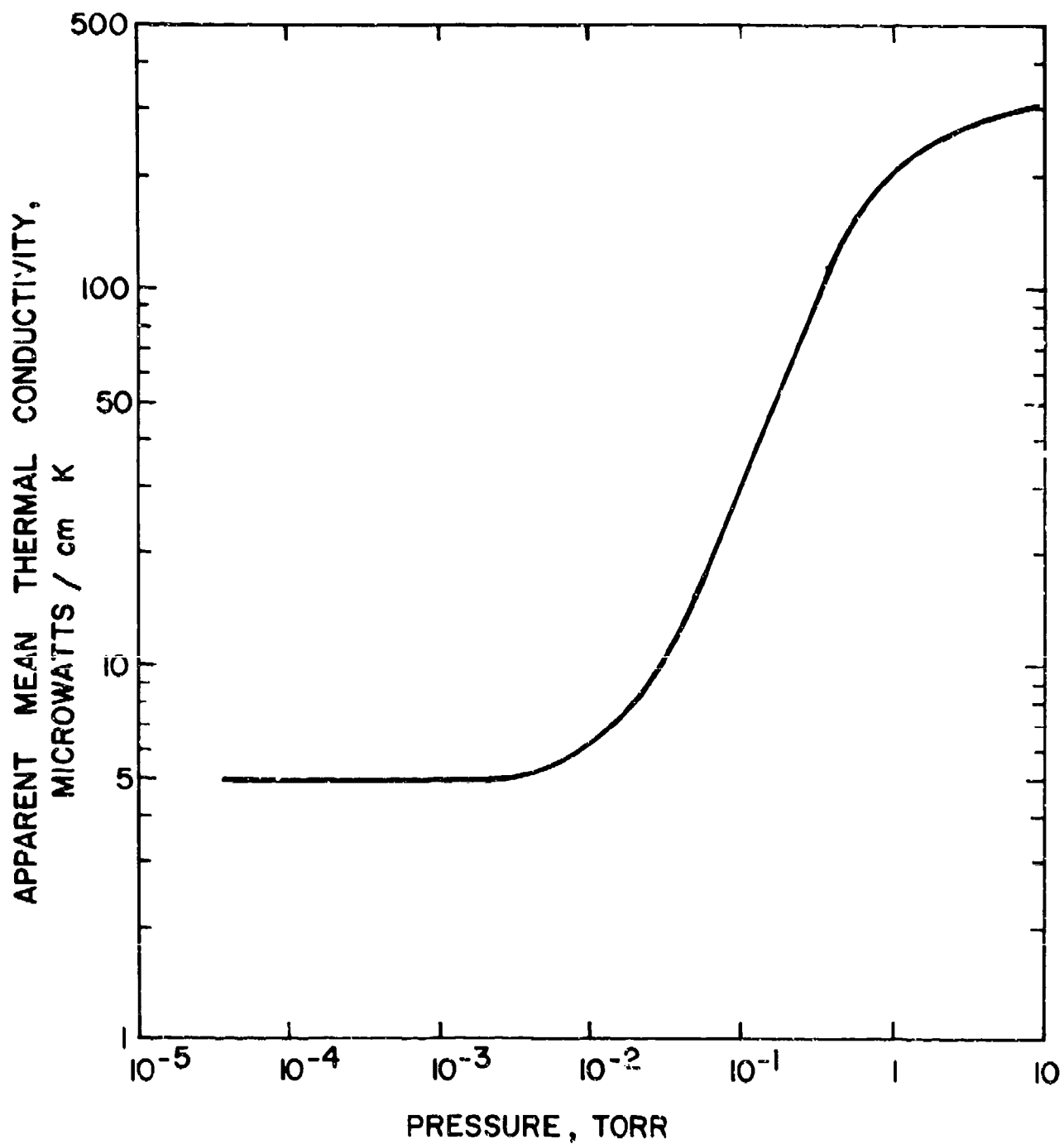


Figure 15 Thermal conductivity of Micro-Cel insulation as a function of pressure.

c. Non-Conducting Materials Investigation

The heaviest element of a liquid helium dewar is the outside room temperature shell since it must be designed to withstand the forces of atmospheric pressure acting on its external convex surface. It is usually constructed of either aluminum or stainless steel, both of which are electrical conductors. Our task was to find a non-conducting material of sufficient strength to replace these materials.

Mechanical tests (1) were conducted on specimens of materials likely to fulfill this requirement. In particular, tensile, compressive and shear properties were determined for various resin/glass composites having potential use as structural elements and shear properties were measured for epoxy resins having potential use as adhesives. Tests were conducted at room temperature and at 77 K. The results of the materials investigation are reported on more fully in AFAPL-TR-72-38, Vol. I which describes work conducted during the early phases of this program. However, a summary of the important aspects is given below.

As a result of these investigations on test specimens it was found that a 2-ounce fiberglass mat with polyester resin binder, and Narmco resin 7343 were suitable mechanically. These materials were therefore selected for further investigation.

To simulate conditions in the outer wall of a vacuum jacket a test chamber approximately 0.91 m long by 0.48 m diameter was fabricated from the 2-ounce polyester/fiberglass mat. The test chamber could be evacuated and could also be connected to a molecular sieve pump.

The test chamber was successfully evacuated and the vacuum pump disconnected. The molecular sieve pump was also disconnected. No leaks to atmosphere existed but because of outgassing from the walls of the chamber the pressure slowly rose. The pressure was monitored over a 64.5 hour test period and from the pressure rise an outgassing rate of $2.33 \times 10^{-7} \frac{\text{Torr l}}{\text{s cm}^2}$ was calculated. This is low enough for the material to be used as a non-conducting dewar fabrication material.

The efficiency of the molecular sieve pump was investigated next. The test chamber was again evacuated and the vacuum pump disconnected but this time the chamber was left connected to the liquid nitrogen cooled molecular sieve material. During a 24 hour test the vacuum was maintained at 0.06 μHg which is a more than adequate ultimate vacuum pressure for walls at room temperature.

A comparison of the results of the tests on non-conducting structural materials, the desired properties of non-conducting structural materials, and stainless steel is summarized in Table III.

d. Model Non-Conducting Dewars

The tests on non-conducting materials described above established that hand laid up polyester fiberglass is mechanically strong enough at

Table III
COMPARISON OF PROPERTIES OF FIBERGLASS AND STAINLESS STEEL

Property	Fiberglass		Stainless Steel
	Desired Value	Measured Value	
Tensile yield strength	10,000 psi	9,000 psi	35,000 psi
Compressive yield strength	10,000 psi	13,000 psi	35,000 psi
Elastic modulus	1×10^6	0.8×10^6	30×10^6
Density	0.07 lbs/in^3	0.05 lbs/in^3	0.3 lbs/in^3
Vacuum outgassing rate	$1 \times 10^{-6} \frac{\text{Torr } \ell}{\text{s cm}^2}$	$2.33 \times 10^{-7} \frac{\text{Torr } \ell}{\text{s cm}^2}$	$1 \times 10^{-7} \frac{\text{Torr } \ell}{\text{s cm}^2}$
Vacuum leak rate	0	0	0
Typical outer shell weight	15 pounds	13 pounds (calculated)	37 pounds

room temperature and liquid nitrogen temperature to withstand the forces due to atmospheric pressure and that at room temperature a shell made from this material is satisfactory from a vacuum standpoint. Therefore, the room temperature shell of a non-conducting dewar could certainly be made from this material. However, it was not at all clear as to whether this material would hold a vacuum if subjected to cryogenic temperatures. Although its gross mechanical properties are satisfactory at liquid nitrogen temperature, none of the tests previously conducted would show whether the material delaminated slightly when cold shocked. Even slight delamination could cause the material to become porous thereby destroying its vacuum integrity. Therefore, before embarking on the design and fabrication of the full scale non-conducting dewar for the 100 kJ coil we decided to build a model dewar and to test it under conditions similar to those to which the full scale dewar would be exposed. Figure 16 is a photograph of the model non-conducting dewar inner shell. The material used for its construction was the same hand laid up polyester/fiberglass that was evaluated in the materials evaluation phase of the program.

A test chamber consisting of a steel jacket and flange was built to house the model non-conducting helium container during evaluation. This test chamber simulates the outer room temperature dewar wall. A scale drawing of the model dewar in its test chamber is shown in Figure 17.

A schematic of the apparatus used to evaluate the model non-conducting dewar is given in Figure 18 and photographs of the same apparatus can be seen in Figure 19. It consists of the test chamber and model non-conducting dewar with a pumpout port connecting to either a mechanical roughing pump or a helium mass spectrometer.

The first tests conducted on the hand laid up polyester/fiberglass model dewar were without the powder insulation in the vacuum space. With the dewar at room temperature the system was evacuated. A pressure of 6 μ Hg was recorded. Liquid nitrogen was then poured into the dewar and the pressure began to fall. This is to be expected since the recorded pressure is due to the vapor pressure of the resin binder which decreases with temperature. After about two minutes the pressure had fallen to about 0.8 μ Hg. However, it then started to rise and after about 10 minutes was up to about 75 μ Hg. It appeared that the cold shock had delaminated the polyester/fiberglass material thus making the dewar walls porous. Later inspection of the dewar confirmed this since the surface of the dewar was crazed with hairline cracks. Obviously, the material under investigation was not suitable for cryogenic use.

Alternative materials were sought and a second model dewar having the same dimensions as the first was made, the material used being hand laid up epoxy/fiberglass. Similar tests were conducted on the second model and similar results were obtained. This material too was not suitable for cryogenic applications.

Since the problem was one of delamination when subject to cold shock clearly what was needed was a material with greater bond strength

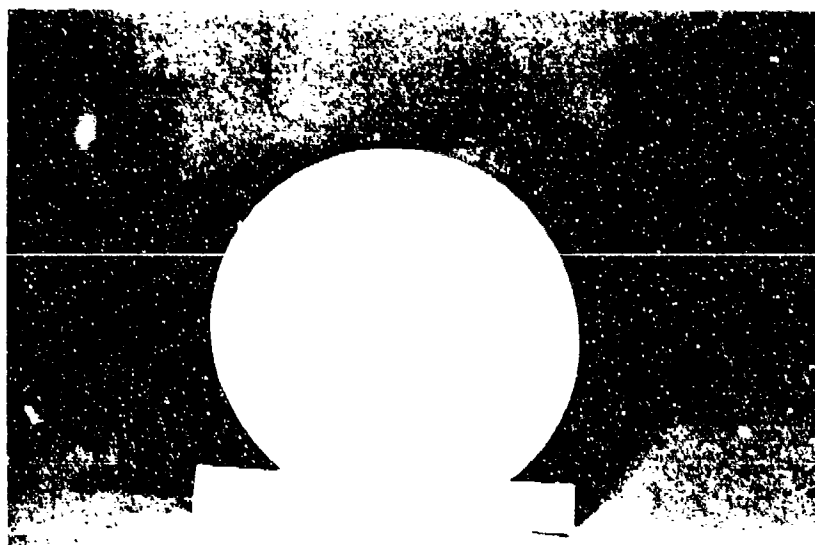
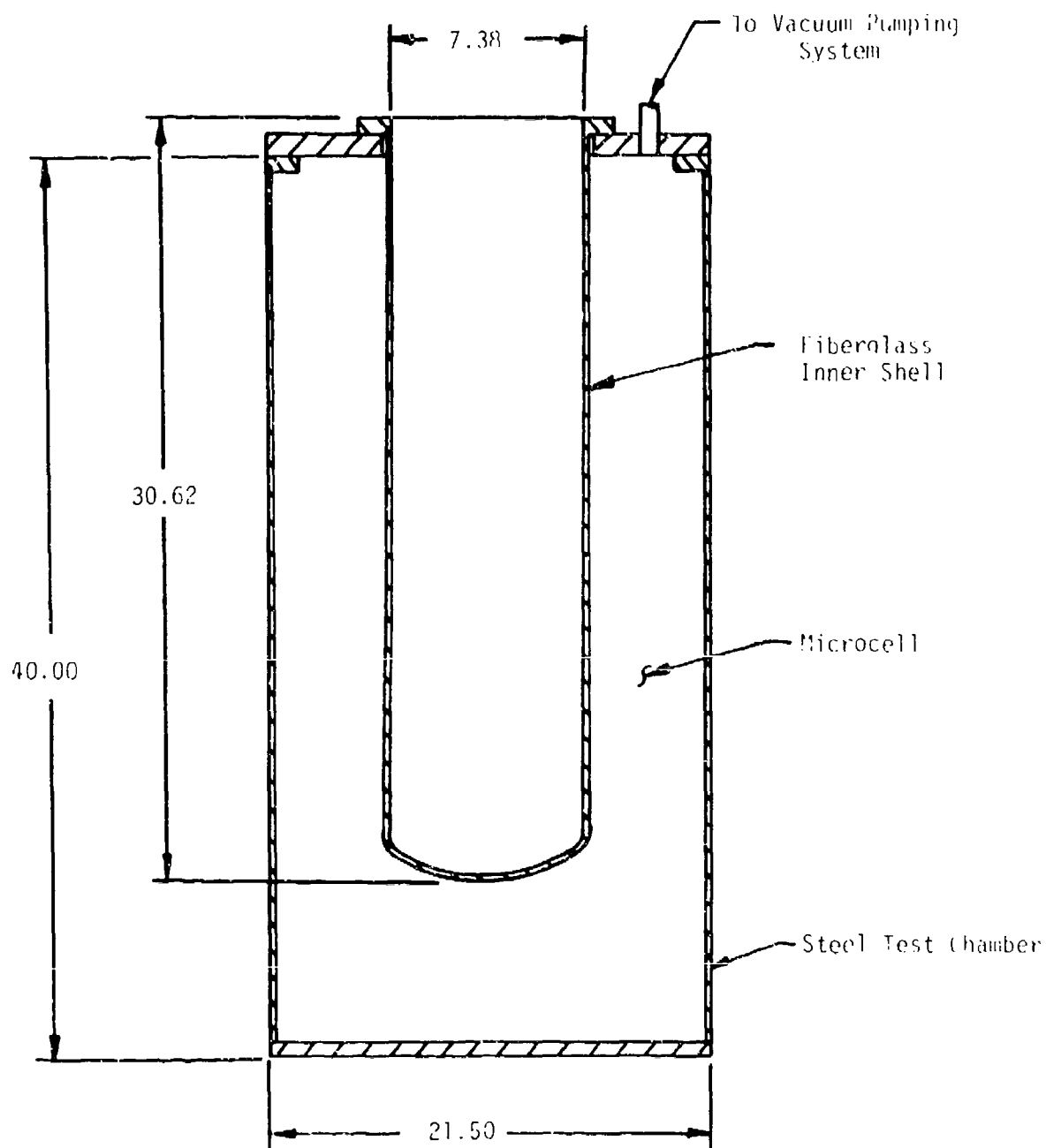


Figure 16

Fiber-glass helium container for model non-conducting
dewar



Dimensions in inches

Figure 17 Model Fiberglass Dewar in a Steel Test Chamber

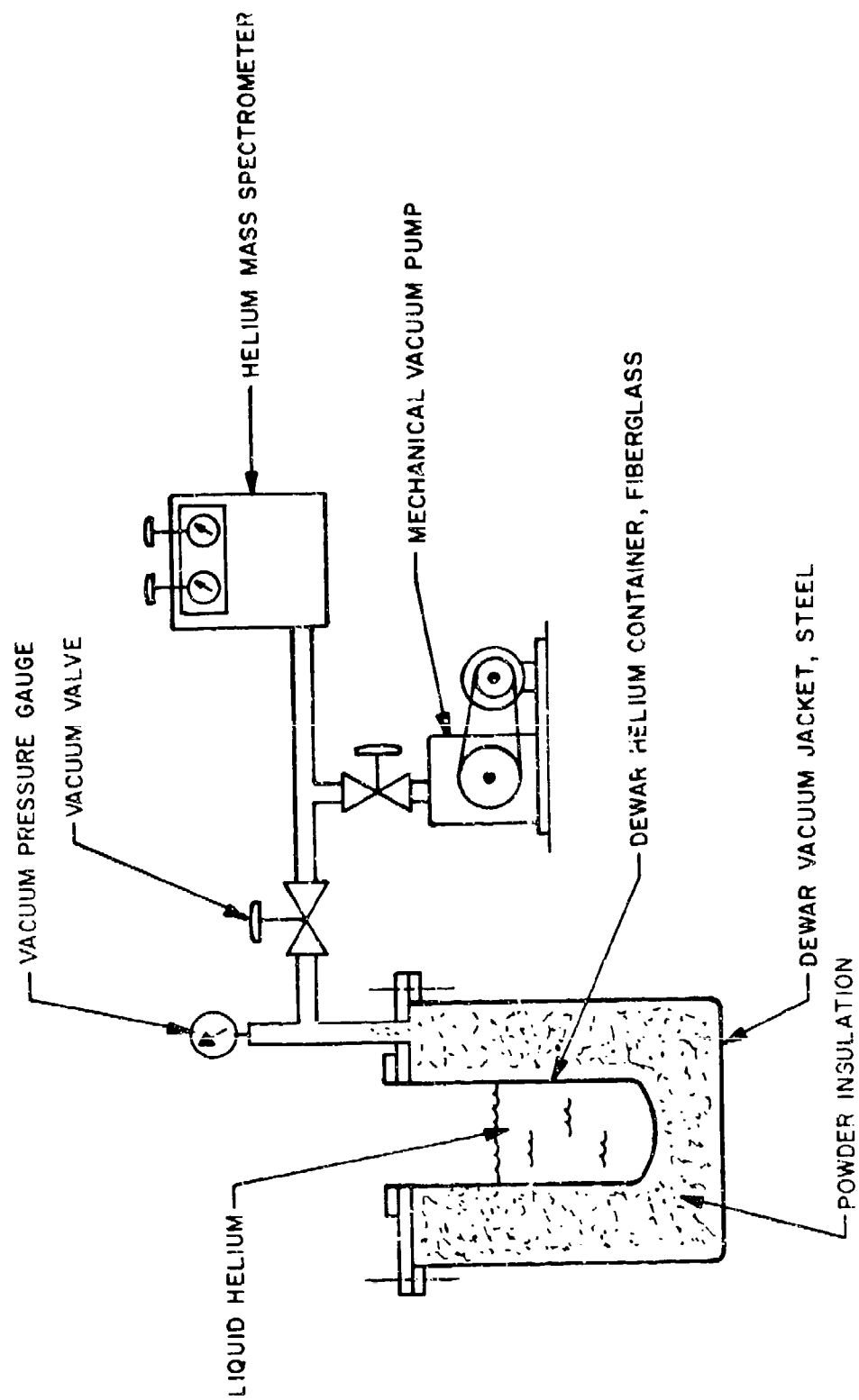


Figure 10 Experimental setup to evaluate helium permeability rate of fiberglass.

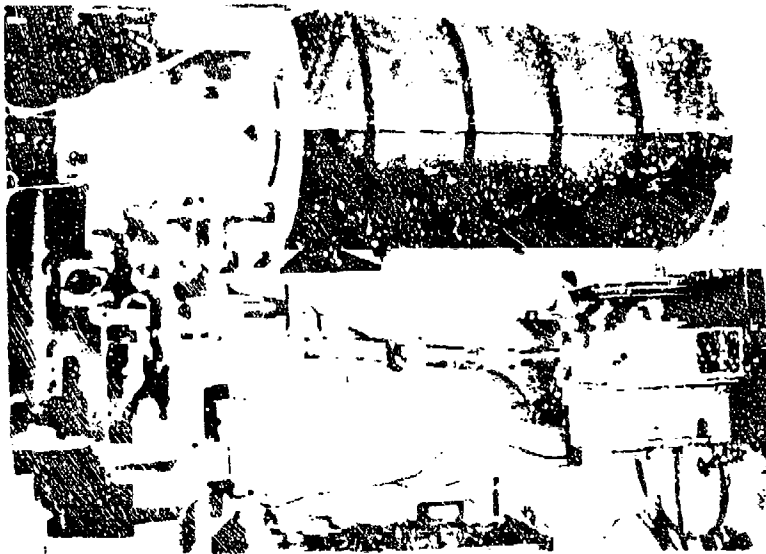


Figure 19 Experimental apparatus used for evaluating various model non-conducting dewars. Apparatus includes vacuum pump, leak detector, and dewar assembly. The dewar assembly consists of an outer metallic container and top plate into which is inserted the model non-conducting dewar which is being evaluated.

between laminations. A material with properties similar to G10 (an epoxy/glass cloth material widely used in cryogenic applications) was required. Eventually such a material was found. It is an epoxy/fiberglass cloth which can be laid up around a mold having the desired shape and then cured in an autoclave under conditions of high temperature and high pressure. The resulting appearance of the material is very similar to G10. A comparison of the properties of this material and the originally used hand laid up polyester-fiberglass is given in Table IV.

A third model dewar was constructed using this G10-like material and testing proceeded as before. At room temperature without powder insulation in the vacuum space a pressure of 0.3 μ Hg was recorded. When liquid nitrogen was poured in, the pressure dropped to 0.02 μ Hg. It was not possible to check the pressure at 4.2 K because without the powder insulation in the system the radiation heat leak from the room temperature walls would have been too great to allow liquid helium to collect in the dewar. However with a pressure of 0.02 μ Hg at 77 K only a factor of two decrease in pressure is required to reach 0.01 μ Hg which is the desired operating pressure for an advanced light weight dewar using multilayer insulation instead of powder insulation. Since the cold surface in such a system would be at 4.2 K it is felt that the desired pressure would be easily attained.

The test chamber was then filled with powder insulation and helium diffusion tests were conducted using the helium mass spectrometer. At room temperature and at 77 K the helium diffusion rate was not measurable. However, when liquid helium was transferred into the model dewar a small but measurable leak rate was measured. In terms of the surface area of the dewar available for diffusion this rate was 3.04×10^{-8} $\text{cm}^3/\text{s ft}^2$. We subsequently found a leak in the test apparatus and so the result quoted above may be spurious. However, taking the above value as a worst case the dewar could be run for three months between dewar evacuations using a 0.5 g of 5X molecular sieve as a getter. This is an entirely satisfactory result from a system operation standpoint. The heat leak as measured by helium boiloff was 0.5 W which is also satisfactory.

The results of the model dewar evaluation tests are summarized in Table V.

e. 100 kJ Coil Non-Conducting Dewar Design

The selection of materials for the 100 kJ coil non-conducting dewar was based on the evaluation tests described above. The following is a summary of the results of the test program and the reasoning used for selecting materials for the various components of the dewar.

A number of model dewars were tested under operating conditions. Both hand laid up polyester/fiberglass and epoxy/fiberglass were found to be suitable for the room temperature shell of a dewar, but were found lacking for cryogenic use; the hand laid up materials would not withstand the cold shock when subjected to cryogenic temperatures. However,

Table IV
COMPARISON OF PROPERTIES OF NON-CONDUCTING MATERIALS

<u>Material characteristics</u>	<u>Hand laid up fiberglass, polyester (failed in test)</u>	<u>Autoclaved fiberglass, epoxy (new material)</u>
Tensile strength	9,000 psi	51,000 psi
Elastic modulus	0.8×10^6 psi	3.3×10^6 psi
Compressive strength	13,000 psi	57,000 psi
Specific gravity	1.38	1.80

Table V
SUMMARY OF MODEL DEWAR TESTS

	Model 1	Model 2	Model 3
Material	Polyester fiber-glass (hand laid up)	Epoxy fiber-glass (hand laid up)	Epoxy fiber-glass (autoclave)
<u>WITHOUT MICRO-CEL INSULATION</u>			
<u>Vacuum Tests</u>			
Pressure at 293 K	6 μ	---	0.3 μ
Pressure at 77 K	0.8 μ after 2 min 75 μ after 10 min	---	0.02 μ
No. of Cycles 293K-77K-293K	1	1	3
Conclusion	Failed	Failed	Satisfactory
<u>WITH MICRO-CEL INSULATION</u>			
<u>Helium Diffusion Tests</u>			
Temperature 293 K	---	---	Not measurable
Temperature 77 K	---	---	Not measurable
Temperature 4.2 K	---	---	3.04×10^{-8} $\text{cm}^3/\text{sec ft}^2*$
Estimated running time between dewar evacuations	---	---	3 months with 0.5 g 5X mole- cular sieve [†]
Conclusion	---	---	Satisfactory
<u>Heat Leak</u>			
Measured by He boiloff	--	---	0.5 Watts
Conclusion	---	---	Satisfactory

*Possibly spurious because of leak subsequently found in test apparatus.

[†]Worst case calculation based on the above possibly spurious result.

the model dewar made from epoxy/fiberglass fabricated under high temperature and high pressure conditions was found to have excellent properties both at room temperature and cryogenic temperature. Experiments indicated that it would hold liquid helium with acceptable heat leaks, would not allow appreciable amounts of helium to diffuse through the walls and would withstand cold shock repeatedly. This material would be more than adequate both at room temperature and liquid helium temperature. However, since it is much more expensive than hand laid up material, in the interests of economy we decided to use this material for the helium can only and to use hand laid up polyester/fiberglass (whose room temperature properties are adequate) for the much larger room temperature shell.

Since the adaptor flange which connects the inner shell to the outer shell is always exposed to room temperature the structural material used in this was polyester/fiberglass. However, to limit the stress and deflection in this plate when the dewar is evacuated, this plate must be several inches thick. Therefore, for ease of handling and to reduce costs it was made lighter by employing a laminated type of construction. The flange consists of a central layer of polyester/fiberglass sandwiched between two layers of balsa wood which in turn are sandwiched between two more layers of polyester/fiberglass. The polyester/fiberglass layers are 0.5 inch thick and the balsa wood layers 0.75 inch thick. The whole assembly is vacuum sealed with a thin layer of polyester/fiberglass. This type of construction increases the modulus of the flange without a large increase in weight. The specific gravities of polyester/fiberglass and balsa wood are 1.38 and 0.25 respectively.

Since for this system weight is not of prime importance, it was decided that the expense of developing a light weight radiation shield should be eliminated by using Micro-Cel T-4, a powder insulation, in the vacuum space. This material is suitable provided that the pressure in the vacuum space can be maintained below about 10 μ Hg. This material was used in the evaluation tests on the model dewars and it was found that the pressure could indeed be kept below 10 μ Hg and that under these conditions the heat leak was acceptable. Therefore, Micro-Cel T-4 was used in the design of the 100 kJ coil dewar.

To minimize heat leak due to radiation down the mouth of the dewar a large foam plug was built from open cell expanded polyurethane foam. The length of this plug is about 30 inches and its diameter is about 34 inches. It is attached to the lower face of the dewar cover plate. The temperature at the bottom of the neck plug was estimated to be well below liquid nitrogen temperature which is more than adequate.

The 100 kJ coil non-conducting dewar was designed and built according to the results of the evaluation program and the arguments outlined above. For a detailed description of the mechanical design, the reader should refer to technical report AFAPL-TR-72-38, Vol. I. The dewar eventually built differs little from the dewar described in that report. The most important differences are as follows. Firstly, the inner liquid helium vessel was made from the G10 like material which was successfully used in the third model dewar and because of this material's superior

mechanical properties it was made with a smaller thickness (0.13 inch instead of 0.25 inch). Secondly, the adaptor flange which connects the inner vessel from the outer vessel was made thicker to give a smaller deflection when the dewar was evacuated. Table VI summarizes the specifications of the dewar. Figure 20 and Table VII are a schematic of the dewar and a list of components of the dewar respectively. Figures 21 and 22 are photographs of the inner shell and outer shell of the dewar respectively.

In spite of the extensive testing program described above, some uncertainty existed as far as the performance was concerned because of the large scaling factor involved in going from the small (~7.4 inch diameter by 30.6 inch long) model dewar to the 100 kJ coil dewar. This was particularly so with respect to the expected heat leak and the quantity of cryogen required to cool the system down.

The heat leak into the dewar arises from a number of sources such as: through the dewar insulation, down the neck of the dewar, down the neck plug walls, down the foam of the neck plug, and down the current leads. The heat leaks for all these sources were estimated and are tabulated in Table VIII. As will be seen in the next section concerning the results of testing the 100 kJ coil dewar there was good agreement between the predicted and measured values.

It is of some importance to know how much cryogen is required to cool the dewar from room temperature to cryogenic temperatures, especially in a system such as this where a large mass of thermal insulation has to be cooled. (In passing it should be noted that in an operating system as opposed to an experimental system, a non-conducting radiation shield would be developed and used, thereby eliminating the disadvantages incurred by using a large mass of powder insulation.) Therefore, estimates were made of the quantity of liquid nitrogen which would be required for cooling from room temperature to 77 K and of the quantity of liquid helium which would be required for cooling from 77 K to 4.2 K. (This two-stage cooling procedure was adopted because the quantity of liquid helium required to cool directly from room temperature to 4.2 K would result in a prohibitively high cost.)

The problem of calculating the cryogen requirements for cooldown was attacked in the following way:

1. Estimate the temperature distribution of the system components when the inner dewar is filled to the desired level with cryogen.
2. Estimate the masses of material at various temperatures according to this temperature distribution.
3. Estimate the heat content of these masses at their respective temperatures.

Table VI
SPECIFICATIONS FOR NON-CONDUCTING DEWAR

Overall Height of Dewar	2.37 m	(93.5 inch)
Total Weight	423 kg	(931 lb.)
<u>OUTER SHELL</u>		
Height	2.21 m	(87.0 inch)
Outer Diameter	1.34 m	(52.8 inch)
Wall Thickness	$0.94 \times 10^{-2} \text{ m}$	(0.37 inch)
Material	GP-100P Polyester fiberglass	
Weight	129.4 kg	(285.6 lb.)
<u>INNER SHELL</u>		
Height	1.96 m	(77.0 inch)
Inner Diameter (Top)	0.94 m	(36.5 inch)
Inner Diameter (Bottom)	0.84 m	(33.0 inch)
Wall Thickness	$0.33 \times 10^{-2} \text{ m}$	(0.13 inch)
Material	Pressure laminated epoxy fiberglass	
Weight	34.6 kg	(76.3 lb.)
<u>ADAPTOR FLANGE</u>		
Thickness	$10.2 \times 10^{-2} \text{ m}$	(4.0 inch)
Outer Diameter	1.47 m	(58.0 inch)
Inner Diameter	0.97 m	(38.0 inch)
Material	GP-100P Polyester fiberglass/ balsa laminate	
Weight	55.4 kg	(122.1 lb.)
<u>THERMAL INSULATION</u>		
Material	Microcel T-4	
Weight	204 kg	(449 lb.)

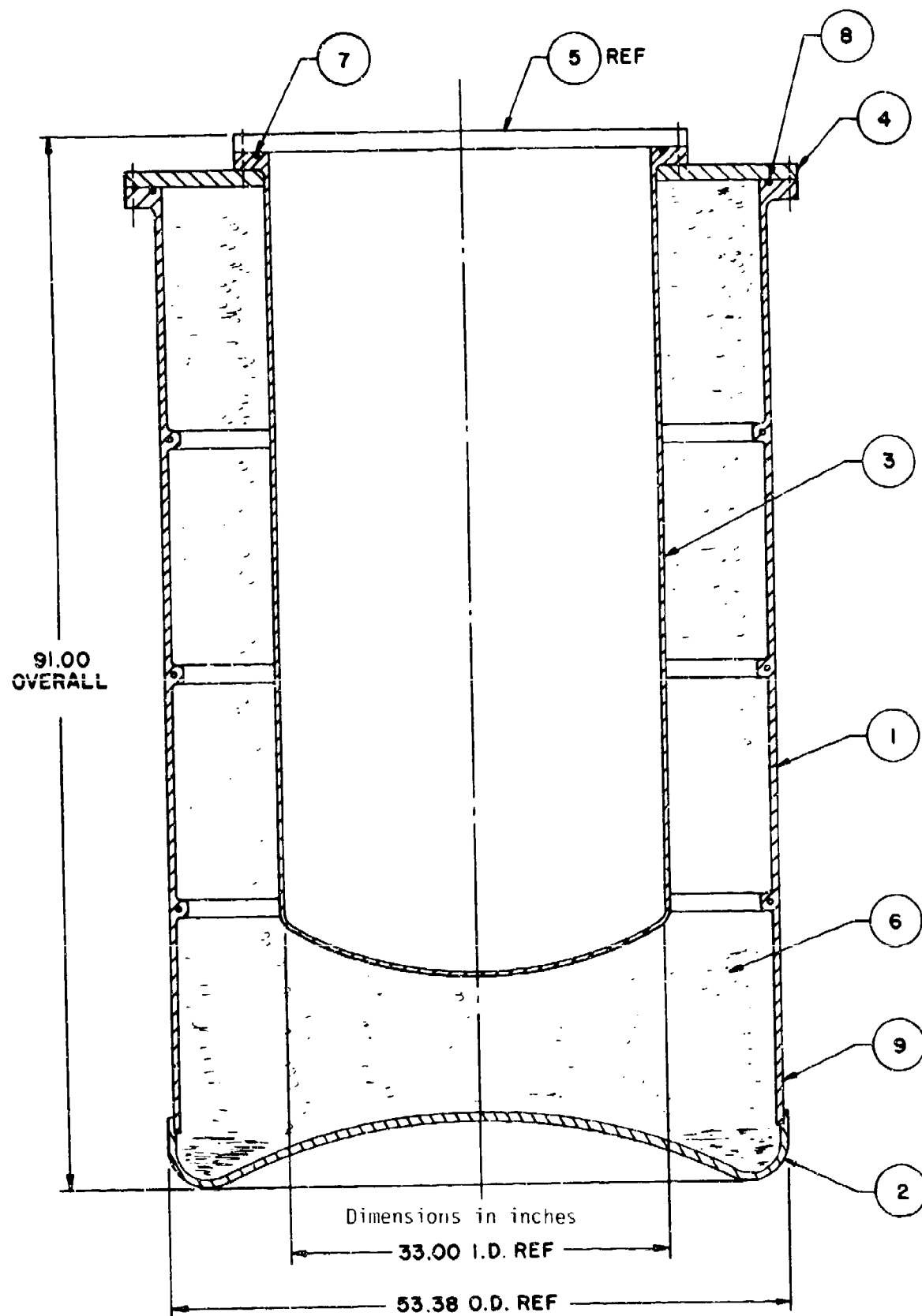


Figure 20 Schematic of Non-Conducting Dewar for 100 kJ Coil.

Table VII
COMPONENTS OF 100 kJ COIL NON-CONDUCTING DEWAR

Parts List

<u>Item No.</u>	<u>Description</u>
1	Dewar outer shell
2	Bottom closure head
3	Inner dewar
4	Adapter flange
5	Coil support flange
6	Micro-cel Celite Div J-M
7	"O" ring, .25" nom w x 35.0" I.D.
8	"O" ring, .25" nom w x 54.0" I.D.
9	Narmco epoxy

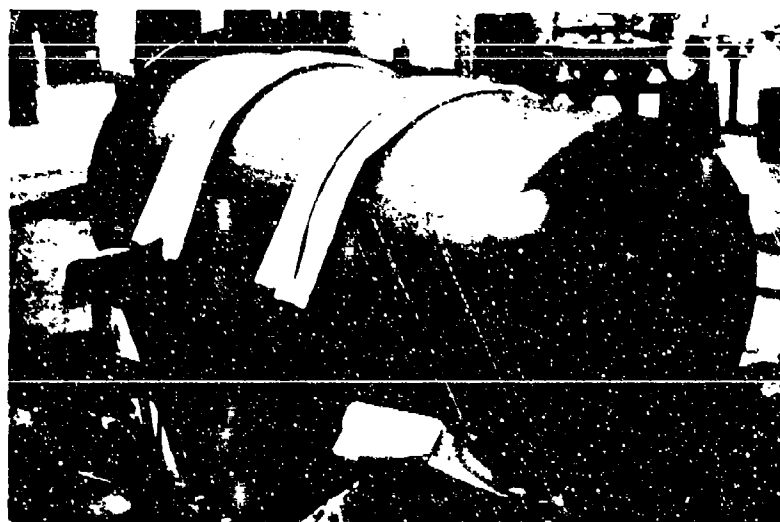


Figure 21

Inner shell (helium container) of nonconducting dewar for 100 kJ energy storage coil. The container is made of a high pressure laminated epoxy/fiberglass material.

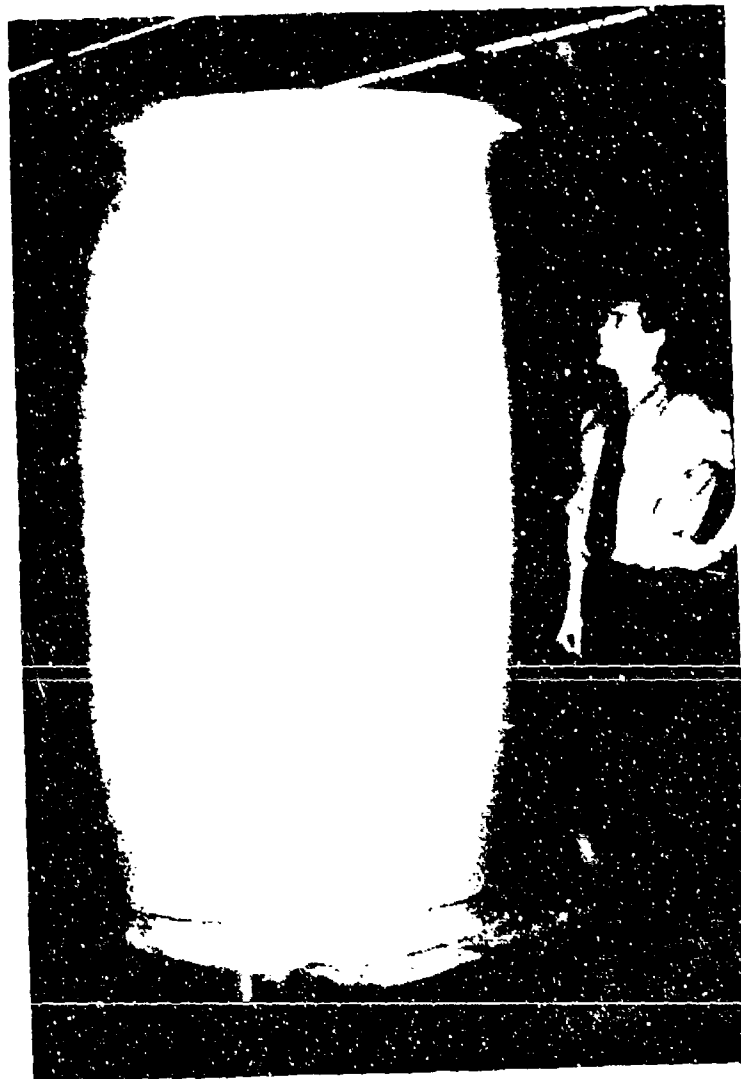


Figure 22 Outer container of non-conducting dewar
for 100 kJ pulsed inductive energy storage
coil.

Table VIII

COMPARISON OF PREDICTED AND MEASURED CRYOGEN USAGE IN
100 kJ COIL NON-CONDUCTING DEWARCryogen used for cooldown (excluding cryogen to cover coil)

	<u>Predicted¹</u>	<u>Measured</u>
Liquid Nitrogen	73 ³ to 158 ²	159 liters liquid
Liquid Helium	145 ⁴	140 liters liquid

1. Basis of Estimate. Based on the weights of the various components and:

<u>Item</u>	<u>Final Temperature</u>	<u>Enthalpy Difference as for:</u>
Micro-Cel T4	Profile varying linearly from room temperature to cryogen temperature	Glass
Inner dewar, coil form, electrical insulation and support structure	Cryogen temperature	Teflon
Conductor	Cryogen temperature	Cu

2. Using latent heat of LN₂ only.

3. Using latent heat plus enthalpy to room temperature.

4. Using 25 kJ/liter (this is equivalent to the yardstick of 0.1 ϵ /lb of Cu)

Heat Leaks at 4.2 K

<u>I</u> <u>Predicted</u>			<u>II</u> <u>Total measured</u>		
<u>Source</u>	<u>Watts</u>	<u>Liters per hour</u>	<u>Height of Cryogen Over Coil (Inches)</u>	<u>Watts</u>	<u>Liters per Hour</u>
Neckplug wall ^c	1.50	2.07			
Neckplug foam	2.31	3.18	12.9	9.5	13.1
Dewar neck	1.25	1.72	7.9	8.0	11.1
Dewar insulation	3.82	5.27	4.3	7.3	10.1
Leads (at zero current)	1.83	2.52			
	<u>10.7</u>	<u>14.8</u>			

4. Subtract the heat content from the heat content at the initial temperature (room temperature in the case of liquid nitrogen and liquid nitrogen temperature in the case of liquid helium).
5. Estimate the quantity of cryogen required to abstract that amount of heat from the material.

The system was divided up into the following four components: conductor; coilform, structure and electrical insulation; inner dewar; and Micro-Cel T-4 thermal insulation. The first three components were all assumed to be at a final temperature throughout their volume equal to the cryogen temperature. The thermal insulation, however, was assumed to have a final temperature distribution such that near the inner dewar it was at cryogen temperature and near the outer dewar it was at room temperature. In between, the temperature was assumed to vary linearly. This continuous distribution of temperature with position was approximated to by dividing the Micro Cel T-4 insulation up into a number of regions and assuming that the temperature of the whole of a particular region was at the temperature of its midpoint (given by the continuous linear variation described above). The mass of each of these regions was calculated as were the masses of the other components in the system. Knowing the mass and temperature of each region, the heat content of each region was calculated by taking the product of the mass and the enthalpy for the particular region at the corresponding temperature.

Unfortunately, enthalpy data for the particular materials used is not available so an approximation had to be made. The enthalpy data used for each system component was as follows:

<u>System Component</u>	<u>Enthalpy Taken As For</u>
Micro-Cel T-4	glass
Inner dewar, coilform, structure, electrical insulation	teflon
Conductor	copper

The total heat content for the system was found by summing the heat contents of the system components. This procedure was carried out for room temperature, 77 K and 4.2 K and the amount of heat to be abstracted from the system was found by taking the appropriate differences between the heat contents at the various temperatures.

Thus, the total quantity of heat to be removed by the appropriate cryogen was known and it only remained to estimate the quantity of cryogen required to remove this amount of heat.

The amount of cryogen required depends upon the latent heat of the cryogen, the enthalpy of the cryogen between room temperature and

cryogen temperature and the efficiency of heat exchange between the cryogen and the material which is to be cooled.

For nitrogen, the latent heat of the liquid to gas transition is 160 kJ/l and the enthalpy of the gas from boiling point to room temperature is 186 kJ/l. These two values should set limits on the quantity of nitrogen required. Using only the latent heat of the liquid would imply that no heat was transferred from the mass to be cooled to the gas and using the latent heat of the liquid plus the enthalpy of the gas between the boiling point of the cryogen and room temperature would imply perfect heat exchange. The quantity of liquid nitrogen required based on these two limits was found to be 158 l and 73 l, respectively.

By similar reasoning, the quantity of helium required to cool from 77 K to 4.2 K can be calculated. The latent heat for the liquid to gas transition is 2.6 kJ/l and the enthalpy of the gas between 77 K and 4.2 K is 48.7 kJ/l. Based on these values, the limits for the liquid helium requirements would be 1,390 l using only the latent heat of the liquid to gas transition, and 70.5 l using the total of the latent heat plus the enthalpy of the gas from 4.2 K to 77 K. Clearly the spread between these two limits is too large to be of any practical use, and estimating a heat transfer coefficient between the helium gas and the mass to be cooled would also be too uncertain to be useful.

We finally based our estimate on a rule of thumb commonly used by superconducting magnet manufacturers, which is: it requires 0.1 liters of liquid helium to cool one pound of material from 77 K to 4.2 K. If copper is taken as the material, this can be rewritten as one liter of liquid to remove 25 kJ of heat from material from 77 K to 4.2 K. Based on 25 kJ/l, the estimated quantity of liquid required to cool the system from 77 K to 4.2 K is 145 liters.

These estimates are tabulated in Table VIII. As will be seen in the next section which concerns the testing of the 100 kJ coil dewar, these results are in reasonable agreement with the measured values.

f. 100 kJ Coil Non-Conducting Dewar Testing & Experimental Results

Having assembled the dewar, the first series of tests were conducted with no powder insulation in the vacuum space. A schematic of the experimental setup is shown in Figure 23.

The vacuum jacket was pumped at room temperature to a pressure of 200 μ Hg according to the thermocouple gauge or 30 μ Hg according to the ionization gauge. It was cold shock tested by pouring in liquid nitrogen and the pressure dropped to 0.4 μ Hg measured by the ionization gauge. This pressure was maintained as long as the liquid nitrogen remained in the dewar. The vessel was allowed to warm up to room temperature and was then cycled twice more. It showed no signs whatsoever of structural or vacuum problems. These results are summarized in Table IX. The insulating jacket was then raised to atmospheric pressure and the Micro Cel T-4 powder insulation was installed. The powder insulation

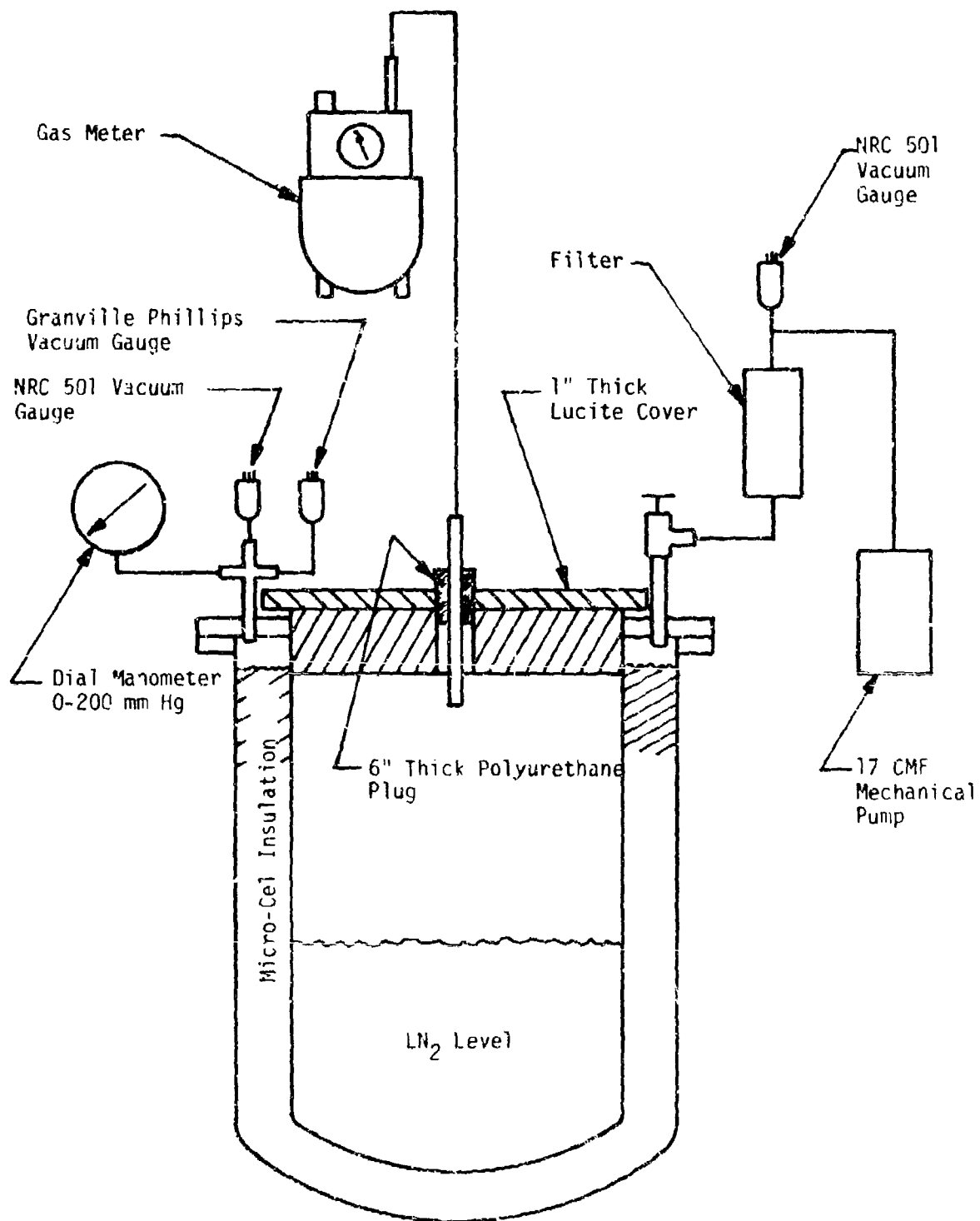


Figure 23 Experimental set-up used for evaluating the non-conducting dewar performance.

Table IX
SUMMARY OF TESTS ON 100 kJ COIL DEWAR

Without Micro-Cel insulation

<u>Vacuum</u>	<u>Measured On</u>	
	<u>Thermo- couple Gauge</u>	<u>Ion Gauge</u>
Pressure at 293 K	200 μ	30 μ
Pressure at 77 K	<1 μ	0.4 μ
No. of Cycles 293K-77K-293K	3	

With Micro-Cel insulation (after several months pumping to dry the Micro-Cel)

<u>Vacuum</u>		
Pressure at 293 K	16 μ	---
Pressure at 77 K	<1 μ	---
Pressure at 4.2 K	<1 μ	---
<u>Heat Leak</u>	<u>Watts</u>	
At 77 K ¹	10.5 with 10 inches over bottom of dewar	
At 77 K ²	88 with 15.1 inches over coil	
At 4.2 K ²	9.5 with 12.9 inches over coil	
Number of Cycles 293K-77K-293K	2	
Number of Cycles 293K-4.2K-293K	1	

¹Tests conducted shortly after installation of the Micro-Cel T-4 thermal insulation without coil in dewar; the dewar vacuum pressures was 375 μ Hg.

²Tests conducted during the test on the 100 kJ coil.

which is similar in consistency to bakers flour was poured into the vacuum space through four separate three inch diameter access ports in the adaptor flange. When this was completed, the dewar was re-evacuated through a multi-stage filtering system to prevent the powdered insulation from ruining the mechanical vacuum pumps. Unfortunately, the Micro Cel T-4 thermal insulation is hygroscopic and prior to filling the dewar it had absorbed much water. Consequently, the dewar pressure initially was higher than desirable because of the vapor pressure of the water, and only after some time was the water pumped out.

During the early stages before all the water had been pumped out of the system the heat leak as measured by nitrogen boiloff was 10.5 W with about 10 inches of liquid nitrogen in the bottom of the dewar. The vacuum pressure was 375 μ Hg during this test. It was subsequently found that the effect of the water on the pressure in the dewar had been made worse by the presence of the filters in the pumping line. When these filters were removed, the increase in the pumping line conductance was such that the pressure immediately dropped from 375 μ Hg to 100 μ Hg. Eventually after some months of pumping a vacuum pressure below 10 μ Hg was obtained. In future applications in which powdered insulation is used, a scheme whereby the powder can be baked out before insertion into the dewar should be devised.

Further measurements of vacuum pressure and heat leak were made during the testing of the 100 kJ coil. Before cryogen transfer was started the pressure at room temperature as measured by a thermocouple gauge was about 16 μ Hg. After liquid nitrogen had been transferred into the dewar, the same gauge read less than 1 μ Hg. (This is outside the range of pressures that thermocouple gauges can accurately measure). It continued to read less than 1 μ Hg throughout the test after liquid helium had been transferred. The results of these tests are summarized in Table IX.

Boiloff measurements were made by monitoring the change in level of the cryogen and by use of a rate flow meter. The heat leaks arrived at by each method were in fair agreement. With 15 inches of liquid nitrogen over the coil, the measured heat leak was 88 W. At first sight this may appear to be very high and indeed it would be if it were at 4.2 K. However at liquid nitrogen temperature, thermal conductivities are much higher than they are at liquid helium temperature and the heat leak decreases in the range of 77 K to 4.2 K.

The heat leak is also a function of the level of the cryogen in the dewar (i.e., the higher the level, then the shorter is the distance between room temperature and cryogen temperature and therefore the higher is the heat leak). Boiloff measurements were made for liquid helium at various levels of liquid helium in the dewar. The heat leak varied between 7.3 W and 4.3 inches of liquid helium over the coil to 9.5 W with 12.9 inches over the coil. This range in height is approximately

the operating range for the liquid helium level. These results are summarized in Tables VIII and IX. Also shown in Table VIII is the predicted heat leak of 10.5 W. Thus there is good agreement between the predicted and measured heat leaks.

The quantity of cryogen used for cooldown was also monitored during the test. 159 liters of liquid nitrogen and 140 liters of liquid helium were used. The values predicted as outlined in Section II-3-e, 100 kJ Coil Non-Conducting Dewar Design were 73 to 158 liters for liquid nitrogen and 145 liters for liquid helium. The values for liquid helium are in good agreement. The measured value for liquid nitrogen is slightly higher than the upper limit as previously calculated would allow. However, considering the crudity of the model and the complete lack of data concerning the thermal properties of Micro Cel T-4, this was considered to be reasonable agreement. The results are summarized in Table VIII.

g. Conceptual Light Weight Non-Conducting Dewar

This dewar is more fully described in technical report AFAPL-TR-72-38, Vol. I. However, for convenience, a brief description is given below.

The dewar is shown in Figure 24 and a summary of its specifications is given in Table X. Based on the results of the model non-conducting dewar evaluations, some minor changes have been made to the design presented in AFAPL-TR-72-38, Vol. I. As before, it is proposed that the outer shell be made from hand laid up 2-ounce fiberglass mat using GP-10CP polyester resin as a binder, but that the inner shell be made from the high density epoxy/fiberglass material made by an autoclave process.

The non-conducting dewar provides the thermal insulation, the structural support, and the dielectric characteristics required by the coil during pulsing operations. Very high voltages occur during pulsing in the electrical connection between the coil terminals and the vacuum interrupter terminals; therefore it is desirable to mount the circuit components exposed to this voltage as close as possible to the coil. The dewar design permits the mounting of these components directly to the upper closure head of the dewar, where they are surrounded by an electrically insulating cover.

The outer shell is designed to withstand 15 psia external pressure and integral stiffeners are used to minimize the shell weight. For the same reason reverse dished heads are used for the end plates. The inner, helium vessel is an internally loaded shell. To minimize the quantity of helium dead space, it was designed to re-enter the bore of the coil. The radiation shield is cooled by boiloff gas from the helium vessel thereby eliminating the need to carry liquid nitrogen. The shield is insulated on its outer surface with aluminized mylar. This material is electrically conducting and to avoid circulating currents induced by the changing magnetic field, it must not be allowed to form a closed loop.

Table X
SPECIFICATIONS FOR THE FLIGHT SYSTEM
NON-CONDUCTING DEWAR

Overall size	32" dia. x 66" high
Weight (excluding coil)	246 pounds
Insulation	Aluminized mylar
Shell and head material	Fiberglass
Radiation shield cooling	Boil off helium
Outer shell thickness	0.250"
Inner shell thickness	0.187"
Color	White
Helium volume over coil	~100 liters
Steady state boil off, estimated	<3 liters/hour

This is achieved by covering the readiation shield alternately with "shingles" of mylar and aluminized mylar so that there is no continuous conducting path to form a closed loop. The pressure in the vacuum jacket will be maintained in the 0.01 μ Hg to 0.001 μ Hg range by using a molecular sieve material bonded to liquid helium temperature panels. It has been shown (3, 4) that helium gas can be readily pumped at 4.2 K using this technique. The molecular sieve pump will be fitted with a heater so that it may be activated during evacuations of the vacuum jacket.

This design was developed from results obtained during a parametric study the purpose of which was to minimize the weight of inductive energy storage systems having particular mission constraints. Part of this optimization procedure involved the use of a computer sub-program which designed a minimum weight dewar around the coil. The parametric study is described fully in technical report AFAPL-TR-72-38, Vol. I. An appendix in that technical report describes the dewar weight of optimization sub-program and Volume III of the report details weights for systems having a large range of mission constraints.

h. Summary and Conclusions

To advance the state of the art of non-conducting dewar design to the point where a reliable non-conducting dewar could be used to contain and operate a superconducting energy storage coil, a development program was carried out. This program involved evaluating likely non-conducting materials and using these materials to build model non-conducting dewars.

These non-conducting dewars were tested under operating conditions. The information acquired in this experimetnal program was used to design a non-conducting dewar to contain a 100 kJ energy storage coil.

The dewar was operated successfully and measurements made during testing confirmed the validity of the design techniques employed and of the methods used to predict its performance.

Starting with the results of a parametric study the purpose of which was to create minimum weight inductive energy storage system designs, a conceptual design for a light weight flight system was produced.

4. VAPOR COOLED LEADS

a. Introduction

The use of electrical leads to carry current from room temperature to a coil at liquid helium temperature results in a heat leak into the cold region. The effect of this heat leak is to increase the quantity of helium which must be carried during a mission thereby increasing system weight. Therefore, efforts must be made to minimize this heat leak. There are a number of approaches to the solution of this problem

and the best method depends upon the mission constraints of the particular system.

In this program the greatest emphasis was placed on designing the leads for the experimental system. They were designed in such a way that they could be reliably operated over a range of operating conditions, the most stringent of which was continuous operation at high current. Consequently, they do not give the minimum achievable heat leak for pulsed current conditions. However, analyses were conducted which led to design criteria and predicted performance for current leads intended for pulsed applications.

In inductive energy storage systems which operate under pulsed current conditions, high voltages are generated between the two leads carrying current to the system. Thus, in addition to the cryogenic aspects, careful consideration was given to the problems involved in avoiding voltage breakdown between a pair of leads. The situation is aggravated by the fact that in superconducting systems the environment of the current leads is gaseous helium which has particularly poor breakdown characteristics.

b. Cryogenic Aspects of the Current Lead Design

Most electrical leads for helium temperature use are designed for steady state operation. The lead design is a compromise between heat conduction down the lead and electrical resistance of the lead. To reduce the heat leak at the low temperature, the boiloff helium is normally used to cool the lead and counterbalance the heat conduction down the lead. Scott (5) discusses the principles involved in counter-flow current lead design and derives a solution for the differential equation determining the temperature of a current lead. The paper contains an adequate bibliography.

For steady state leads which use the boiloff gas to reduce heat flow the amount of helium required is proportional to the current the leads are designed to carry. Under these conditions the required amount of helium is approximately 3 liters/hour per 1000 A for a pair of leads. When the current is not flowing, the boiloff rate drops to about 1.6 liters/hour for the same leads. Typical boiloff rate data is shown in Figure 25 for several sets of leads designed for steady state operation at an optimum design current. The data is plotted as a function of the ratio of operating current to design current.

It is in the interests of economy to minimize the helium boiloff during the course of the experiment. Since the leads for the greater part of the experiment do not carry any current the cross sectional area of the leads should be as small as possible to minimize the zero current heat leak into the dewar through the leads. On the other hand, the area of cross-section of the leads should be large enough that they do not burn out when operated at the maximum RMS current at which experiments are to be run. Furthermore, the optimum current should not be so far below the maximum operating current that excessive boiloff is incurred when operating at the maximum current. The current at which the coil

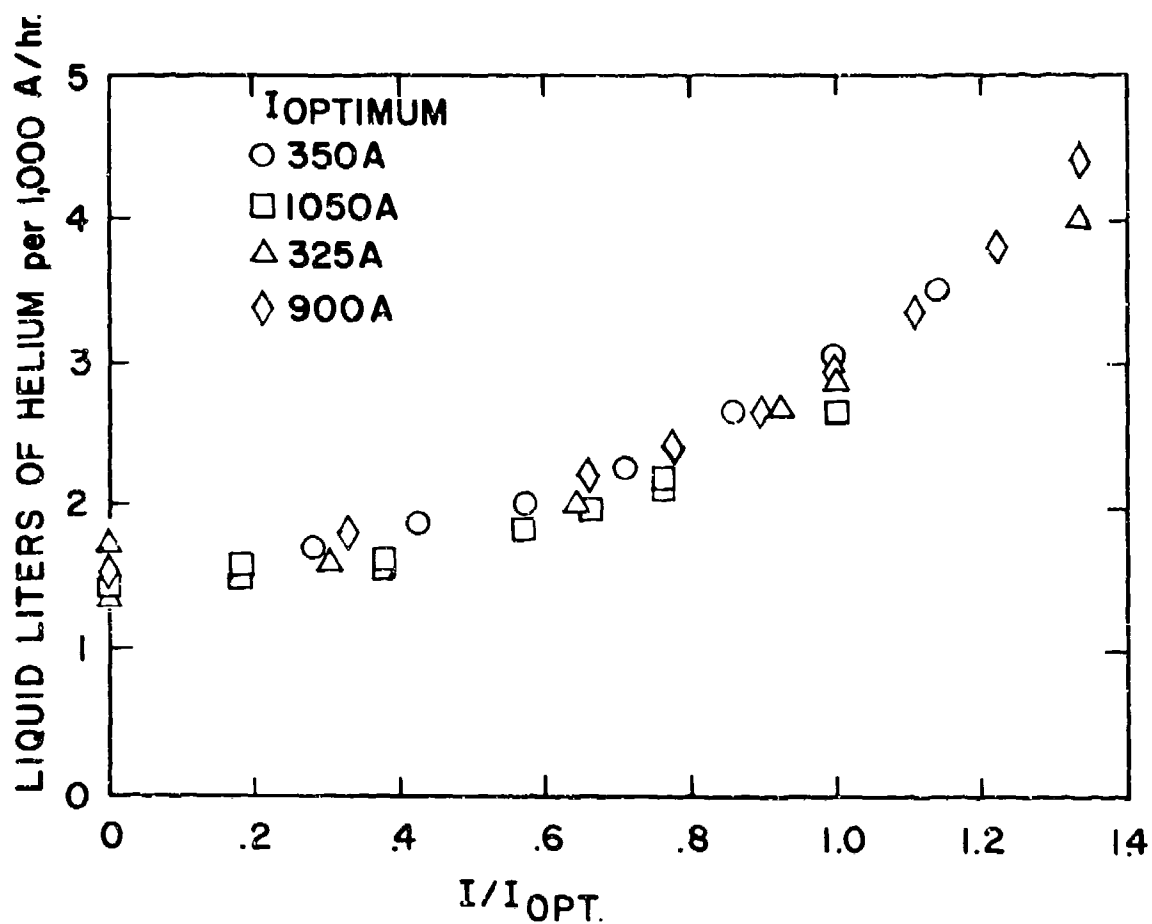


Figure 25 Boiloff data in several sets of vapor-cooled current leads.

stores 100 kJ of energy is 2,000 A and since experiments which involved continuous operation at this current were planned, it was necessary to ensure that the leads would not become overheated at this current. The current for which the leads were optimized was thus a compromise between these conflicting requirements. The current eventually chosen was 1,250 A. Leads optimized at this current can be safely operated at 2,000 A and without excessive boiloff. On the other hand, at zero current the heat leak due to the leads is only about 17% of the heat leak into the dewar from all sources. Under normal operating conditions the design is conservative since it was assumed that the only gas vented through the leads was that due to the leads themselves. In practice, the flow through the leads is greater than this since a portion of the boiloff due to other sources is channeled through them. This has the effect of providing additional cooling thereby increasing the margin of safety and decreasing the heat leak to the dewar through the leads. Figure 26 shows the predicted boiloff for the pair of leads designed for the 100 kJ coil system. It is assumed that no additional background boiloff is available for cooling.

Figure 27 is a schematic of one of the current leads. The current flows along 37 O.F.H.C. copper tubes. Each tube is 55 inches long and has a 0.125 inch diameter. The wall thickness is 0.015 inch. The 37 tubes are assembled in a hexagonal pattern and are soldered into copper header blocks at each end. The whole assembly is held in place by a 304 stainless steel tube (1.25 inch OD, 0.035 inch wall) which is soldered to the header blocks. The boiloff helium gas flows up the inside of the tubes only.

As was indicated above, in the experimental 100 kJ coil system the boiloff due to the leads is only a relatively low fraction of the boiloff due to all sources. Consequently, the total system boiloff is insensitive to current lead design. However, in a light weight system the heat leak due to other sources would be much smaller. Therefore, in such a situation more attention must be paid to minimizing the boiloff due to the current leads. Clearly, in a light weight system the background boiloff due to the dewar components would be used in the design to give a smaller area of lead cross-section. In addition to this, in the systems under consideration, relatively large quantities of boiloff gas are produced due to coil losses arising from transient operation. This additional boiloff may be used to cool the electrical leads, hence, the leads may carry currents considerably in excess of their capability under conditions of zero additional boiloff.

The relationship between the steady state design current for a pair of leads and their current carrying capability when additional boiloff is available is analyzed in detail in Appendix VII (Vapor Cooled Leads for Pulsed Operation) of technical report AFAPL-TR-72-38, Vol. I.

For the convenience of the reader the results of this analysis are summarized in Figures 28 and 29. The symbols used in this figure are given below

I_s = steady state operating current (at optimum value for the particular lead)

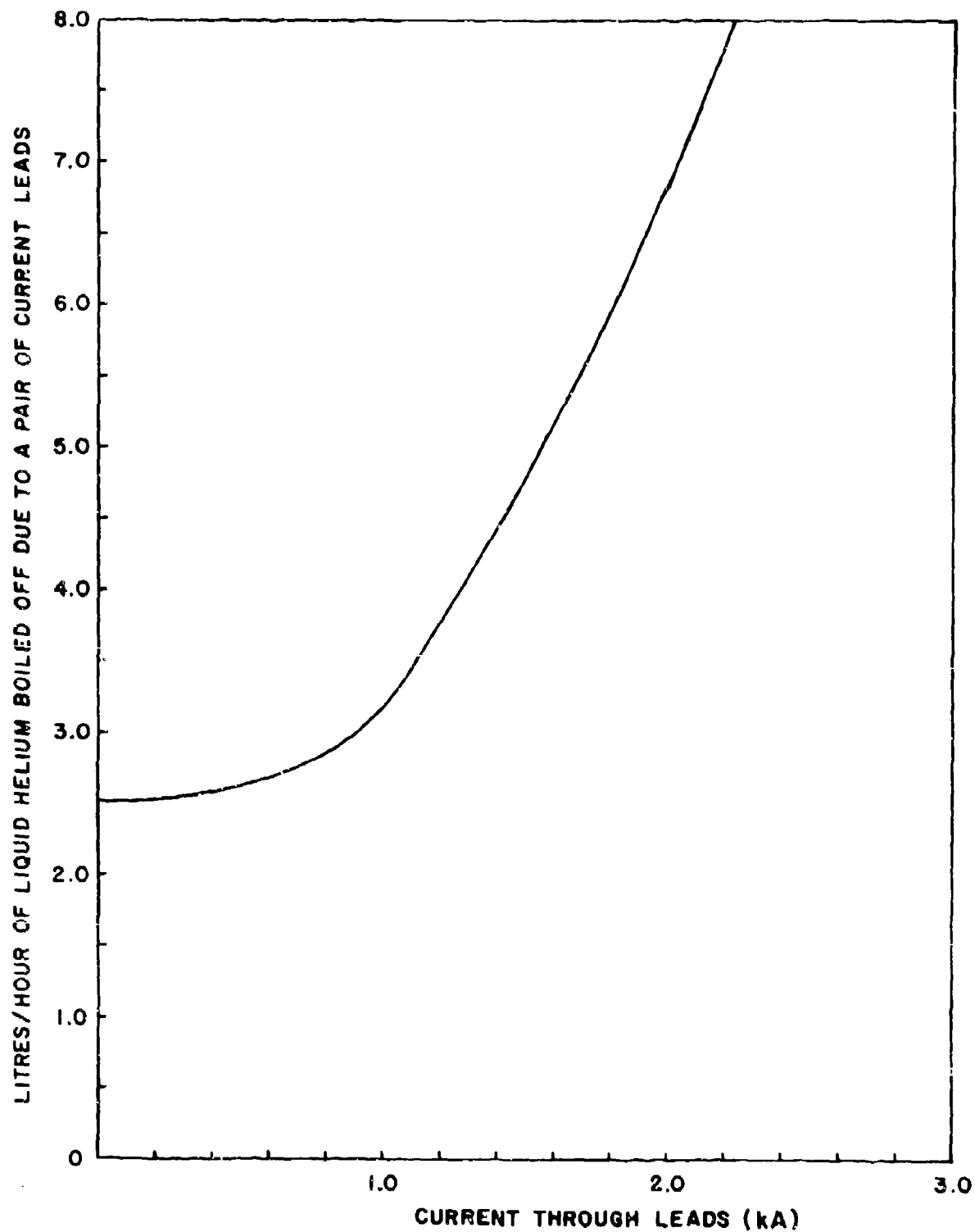
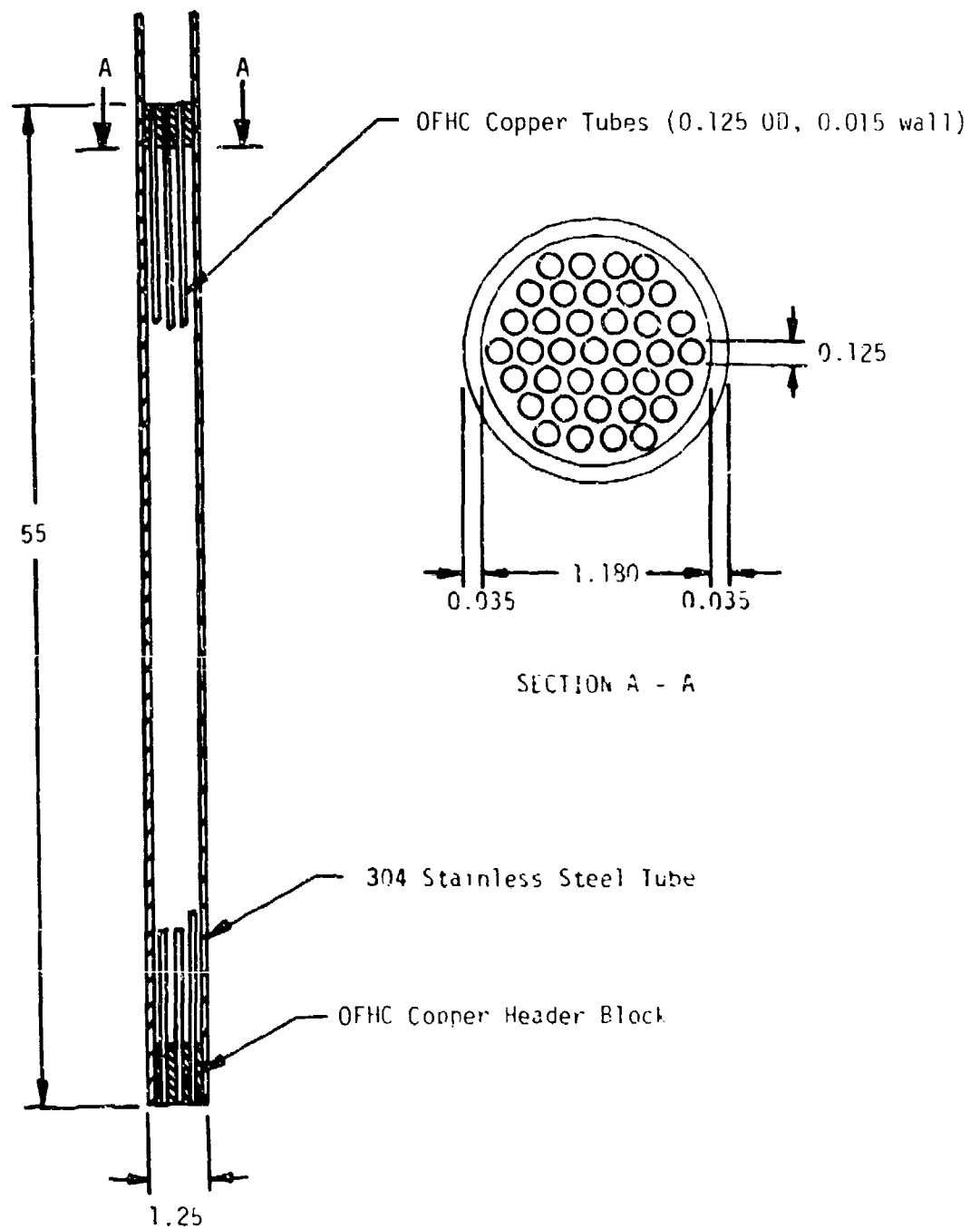


Figure 26 Predicted boil off due to vapor cooled leads on 100 kJ coil system v. current through leads.



Dimensions in Inches

Figure 27 Schematic of Vapor Cooled Current Lead for 100 kJ Energy Storage Coil.

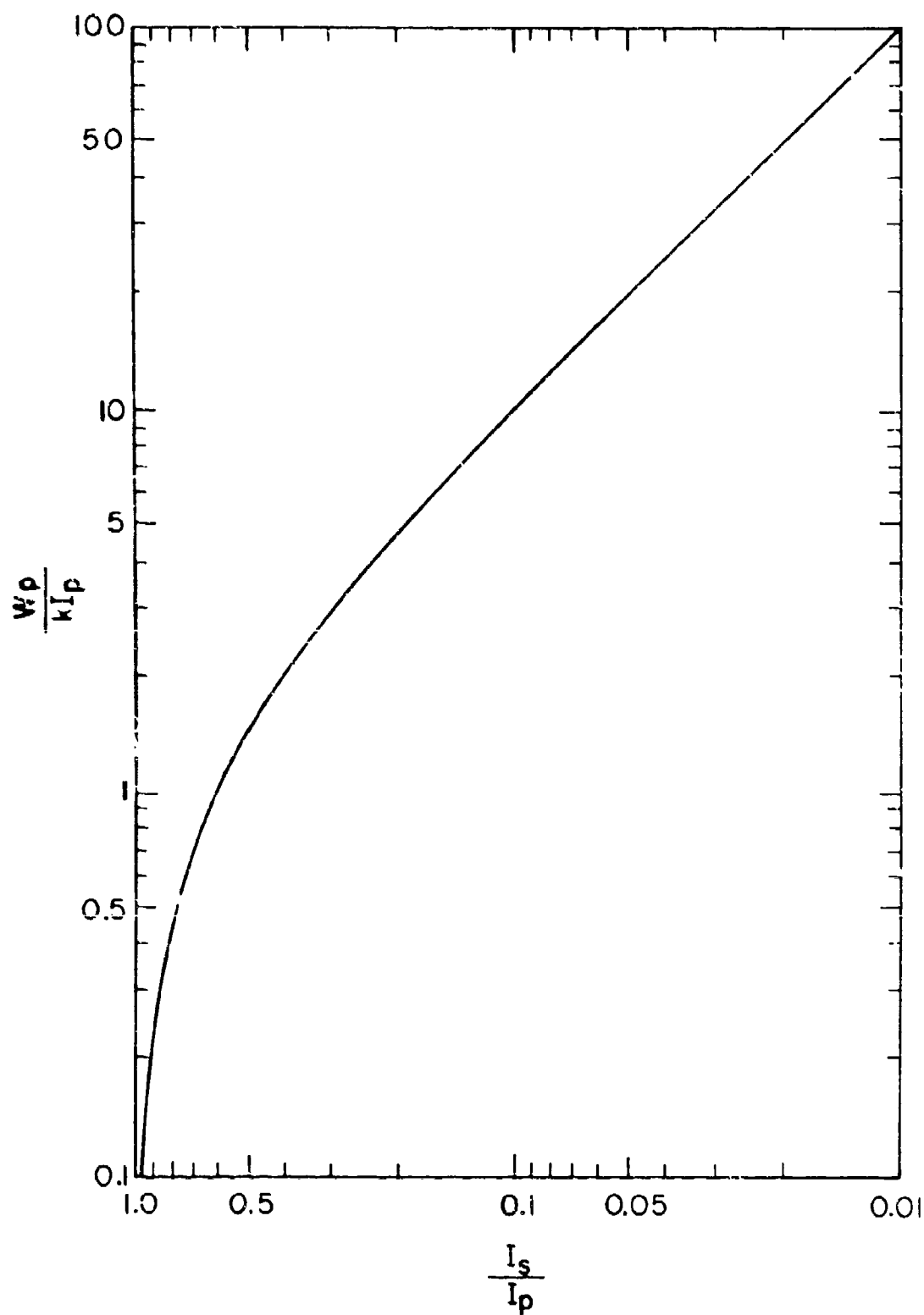


Figure 28 Effect of additional helium boiloff on design current for vapor cooled leads.

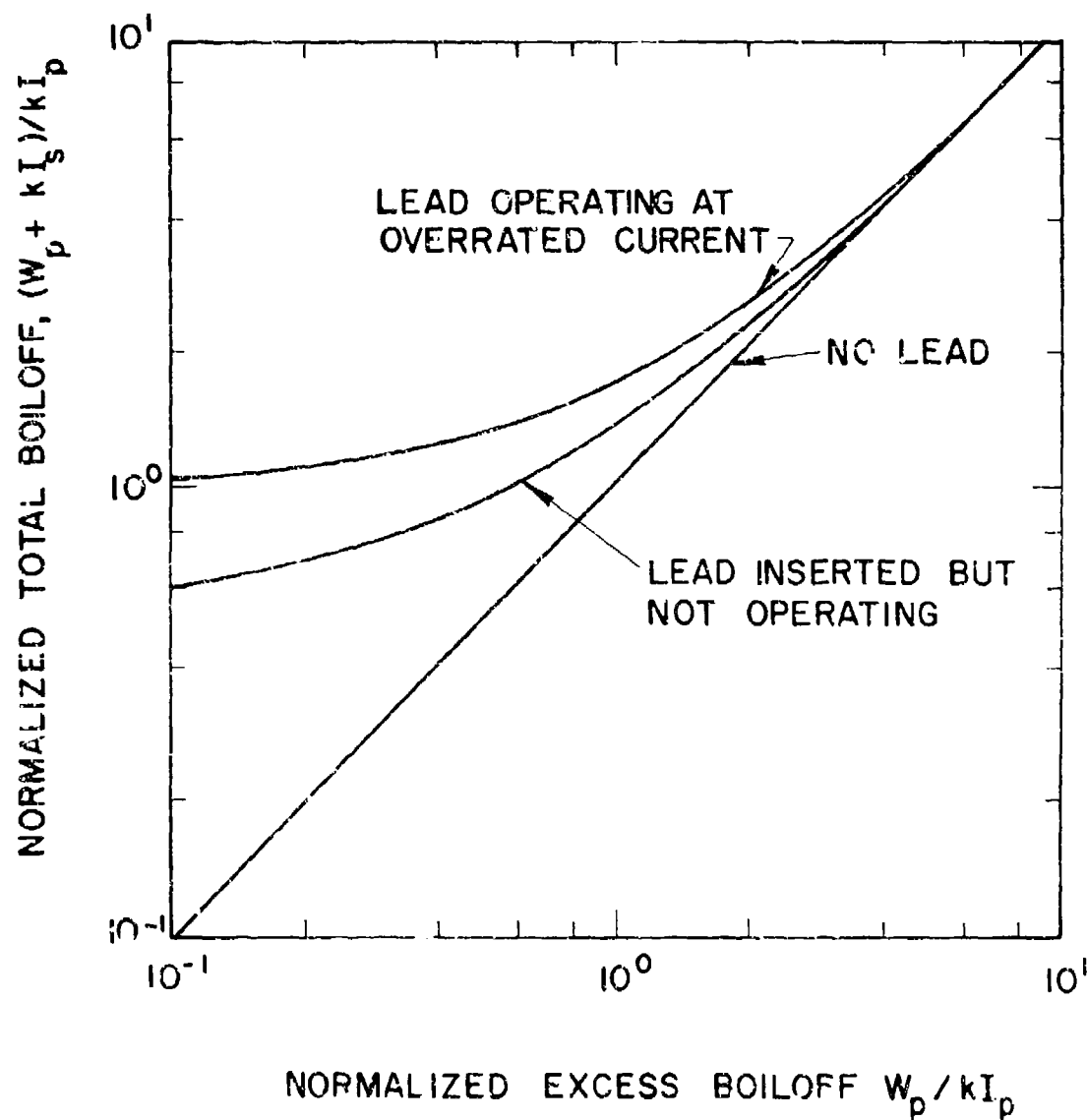


Figure 29 Normalized total boiloff vs. excess boiloff for configurations with leads operating, leads not operating, and leads removed.

I_p = R.M.S. current during transient operation

W_p = helium flow rate generated by losses within the cryostat

k = a constant of about 3 liters/hour/kA/pair of leads

Figure 28 shows in normalized form the effect of additional helium boiloff on design current for vapor cooled leads. Given the additional boiloff available during operation (W_p) and the R.M.S. current during operation (I_p), the steady state design current (I_s) may be found.

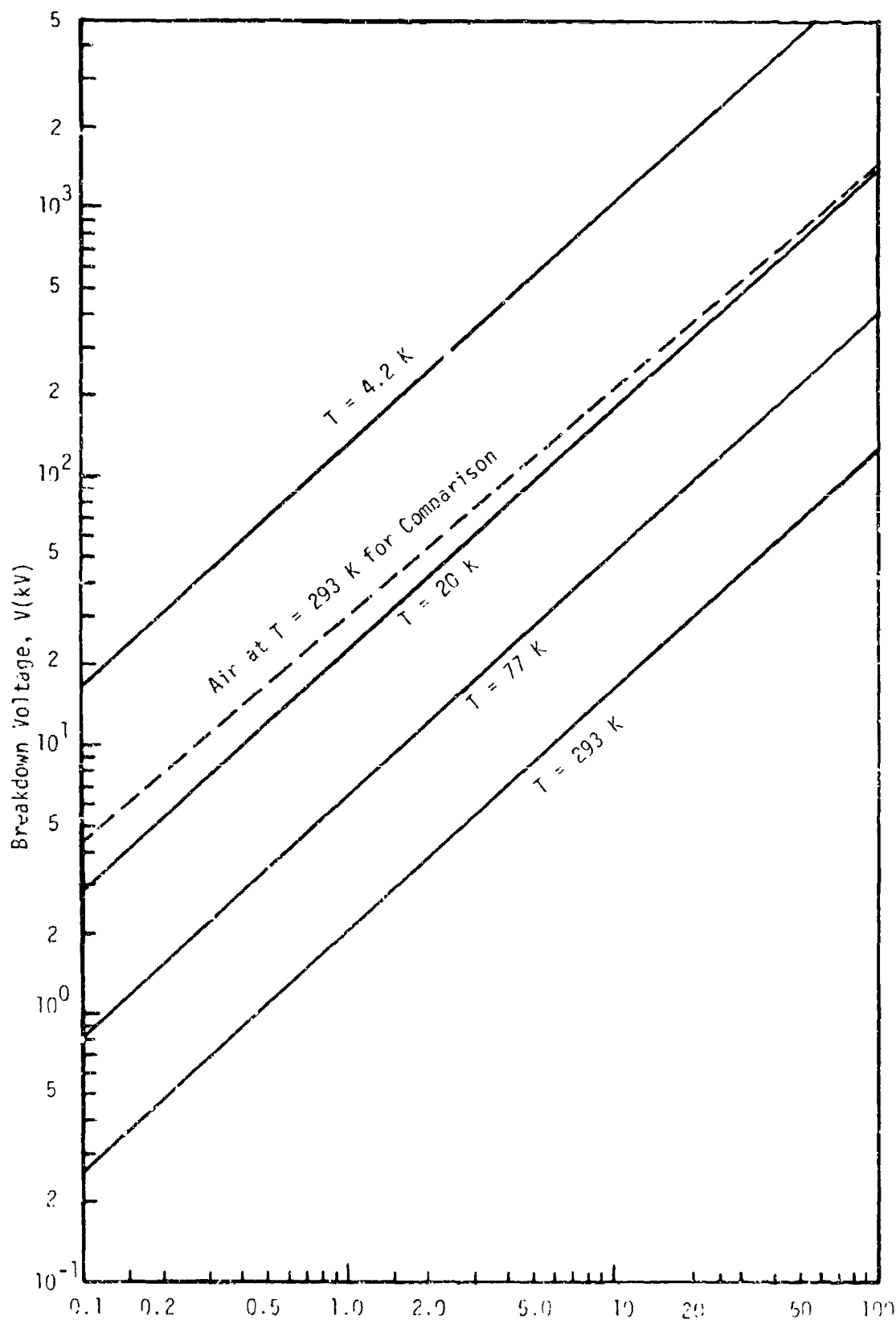
Figure 29 shows in normalized form the effect of the leads on the total boiloff as a function of the additional available boiloff. Three cases are shown: (1) no leads, where the excess boiloff equals the total boiloff; (2) leads inserted, but not operating; and (3) leads operating at the overrated current made possible because of the excess boiloff due to the other sources. Note that the leads have very little effect on total boiloff when the excess boiloff is high enough.

c. High Voltage Aspects of the Current Lead Design

In inductive energy storage systems in which high energies are discharged in short times, large voltages appear between the current leads. The leads must be designed in such a way that voltage breakdown is prevented. In systems which make use of helium particular care must be exercised because helium gas has very poor voltage breakdown characteristics.

In any gas the breakdown voltage for uniform electric fields is a function of the product of gas density and electrode separation only (Paschens Law)(6). The gas density is a function of pressure and temperature. Since for a number of reasons superconducting energy storage systems operate with the helium at atmospheric pressure the breakdown characteristics of the helium within the system depend only on the lead separation and on the temperature of the helium gas between the leads. Figure 30 was derived from data given by Gerhold (7). This figure gives the voltage breakdown for uniform field strength of helium gas at atmospheric pressure as a function of electrode separation at various temperatures. Also shown in the figure for comparison is the breakdown voltage for air at room temperature. It can be seen that at room temperature the properties of helium gas are about a factor of 18 worse than those of air and only when the temperature of helium gas has dropped to about 20 K do the properties of helium gas approach those of air. At 4.2 K helium gas is superior to air.

The temperature of the gas in the dewar varies from 4.2 K near the liquid helium surface to room temperature near the dewar cover plate. Since the leads are equidistant at all points, the critical region then is near the top of the leads where they pass through the cover plate. The leads were placed so that there was the greatest distance possible between them consistent with the constraints imposed by the dimensions



about 60 cm and reference to Figure 30 shows that the breakdown voltage for this separation is about 80 kV. If there were no other effects this separation would be adequate since the maximum voltage planned during testing was 60 kV. Unfortunately, there are further complications. It will be remembered that the data given in Figure 30 is for a uniform electric field strength which in practice is difficult to achieve. It certainly is not the situation in this system. The geometry of this system is that of two parallel cylinders and this gives rise to a non-uniform electric field distribution; the electric field strength peaks at the surface of the cylinders. The ratio of the peak field strength to the average field strength is a function of the electrode separation and the radii of the cylinders. Figure 31 shows the electric field concentration factor for equal radius parallel cylinders as a function of the ratio of cylinder radius to cylinder separation (8).

A schematic of the current leads in relation to the coil and dewar system is shown in Figure 32. The leads themselves are 3.2 cm in diameter and their center to center separation is 62.2 cm. Below the neck plug electrostatic shields of diameter 7.2 cm were fitted. The effect of the shields is to reduce the ratio of cylinder separation to diameter thereby reducing the electric field concentration factor. Because of the presence of the neck plug, it was not possible to extend these shields to the top of the leads.

The electric field concentration factors for the leads in the region of the shields and in the region away from the shields are 3.0 and 6.3, respectively (see Figure 31). To decide whether or not there is sufficient separation between the leads in the two regions described above involves comparing the expected electric fields in the two regions (taking into account the concentration effect) with the breakdown electric field strength at the temperature of the leads in the two regions. The data given in Figure 30 was rearranged to give Figure 33 which is the electric field breakdown strength of helium gas at atmospheric pressure at various temperatures. The properties of air are again shown for comparison.

The worst case for each region is for the part of the region at the highest temperature. In the region which has the electrostatic shields the maximum temperature occurs at the bottom of the neck plug. The temperature here was estimated to be about 20 K. In the region which has no electrostatic shields the hottest part is at room temperature, at the top of the leads.

Figure 34 shows the peak electric field strength in the two regions as a function of the voltage applied between the leads. Also shown are the breakdown electric field strengths for helium gas at the temperatures of the hottest parts of the two regions. The points at which the breakdown electric field strengths for the two regions intersect their respective voltage/electric field load lines give the predicted maximum voltages which can be applied to the coil terminals before breakdown occurs.

$$f = \frac{(r^2 + 4v)^{0.5}}{2 \ln \left[\frac{\frac{v}{2} + 1 + \frac{1}{2}(r^2 + 4v)^{0.5}}{\frac{v}{2}} \right]}$$

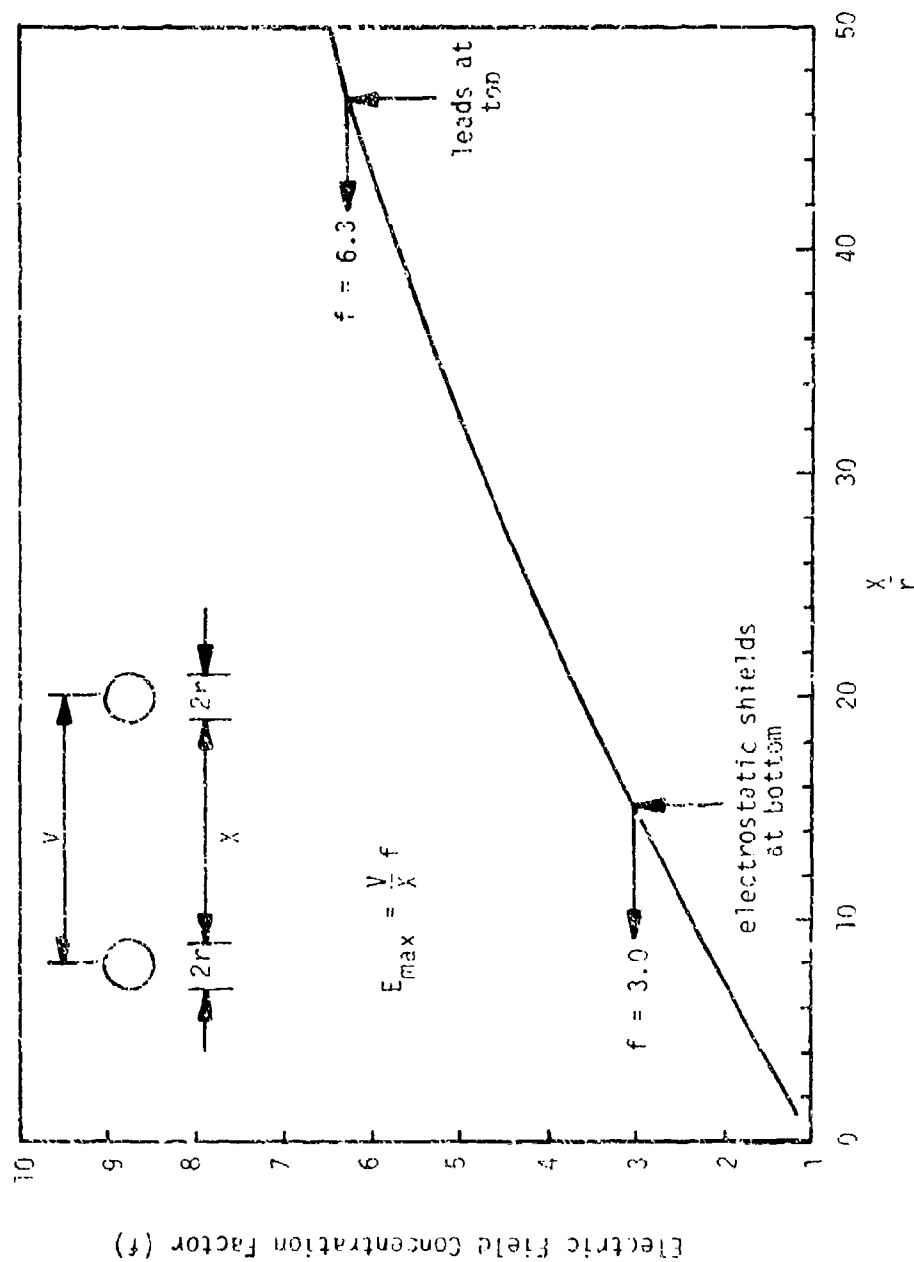


Figure 31 Electric Field Concentration Factor for Equal Parallel Cylinders.

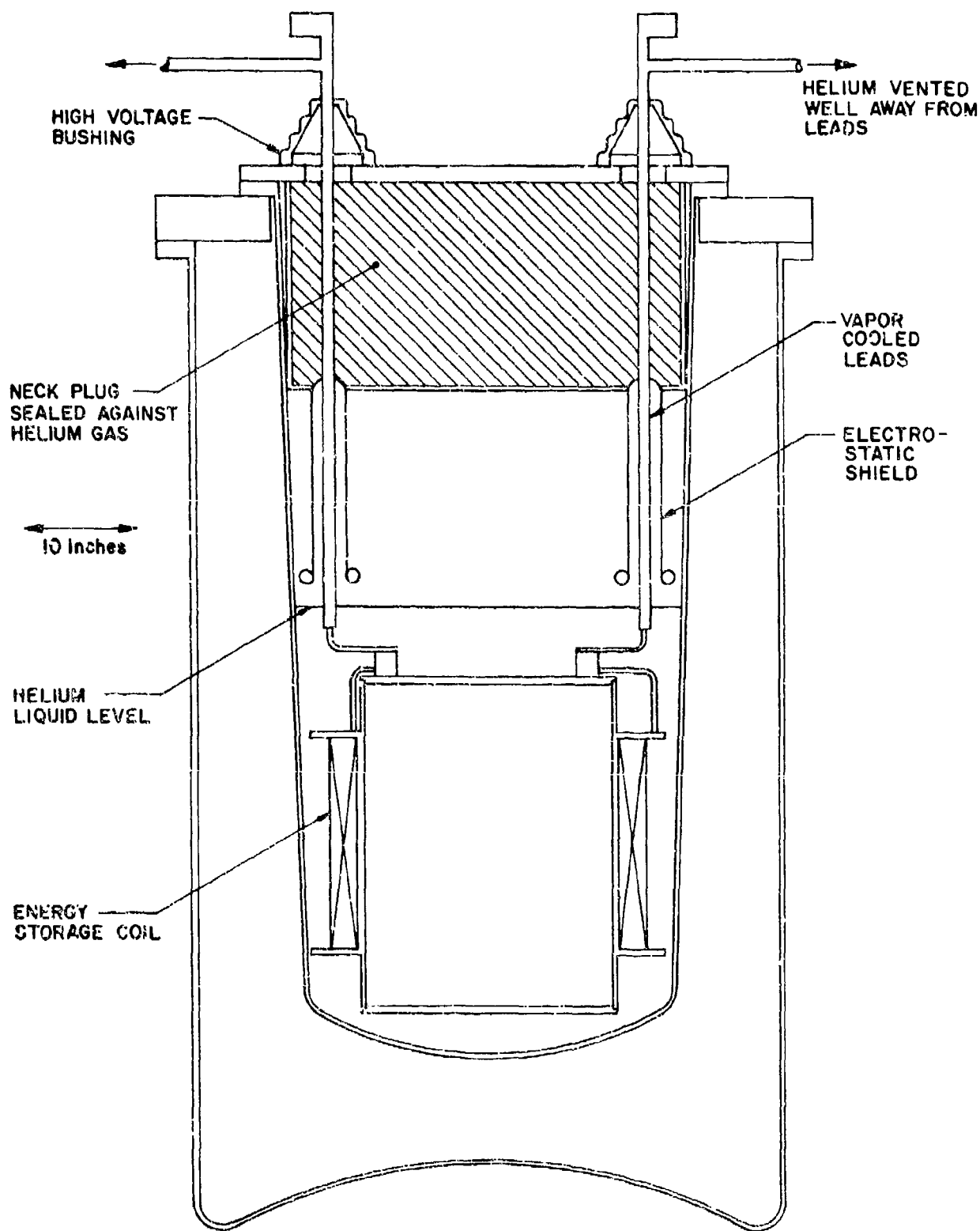


Figure 32 Schematic of Non-Conducting Dewar Showing Arrangement of Current Leads.

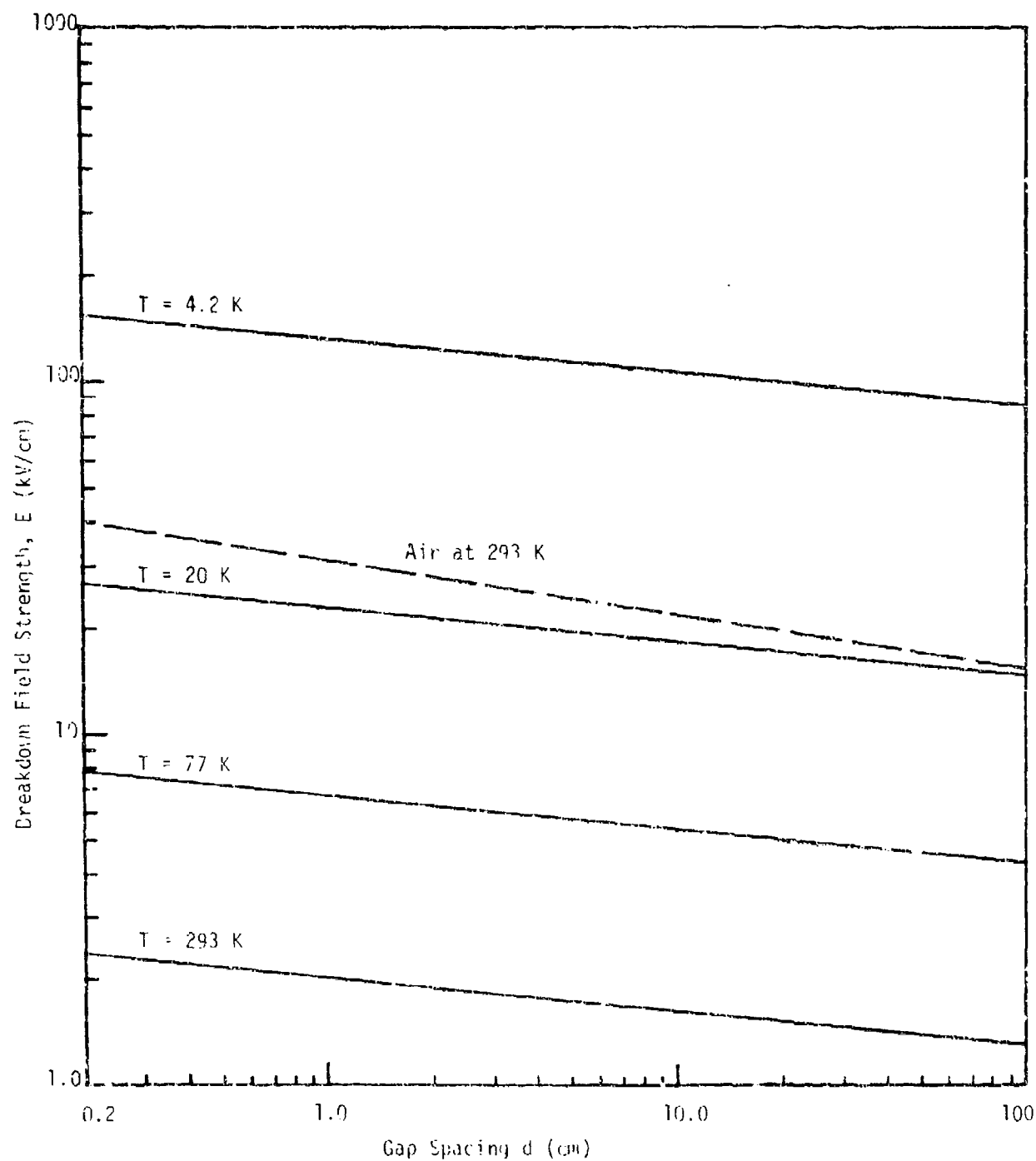


Figure 33 Breakdown Field Strength of Helium Gas at 1 Atmosphere for Various Temperatures vs. Gap Spacing.

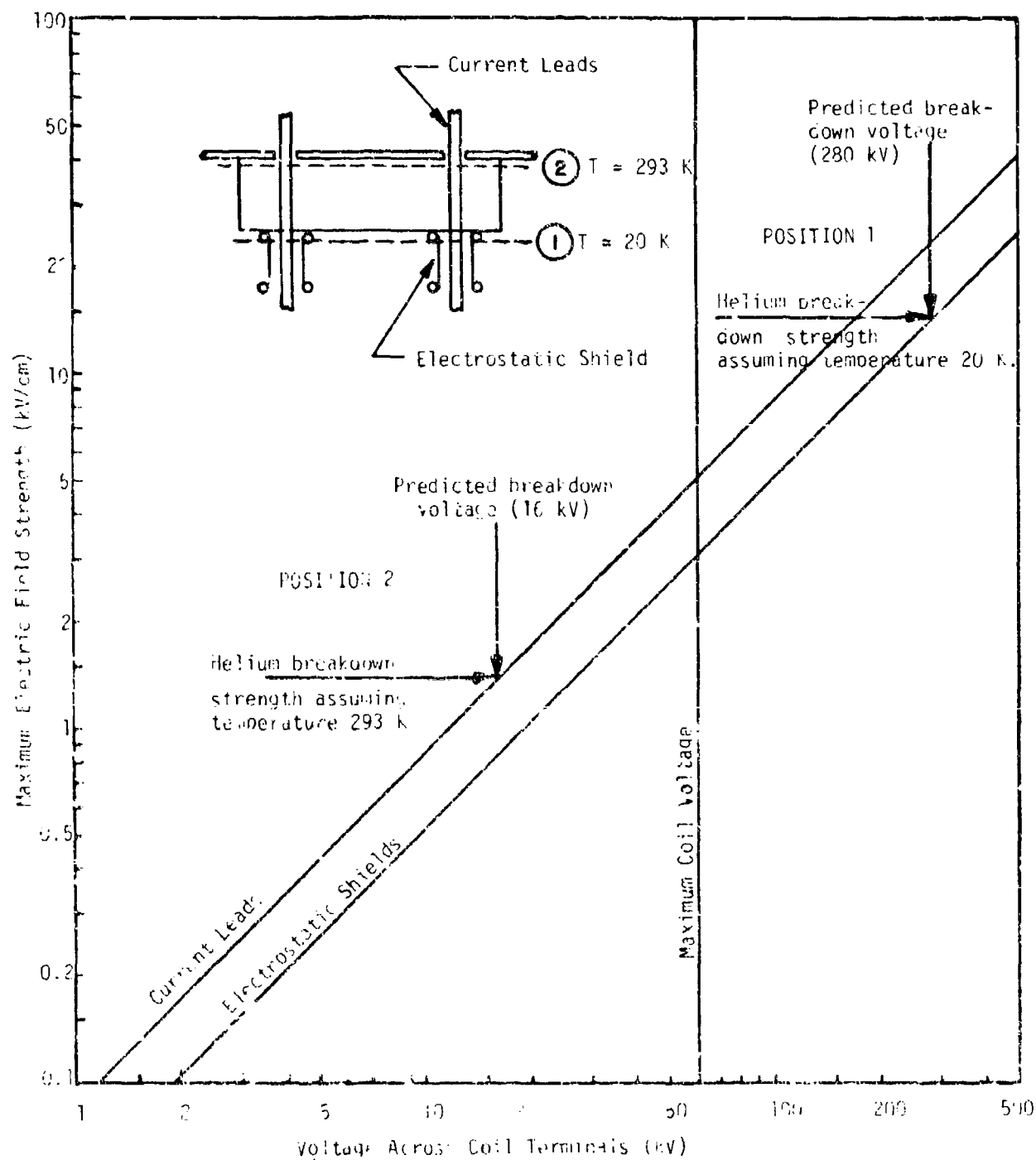


Figure 34 Maximum Field Strength for Current Leads and Electrostatic Shields vs. Voltage Across Coil Terminals

It can be seen that the predicted breakdown voltage for the region which has the electrostatic shields is 280 kV which is very safe. However, the predicted breakdown voltage for the region without shields is only 16 kV which is quite unsatisfactory. Consideration was given to surrounding the leads in the unshielded region with a teflon or other insulating barrier but it was found that for it to be effective it would have to be inconveniently thick.

The analyses conducted so far assumed that the region between the leads was occupied by nothing but helium gas. In fact, this is not the case since in the critical unshielded region the foam of the neck plug fills the gap. It might be expected that this material, since it is an electrical insulator, would have the effect of increasing the electric breakdown strength of the gap. However, data concerning the properties of open cell polyurethane foam in the presence of helium gas was not available, so no theoretical predictions could be made. It was therefore decided to examine this situation experimentally. This is described in the next section.

d. Experimental Program for Testing the Current Leads

In order to determine the electrical breakdown characteristics of the helium gas permeated open cell polyurethane foam between the electrodes a full scale mockup of this region was made. This is shown schematically in Figure 35. Holes having the same diameter as the current leads and with spacing equal to the current lead separation were cut in a 6 inch by 6 inch block of open cell polyurethane foam. Stainless steel tubes with the same diameter as the current leads were inserted into the holes in the foam and were electrically connected to a high voltage power supply through a current limiting resistor and a current monitor. The assembly was placed in an airtight container which was then evacuated. After the air had been removed, the container was back-flushed with helium. A voltage was applied between the stainless steel tubes and the current through the circuit was recorded. The highest voltage applied was 50 kV (the highest available to us at that time). Several runs were carried out and the results are summarized in Table XI. The current readings were converted into an effective resistance for the helium gas/foam environment. As can be seen from Table XI the resistances measured were very high and at no time was breakdown observed. The results of these tests gave confidence that the electrically most highly stressed part of the system could be operated safely with 50 kV across the coil terminals. However, the voltage at which arcing would occur was not known.

Further experiments were carried out during the tests on the 100 kJ coil system. A capacitor (.25 μ F) was charged to voltages up to 50 kV (the limit of the power supply). It was then switched on to the coil with the vacuum interrupter and allowed to ring; this circuit is shown in Figure 36. As can be seen from Figure 37, no arcing was observed at up to 50 kV. In this figure the break in the current waveform and rapid decay during the first three cycles is caused by the bounce of the vacuum interrupter contacts on closing; this phenomenon was observed

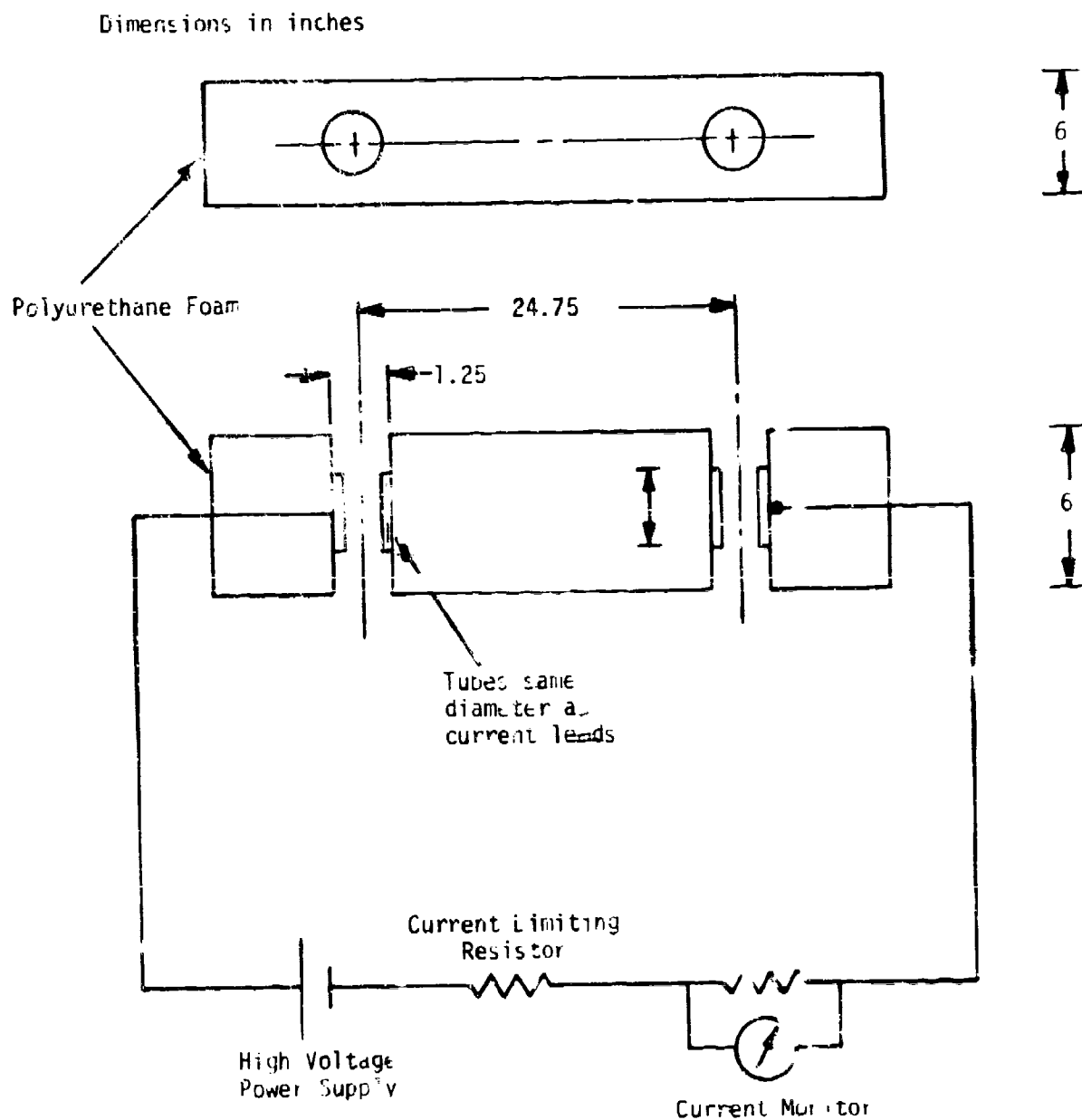
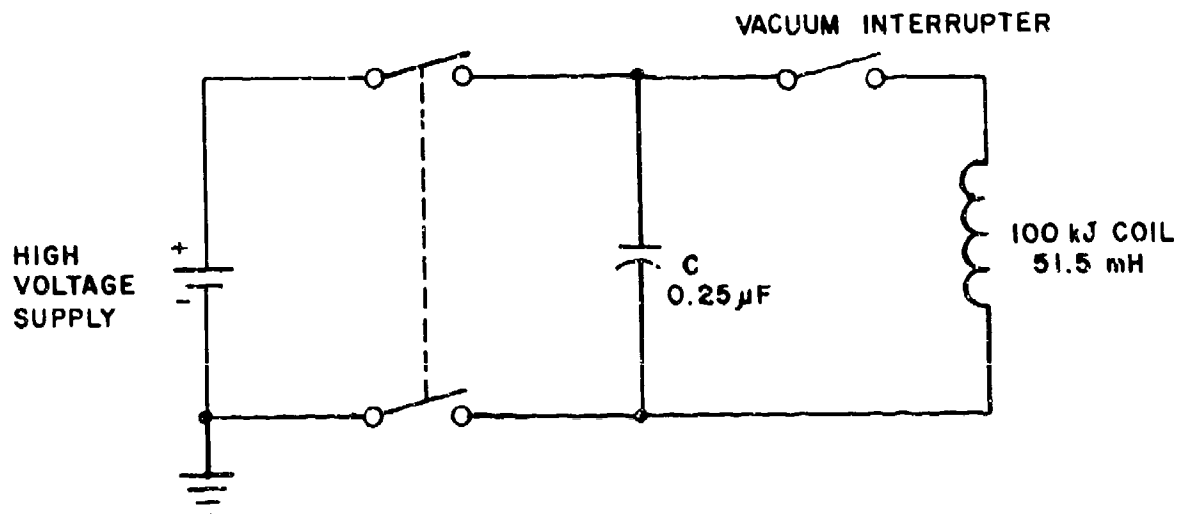


Figure 35 Schematic illustrating experiment to measure breakdown properties of current lead configuration using full scale mode.

Table XI
EFFECTIVE RESISTANCE OF HELIUM AND FOAM AT 50 kV

<u>Run</u>	<u>Resistance (MΩ)</u>
1	60
2	74
3	64
4	74
5	81



COIL TERMINAL VOLTAGE (kV)

50

63

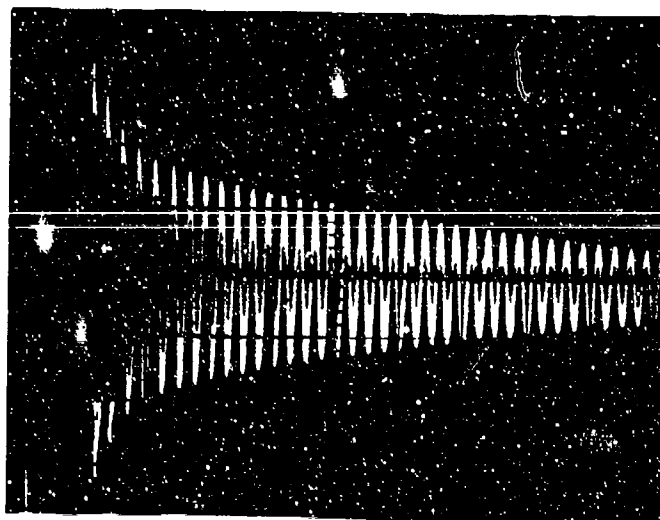
RESULT

NO VOLTAGE BREAKDOWN

ARCING WITHIN DEWAR

Figure 36 Schematic of Circuit Used for High Voltage Ringing Tests

Current 50 A/cm



Time 5 ms/cm

Figure 37

High Voltage ringing test on a 100 kJ coil
(50 kV); Capacitance - 0.25 μ F; Switch,
vacuum interrupter.

at all voltages from 5 kV to 50 kV. In order to extend this test to higher voltages, the sense coil (used as a secondary transformer winding) was driven by a 1 μ F capacitor through the vacuum interrupter. As illustrated by Figure 38 arcing occurred when the coil terminals were driven to 63 kV. Thus, the maximum operating voltage of the present system is between 50 kV and 63 kV. This is consistent with the tests previously carried out on the full-scale mockup of the lead assembly.

e. Summary and Conclusions

A pair of vapor cooled current leads were designed which were optimized for continuous operation at a current of 1,250 A but which could also be safely operated at a steady current of 2,000 A without excessive helium boiloff. The predicted boiloff due to the leads was 2.5 l/hour, 3.9 l/hour and 6.9 l/hour for zero current, 1,250 A and 2,000 A respectively. It was not possible to measure separately the boiloff due to the leads themselves, but measurements of total boiloff from the system were consistent with the predicted boiloff due to the leads.

In this lead design no attempt was made to reduce the boiloff due to the leads to the minimum possible for leads operating under pulsed conditions. However, analyses were conducted to arrive at design criteria for current leads operating in a pulsed mode. The results of these analyses are presented.

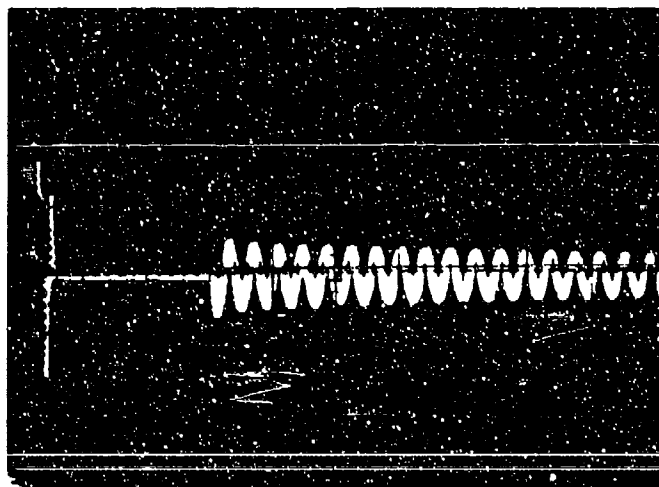
Since the leads were to be run with high voltages between them, both theoretical and experimental studies were conducted to arrive at a suitable design. High voltage experiments conducted during the test on the 100 kJ coil system indicated that limiting operating voltage lay between 50 kV and 63 kV. This was consistent with the results of the studies conducted during the design of the leads.

5. 100 kJ COIL DESIGN

a. Introduction

A light weight 100 kJ superconducting energy storage coil capable of being pulsed repetitively at a rapid rate with high voltages appearing across its terminals is not a trivial design problem. Such a coil is at the state of the art of superconducting magnet technology. There are many design aspects which must be thoroughly investigated in order to arrive at a successful coil design. The conductor must be such that when the coil is operated in a transient mode the heat which is generated within the windings must not be so great as to raise their temperature beyond critical and the cooling channels must be large enough that the helium gas evolved does not choke them. The windings must be supported against electromagnetic forces with a structure which is both light (to minimize the coil weight) and non-conducting (to avoid energy dissipation due to eddy current heating). The layers of windings in the

Current 200 A/cm



Time 1 ms/cm

Figure 38

High voltage ringing test on a 100 kJ coil with arcing. Applied voltage: 15 kV on sense coil, hence 63.3 kV on main winding. Capacitance, 1 μ F; switch, vacuum interrupter.

coil must be well insulated from one another to avoid voltage breakdown between them but their separation and the weight of the insulation between them must be made as small as possible to achieve low weights. These requirements and many others are frequently conflicting and a successful design involves an overview of all design aspects so that appropriate compromises may be made between contradictory demands.

To achieve this overview a theoretical and experimental program was embarked upon. Particular attention was paid to conductor design since it is this design aspect which has the greatest impact on the final coil configuration. Much of this work was reported on in technical report AFAPL-TR-72-38, Vol. I but summaries will be given here in the appropriate places.

This section of the report will deal with: analyses conducted to achieve a coil design which would be suitable for a light weight system; analyses which predicted certain coil operating limits; a description of the construction of model coils built to test the validity of conclusions reached from these analyses; and details of the electromagnetic, mechanical and high voltage aspects of the 100 kJ coil design. The results of testing the model coils and the 100 kJ coil will be described in Section III-2, Coil Evaluation Program, Limits of Performance. Although the relevance with respect to coil design of the losses due to pulsed coil operation will be described in this section, details of the loss mechanisms, loss models and loss measurements will be described in Sections III-3, 5, 6, 7, Coil Evaluation Program.

b. Optimization of Coil for Minimum System Weight

The weight of a superconducting inductive energy storage system is determined by the weights of a number of system components. These components fall into the following categories: energy storage coil and current leads; dewar; cryogen; current switch and switch actuator; power supply; and electrical circuitry. For a given set of mission constraints, the latter three items are ultimately determined by the characteristics of the load and there is only a small amount of freedom for varying their weights. The first three items however are strongly dependent on the choice of coil geometry, operating field, and conductor. It is the influence of the coil design on the total weight of coil, dewar and cryogen that will be described in this section. For a more detailed account the reader should refer to technical report AFAPL-TR-72-38-Vol. I, Section II Parametric Analyses, and AFAPL-TR-72-38-Vol. III, Weight Optimization for Energy Storage Coil, Cryogen and Dewar.

When a superconducting magnet is operated in a pulsed mode, energy is dissipated in the windings. The amount of energy dissipated depends upon the characteristics of the conductor, the quantity of conductor in the coil, the maximum field to which the coil is charged and the rate of change of field which the conductor experiences. The details of this loss mechanism are treated more fully in technical report AFAPL-TR-72-38-Vol. I, Appendix II Conductor Losses During Transient Operation, and also in Section III-3, Theory of Losses in Pulsed Coils, of this report; a brief outline, however, will be given here. The energy losses

fall into three categories depending on the regime in which the coil is operating. These are: magnetization loss due to the superconductor itself; eddy current loss due to currents induced in the normal matrix surrounding the superconductor; and transport current loss due to the normal matrix, should the superconductor go normal.

The magnetization energy loss is not time rate dependent. It is a hysteretic type loss whose magnitude depends for a given conductor only on the size of the hysteresis loop. The loss is approximately proportional to the maximum field experienced by the conductor. The energy loss per unit volume of the superconductor is proportional to the diameter of the superconductor. Thus, to minimize the magnetization energy loss per unit volume both the wire diameter and the maximum field excursion should be as small as possible.

The eddy current energy loss per unit volume is proportional to the rate of change of magnetic field, to the square of the wire diameter and is inversely proportional to the normal matrix resistivity. Therefore, for a given set of mission constraints (which define the pulse shape) to minimize the eddy current energy loss per unit volume the wire diameter and the maximum field should be as small as possible and the matrix resistivity should be as high as possible.

The transport current loss per unit volume (in the situation where the superconductor goes normal) is proportional to the transport current density in the matrix and the matrix resistivity and is inversely proportional to the time over which the superconductor is normal. Thus, to minimize the transport current loss, the current density and the resistivity should be as low as possible and the time over which the conductor is normal should be as small as possible. It can be seen immediately that there is a conflict in the resistivity requirements for minimum eddy current loss and minimum transport current loss. Other conflicts occur when the weight of the coil is considered; for example, a low transport current density in the matrix would imply a large area of cross section of matrix and therefore a high coil weight. The final choice of conductor involves a compromise between these conflicting requirements. Clearly whatever the final choice of coil geometry and operating field is the situation can only be improved by reducing the losses by a suitable choice of wire diameter, matrix resistivity and transport current density. Leaving aside for the moment the impact on system weight of the geometry and operating field of the magnet, consider the effect of wire size, matrix resistivity, transport current density and pulse shape on the energy losses.

As far as the transport current density is concerned, there is little choice. The area of cross section of normal matrix must be low so as to minimize the conductor weight. The mode of operation of the 100 kJ energy storage coil is for a relatively long (about 0.2 s) charge and a rapid discharge (about 1 ms). Of all the losses considered, if a low area of cross section matrix is used, the transport current density loss is potentially the highest. It would be greater than either the

magnetization loss or the eddy current loss, both on discharge and on charge. The losses due to the transport current on charge would be totally unacceptable. Therefore, since it is not possible to reduce the current density, it is essential that the coil be prevented from going normal during charge and extremely desirable that it should remain superconducting on discharge.

This is achieved by putting sufficient normal matrix around the superconductor to meet stability (9) criteria and by reducing the losses due to eddy currents and superconductor magnetization to a point where the temperature rise in the conductor does not exceed the superconducting to normal transition temperature of the superconductor. Analyses were conducted to estimate the magnitude of this effect and they will be described in detail in Section 11-5-c. Fortunately the eddy current losses at discharge times of the order of 0.2 s are small in comparison with the magnetization losses even when a low resistivity matrix such as copper is used. The problem then reduces to minimizing the magnetization losses in the superconductor itself. Thus, since the magnetization loss per unit volume is proportional to the diameter of the superconductor, the diameter must be made as small as possible.

A possible way of achieving this would be to make a twisted multifilamentary wire in which superconducting core diameters of the order of 4 μm can be obtained. However, the filaments in such wires behave independently only if the twist pitch is less than a certain critical value (10) dependent among other things on matrix resistivity and the rate of change of magnetic field to which the wire is subjected. Above this critical twist pitch the bundle of wires behaves as if it were a solid wire having the same diameter as the bundle. For a copper matrix the twist pitch could be made small enough for conditions during charge (about 0.2 s) but during discharge (about 1 ms) the twist pitch would have to be impractically small. The critical twist pitch could be made larger by using a higher resistivity matrix such as cupro-nickel but this is not desirable since if this were done then: (1) the stability criterion would require a larger area of normal matrix thereby increasing the weight; and (2) if the conductor should go normal on discharge then the transport losses would be correspondingly higher. The multifilament cupro-nickel matrix wire was therefore rejected in favor of single core material with a copper matrix.

Thus to achieve minimum losses and to ensure that the conductor remains superconducting on charge a single core of niobium titanium with as small a diameter as possible surrounded by the minimum amount of copper necessary to meet the stability criterion is required.

Magnetic Corporation of America has produced niobium-titanium/copper wires of diameter as small as 2.0×10^{-3} inch diameter in developmental quantities and 4.5×10^{-3} inch diameter wires in production quantities. Analyses indicated that 4.5×10^{-3} inch diameter wire having a copper to superconductor ratio of 1.4:1 would have losses much smaller than those necessary to drive the conductor normal during charge. During discharge the situation appeared to be marginal in that under certain circumstances parts of the coil in the high field regions might go normal (this will

be discussed further in Section II-5-c, Effect of Transient Heating on Coil Performance). In view of the results of these analyses, it was decided to use 4.5×10^{-3} inch diameter wire as a basis for further theoretical and experimental studies. This avoids the expense which would be involved in developing capabilities for large scale production of 2×10^{-3} inch diameter wire. Depending on the particular circuit requirements of a system a number of these 4.5×10^{-3} inch diameter wires would have to be grouped in some way to attain the desired operating current.

Having arrived at a particular conductor design by a process of compromise involving: minimizing losses; minimizing weight, ensuring superconductive properties throughout the cycle; and practicality of manufacturing, we can now turn our attention to the influence of coil characteristics on system weight.

The cryogenic system consists of the coil, the dewar and the cryogen. It is the combined weights of these three items which must be minimized. At a given current density, the coil volume (and therefore coil weight, given a particular method of construction) may be minimized, for a given stored energy by giving it the dimensions of a Brooks Coil (11). However, this geometry gives a high field and therefore such a coil would generate high losses. This results in a high cryogen consumption and therefore a large weight of cryogen to be carried. Since this cryogen must be contained, a large dewar is necessary which further adds to the system weight. The net result is a high system weight. Furthermore, the critical current/critical field characteristics of superconductors are such that at higher fields smaller currents can be carried. Since the current density is lower more conductor is required for a Brooks coil than that required for a non-Brooks coil operating at a lower field. Thus by reducing the operating field strength the losses become lower, thereby reducing the weights of the cryogen and dewar, and the coil weight becomes lower because it is possible to operate the coil at a higher current density.

This saving in coil weight is made possible to a large extent by the fact that large excursions in geometry from the minimum volume Brooks coil shape do not result in large increases in coil volume, i.e., the optimum is very flat. The small increases in volume are more than compensated for by the reduction in field strength that allows a higher operating current density. The deviation from the optimum which reduces the field strength is one in which the coil diameter is increased. However, as the coil diameter is increased more and more there eventually comes a point at which the volume increases so quickly that the increase in current carrying capability of the superconductor cannot compensate for it and the coil weight then begins to increase. This is the point at which the coil weight is optimized. It is still not necessarily the point at which the system weight is optimized though.

If the coil diameter is allowed to continue to increase past the point of minimum coil weight the field is still being reduced and therefore the cryogen weight is still falling as is the weight of that part of the dewar which contains the cryogen. However, it must be remembered

that in addition to containing the cryogen, the dewar also contains the coil and this part of the dewar has been growing during the time the coil has been increasing in diameter. There eventually comes a point (on the higher diameter side of the coil minimum weight) where the combined increases in weight of the coil and that part of the dewar which contains the coil exceeds the combined decreases in weight of the cryogen and that part of the dewar which contains the cryogen. This is the point of minimum system weight.

Thus in general in a minimum weight system the coil weight is not the minimum achievable. How far the coil weight is from its minimum weight depends strongly on the magnitude of the cryogen weight with respect to the weight of the coil. The cryogen weight is determined by the loss per pulse and the total number of pulses required per mission. The smaller the losses per pulse and the smaller the number of pulses per mission then the closer is the coil weight to its minimum achievable weight. For a more detailed description of this analysis, the reader should consult technical report AFAPL-TR-72-38-Vol. I, Section II, Parametric Analyses.

The results of applying this optimization procedure to a light weight 100 kJ coil system are shown in Table XII. System and coil weights are shown for systems in which the coil weight is optimized and in which the system weight is optimized. Two conductor diameters are considered. It can be seen that:

- (1) For both wire sizes the optimum coil weight is the same. This would be expected since the coil weight is not a function of wire diameter.
- (2) When the wire size is reduced the system weight falls irrespective of whether the coil weight or the system weight is optimized.
- (3) When the wire size is reduced the coil weight for the system optimized situation is nearer the optimum coil weight.
- (4) For both wire sizes a small deviation from the optimum coil weight produces a large reduction in system weight.

This table is presented as an illustration of the preceding arguments; the system shown in Table XII is not relevant to the experimental 100 kJ coil system.

Technical report AFAPL-TR-72-28-Vol. III gives a detailed description of the optimization procedure outlined above and presents the results of a parametric study for a large number of systems. The range of variables used in this parametric study are shown in Table XIII.

To summarize: based on the results of an analysis of losses dissipated in superconducting wire experiencing transient magnetic field conditions, a 4.5×10^{-3} inch diameter superconducting wire was chosen

Table XII

COIL AND SYSTEM WEIGHTS FOR A 100 kJ COIL SYSTEM

Energy = 100,000 J Pulse Duration = 250 μ s
 Pulse Rate = 5 pps Total Pulses = 3,000
 Copper/S.C. = 3

	Coil Weight	Total Weight	Loss/Pulse	Specific Energy
	kg	kg	kJ	kJ/kg J/lb
Large Wire (5×10^{-3} in.)	System Optimized	44	0.38	313
	Coil Optimized	312	1.08	149
Small Wire (2×10^{-3} in.)	System Optimized	42	0.132	560
	Coil Optimized	122	0.255	182

Table XIII

RANGE OF MISSION CONSTRAINTS USED IN THE PARAMETRIC STUDY
TO DETERMINE SYSTEM WEIGHTS

Stored Energy (J)	10^4 , 10^5 , 10^6 , 10^7
Pulse Length (μ s)	10, 50, 100, 250, 400
Total Pulses	3×10^2 , 3×10^3 , 3×10^4
Superconducting Wire Diameter (10^{-3} inch)	0.5, 2, 5
Copper to Superconductor Ratio	1, 3

as the most suitable component for constructing the conductor for the 100 kJ coil. An analysis of the effect of coil geometry and operating field on system weights indicated that the coil should be of large diameter and low field. The conductor and coil geometry for the experimental 100 kJ coil system were chosen with the results of these analyses in mind.

c. The Effect of Transient Heating on Coil Performance

As was indicated in Section II-5-b, Optimization of Coil for Minimum System Weight, when the conductor in a superconducting coil is subjected to transient field conditions energy is dissipated within the conductor. This energy dissipation results in a temperature rise within the windings, the magnitude of which depends on the power dissipation per unit volume, the time over which this dissipation occurs, the thermal diffusivity of the windings and the heat transfer characteristics between the windings and the helium bath. Since superconductors exhibit a temperature (dependent on ambient field and current density conditions) above which they revert to the normal state, the allowable temperature rise is limited. Cooling must be adequate to allow the peak current level to be reached while the conductor is in a superconducting state and must be good enough to allow the temperature of the windings to decay in such a way that over a long train of pulses, there is no cumulative increase in temperature.

To investigate the transient thermal behavior of the windings two models were considered. In each case for mathematical tractability a one dimensional model was chosen. The windings were considered to be slabs with homogeneous thermal properties infinitely wide in two dimensions and having a thickness of 2λ where λ is the thickness of the actual windings. Cooling was assumed on both faces.

In the first model, uniform heat production per unit volume was assumed. The purpose of this model was to estimate the temperature at the center of the slab as a function of time. This model simulates conditions during the charge or discharge period. Physically what happens is as follows: when energy dissipation starts the temperature of the windings is the same as the bath temperature so there is no temperature differential to drive the heat into the bath. Therefore, the temperature of the windings at first rises rapidly. As a temperature difference between the windings and the bath builds up more and more heat is driven into the bath. This, together with the fact that the specific heat and thermal conductivity are rising, causes the rate of temperature rise to fall. Eventually an equilibrium situation is reached where the energy dissipated per unit time within the windings is exactly matched by the energy transferred into the bath per unit time and the temperature of the windings reaches a plateau.

The second model pertains to conditions during the period between pulses. It is assumed that the temperature of the windings has an initial parabolic distribution (maximum temperature at the center of the windings and minimum at the cooled surfaces). In this case there

is no heat production and the purpose of the model is to estimate the maximum temperature of the windings as a function of time as the temperature decays.

Carslaw and Jaeger (12) give solutions to both of these models and a detailed account of the analyses are given in technical report AFAPL-TR-72-38-Vol. I, Appendix IV Thermal Transients While Pulsing. The windings of course are not homogeneous so in using these models to predict winding temperatures suitably averaged values of thermal properties were used.

Figure 39 shows the predicted temperature rise at the hottest part of the windings in the 100 kJ experimental coil during the charge period (assumed to be 0.167 s). The assumption was made that the energy generated during the charge time was generated uniformly over the charging period. A maximum value of temperature is reached in about 20 ms which is short compared with the charge time of 167 ms. This means that the winding comes into thermal equilibrium and loses heat at the same rate as it is generated. The value of temperature rise of 0.22 K is small, which means that no superconducting to normal transition will occur during the charge provided that the initial temperature of the windings is near liquid helium temperature. The heat which is generated during the discharge part of the cycle is generated in a short time, and since very little heat can escape, the situation is essentially adiabatic. Enthalpy calculations indicate that the temperature of the windings rises several Kelvins in this time. If values of the energy dissipation averaged over the coil are used the maximum rise in the winding temperature is about 3.5 K. If values of energy dissipation at the peak field position are used, the temperature rise is 7.3 K. This temperature rise is high enough to suggest that some parts of the windings (in the higher field regions) would go normal for part of the discharge period and from the results of the loss measurements made on model coils there are indications that this is happening. These results will be described in Section III-2-a, 1 kJ Coil Evaluation Tests.

During the interpulse period, the windings cool. The initial temperatures are those which the windings have reached at the end of the charge-discharge period, i.e., the sum of the steady state temperature rise during charge and the adiabatic temperature rise during discharge as described above. Figure 40 shows the temperature of the windings during the interpulse period for initial temperatures based on average energy per unit volume and the peak energy per unit volume. A 167 ms charge time and a 33 ms interpulse time was assumed for a repetition rate of 5 pulses per second. These curves show that the windings cool in about 30 ms. This implies that for pulse repetition rates of five per second, the charge time may have to be increased in order to give a longer cooling off period between pulses to ensure that the temperature of the windings at the beginning of each pulse period is near 4.2 K.

If at the end of a pulse period, the windings have not cooled to their temperature at the beginning of the pulse period, the temperature

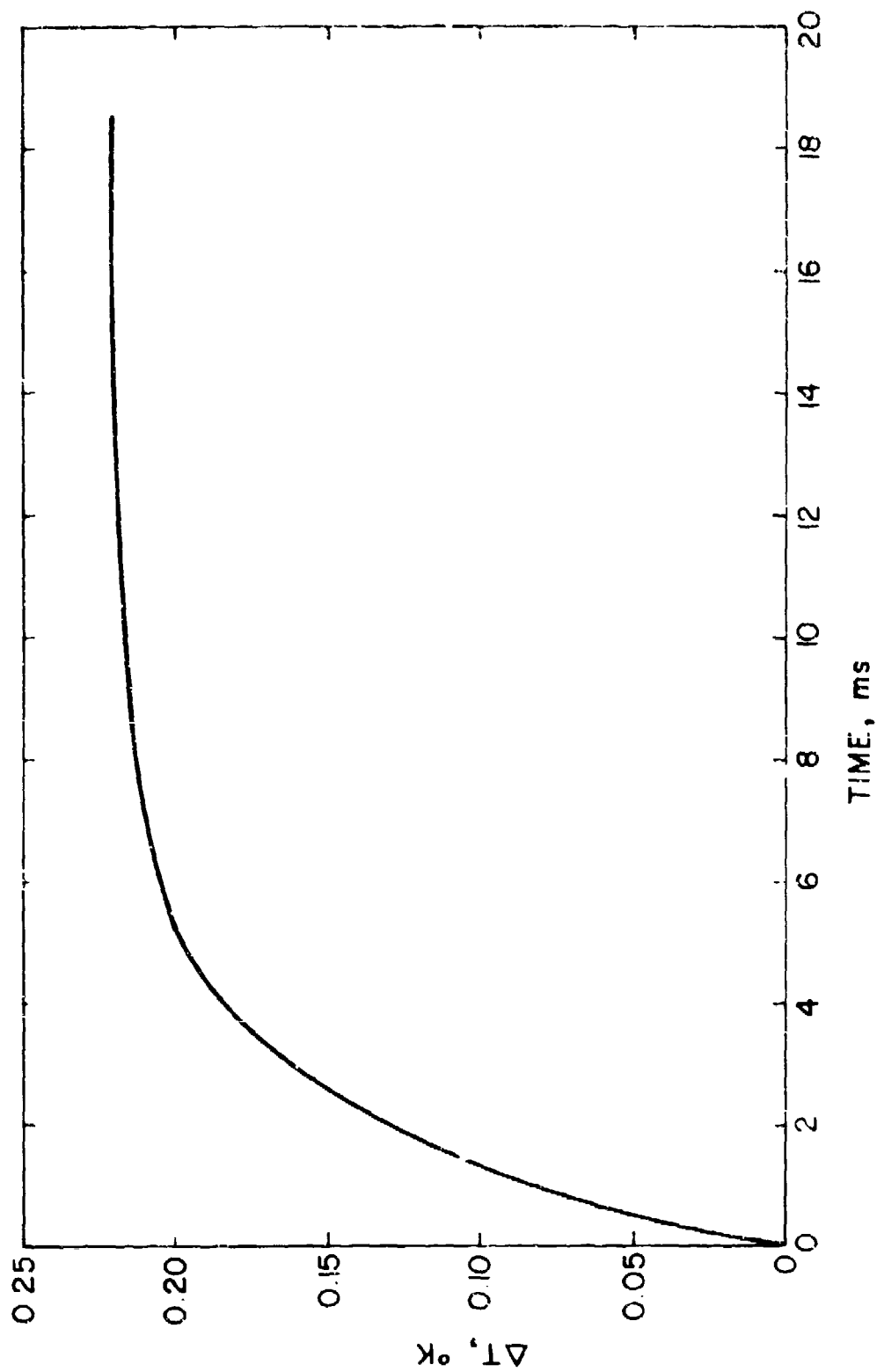


Figure 59 Temperature rise in hottest part of winding bundle as a function of time after beginning of pulse.

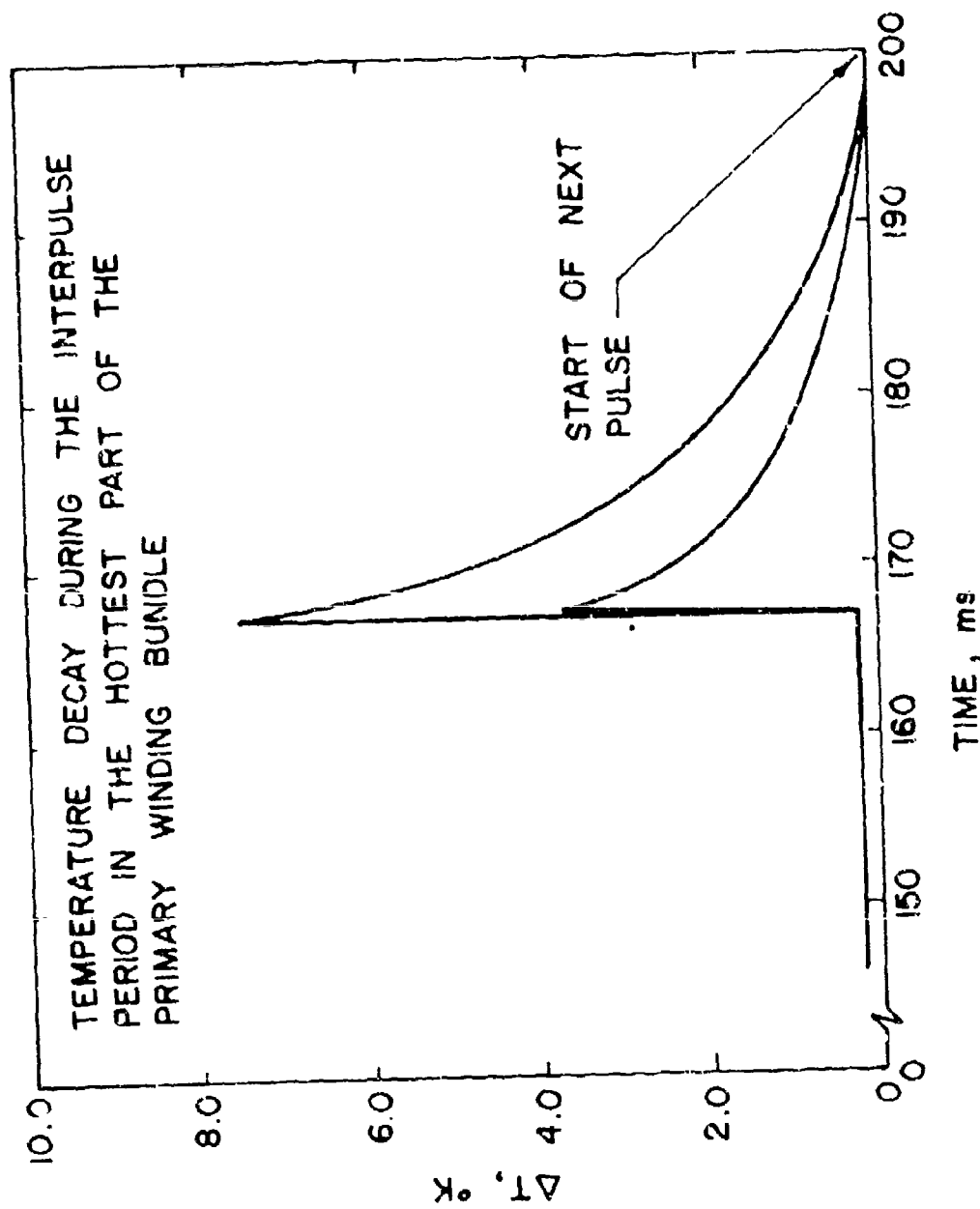


Figure 40 Lower curve for average conditions throughout magnet. Upper curve for situation in peak field position of magnet.

on successive pulses will progressively rise until it exceeds the transition temperature for the operating current and field. The coil would then go normal.

There were indications during tests on the model coils that under certain circumstances (high currents and short interpulse times) this effect occurs. These results will be described in Section III-2-a, 1 kJ Coil Evaluation Tests.

In addition to ensuring that the temperature of the windings does not rise to temperatures whereby transition to the normal state occurs precautions must be taken to limit the heat flux into the cooling channels to values such that the cooling channels do not become choked with helium gas.

Figure 41 is a figure taken from Smith (13) which illustrates the boiling heat transfer characteristics of liquid helium I for vertical flat plates. The characteristic can be divided up into three regimes. For temperature differences between the plate and the bath of up to about 0.8 K and heat fluxes up to about 1 W/cm^2 the mechanism of heat transfer is by nucleate boiling, and heat transfer coefficients are high. Above temperature differences of about 2 K the mechanism is film boiling and heat transfer coefficients are low. Between these two is a transition regime which is not of much interest. This heat transfer characteristic should be interpreted in the following way. If we start with very low heat fluxes (in the nucleate boiling regime) only small temperature differences are necessary to drive the heat across the interface. As the heat flux increases (still in the nucleate boiling regime) the necessary temperature difference rises but is still small. Eventually at heat fluxes of the order of 1 W/cm^2 the peak nucleate boiling heat flux is reached and if attempts are made to increase the heat flux beyond this point a transition to film boiling occurs and the temperature difference increases to tens of Kelvins. Clearly in a superconducting coil heat fluxes must be limited to values such that this peak nucleate boiling heat flux is not exceeded. The situation is somewhat worse than that indicated in Figure 41 since this is for a well ventilated plate. If the ventilation is reduced as it is in a narrow cooling channel, the peak nucleate boiling heat flux is also reduced. Figure 42 is due to Johannes (14) and illustrates the way in which the peak nucleate boiling heat flux varies with the ratio of length to diameter of the cooling channel. It can be seen that the curve if projected to small length to diameter ratios would cross the peak nucleate boiling heat flux axis at about 0.7 W/cm^2 . This corresponds to a well ventilated vertical plate and is consistent with the information given in Figure 41. As the channel length to diameter ratio is increased, the peak nucleate boiling heat flux decreases and at large length to diameter ratios is of the order of 0.1 W/cm^2 .

The cooling channels should be sized so that during the charging period, boiling is always in the nucleate boiling regime. This means that the rate of heat transfer into the helium should be below the peak nucleate boiling flux for the particular combination of channel length and diameter. Should the heat transfer rate rise above this peak

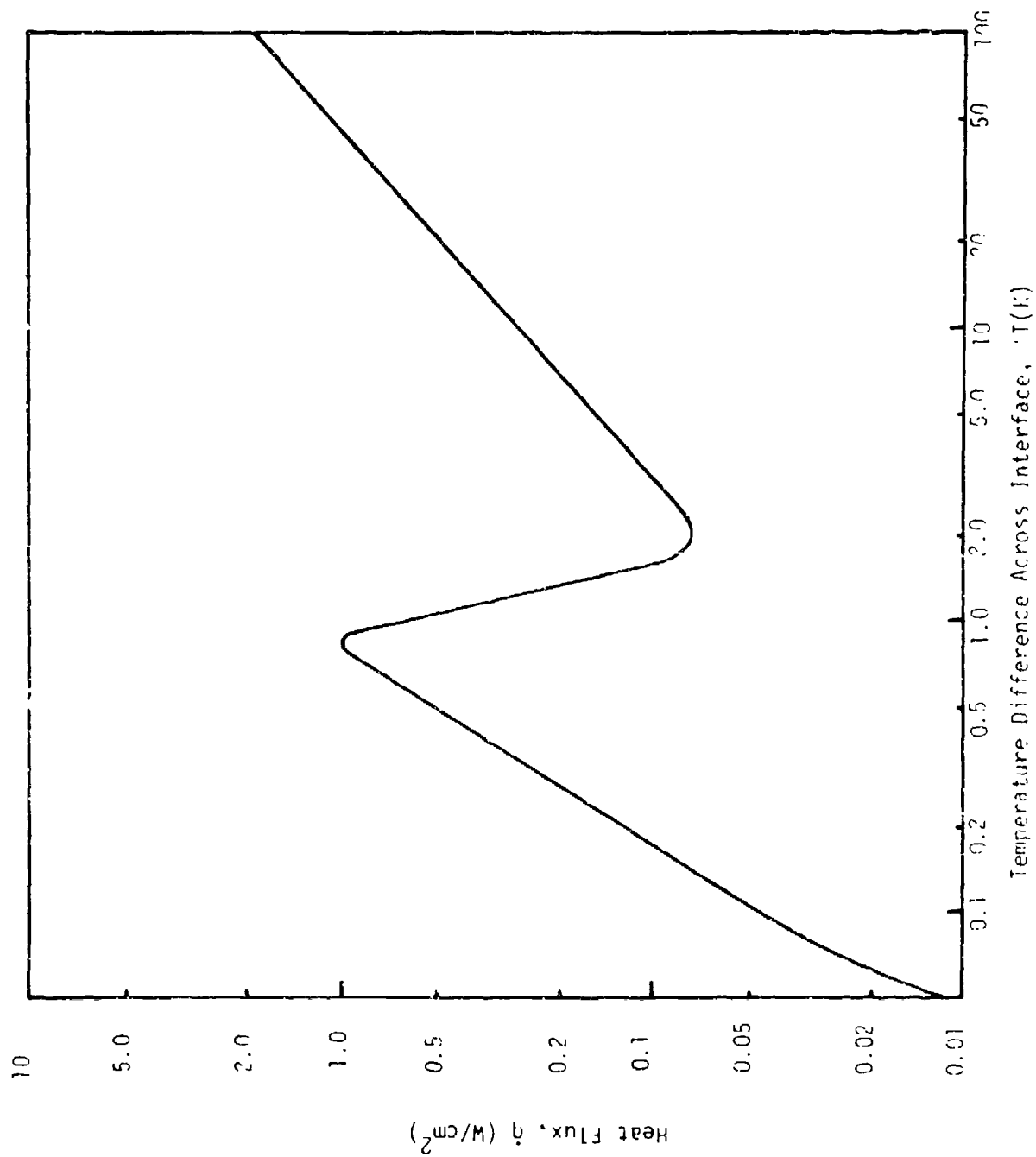


Figure 4) Boiling Heat Transfer Characteristic for Liquid Helium I for Well Ventilated Vertical Flat Plates.

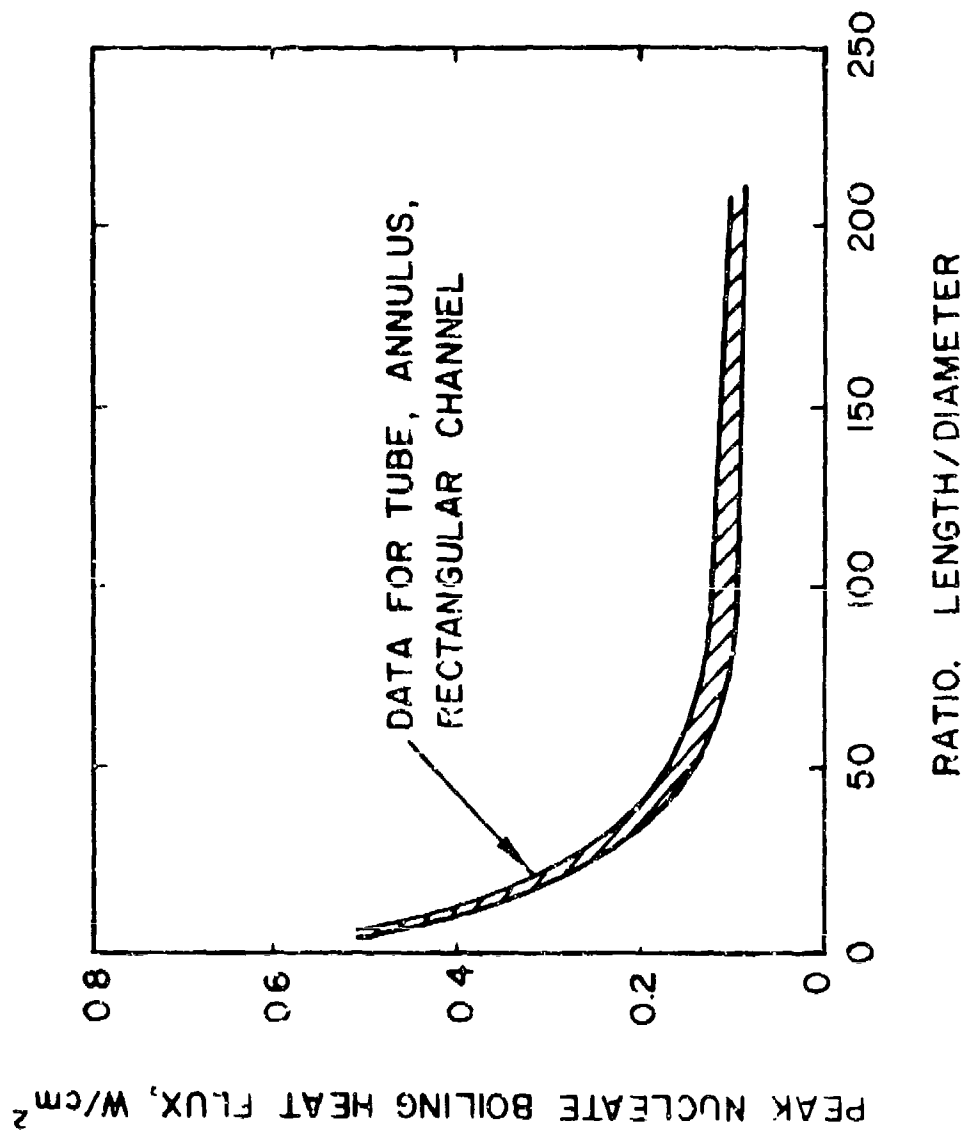


Figure 42 Peak nucleate boiling heat flux for vertical channels in liquid helium (continuous, heat-transfer conditions). (From Johannes, *op cit*).

nucleate boiling flux, transition to film boiling would occur with an accompanying increase in the temperature difference between the helium and the conductor surface. The channel would choke and the temperature of the conductor would exceed the critical temperature for ambient field and current conditions, thereby sending the coil normal.

In the 100 kJ coil design the estimated heat flux during charge is about 0.021 W/cm^2 in the peak field region of the coil (where the losses are highest). The length to diameter ratio of the channel eventually chosen is about 226. This corresponds to a peak nucleate boiling heat flux of about 0.08 W/cm^2 which is a factor of about 4 larger than the expected heat flux. This is a satisfactory margin of safety and it is also conservative since the cooling channels which include the peak field region also include conductor which is in lower field regions and which therefore experience lower energy losses. Thus, the conditions for the channels which include the peak field region may be such that the average heat flux for those channels is lower by a factor of perhaps two. This of course will increase the margin of safety by the same factor. Thus, there is no danger of the channels choking on charge.

During discharge of course conditions are much more severe since approximately the same amount of energy is dissipated as that dissipated during charge and the time available for heat transfer is approximately 100 times shorter. Under these conditions it is impossible to get rid of the heat dissipated in the windings. Therefore, as was indicated earlier in this section the thermal analysis of the windings was treated in an adiabatic manner, i.e., it was assumed that all heat dissipated was absorbed in raising the temperature of the windings.

To summarize: as far as coil performance is concerned there are two important aspects of thermal effects which must be considered. Firstly there is the question of whether the heat dissipated in the windings can escape from the conductor to the helium and secondly whether the helium vapor so formed can escape from the cooling channels. Analyses were performed to estimate the magnitude of these effects and it was concluded that during the critical charge period these effects would not adversely affect the coil performance. During discharge, however, when conditions are much more severe it was concluded that parts of the coil in the higher field regions would go normal for part of the discharge time. It was also concluded that there was the possibility that, under certain conditions such as high operating current and short interpulse time, the windings might not cool to the bath temperature by the time the next pulse began. Thus, under these conditions, the temperature of the coil might steadily rise during the course of a long pulse train.

d. Conductor Selection

Section II-5-b, Optimization of Coil for Minimum System Weight, described the reasoning which led to the selection of a 4.5×10^{-3} inch diameter niobium-titanium/copper superconducting wire as the basic component for the conductor. Section II-5-c, Effect of Transient Heating on Coil Performance, illustrated the necessity of limiting the temperature rise within the conductor and limiting the heat flux into the cooling channels.

The requirements of the electrical circuit determine the operating current of the coil. In this case, current switching requirements fix the current level at 2,000 A for the 100 kJ coil. The basic wire has only a small current carrying capacity (a few amperes) and circuit requirements for the coil system are such that some hundreds of amperes are needed. Thus, a number of these small wires must be grouped in such a way that the current requirement is met and the limitations regarding allowable temperature rise and allowable heat flux are also met. What is required is a configuration for the conductor such that it has a small thickness (to limit the temperature rise at the center of the wire bundle) and a large surface area (to limit the heat flux from the surface). A configuration which meets these requirements is a braid composed of the appropriate number of basic wires. Thus, the conductor chosen for the 1 kJ model coils was a flattened tubular braid of 48 of the basic 4.5×10^{-3} inch diameter wires, each wire being individually insulated. Figure 43 is a photograph of braid used in one of the model coils.

The conductor selected for the 7 kJ model coil was exactly the same except that because of higher current requirements, three such braids were wound in parallel.

The current requirements for the 100 kJ coil (2,000 A) called for an even greater total number of strands. The conductor selected for this was again a braid with 48 components but in this case each component consisted of 3 of the 4.5×10^{-3} inch diameter wires. The 100 kJ coil was wound with two such braids in parallel so the total number of strands was 288. Figure 44 is a photograph of this braid. Although the braided configuration is good with respect to its thermal characteristics there are some disadvantages associated with it. These are associated with problems involved in fabricating the braid since in producing long lengths of such braid occasional strand breakage is unavoidable. The implications of this are treated in detail in technical report AFAPL-TR-72-38-Vol. I, Appendix III Operational Characteristics of Braided Superconductor. However, a brief summary will be given here.

If the break is detected and repaired the strand having the break will have a resistance which the other strands do not have. Under steady state conditions this strand will not carry current. Thus, even if the break is repaired, under steady state conditions the current carrying capacity of the braid is impaired. Fortunately, the time required to reach steady state under certain circumstances can be so long that the effect of the joint is not noticeable. It is shown in Appendix III of technical report AFAPL-TR-72-38-Vol. I that, provided the charge time of the coil is less than a certain critical time depending on the inductance of the strand, the joint resistance and the coefficient of coupling between strands, the effect is negligible. This condition may be written:

$$t_{ch} \ll \frac{2L}{R} \left\{ \frac{1 + (n-1)k - nk^2}{1 + (n-1)k} \right\}$$

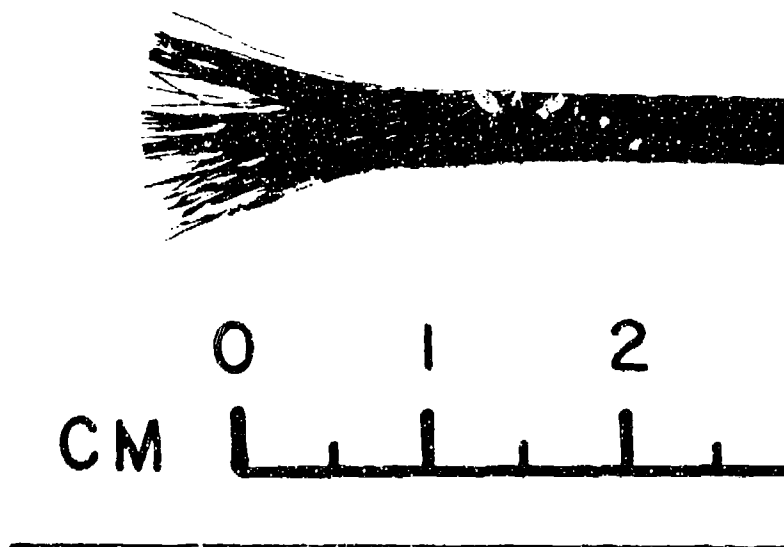


Figure 43

Braid consisting of 1×48 strands of 4.5×10^{-3} inch diameter superconducting wire. Each strand consists of a single core of niobium titanium in a high conductivity copper matrix. The copper to superconductor ratio is 1.4:1.

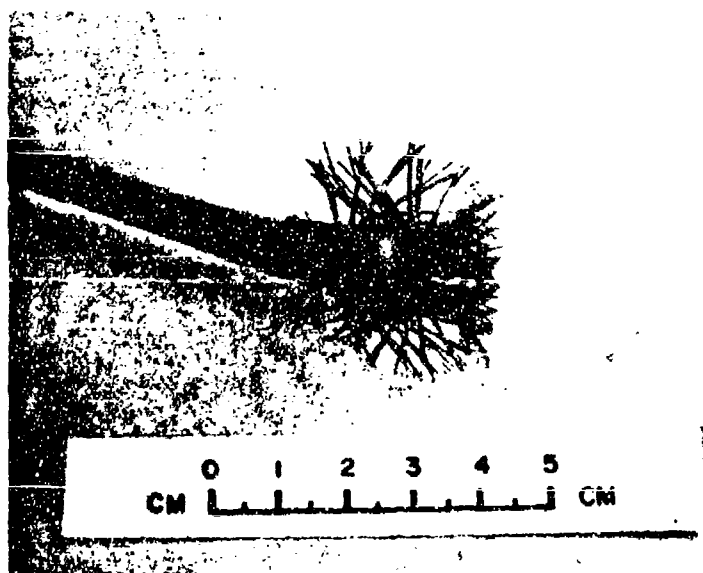
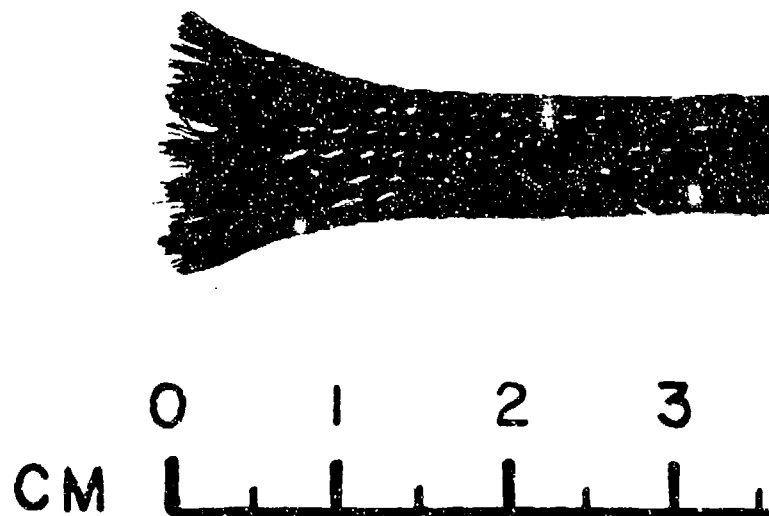


Figure 44

Shown above are photographs of a braid containing 144 strands of .0045 inch diameter superconducting wires. This braid is manufactured by MCA HIconductor Division for use in pulsed superconducting magnets. The braid shown is capable of carrying over 2000 A of electric current.

t_{ch} = charge time

L = self inductance of a single strand

R = resistance of repaired break

k = coefficient of coupling between strands

n = number of strands in braid

When this formula is applied to conditions pertaining to the 100 kJ coil, it is found that the intended charge time is orders of magnitude less than the critical charge time described above.

If the break is not repaired, the current carrying capacity of that strand is lost and the current load on remaining strands is increased. Under certain conditions (e.g., very many fine strands with the break occurring in handling after production) the break may not be detected; consequently, it may be desirable to periodically short all conductors in the braid at intervals along its entire length. Shorts of this type however may effect braid losses and operational characteristics. This occurs because there are now closed loops in the braid and it is possible under certain circumstances that the changing magnetic field could induce a circulating current through the shorted region thereby causing energy dissipation because of the resistance of the short. Appendix III of technical report AFAPL-TR-72-38-Vol. I derives an expression for a minimum length between shorts if the energy dissipation within the windings is not to exceed a certain fraction of the energy stored in the coil.

There is, however, a more stringent condition. This is because if a circulating current is set up it will add to the transport current on one side of the loop and subtract from it on the other side. The danger is that the total current in the side of the loop where the two add will exceed the critical current for the ambient field. This situation is also described in Appendix III of technical report AFAPL-TR-72-38-Vol. I and a criterion for the minimum distance between strands is derived.

There is yet another situation which must be considered. This concerns the effect on strand should it go normal without other strands in the braid going normal. The danger here is that the current in the normal strand will not transfer out of the strand quickly enough to prevent the temperature of that strand from reaching damagingly high temperatures. This sets a maximum allowable distance between strands.

It happens that this maximum distance, for the case of the 100 kJ coil, is greater than the length of conductor in the coil so there is no need to introduce periodic shorts to prevent single strand damage.

During conductor fabrication where breaks occurred and were detected they were repaired but because of the danger associated with periodic shorting described above (i.e., that of introducing additional losses and

that of exceeding the critical current because of superimposed circulating currents) it was decided not to deliberately introduce them into the 100 kJ coil. It happened that during the fabrication of the conductor only two breaks were detected and because of close scrutiny during the fabrication and winding operations it is unlikely that any were undetected. However, if there were any, there would be so few that the effect in the current carrying capacity would be negligible.

To summarize: so as to meet the current requirements for the coil and also the conditions necessary to avoid thermal problems in operating the coil, a conductor consisting of a number of 4.5×10^{-3} inch diameter wires in the form of a flattened tubular braid was selected for the 100 kJ coil. This type of conductor has a large surface area and a small thickness and as such has good thermal characteristics. Analyses indicated that detected broken strands should be repaired but that it would be better not to deliberately introduce shorts periodically in the braid as it was being wound because:

- (1) this is not necessary for avoiding burnout in an individual strand should it alone go normal;
- (2) the effect on current carrying capacity would be negligible if a few broken strands remained undetected and unrepaired;
- (3) there is some danger if the shorts are too close together because of additional heating within the windings and because of circulating currents creating a condition where the critical current is exceeded in parts of the conductor.

e. Model Coils

To determine the effects of the various system operating parameters and coil construction details on coil losses, three coils were designed and built. The first two coils are nominally capable of storing one kilojoule, while the third coil is capable of storing 7 kilojoules. This section will describe details of their construction. Details of results obtained during their testing will be presented in Section III, Coil Evaluation Program.

The two 1-kilojoule coils differ primarily in the details of the construction of the superconductor. Both of the conductors were made up of a flattened tubular braid of 48 strands of a niobium-titanium copper composite with each individual strand insulated from the other and having a diameter of 4.5×10^{-3} inches. One of the conductors is made up of strands containing 121 individual filaments of NbTi while the other is made up of strands having a single core of NbTi. The multifilament strands have a copper to superconductor ratio of 3:1, while the single filament strands have a copper to superconductor ratio of 1.4:1. The multifilament strands were insulated with Formvar and the single filament strands with Polybondex. Both insulations were 0.25×10^{-3} inches thick and both braids are approximately 0.100 inches wide by 0.020 inches thick.

The coil mandrel and end flanges are of linen phenolic. The windings are separated by strips of paper phenolic 0.031 inch thick by 0.12 inch wide placed on 0.50 inch centers. This provides 0.37 inch by 0.031 inch cooling passages. The interlayer insulation is mylar double wrapped. The insulation extends 0.50 inches beyond the ends of the windings to prevent voltage breakdown between layers. The space between the ends of the windings and the flanges is filled with mylar tape to give support to the windings. The flanges have large sections cut away to ensure good helium ventilation. The windings are impregnated with epoxy to prevent premature quench caused by wire movement.

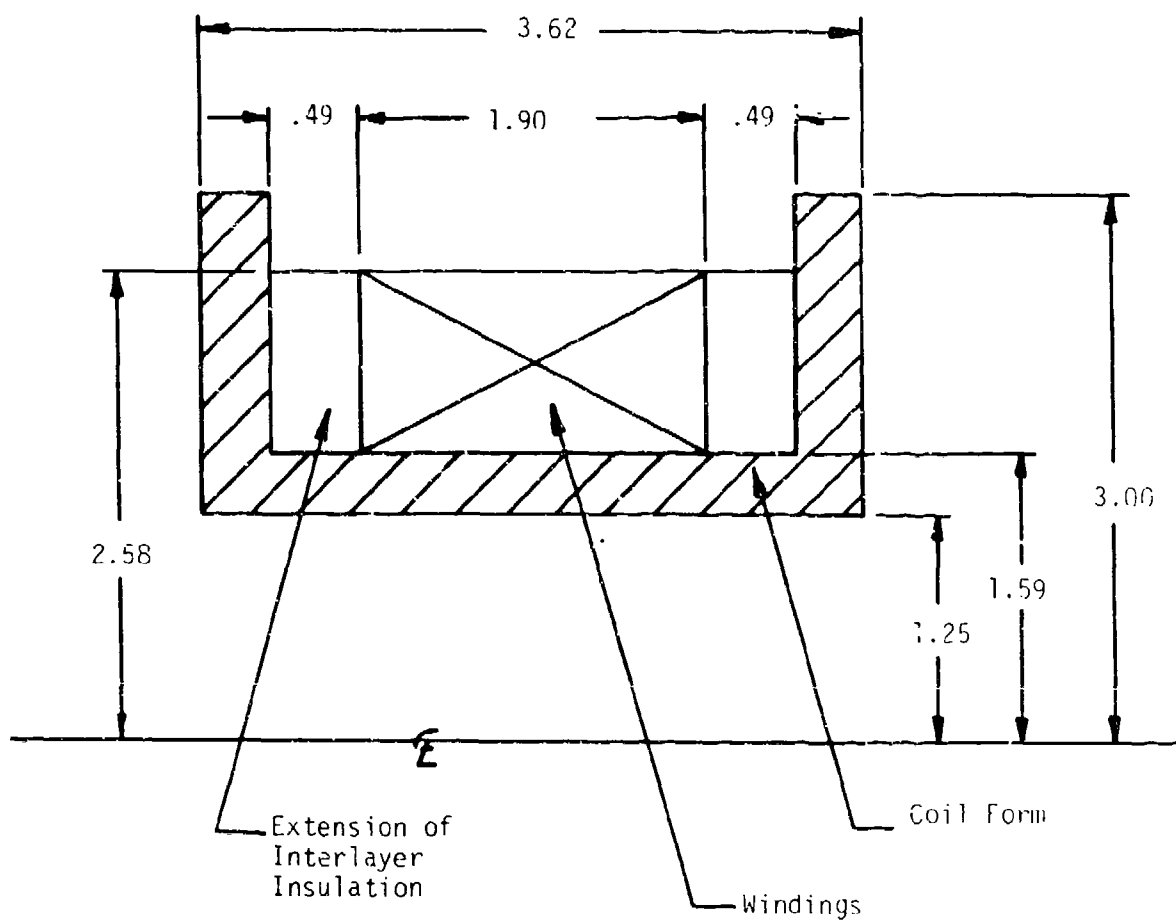
Figure 45 is a schematic showing the dimensions of the 1 kJ energy storage coil, Figure 46 is a photograph of the coil and Figure 47 shows a detail of the winding construction. Table XIV summarizes the specifications of the 1 kJ coil which used the single core material. The specifications of the 1 kJ coil which uses the multifilament wire are almost exactly the same except for the basic strands of superconductor. The multifilament wire has 121 filaments and a copper to superconductor ratio of 3:1. Figure 48 shows the critical field/critical current characteristic for the material used in the 1 kJ coil which has single core material and also the central and peak field load lines for the coil. Details of performance are given in Section III, Coil Evaluation Program.

The 7 kilojoule coil was wound with a 48-strand, single core braid identical to that used in the one kilojoule coil. However, to obtain the desired operating current, the coil was wound with three of the 48-strand braids in parallel. The method of construction was identical to that used in the 1 kJ coils.

Figure 49 is a schematic showing the dimensions of the 7 kJ coil. Figure 50 is a photograph illustrating the winding technique. After a layer of conductor was wound epoxy resin was brushed on to the exposed surface. Care was taken to ensure that there was sufficient epoxy resin to saturate the windings but that none dropped through the braid to block a cooling channel. While the epoxy resin was still wet, layers of mylar electrical insulation were wrapped around the windings. Figure 51 is a photograph of the completely wound coil. The three parallel braids can be clearly seen entering the coil at 120° intervals. Table XV summarizes the specifications of the 7 kJ energy storage coil. The operating current, central field and peak field in this table correspond to a stored energy of 7 kJ. These values are 0.65 times the values occurring when the coil is at the critical state. When the coil is in this situation, the current is 932 A, the central field is 3.12 Wb/m², the peak field is 3.96 Wb/m² and the stored energy is 16.5 kJ. Details of the performance of this coil are given in Section III, Coil Evaluation Program.

f. 100 kJ Coil Electrical and Magnetic Design Aspects

As described in Section II-5-b, Optimization of Coil for Minimum System Weight, a computer optimization procedure was carried out to



Dimensions in Inches

Figure 45 Schematic Illustrating Dimensions of the 1 kJ Energy Storage Coils.

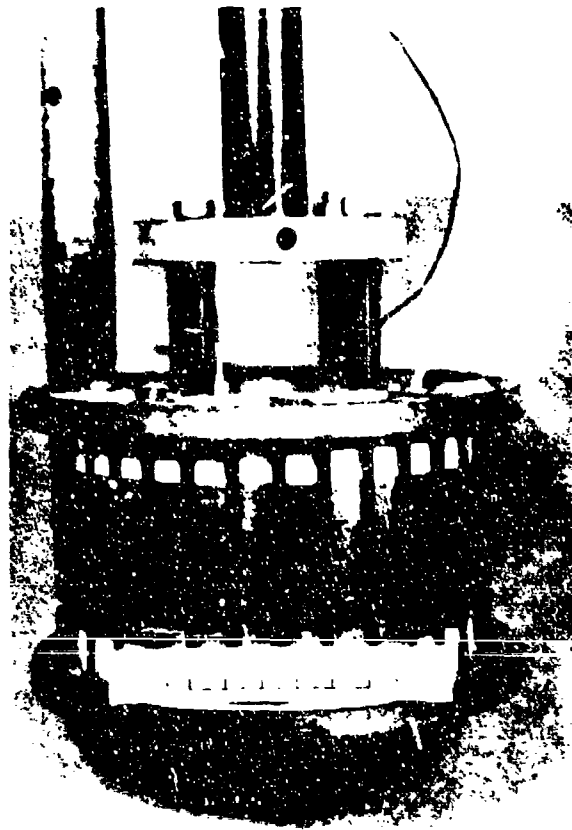


Figure 46 Model pulsed energy storage coil. At a current of 330 A the coil produces a central flux density of 1.30 Wb/m^2 in a 0.064 m bore. The peak flux density at the winding is 1.85 Wb/m^2 . The conductor is a 48 strand braid. Each strand has a diameter of 4.5×10^{-3} inch and has 121 filaments of niobium titanium in a high conductivity copper matrix. The ratio of copper to superconductor is 3:1. The coil has been operated at 5 pulses per second.

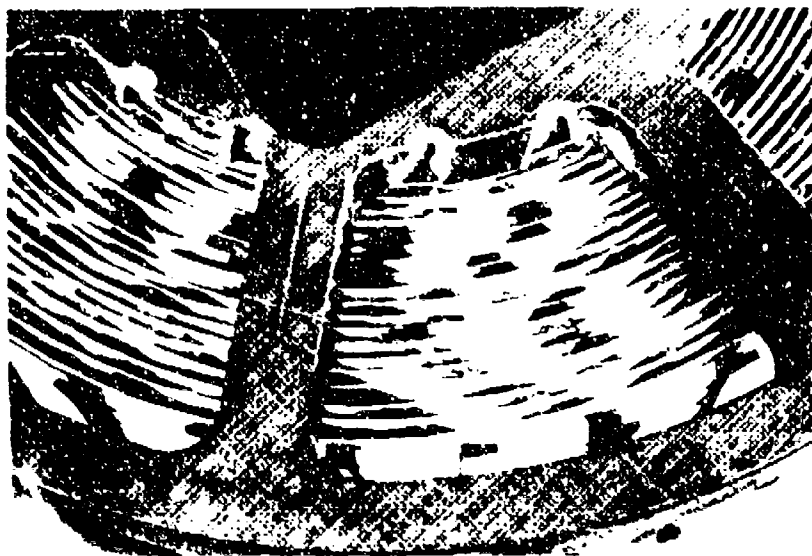


Figure 47 Model pulsed energy storage coil. Detail of winding construction. Each winding face is exposed directly to liquid helium. The ventilation is provided by interposing 0.031 inch x 0.125 inch slats on 0.50 inch centers between layers.

Table XIV

SPECIFICATIONS OF 1 kJ ENERGY STORAGE COIL

Inner winding radius	4.04×10^{-2} m (1.59 inch)
Outer winding radius	6.55×10^{-2} m (2.58 inch)
Winding length	4.82×10^{-1} m (1.90 inch)
Operating current	425 A
Stored energy at operating current	1.0 kJ
Central flux density at operating current	1.78 Wb/m^2
Peak flux density at operating current	2.33 Wb/m^2
Inductance	11.1 mH
Number of layers	19
Number of turns per layer	20
Total number of turns in coil	380

Conductor

Winding configuration	single braid
Approximate braid dimensions	2.4×10^{-3} m by 5.1×10^{-3} m (0.094 inch x 0.020 inch)
Braid configuration	48 strands per braid
Total number of strands	48
Strand diameter	1.14×10^{-3} m (4.5×10^{-3} inch)
Strand insulation material	Formvar
Strand material	Nb/Ti in Cu matrix
Copper to superconductor ratio	1.4
Number of filaments of Nb/Ti per strand	1

Voltage Insulation

Material	Mylar film
Configuration	4 layers between each layer of windings
Film thickness	1.3×10^{-5} m (0.5×10^{-3} inch)

Support Structure

None

Cooling Configuration

Cooling channels formed by axial slats 0.13 inch wide by 0.031 inch thick on 0.5 inch centers.

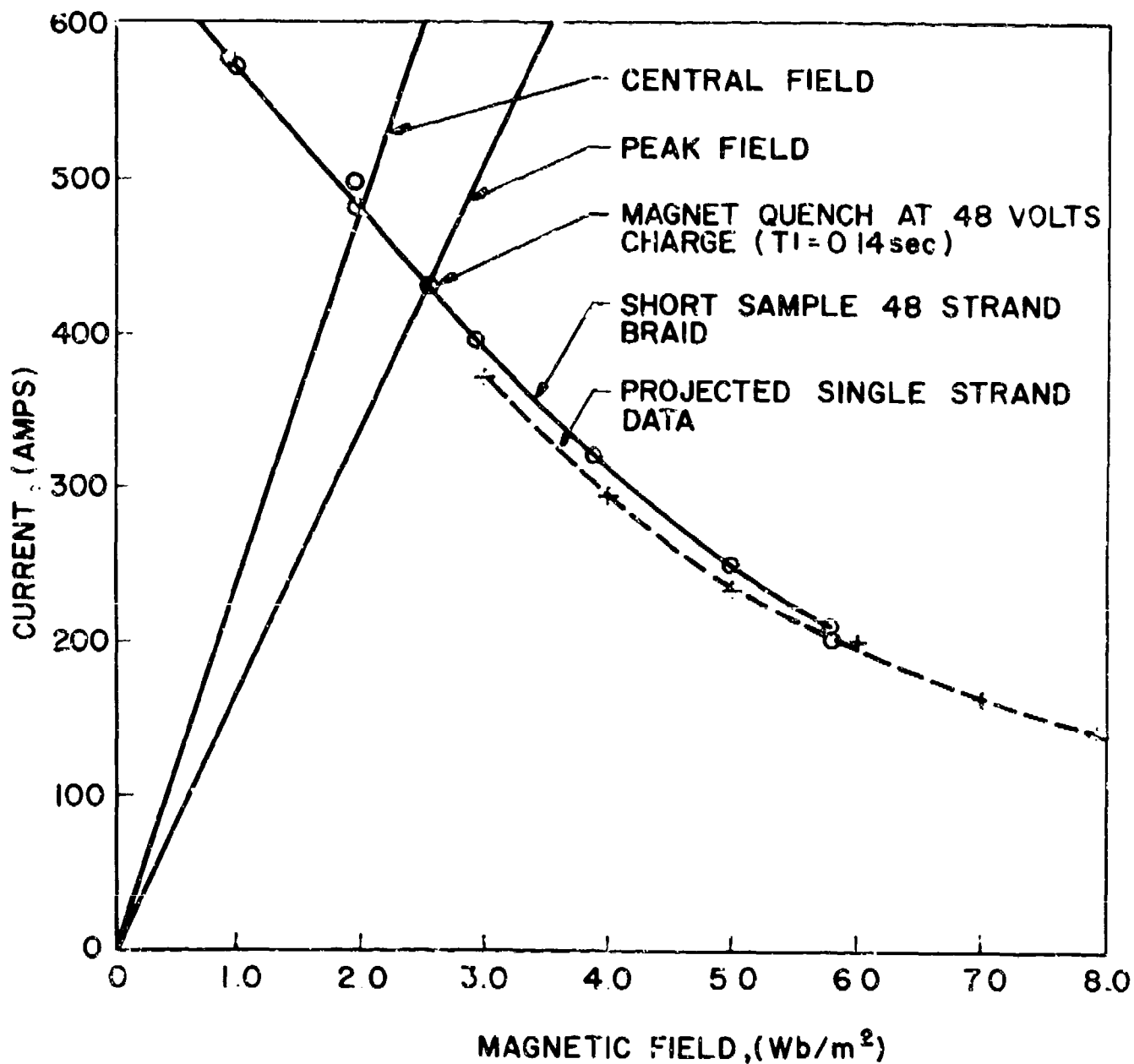
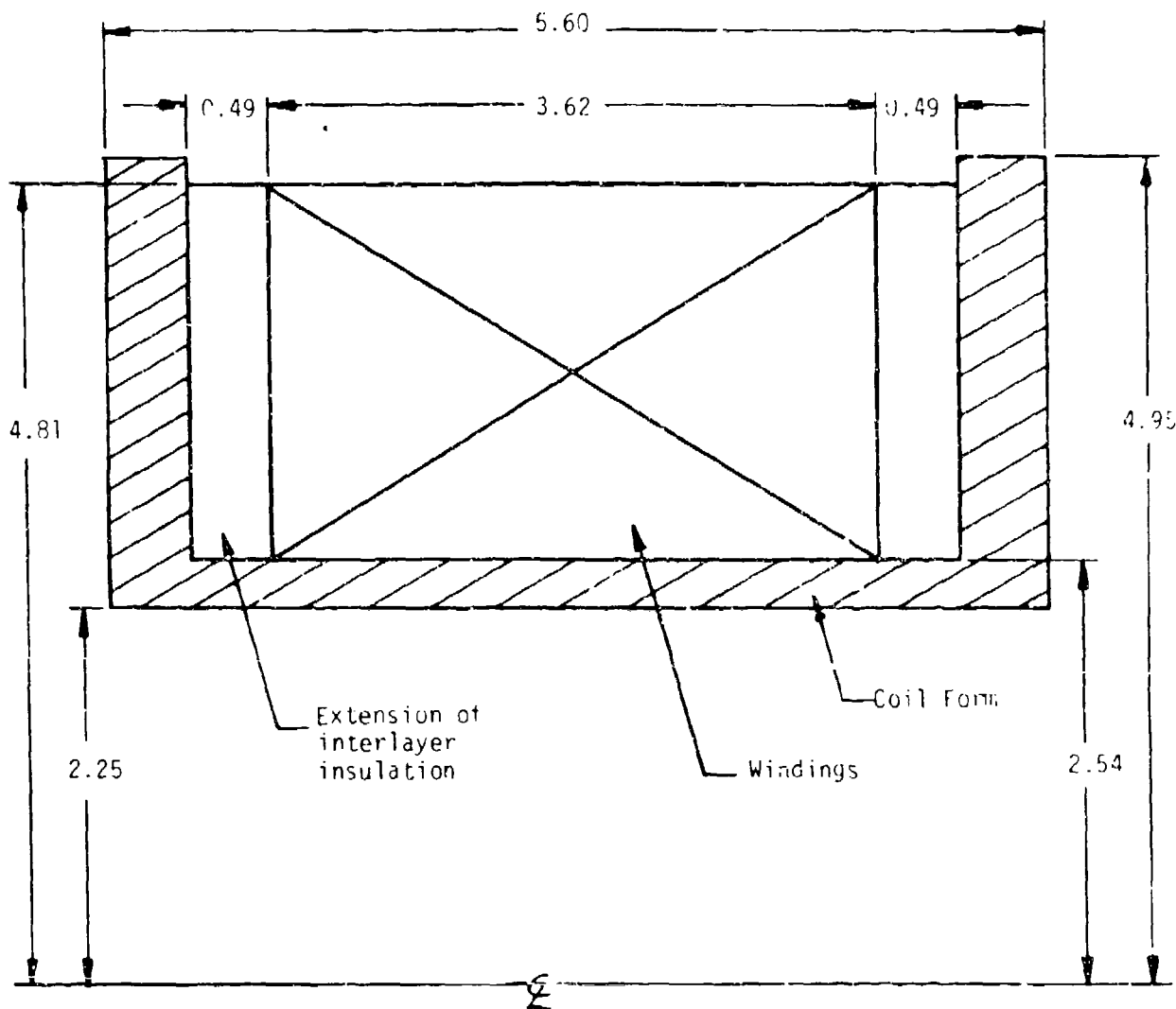


Figure 48 H-I characteristics for a 1900 joule coil wound with a 48 strand braid made up of .0045 inch diameter single NbTi copper composite strands having a copper to superconductor ratio of 1.6 to 1.



Dimensions in Inches

Figure 49 Schematic Illustrating Dimensions of 7 kJ Energy Storage Coil.

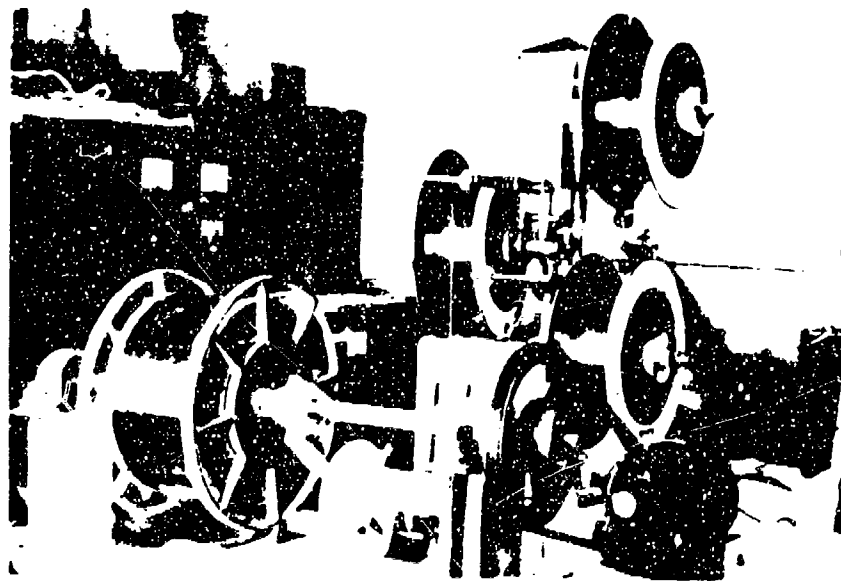


Figure 50. 7 kilojoule model coil during winding. Upper illustration shows trifilar winding technique. Lower illustration shows application of epoxy resin to layer of conductor.

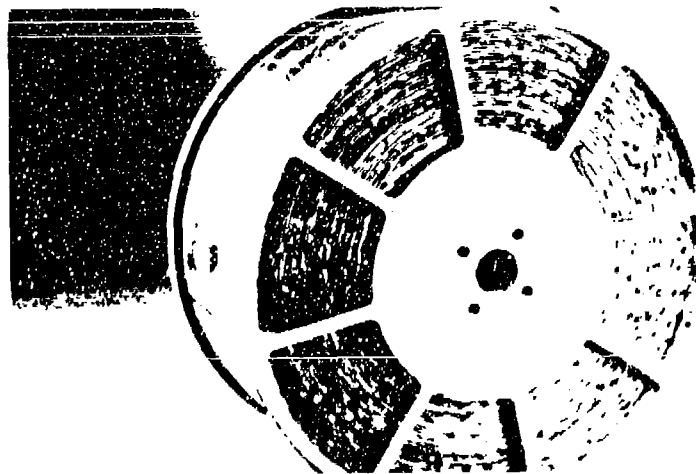
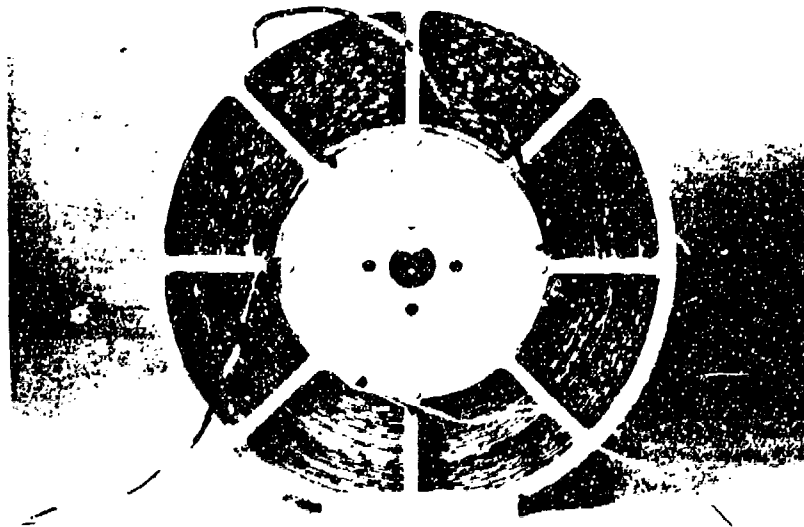


Figure 51 7 kJ model energy storage coil. The coil is wound trifilar with three braids each consisting of 1×48 strands. Each strand is a single core niobium titanium copper composite with a copper to superconductor ratio of 1.4:1.

Table XV

SPECIFICATIONS OF 7 kJ ENERGY STORAGE COIL

Inner winding radius	6.35×10^{-2} m (2.54 inch)
Outer winding radius	12.2×10^{-2} m (4.81 inch)
Winding length	9.19×10^{-2} m (3.52 inch)
Operating current	616 A
Stored energy at operating current	7.0 kJ
Central flux density at operating current	2.46 Wb/m ²
Peak flux density at operating current	1.93 Wb/m ²
Inductance	36.9 mH
Number of layers	39
Number of turns per layer	13
Total number of turns in coil	507

Conductor

Winding configuration	3 braids wound 3 in hand
Approximate braid dimensions	2.4×10^{-3} m x 5.1×10^{-4} m (0.094 inch x 0.020 inch)
Braid configuration	48 strands per braid
Total number of strands	144
Strand diameter	1.14×10^{-4} m (4.5×10^{-3} inch)
Strand insulation material	Formvar
Strand material	Nb/Ti in Cu matrix
Copper to superconductor ratio	1.4
Number of filaments of Nb/Ti per strand	1

Voltage Insulation

Material	Mylar film
Configuration	4 layers between each layer of windings
Film thickness	1.3×10^{-5} m (0.5×10^{-3} inch)

Support Structure

None

Cooling Configuration

Cooling channels formed by axial slats 0.13 inch wide by 0.031 inch thick on 0.5 inch centers.

determine the minimum weight system with the specified mission requirements. The optimization procedure minimizes the sum of the weights of coil, dewar and cryogen. The shape and size of the coil determine the energy loss. The energy loss determines the weight of cryogen used and both the coil and the cryogen requirement determine the size and therefore the weight of the dewar. Coils optimized for minimum weight have high fields and therefore high losses. If the required number of pulses is high, the additional weight of cryogen and therefore dewar far exceeds the advantage of a light coil. The system therefore optimizes around large diameter low field coils where the energy losses are lower.

If losses could be reduced by advancing the state of the art in small wire superconducting braids, the coil could be optimized nearer the minimum weight coil design thereby reducing the weight of all system components.

The current switching requirements fix the current level at about 2,000 A and the peak flux density in the coil at the operating point dictates that the total number of strands within the braid should be about 300 if the coil is to be reliably operated at fractions of the critical current similar to those at which the 1 kJ model coil operated. This number of strands is equivalent to about 6 of the braids used in the model coils. Figure 43 shows the braid used in the models. It is a flattened tubular braid consisting of 48 strands. The 1 kJ model coil was wound with one such braid and the 7 kJ model coil was wound trifilar with three such braids. Figure 44 is a braid consisting of 144 strands. The braid has the same pattern as the 48 strand braid illustrated in Figure 43 inasmuch as it has 48 elements; however, each element consists of three strands instead of one. The 100 kJ coil was wound bifilar two such braids. Thus, each turn in the coil has 288 strands, fulfilling the requirement of about 300 strands mentioned above. The critical current-critical field characteristic of the conductor together with the design point of the coil is shown in Figure 52.

The choice of two braids each of 3 x 48 strands is a compromise between ease of construction and thermal considerations. Ideally, to facilitate winding, one would like to handle just one conductor. However, a single conductor consisting of 6 x 48 strands would be too thick to ensure that it would cool down between successive pulses of the energy storage coil. The proposed conductor is already approximately 1.4 times thicker than that used in the model coil tests. The overall dimensions of each braid are 0.028 inch x 0.21 inch.

The coil was wound with 297 turns of the 288 strand double braid in 9 layers. The inductance is 51.5 mH and the operating current is 1.97 kA for 100 kJ energy stored in the coil. At this operating current the central and peak flux densities are 1.06 Wb/m² and 1.56 Wb/m² respectively. A summary of the 100 kJ coil specifications appears in Table XVI.

Table XVI

SPECIFICATIONS OF 100 kJ ENERGY STORAGE COIL

Inner winding radius	0.292 m (11.5 inch)
Outer winding radius	0.320 m (12.6 inch)
Winding length	0.338 m (13.3 inch)
Operating current	1.97 kA
Stored energy at operating current	100 kJ
Central flux density at operating current	1.06 Wb/m ²
Peak flux density at operating current	1.56 Wb/m ²
Inductance	51.5 mH
Number of layers	9
Number of turns per layer	33
Total number of turns in coil	297
<u>Conductor</u>	
Winding configuration	two braids wound 2 in hand
Approximate braid dimensions	5 x 10 ⁻³ m x 8 x 10 ⁻⁴ m (0.2 inch x 0.03 inch)
Braid configuration	3 x 48 strands per braid
Total number strands	288
Strand diameter	1.14 x 10 ⁻⁴ m (4.5 x 10 ⁻³ inch)
Strand insulation material	Sodereze
Strand material	Nb/Ti in Cu matrix
Copper to superconductor ratio	1.4
Number of filaments of Nb/Ti per strand	1
<u>Voltage Insulation</u>	
Material	Kapton H film
Configuration	8 layers between each layer of windings
Film thickness	7.6 x 10 ⁻⁵ m (3 x 10 ⁻³ inch)
<u>Support Structure</u>	
Material	Epoxy impregnated glass rovings
Thickness	7.9 x 10 ⁻⁴ m (31 x 10 ⁻³ inch) per layer of windings
<u>Coil Weight</u>	
Conductor	12.9 kg (28.4 lb.)
Insulation and structure	23.6 kg (52.1 lb.)
Coil form	32.9 kg (72.5 lb.)
TOTAL	<u>69.4 kg</u> (<u>153.0 lb.</u>)
<u>Cooling Configuration</u>	
Cooling channels formed by axial slats 0.13 inch wide by 0.031 inch thick on 0.5 inch centers.	

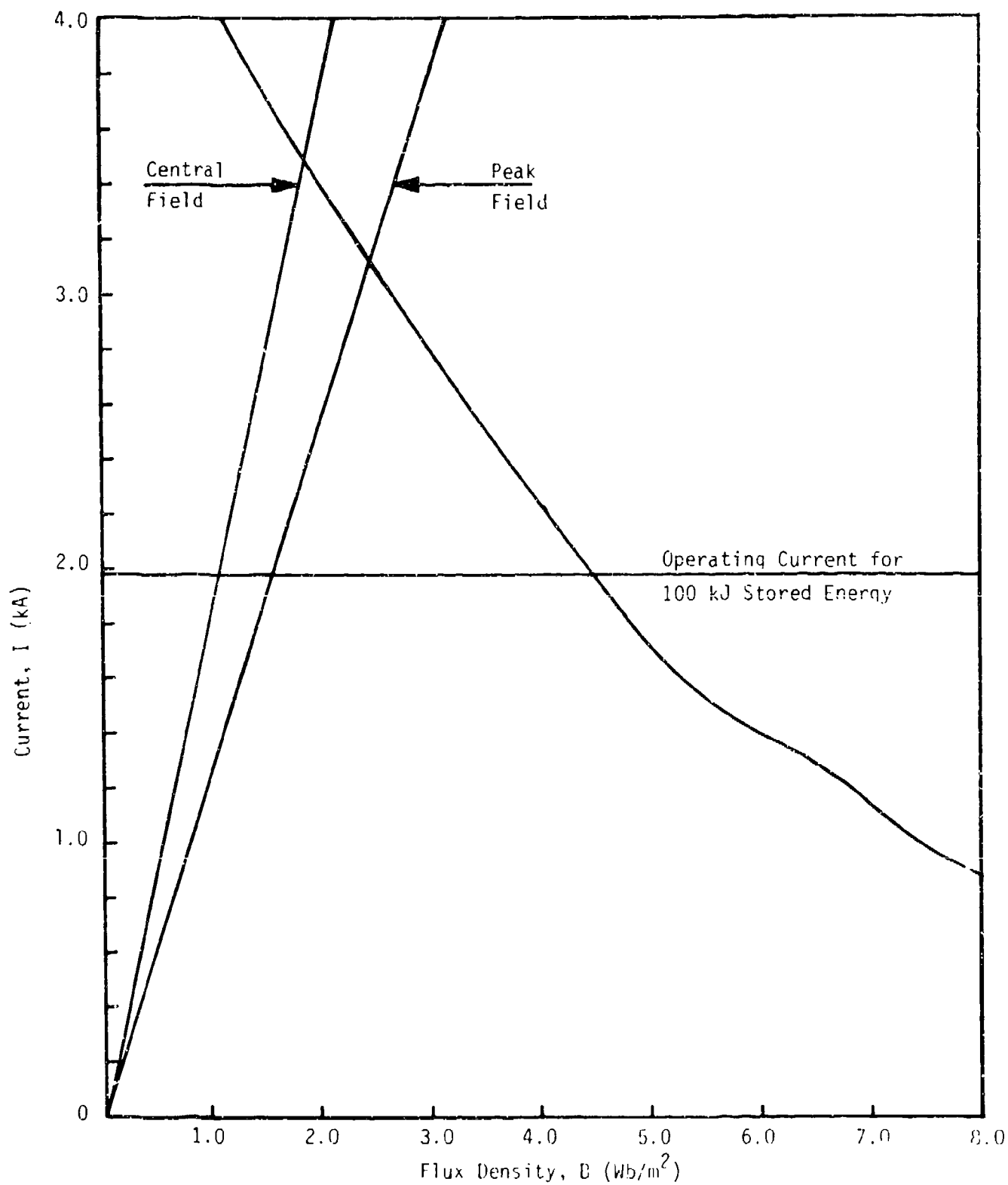


Figure 52 H-I curve for 100 kJ coil conductor and central and peak field load lines for coil.

g. 100 kJ Coil High Voltage Design Aspects

As far as high voltage aspects are concerned, the coil was designed in such a way that 60 kV could safely be applied across the terminals. The implications of this high voltage as far as the current leads are concerned are discussed in Section II-4-c, High Voltage Aspects of the Current Lead Design. As far as the coil itself is concerned, attention must be paid to the possibility of breakdown between layers and breakdown between turns.

There are 297 turns in the coil and at 60 kV the interturn voltage would be 202 V. However, each turn consists of two braids wound in parallel and the starting points of these braids are 180° apart. Thus the voltage between braids is 101 V. Figure 53 shows this inter-braid voltage as a function of coil terminal voltage. The insulation on the individual wires is sodereze (polyurethane) and each wire has an insulation thickness of 0.25×10^{-3} inch on the radius. Thus between one wire and the next there is a total thickness of 0.5×10^{-3} inch of insulation. The breakdown strength of this material is about 2500 V/mil; thus breakdown between adjacent braids would be expected when the voltage between them reached about 1,250 V. The breakdown strength then is an order of magnitude greater than the anticipated maximum voltage between braids. This is more than adequate.

Electrical insulation from layer to layer within the coil was provided by sheets of kapton H film. Electric stress calculations were conducted for the following model: three sheets of 3×10^{-3} inch thick kapton wound around each layer of windings, epoxy/glass composite support structure laid up on top of this, and a further three sheets of 3×10^{-3} inch thick kapton wound around the support structure. The thicknesses of the various components are given in Figure 54.

The electric field strength in the kapton was calculated using the relationships:

$$E_K d_K + E_S d_S + E_G d_G = V$$

$$\epsilon_K E_K = \epsilon_S E_S = \epsilon_G E_G$$

Where:

- K signifies kapton
- S signifies epoxy/glass support structure
- G signifies G10 spacers
- d signifies thickness of material
- E signifies electric field strength in material
- ϵ signifies dielectric constant of material
- V signifies total voltage across all materials

It was assumed that a pinhole would make one layer (3×10^{-3} inch) of kapton useless for insulation and furthermore that there would be hemispherical bumps in the kapton giving local field amplification by a factor of three.

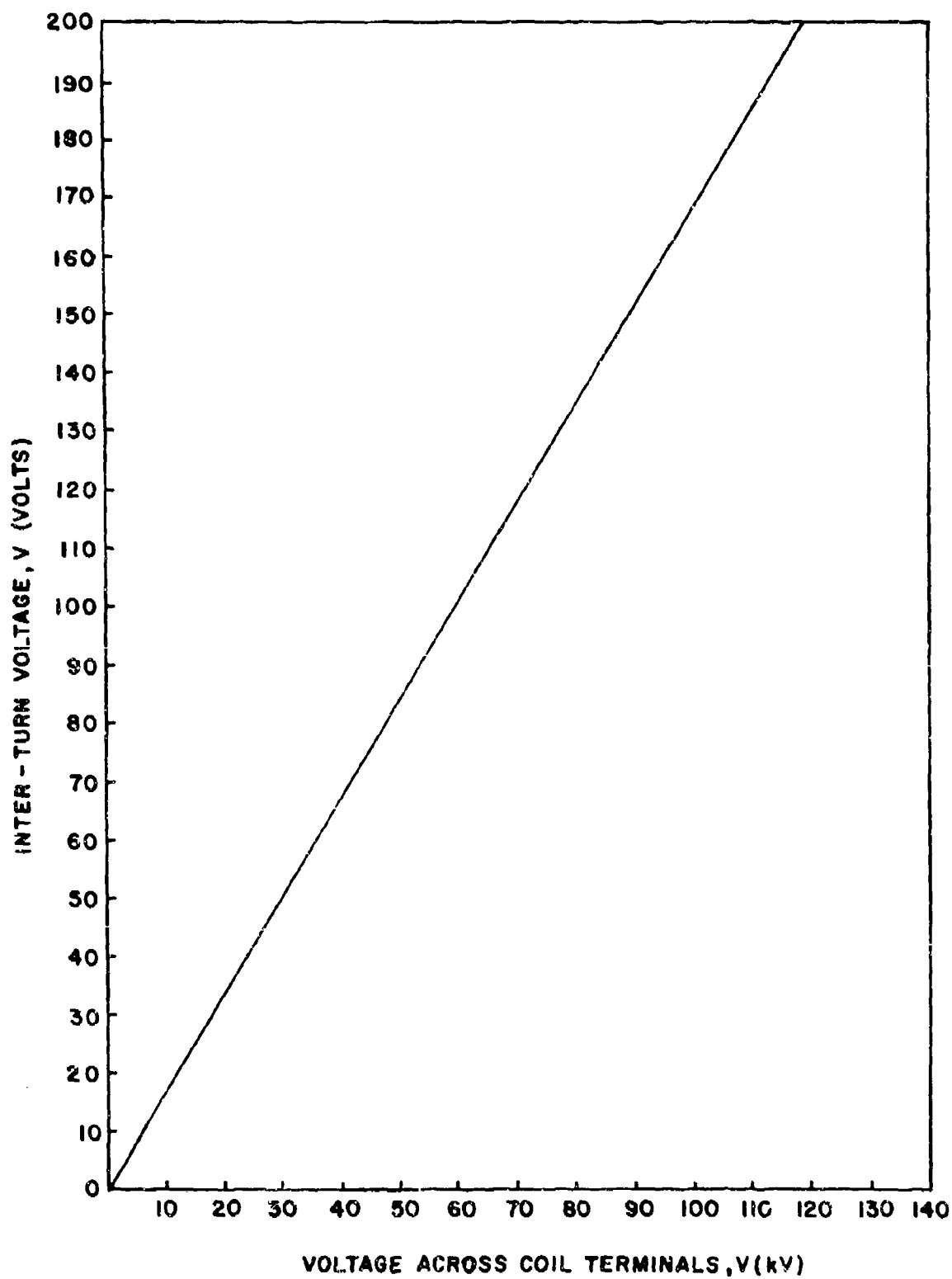


Figure 53 100 kJ Coil Inter-Braid Voltage vs. Coil Terminal Voltage.

The field strength in the kapton is then given by:

$$E_K = 3 \times \frac{V}{d_K + \frac{\epsilon_K d_S}{\epsilon_S} + \frac{\epsilon_K d_G}{\epsilon_G}}$$

The values of d and ϵ used were:

	<u>$d(10^{-3} \text{ inch})$</u>	<u>$\epsilon(F/m)$</u>
K	15	3.5
S	30	5.6
G	31	4.5

The field strength in the kapton is shown in Figure 54 as a function of coil voltage together with the dielectric strength of kapton at various temperatures.

It can be seen that at 60 kV across the coil the maximum electric stress in the kapton is 750 kV/inch and that the kapton manufacturers' data for the dielectric strength of kapton at 78 K is 10,800 kV/inch.

This is already a large safety margin but, because no guarantees were made by the manufacturers of this material, an additional layer of 3×10^{-3} inch thick kapton H film was placed on each side of the epoxy glass support structure. Thus the coil was actually constructed using a total of eight 3×10^{-3} inch thick layers of kapton H film between layers of windings. Figure 55 shows the dielectric strength of kapton H film as a function of temperature.

No problem exists as far as the helium in the cooling channels is concerned since as can be seen from Figure 56 at spacings of the order of less than 25×10^{-3} inch the breakdown characteristics of liquid helium are comparable with those of transformer oil.

To prevent voltage breakdown around the ends of layers the inter-layer insulation was extended about 2.5 inches beyond the ends of the windings to give a long tracking path.

h. 100 kJ Coil Mechanical Design Aspects

In a solenoidal magnet the forces acting on the conductor due to the interaction of the field and current are such that there are radial forces which tend to expand the windings radially and axial forces which tend to compress the windings towards the median plane of the coil.

In this design the layers of windings are stuck with epoxy resin to the electrical insulation and support structure which surrounds them. The axial forces are then transmitted in shear to the surrounding

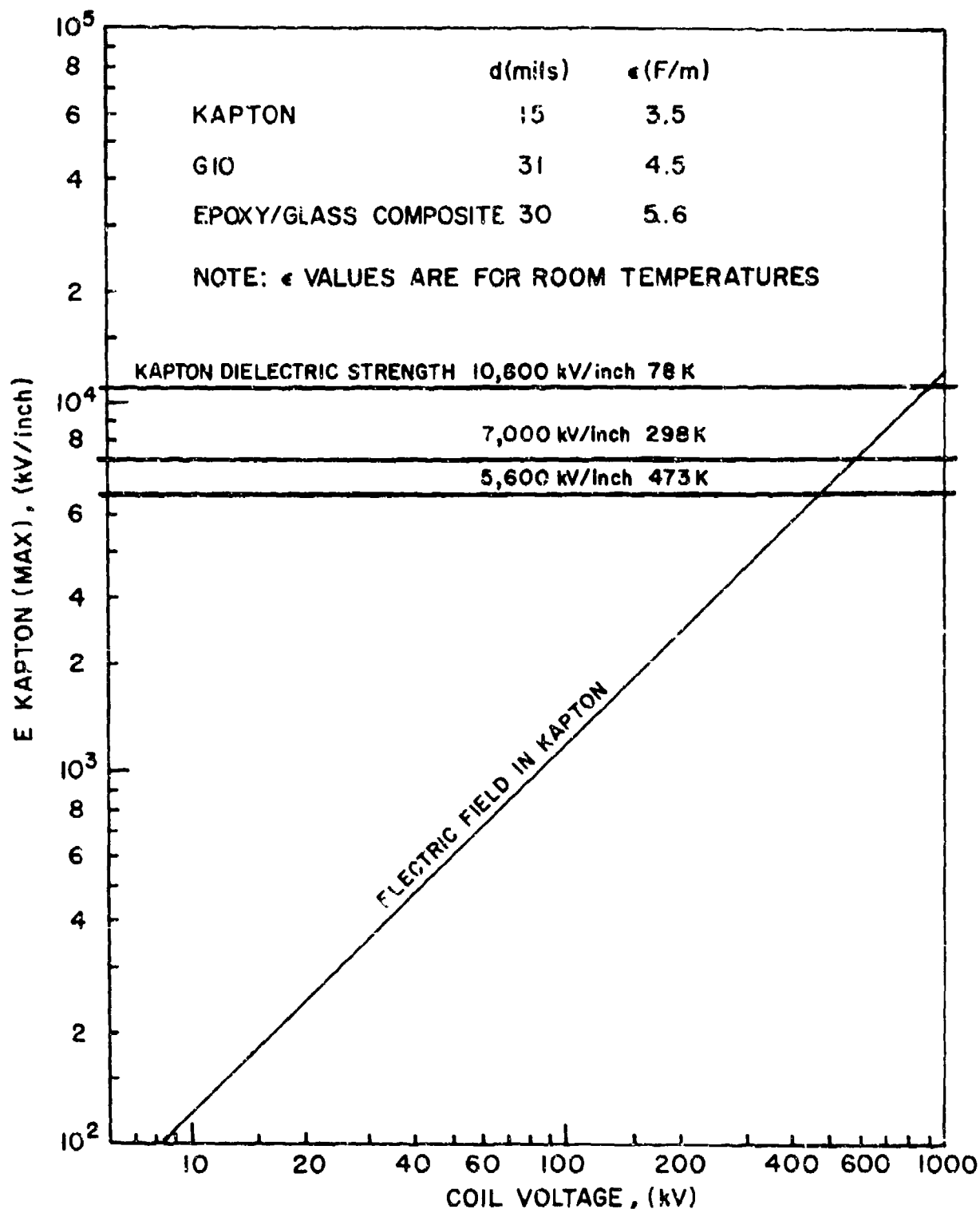


Figure 54 Maximum electric field in kapton, assuming 6 layers of 3 mil kapton with a pinhole in one and an amplification factor of 3 due to a hemispherical lump in the kapton surface.

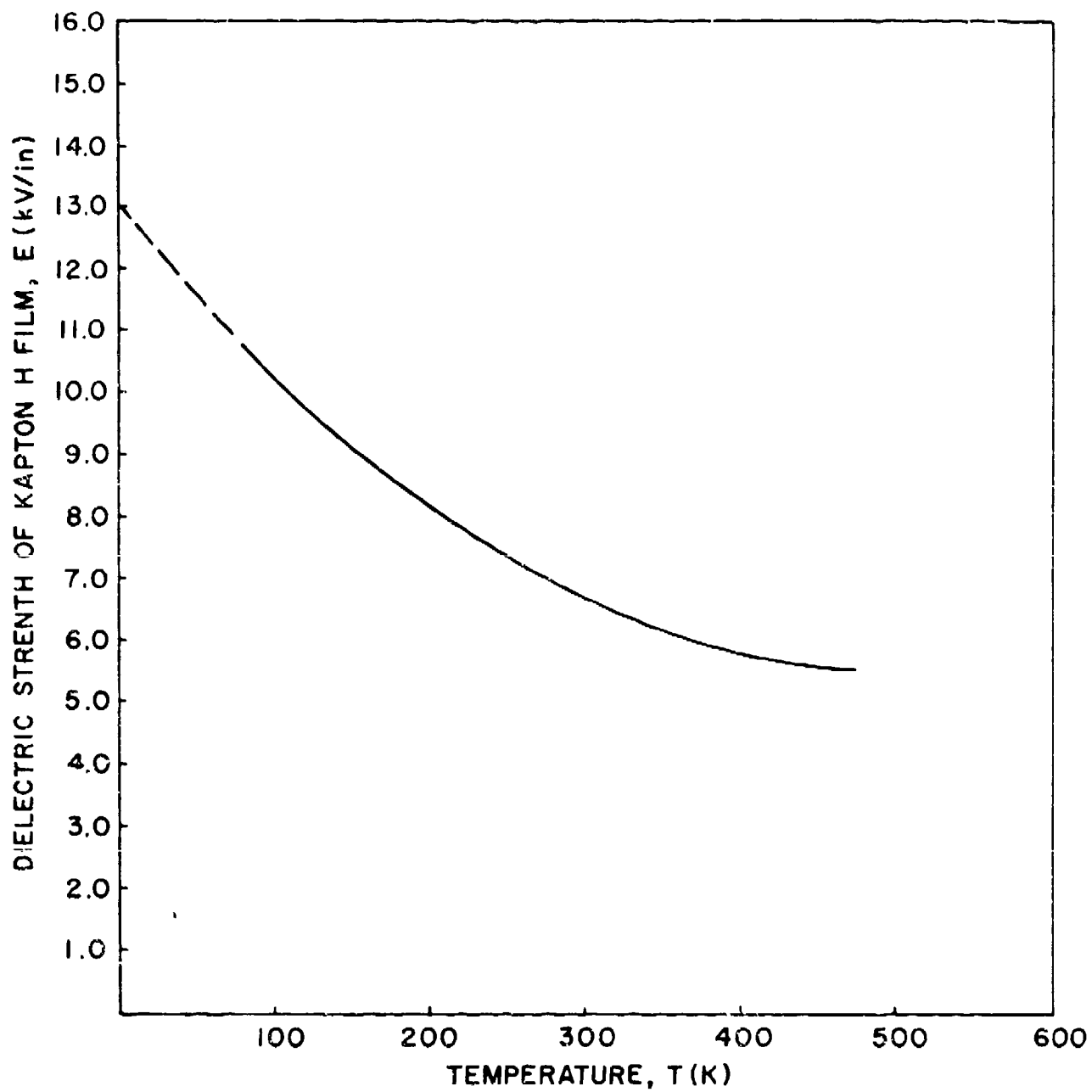


Figure 55 Dielectric Strength of Kapton H Film vs. Temperature

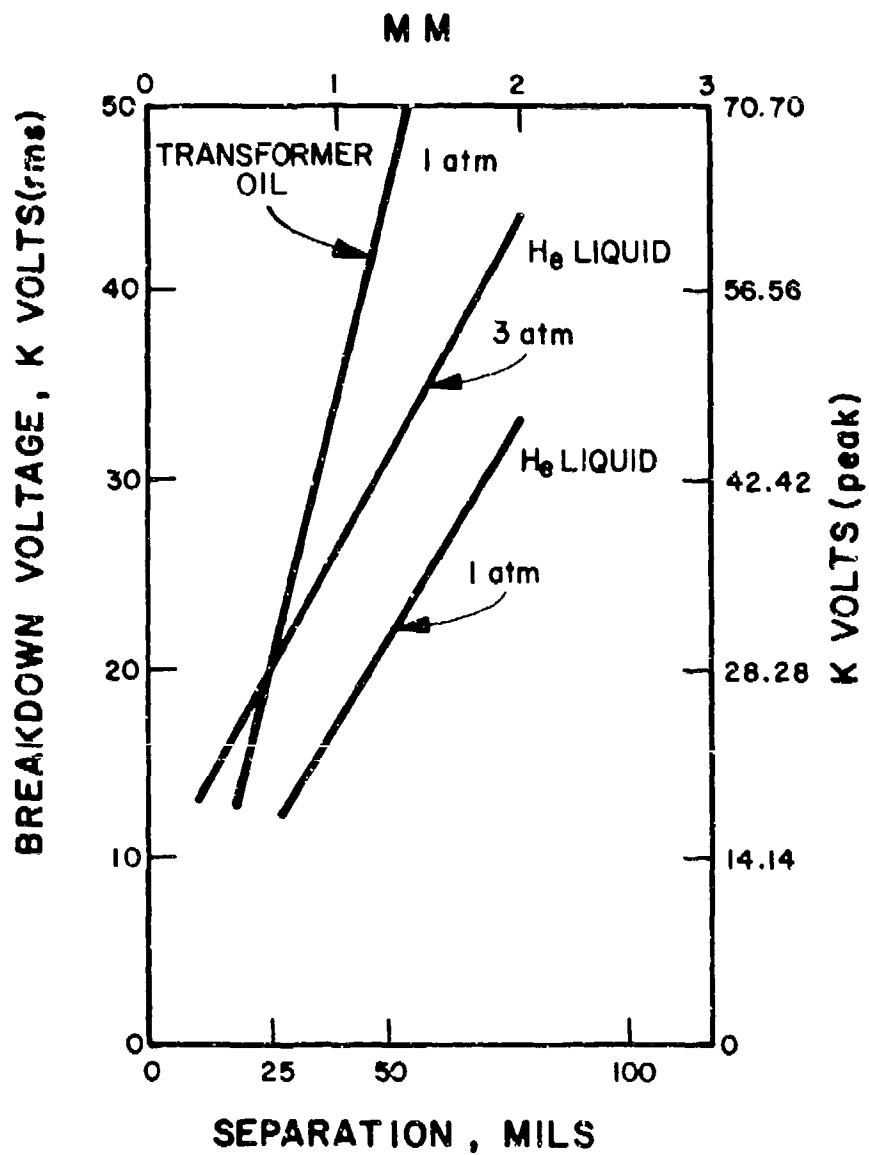


Figure 56

Breakdown strength of liquid helium and transformer oil for two 26.5 mm diameter spheres.

support structure. Because of the large surface area this shear stress is small and presents no problems.

However, containment of the radial forces requires careful structural design. The radial forces are taken in hoop tension in the windings and support structure. They are greatest in the median plane of the magnet at the peak field position where the axial field is greatest.

In the median plane the hoop forces are largest in the innermost layer and decrease from one layer to the next in the radial direction. However, there is a redistribution of forces such that the innermost layers are somewhat relieved and the outermost layers are somewhat more loaded. The extent to which this happens is a function of the modulus of the material and the ratio of the build of the windings to the radius of the windings. The lower this ratio is then the greater is this redistribution effect. For this coil the ratio is very low and therefore the redistribution is large. Thus it would be too severe to take the worse case as being an isolated hoop at the peak field position. It is more realistic to take an average based on the total force due to all layers in the median plane and the total area of cross section of the material in the median plane. This results in a slight underestimate of the actual stresses but as will be seen later the safety margin is so great that this small underestimate becomes insignificant.

Figure 57 shows the hoop stress at the coil median plane as a function of current for various models. Model 1 assumes that there is no support structure and that the braid behaves as if it were a rigid conductor. It is assumed that the forces distribute themselves between the copper and the niobium-titanium according to their respective elastic moduli. It can be seen that at the operating current of 2,000 A the copper is stressed to about 25 kpsi and the niobium titanium to about 18 kpsi. This is safe for the niobium titanium but exceeds by a factor of about 3 the yield strength for copper. Clearly the conductor cannot be self supporting: support structure must be added.

Model 2 assumes that there are three layers of epoxy/glass composite around each layer of windings. Again, it is assumed that the forces are distributed between the copper, the niobium-titanium and the epoxy/glass composite according to their respective elastic moduli; the braid is assumed to behave as if it were a rigid conductor. The stresses of niobium-titanium at 8 kpsi and the glass at 7 kpsi are both acceptable but again the stress in the copper at 11 kpsi is higher than yield.

This model however is not realistic since the braid does not behave as a rigid conductor. Because the components in the braid can move somewhat laterally the effective modulus is very low and it is more realistic to assume that this effective modulus is very much lower than the epoxy/glass composite. This is equivalent to saying that the epoxy/glass composite takes all the load. If this is so, then the situation in model 3 occurs. Model 3 gives a stress in the glass of about 12 kpsi

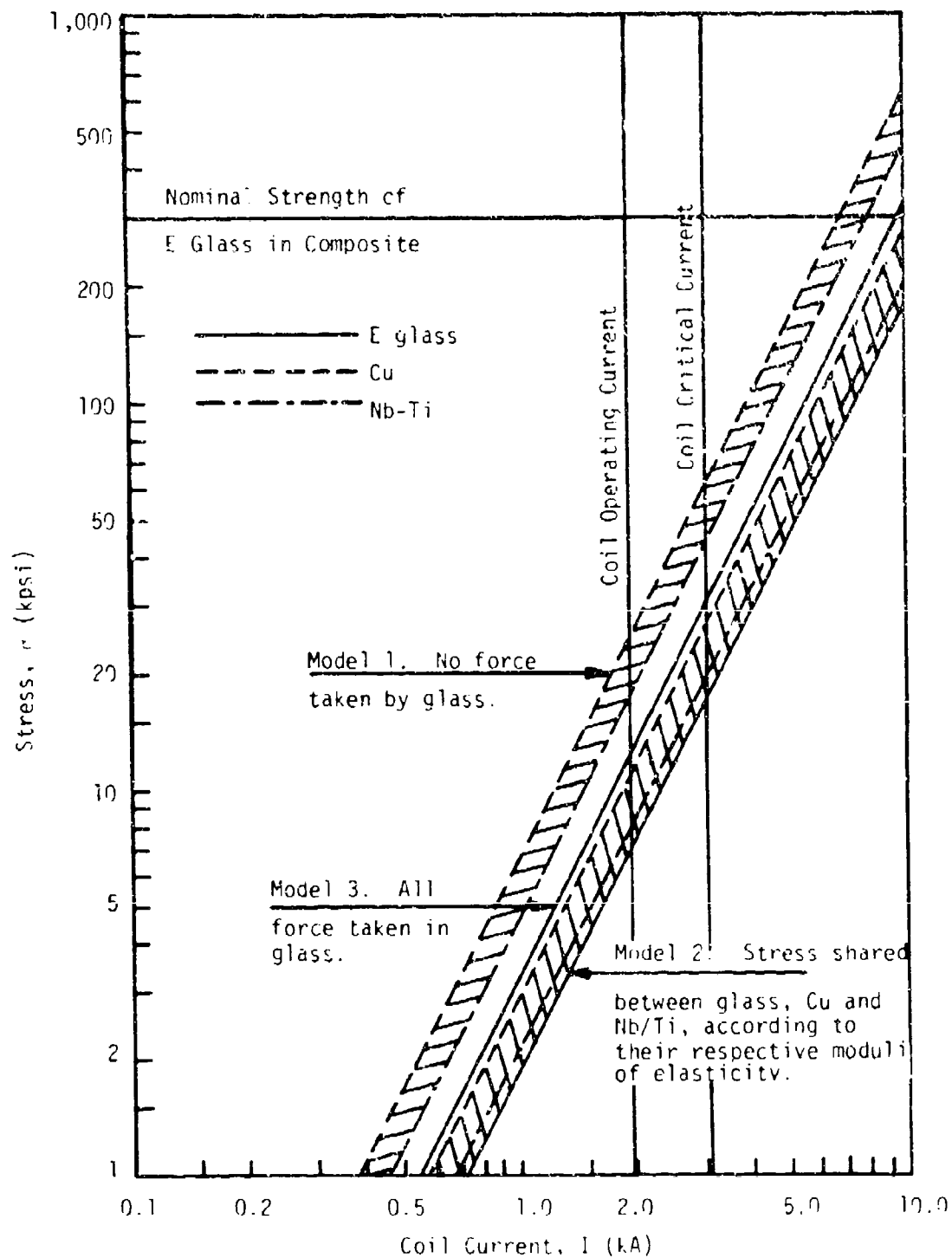


Figure 57 Average Hoop Stress at Coil Median Plane vs. Coil Current.

at a coil current of 2,000 A (the operating current) and a stress of about 30 kpsi at 3,100 A (the coil critical current). These values are more than adequate. Figure 58 shows the strength of fibers of E glass as a function of temperature. At room temperature (the lowest temperature for which data is available) the strength is about 500 kpsi and the trend is towards higher strengths at lower temperatures. When this material is used in a composite however, the room temperature strength must be derated to about 300 kpsi. This is the value which was used as the nominal strength of the E glass in the coil structure. Thus with a maximum possible stress in the glass of 30 kpsi (at the coil critical current) the safety margin is a factor of 10 which is quite safe.

The method of fabrication of the coil was as follows. A linen phenolic mandrel with open flanges was used to wind the coil on. This is shown in Figure 59. Slats of G10 were epoxied onto the coil form between the flanges on 0.5 inch centers. These slats were 0.13 inch wide by 0.031 inch thick. The spaces between these slats form the cooling channels which are 0.031 inch thick by 0.38 inches wide. The conductor was then wound on top of these slats. Two braids wound in parallel were used, the starting points of each being 180° apart. Each layer of the windings was about 13.3 inch wide. The distance between the flanges was about 18.9 inch so there was a space of about 2.8 inch between the ends of the windings and the flanges. This space at the ends of the layers is necessary to prevent voltage breakdown around the ends of layers. The windings were then coated with epoxy resin and 4 layers of 3×10^{-3} inch thick kapton H film were wrapped around them. The support structure was then applied. The glass used in the support structure is an E glass type 30 continuous filament roving and yields 675 yards/pound. The approximate size of this roving is 0.1 inches wide by 0.01 inches thick. Three layers of this glass roving were wound around each layer of windings. Epoxy resin was applied continuously during the winding process to ensure that the roving was saturated. An additional 4 layers of 3×10^{-3} inch thick kapton H film was then wound around the epoxy/glass structure. Figure 60 is a schematic of a cross section of the windings. It can be seen that the G10 spacers are aligned from one layer to the next so that the forces acting on the inner layers can be partially transferred to the outer layers. Figure 61 is a schematic of a section through the coil drawn to scale and showing pertinent dimensions. Figure 62 shows two photographs of the assembled coil, its support structure and the foam neck plug. Figure 63 is a schematic showing the assembly of the coil, current leads, support structure, neck plug and dewar.

i. Summary and Conclusions

A theoretical investigation of losses in superconductors experiencing transient conditions led to the selection of a 4.5×10^{-3} inch diameter single core niobium-titanium in copper wire having a copper to superconductor ratio of 1.4:1 as the basic component for the 100 kJ coil conductor. This is the smallest diameter wire that present technology allows for large scale production. Analyses concerning optimizations for minimum weight systems indicated that the coil should

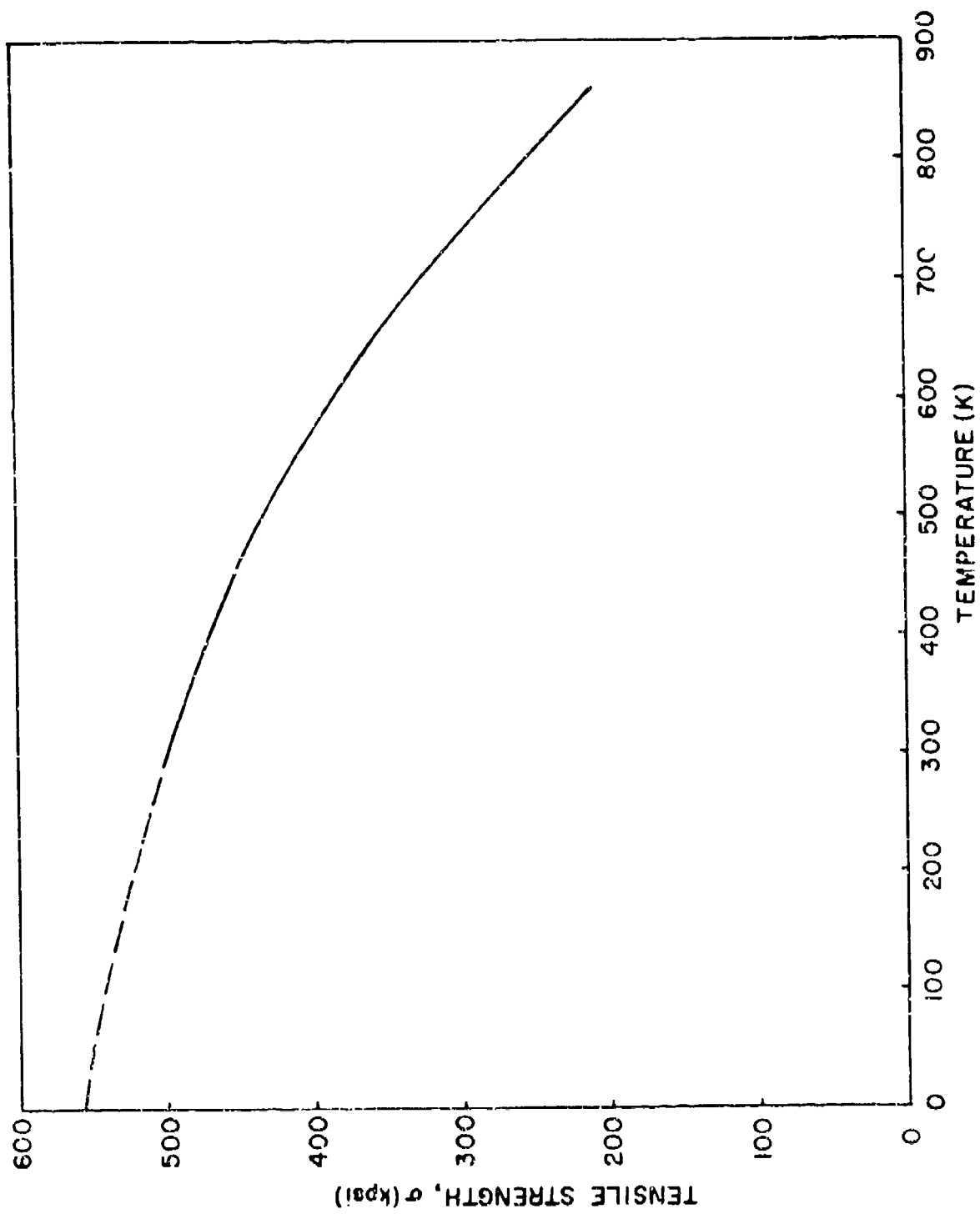


Figure 58 Strength of E Glass Fibers vs. Temperature.

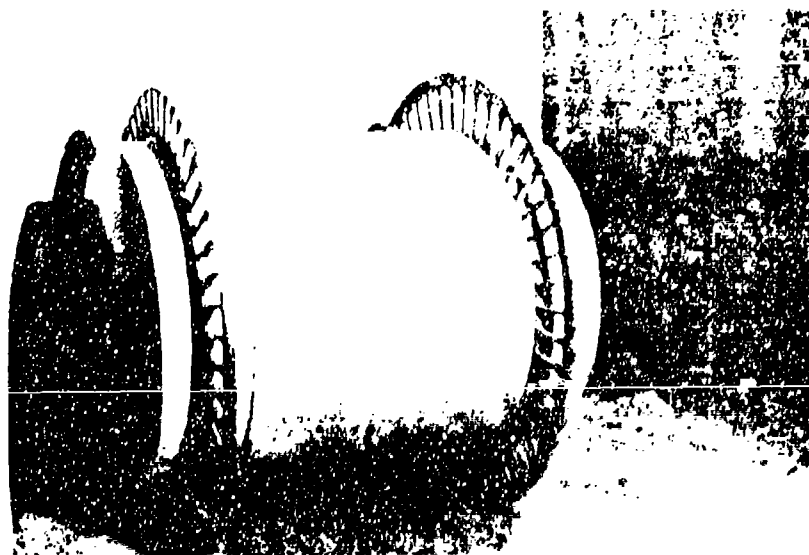
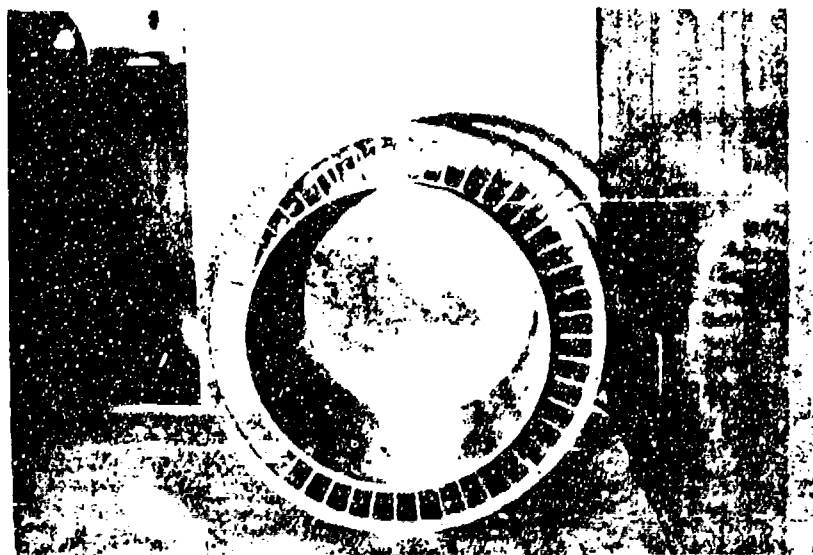


Figure 59 Coil form and flanges used for construction of the 100 kJ energy storage coil. The outer diameter of the coil form is 0.292 m.

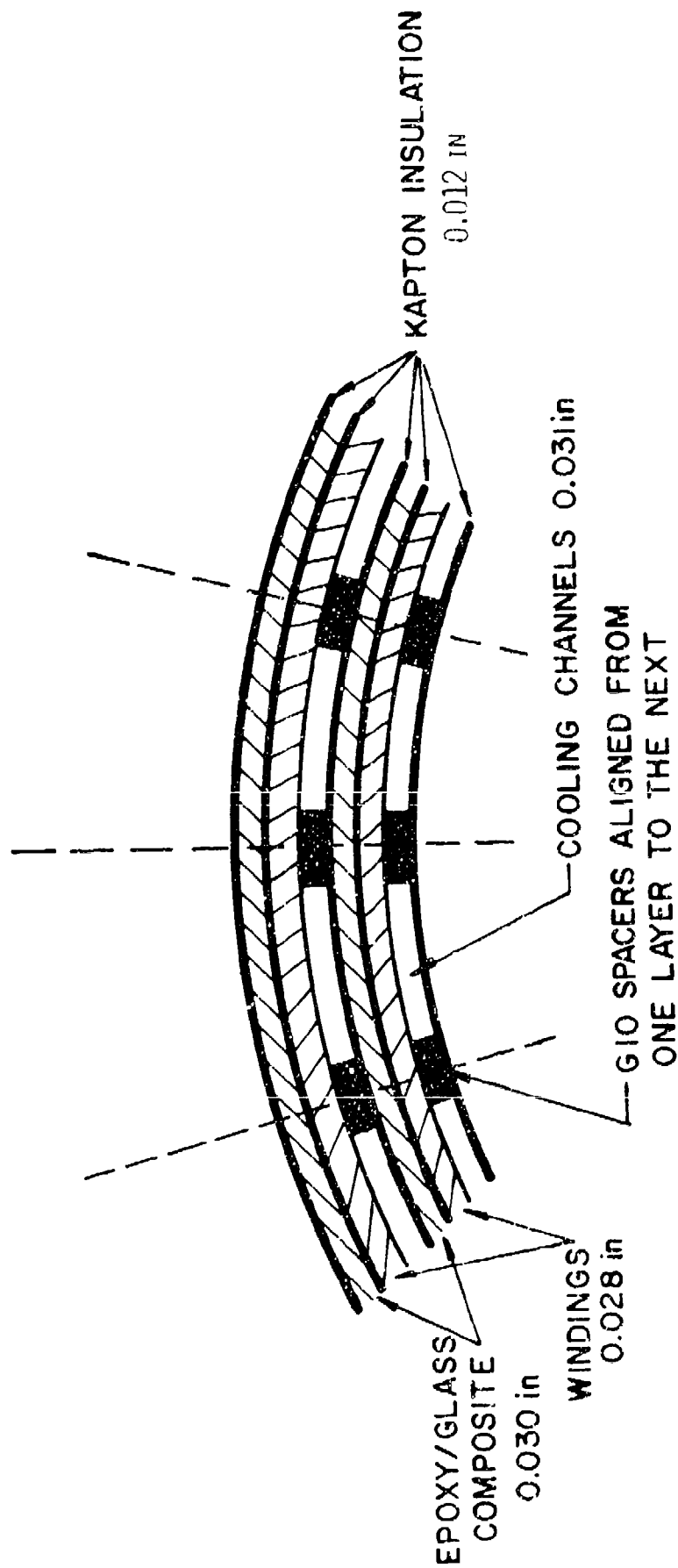


Figure 60 Schematic showing section of windings. G10 spacers are aligned along radii to provide support from one layer to the next.

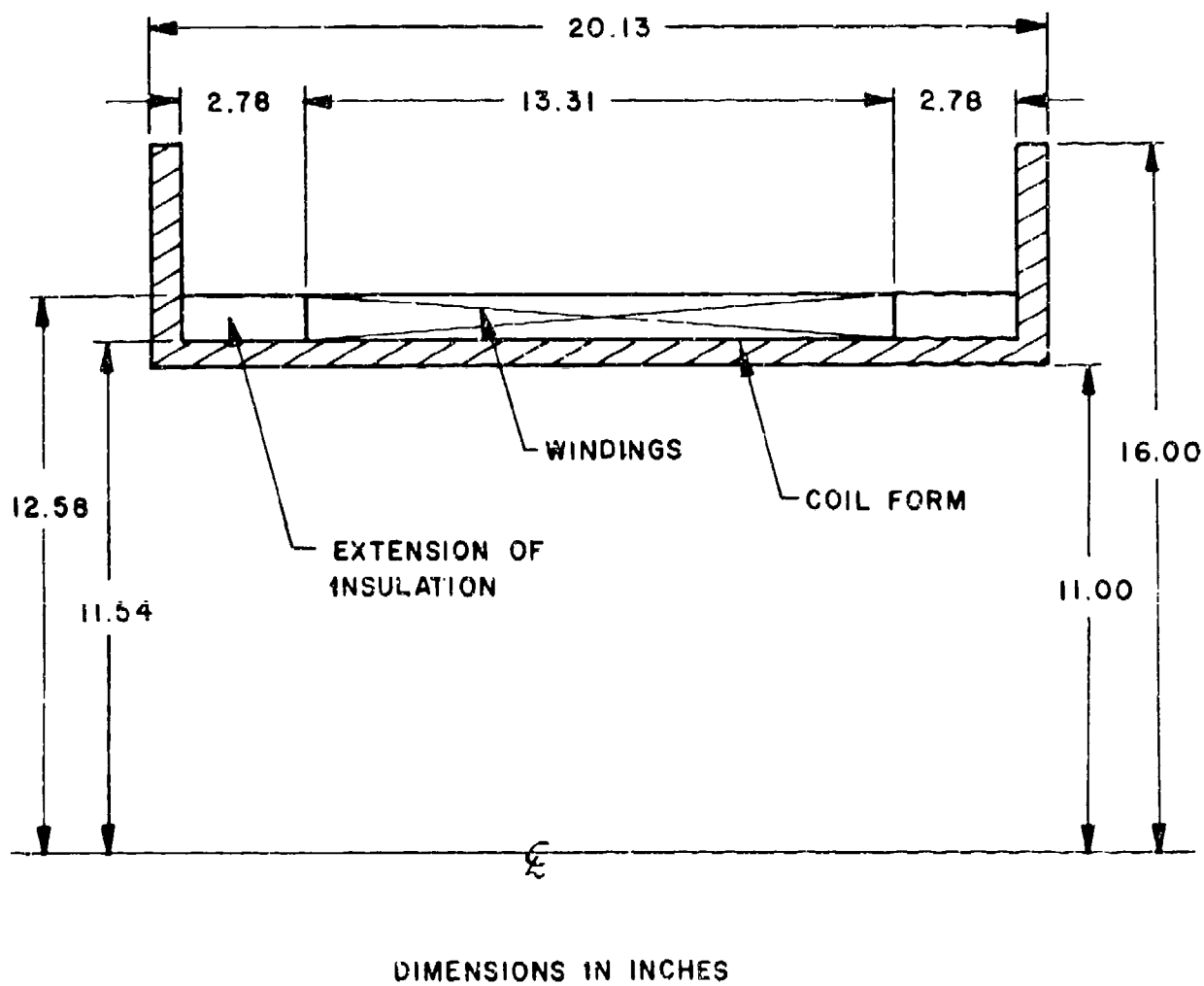


Figure 61 Schematic Illustrating Dimensions of 100 kJ Energy Storage Coil.

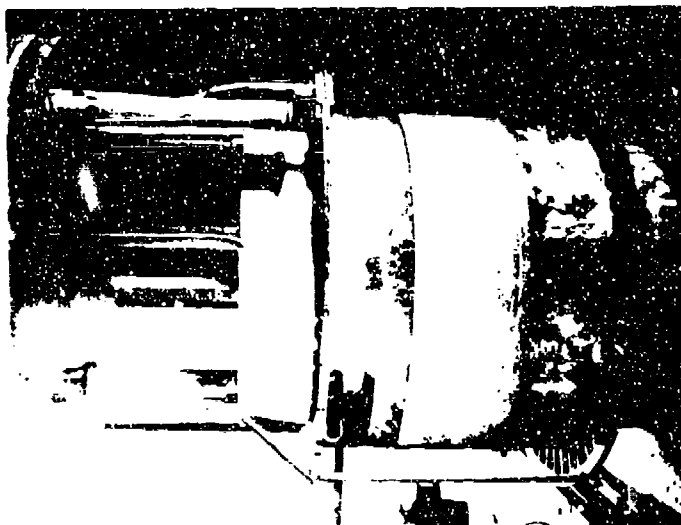
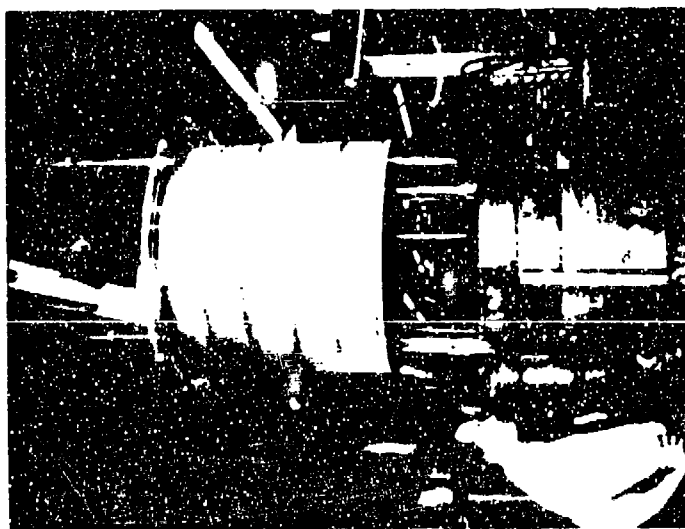


Figure 62 100 kJ Energy Storage Coil with Current Leads,
Supports and Dewar Neck Plug.

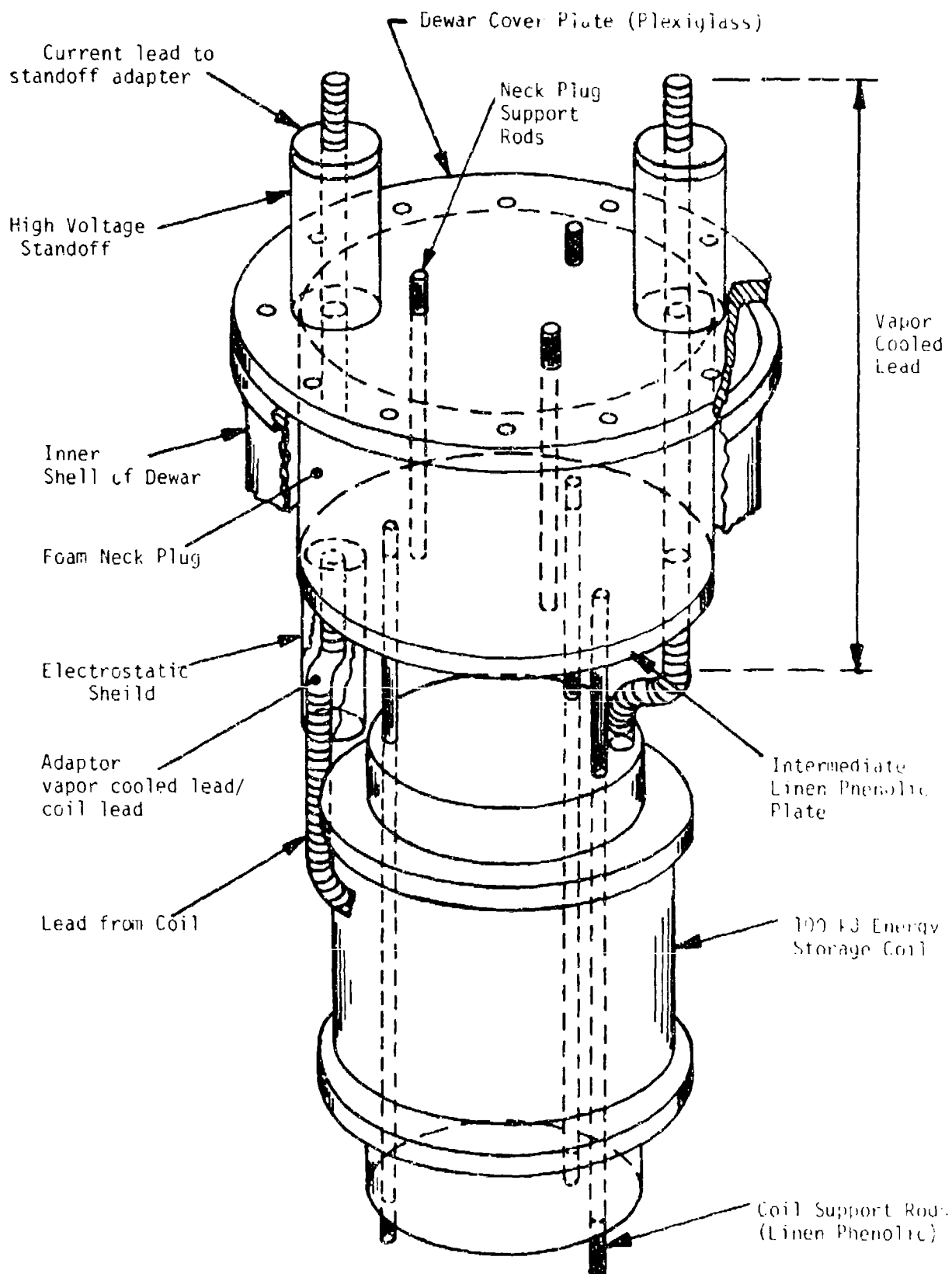


Figure 63 Schematic Showing Assembly of Coil, Current Leads and Dewar

have a large diameter and operate at low fields. Circuit switching requirements fixed the operating current of the coil at about 2,000 A. Analyses concerning thermal effects in the windings led to the selection of two flattened tubular braids consisting of 144 strands of 4.5×10^{-3} inch diameter wire as the conductor for the 100 kJ coil. The thermal analyses indicated that cooling channels 0.031 inch thick would be more than adequate to prevent channels choking with helium gas. It was predicted that the coil would remain superconducting during charge but that on discharge parts of the windings in the higher field regions of the coil might go normal. It was also predicted that depending on the fraction of the critical current to which coil would be charged, a minimum interpulse time would be necessary to prevent a gradual rise in temperature of the windings leading to a quench, if the coil were subjected to a long train of pulses at a rapid repetition rate. Structural analyses indicated that the windings would not be self supporting so additional structure consisting of epoxy impregnated glass rovings were wound around each layer of windings. Electrical insulation consisting of kapton H film was interposed between each layer of windings to prevent voltage breakdown between layers. To test the validity of the results of the theoretical analyses model coils having nominal stored energies of 1 kJ and 7 kJ were constructed. As will be seen in Section III, Coil Evaluation Program, the results of these analyses were confirmed.

SECTION III

COIL EVALUATION PROGRAM

1. INTRODUCTION

As was described in Section II-5, 100 kJ Coil Design: (1) the basic conductor (4.5×10^{-3} inch diameter wire) was selected because of the results of theoretical analyses concerning losses in superconductors subjected to transient field conditions; and (2) the practical conductor (flattened tubular braid consisting of 144 strands of 4.5×10^{-3} inch diameter wire) and the configuration of the cooling channels were selected because of the results of analyses concerning the effects of heating in the windings. Before embarking on the design and construction of the 100 kJ coil it was felt that it would be desirable to test the validity of these results by conducting an experimental program. It was for this purpose that model coils capable of storing 1 kJ and 7 kJ were built. The details of their construction are given in Section II-5-e, Model Coils. These coils were tested at repetition rates of up to 5 pulses per second. Loss measurements were made by various methods and the limits of their performance were investigated by operating them at various fractions of their critical currents.

Based on the results of these tests the 100 kJ coil was designed, built and tested. Section III-2, Limits of Performance, will describe the results of the experiments conducted to determine the performance limits of the 1 kJ, 7 kJ and 100 kJ coils and Sections III-3, 5, 6 and 7 will describe both the theory of the superconductor losses and the results of the loss measurements.

2. LIMITS OF PERFORMANCE

a. 1 kJ Coil Evaluation tests

Two 1 kJ coils were built, one with braid made from single core material and one with braid made from multicore material. They were both tested under dc and pulsed conditions up to five pulses per second. However, because there appeared to be no appreciable differences in the results obtained from either coil and because the analytical work predicted the single core material to be superior, most of our efforts were spent on making measurements on the coil wound with the single-core material. The analysis for the 1 kJ coils (described in detail in Section II-5-c, Effect of Transient Heating on Coil Performance) indicated that for charge times of 0.167 second, the highest energy dissipation region of the coil reaches thermal equilibrium and the temperature rise in the windings would be small and should not appreciably degrade the performance of the conductor. However, during the discharge time (0.25×10^{-3} seconds) the thermal behavior is nearly adiabatic and the windings could rise in temperature to about 18 K thereby causing the superconductor to revert to its normal resistance. After the pulse is over, the windings could cool to the bath temperature in about 8×10^{-3} seconds. However, the time allowed for cooling is about 33×10^{-3} seconds. The additional safety factor was taken because of the considerable uncertainty in these figures due to the lack of information concerning the thermal properties of the mylar

insulation and the epoxy bonding agent. Calculations concerning the vaporization of helium within the cooling channels indicated that vapor lock should not occur.

A series of dc tests were conducted first to determine magnet stability and critical current characteristics. The technique involved the use of a heater embedded in the windings of the coil at the peak field position. The procedure is described fully in technical report AFAPL-TR-72-38, Vol. I, Section III-2 but will be summarized here for convenience. The coil is charged to a known current and the heater power is gradually increased until the magnet begins to go normal. The onset of normality is detected by monitoring the voltage across the normal region by means of voltage taps on the coil terminals. The power at which the coil begins to go normal is recorded. The magnet is then charged to a higher current and the procedure is repeated. As the coil current is increased the amount of power needed to send the coil normal decreases until eventually when the coil current reaches the critical current of the coil at 4.2 K no power is required. If a plot of heater power required to send the coil normal against coil current is made at low currents then an extrapolation of the curve to zero heater power gives the critical current of the coil at 4.2 K. The advantage of this method is that the critical characteristics of the coil can be investigated without charging the coil to its full energy. This avoids danger of damage to the coil during a quench at high energy. The results of this testing on the coil containing multifilament conductor were such that the extrapolation to the critical current was in good agreement with the critical current subsequently measured by charging the coil to its maximum current carrying capability. The critical current was found to be 335 A. The calculated central and peak fields at this current are 1.3 Wb/m^2 and 1.8 Wb/m^2 , respectively. This value of the critical current is about 20% higher than that estimated by short sample tests on single strands of the braid. The discrepancy is due to inaccuracies in such short samples measurements at low fields. The stored energy at this current was 0.57 kJ and the current density in the conductor $6.7 \times 10^8 \text{ A/m}^2$. When tested under similar conditions, the coil wound with the single core strands was found to have a critical current of 430 amperes. This same current was achieved when this coil was fully charged in 0.14 second.

Although both the coil wound with the multicore strands and the coil wound with the single core strands were continuously pulsed at rates up to five pulses per second, complete data was taken only on the coil wound with the single core strands. As a consequence, the remainder of this discussion will concern only this latter coil.

Initially, the pulse repetition rate was restricted to one pulse per second. Under this condition the coil could be charged and discharged without exhibiting any sign of degradation for an indefinite time to as near the critical current as the discrete battery voltage increments allowed. The highest current achieved was 425 A (critical current 430 A). This held true for all discharge time constants in the range covered (0.2 ms to 4.0 ms). Pulse train lengths of the order of

six minutes were achieved and energy loss measurements were made. These pulse trains were terminated only for the convenience of taking data and not due to any operating limitations of the coil.

Figure 64 is a typical current waveform during charge at a repetition rate of one pulse per second and Figure 65 shows a train of such pulses. A constant voltage from a set of truck batteries is applied to the coil and the current rises approximately linearly. The slight deviation from linearity is due to the resistance of the leads. As the current rises a larger fraction of the battery voltage is dropped in the leads thereby reducing the voltage applied at the coil terminals. At the end of the charge period the vacuum breaker opens and there is a short period of arcing. The arc is extinguished when the counterpulse current is driven through the switch. The coil then discharges into a resistive load. The period of arcing can be seen as fuzz at the top of the current trace. The discharge is too rapid to be recorded on the oscilloscope trace because of the time scale necessary to record the charge. Figure 66 shows the voltage across the resistive load during discharge for an exponential discharge time constant of about 0.2 ms. The oscillations which can be seen near the front end of this trace are due to ringing in the arc quench circuit. These oscillations stop when the spark gap in the counterpulse circuit is extinguished.

The coil was then operated at a repetition rate of five pulses per second. Figure 67 shows the current during charge for part of a train of pulses when the 1 kJ coil was operated at a repetition rate of five pulses per second. The discontinuous change in slope near the end of the charge is due to the vacuum breaker arcing prior to firing the arc quench circuit. This voltage drop in the arc results in a reduced voltage at the coil terminals thereby reducing the voltage available for charging the coil. Figure 68 is part of a similar pulse train on a longer time base. Figure 69 shows the voltage across the resistive load when the coil was operated at a repetition rate of five pulses per second. Again the oscillations superimposed on the waveform near the beginning of the trace are due to ringing in the arc quench circuit. The coil was operated over a range of currents and discharge times and loss measurements were made. These are described in detail in Section III-5, Loss Measurements Made Using the 1 kJ Coil. However, when charging and discharging at a repetition rate of five pulses per second, the length of time for which the coil could be operated was found to be sensitive to maximum current, discharge time constant and length of time between pulses. The effects of varying these three parameters was investigated. The length of the interpulse period was varied by keeping the same pulse repetition rate and decreasing the charge time. Generally, lower maximum currents, longer discharge time constants and longer interpulse periods favor longer pulse trains.

At the longer discharge time constants (4 ms), pulse train lengths of greater than one minute were achieved without quenching for interpulse times of 25 ms and maximum currents of 380 A (0.89 of maximum possible). At the shorter discharge times (0.2 ms) pulse train lengths in excess of one minute were achieved without quenching for interpulse times of 55 ms and maximum currents of 352 A (0.82 maximum possible).

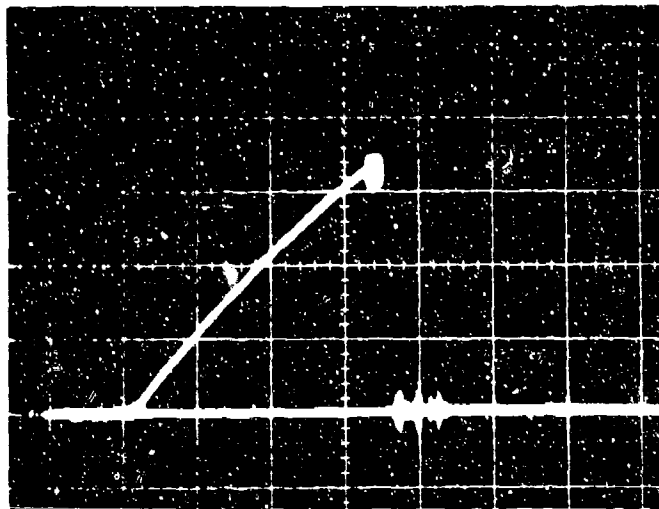


Figure 64

Current during charge of pulsed model energy storage coil constructed with braided single core superconductor. The pulse repetition rate is 1/s.

Time base	0.050 s/div
Sensitivity	120 A/div
Maximum Current	395 A
Charge time	0.16 s

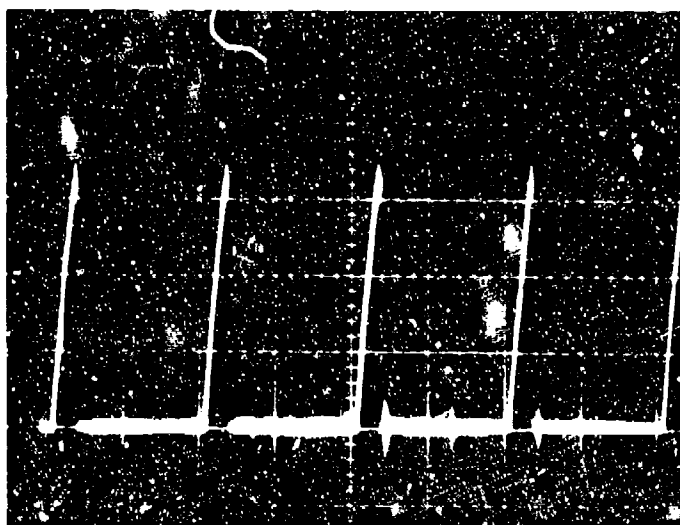


Figure 65

Current during charge of pulsed model energy coil constructed with braided single core superconductor. The pulse repetition rate is 1/s.

Time base	0.50 s/div
Sensitivity	120 A/div
Maximum current	395 A
Charge time	0.16 s

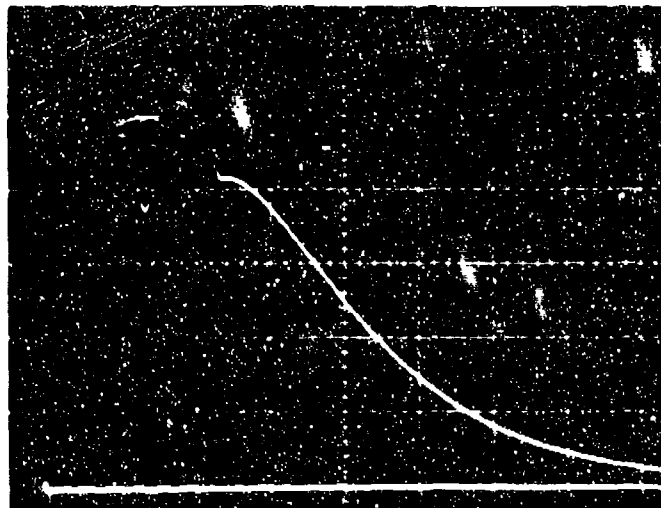


Figure 66

Voltage from model energy storage coil constructed with braided single strand superconductor when discharged into a resistive load at a pulse repetition rate of 1/s.

Time base	0.100×10^{-3} s/div
Sensitivity	1.0 kV/div
Maximum voltage	1.5 kV
Discharge time constant	0.19×10^{-3} s

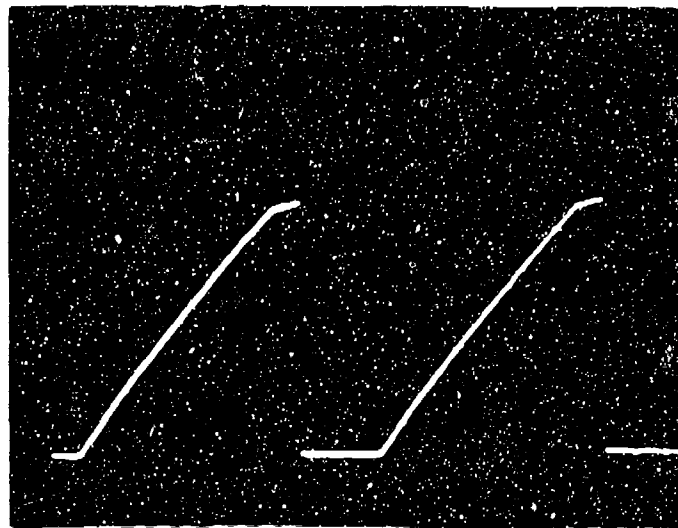


Figure 67

Current during charge of pulsed model energy storage coil constructed with braided single core superconductor. The coil is being discharged into a resistive load. The pulse repetition rate is 5/s. The discharge time constant is about 0.16×10^{-3} s. The energy stored in the coil at peak current is 0.87 kJ.

Time base	0.050 s/div
Sensitivity	120 A/div
Maximum current	395 A
Charge time	0.150 s

The steady state critical current is 430 A

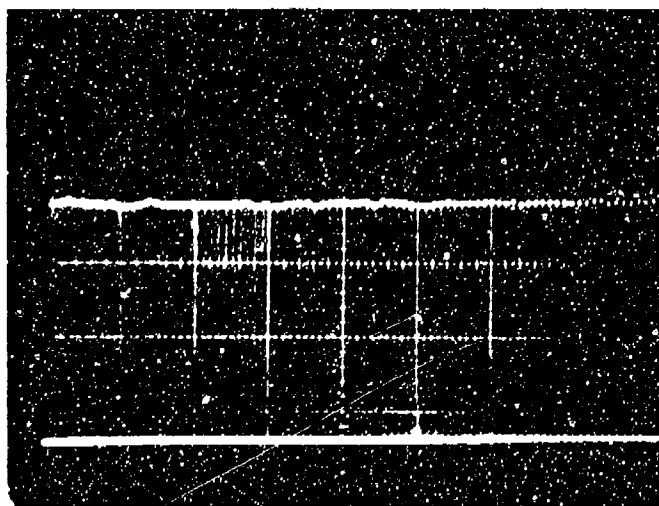


Figure 68

Current during charge of pulsed model energy storage coil constructed with braided single core superconductor. The pulse repetition rate is 5/s. The figure shows part of a pulse train of duration about 15 seconds. The coil is being discharged into a resistive load with a discharge time constant of about 0.16×10^{-3} s. The energy stored in the coil at peak current is 0.82 kJ.

Time base	2 s/div
Sensitivity	120 A/div
Maximum current	385 A
Charge time	0.150 s

The steady state critical current is 430 A.

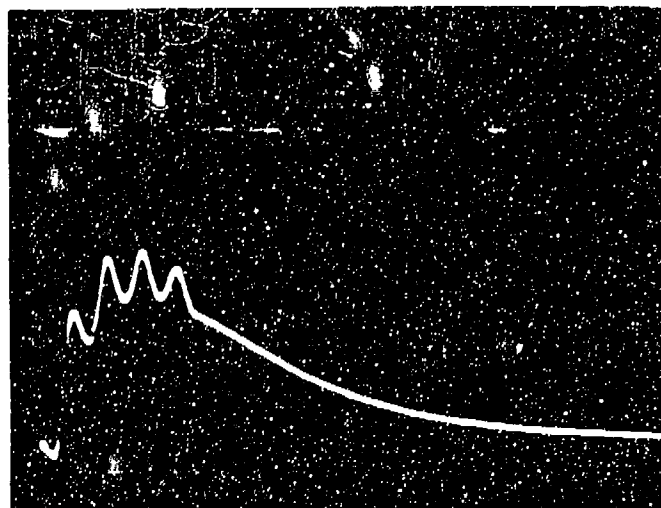


Figure 69

Voltage from model energy storage coil constructed with braided single core superconductor when discharged into a resistive load at a pulse repetition rate of 5/s.

Time base	0.10×10^{-3} s/div
Sensitivity	5.0 kV/div

Maximum voltage	13 kV
Discharge time constant	0.16×10^{-3} s/div

The coil behavior was such that at higher currents the coil would operate for a short period of time before quenching. For example, at a discharge time constant of 0.2 ms and an interpulse time of 55 ms as above, with a maximum current of 385 A (0.87 of maximum) the coil ran 40 seconds without any sign of degradation before quenching.

At a given discharge time and interpulse period, the coil could be pulsed indefinitely only below a certain value of the maximum current. If that value of current were exceeded, the coil would remain superconducting only for a certain number of pulses. It would then go normal. This is illustrated in Figure 70. In this case, the model coil operated properly for about 16 seconds while being pulsed at a repetition rate of five per second and then quenched. It was found that this behavior could be avoided by either reducing the maximum charging current or increasing the interpulse period.

This behavior could be interpreted as being due to vapor lock in the cooling channels. However, this was found not to be the case. Section II-5-c, Effect of Transient Heating on Coil Performance, described a correlation between the peak nucleate boiling heat flux and the ratio of channel length to diameter ratio; the higher the length to diameter ratio, then the lower the peak nucleate boiling heat flux.

In the 1 kJ model coil, the ratio L/d is 33.7 for which the correlation gives a peak nucleate boiling heat flux of 0.23 W/cm^2 . During the five pulses per second tests, the maximum recorded loss per pulse was 2.8 J. The average heat flux per unit cooled area for the coil under this condition is 0.0062 W/cm^2 . Theoretical calculations indicate that the peak flux (in the higher field regions of the coil) is about two or three times the average for the coil as a whole. Taking the factor of three, the maximum value of the heat flux in the magnet is 0.019 W/cm^2 . This is a factor of 12 less than the critical value. We conclude from this that the channels becoming choked with helium was not the cause of the coil quenching under certain conditions while being charged and discharged at five pulses per second.

In view of the thermal analyses conducted concerning the effect of heat generation in the windings, the behavior of the coils is interpreted in the following way. As the current in the coil is changed, energy losses are incurred due to eddy currents in the copper and magnetization effects in the superconductor. During charge these losses are such that the heat can be dissipated to the surrounding helium bath with only small temperature rise in the conductor. However, on discharge when the energy losses are much greater and the time over which they are generated much smaller, the temperature of the conductor rises appreciably. The higher the current and the shorter the discharge time, the higher will be the final temperature of the conductor. The conductor cools during the interpulse period. If the interpulse period is long, then by the time the next pulse starts, the conductor will have reached the bath temperature. However if the period between pulses is short, then the conductor temperature will not have dropped to the bath temperature before the next pulse starts. Consequently, during the next pulse its temperature at any time will be higher than that at the corresponding time on the previous pulse.



Figure 70

Current during charge of pulsed model energy storage coil constructed with braided single core superconductor. The pulse repetition rate is 5/s. After about 16.5 seconds, the coil went normal for reasons explained in the text. As the normal region spreads, the resistance of the coil increases. Since the charging voltage is constant, the peak current decreases on successive pulses.

Time base	5 s/div
Sensitivity	120 A/div

The temperature of the conductor therefore rises with each succeeding pulse until eventually the temperature is higher than the transition temperature for the ambient field and current and the coil then goes normal. This is the behavior that was previously predicted on theoretical grounds.

Table XVII summarizes the range of pulse repetition rates and discharge time constants over which the 1 kJ coil was operated. Figures 71 and 72 are photographs showing the test apparatus used in the model coil tests.

b. 7 kJ Coil Evaluation Tests

Having established experimentally that the principles on which the 1 kJ coils were built were correct, a coil having a higher stored energy was built and tested. This was done to assure ourselves that scaling with size did not introduce any unforeseen detrimental effects. It was felt that scaling from 1 kJ stored energy to 100 kJ stored energy was too big a step. The nominal 7 kJ stored energy coil was built on the same principles as the 1 kJ stored energy coils and is described in Section II-5-e, Model Coils. Although the nominal stored energy is 7 kJ the coil was operated at higher energies.

Under conditions of slow charge the coil could be charged to the short sample H-I curve of the conductor. At the critical current the stored energy was about 16 kJ. At a repetition rate of one pulse per second loss measurements were made for stored energies of 7 kJ and 10 kJ. The coil was run at a repetition rate of five pulses per second for a stored energy of 4.3 kJ; this was the highest energy possible at five pulses per second because of the voltage limitation of the power supply (truck batteries). However to simulate conditions at higher energies at five pulses per second the coil was operated at a repetition rate of four pulses per second with a stored energy of 7 kJ but with an interpulse time which corresponded to a repetition rate of five pulses per second. Thus the time available for cooling between pulses was the same. Loss measurements were made under these conditions. The coil could be operated under all these conditions for indefinitely long periods of time. A summary of the 7 kJ coil performance is given in Table XVIII. Details of the loss measurements made on this coil are given in Section III-6, Loss Measurements Made Using the 7 kJ Coil.

c. 100 kJ Coil Evaluation Tests

Since the 7 kJ coil behaved as expected during testing, the 100 kJ coil was built and tested. The construction technique is similar to that used in the model coils and is described in detail in Sections II-5-f, g and h.

A number of tests were performed on the 100 kJ coil; these are summarized in Table XIX. The tests fall into the following categories: (1) tests concerned with the measurements of losses, which are described in Section III-7, Loss Measurements Made Using the 100 kJ Coil; (2) tests concerned with the high voltage operation, which are described

Table XVII

SUMMARY OF 1 kJ COIL PERFORMANCE (SINGLE CORE SUPERCONDUCTOR)

<u>Repetition Rate</u> <u>(pps)</u>	<u>Stored Energy</u> <u>(kJ)</u>	<u>Discharge Time</u> <u>(ms)</u>
1	~0.8	4, 2, 0.9, 0.3, 0.2
5	~0.8	4, 2, 0.9, 0.3, 0.2

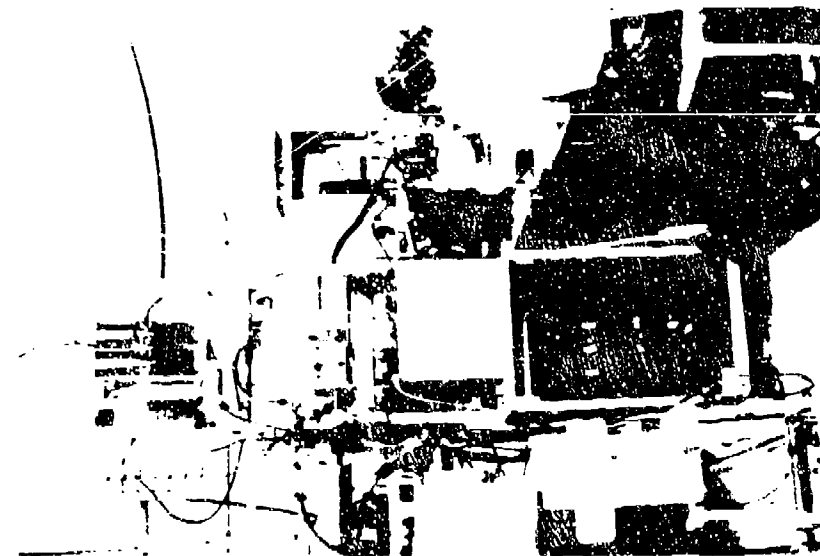


Figure 71 Above: General view of apparatus used during testing and evaluation of 1 kJ model energy storage coil. An experiment to determine the energy loss during transient operation is in progress.

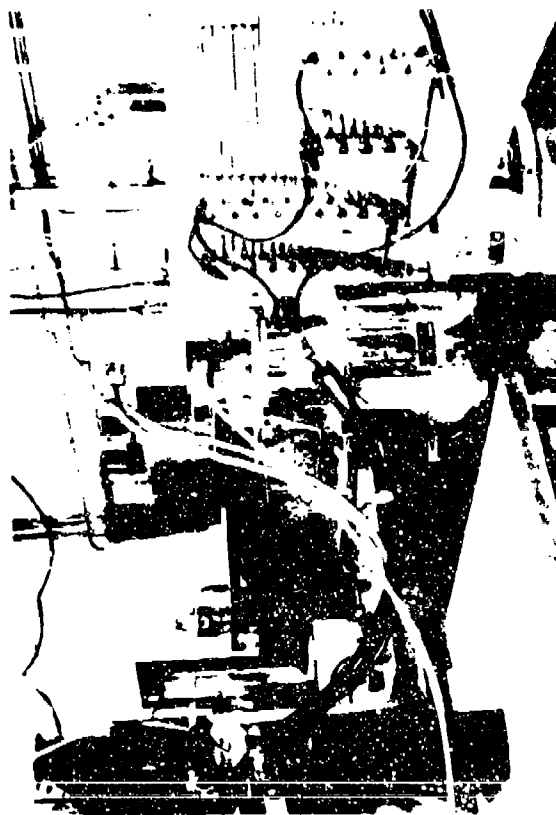


Figure 72 Above: Detail view of 1 kJ model coil and dump resistor. Tube below high voltage bushing carries helium to flow meter for energy loss measurements during pulsing experiments.

Table XVIII
SUMMARY OF 7 kJ COIL PERFORMANCE

<u>Repetition rate</u> (pps)	<u>Stored energy</u> (kJ)	<u>Discharge time</u> (ms)
1	7	4, 2, 1
1	10	4, 2, 1+
4*	7	4, 2, 1
5	4.3	4

*Interpulse time 33 ms which is that which would be used for a repetition rate of 5 pulses per second.

+Voltage across coil 23 kV.

Table XIX

SUMMARY OF TESTS PERFORMED WITH 100 kJ COIL

1. Measure inductance of coil, of sense coil, and mutual inductance between them.
2. Ringing tests at 17 kV; measure losses. Maximum energy, 600 J.
3. Ringing tests at up to 4 kV and up to 11 kJ. Measure losses (use loss loop measurements).
4. Slow charge to maximum of 950 A, discharge into 0.6 ohm. Exercise all control circuitry, arc quench circuit, resistor bank.
5. Test helium switch at coil currents up to 950 A. Maximum voltage about 2,500 V.
6. Attempt to charge coil to full design current (2,000 A - 100 kJ). Quench observed at about 1,200 A which caused about 36 kJ to be dissipated in the coil.
7. Try very slow charging rates (use voltages as low as 50 mV) to see if quenching is rate dependent. Coil appeared to have a dc resistance of about 10 milliohms at this time.
8. Test high voltage limits of the coil by ringing at up to 50 kV with 0.25 μ F capacitor. No breakdowns observed up through 50 kV.
9. Try higher voltages by driving the sense coil (ringing with 1 μ F 4.2:1 turns ratio). Arcing observed at 63 kV (15 kV on the sense coil) both outside dewar and inside dewar.

in Section II-4-d, Experimental Program for testing the Current Leads; (3) tests concerned with the operation of a switch which produces short width pulses at a high repetition rate, which are described in Section III-8-b, Design and Testing of Electric Circuit and of Switch for Pulsed Operation; and (4) tests concerned with testing all control circuitry, arc quench circuits and the resistor bank at high currents, which are described in detail in this section.

Loss measurements were made on the 1 kJ coil by a technique which involved measuring the quantity of helium boiled off during a train of pulses. Similar measurements were made on the 7 kJ coil but in addition measurements were made by using an electronic device which in principle behaves in a similar way to a watt meter. This is described in detail in Section III-4-c, Electronic Method. This device allows loss measurements to be made on a single pulse. The boiloff method is applicable only when a quantity of helium gas is evolved which is sufficiently large to be accurately measured. Since the 100 kJ coil was deliberately designed to have low losses, the only way that a sufficient volume can be generated is to collect the gas evolved over a long pulse train. Since the electrical circuitry was not designed for this mode of operation, loss measurements on the 100 kJ energy storage coil were confined to the techniques involving the electronic measurement device. These loss measurements are described in detail in Section III-7-c, Electronic Loss Measurements on the 100 kJ Coil. In general the measurements are consistent with the theory within the limitations of the model used to derive the theoretical losses.

High voltage tests were conducted up to 50 kV (the limits of the high voltage power supply) by charging up a capacitor to the desired voltage and discharging it into the coil thereby setting up an oscillation between the coil and the capacitor. At this voltage no breakdown was observed. To go to higher voltages the sense coil (part of the instrumentation for the electronic loss measurement device) was used as a secondary. The capacitor was discharged into the sense coil and high voltages were induced on the 100 kJ energy storage coil. In this way, voltages up to 63 kV were applied across the coil terminals. At this voltage breakdown was observed. It appeared that this breakdown was occurring between the current leads near the top of the dewar. The results of these experiments were consistent with theoretical analyses and tests on mockups previously conducted. These experiments are described in detail in Section II-4-d, Experimental Program for Testing the Current Leads.

A series of tests were conducted which produced a burst of short duration pulses at a high repetition rate. A capacitor was placed across the coil terminals and a switch placed across the capacitor. The switch was preset to close at a desired voltage. The coil was charged to the desired energy and then the current through the coil was broken using the vacuum interrupter. The coil then started to discharge into the capacitor. When the voltage on the capacitor rose to the preset voltage, the switch closed and the energy stored in the capacitor discharged through the load. When the current through the switch was low enough, the switch opened thereby allowing the capacitor to be charged again from the coil. This sequence was repeated until the

energy in the coil was exhausted. The results of these tests confirmed the validity of the theoretical analyses which led to the design of the switch and circuit. These experiments are described in detail in Section III-8-b, Design and Testing of Electric Circuit and of Switch for Pulsed Operation.

Finally the high current operation of the system was tested. This experiment consisted of charging the coil with the battery to about 1,000 amps (25 kJ), then discharging it into a low resistance (0.6 ohms). The electric circuit used for this test is given in Figure 73, a photograph showing the top of the dewar and the resistor bank is given in Figure 74, and a typical output current pulse is shown in Figure 75. The purpose of this test was to demonstrate successful operation of all control circuitry and of the coil at moderate (25 kJ) energy levels.

The next test performed was an attempt to charge the coil to its rated capacity (100 kJ, 2,000 amps) using the circuit of Figure 73. A quench was observed at 1,200 amps which caused about 36 kJ to be dissipated in the coil. Subsequent attempts to determine the cause of the quench consisted of charging at low voltages (as low as 50 mV) to see if quenching was rate dependent. No rate dependence was observed.

It was concluded that the coil had suffered damage. Measurements made at this time indicated that there was a resistive region somewhere within the windings. At this time it exhibited a DC resistance of about 10 mΩ.

The coil was warmed up, removed from the dewar and examined. Externally no damage was apparent although debris consisting of what appeared to be burned insulation was observed on the top of the coil form. Close examination indicated that this had been ejected from the inside of the windings. Resistance measurements were made and compared with measurements made prior to cooldown. The resistances measured were higher than before and there was continuity between the two braids which had been wound in parallel. This further suggested severe damage. The damage appeared to be in the layers nearest the coil form.

No further conclusions could be drawn without looking inside the windings so the whole of the winding bundle was removed from the mandrel by removing the flanges, slitting the mandrel and sliding the windings off.

When the inner layers of electrical insulation were removed thereby exposing the inner layer of windings the damaged area was immediately apparent. The damage occurred at the end of the innermost layer where the conductor rose into the second layer. This is at the opposite end of layer from where the leads enter the coil. The area was severely burned, the two braids were shorted together and one braid was completely burned through.

This layer was clearly beyond repair so it was removed by unwinding from the inside. The layers of electrical insulation and structure adjacent to the first layer of windings were removed and the second layer

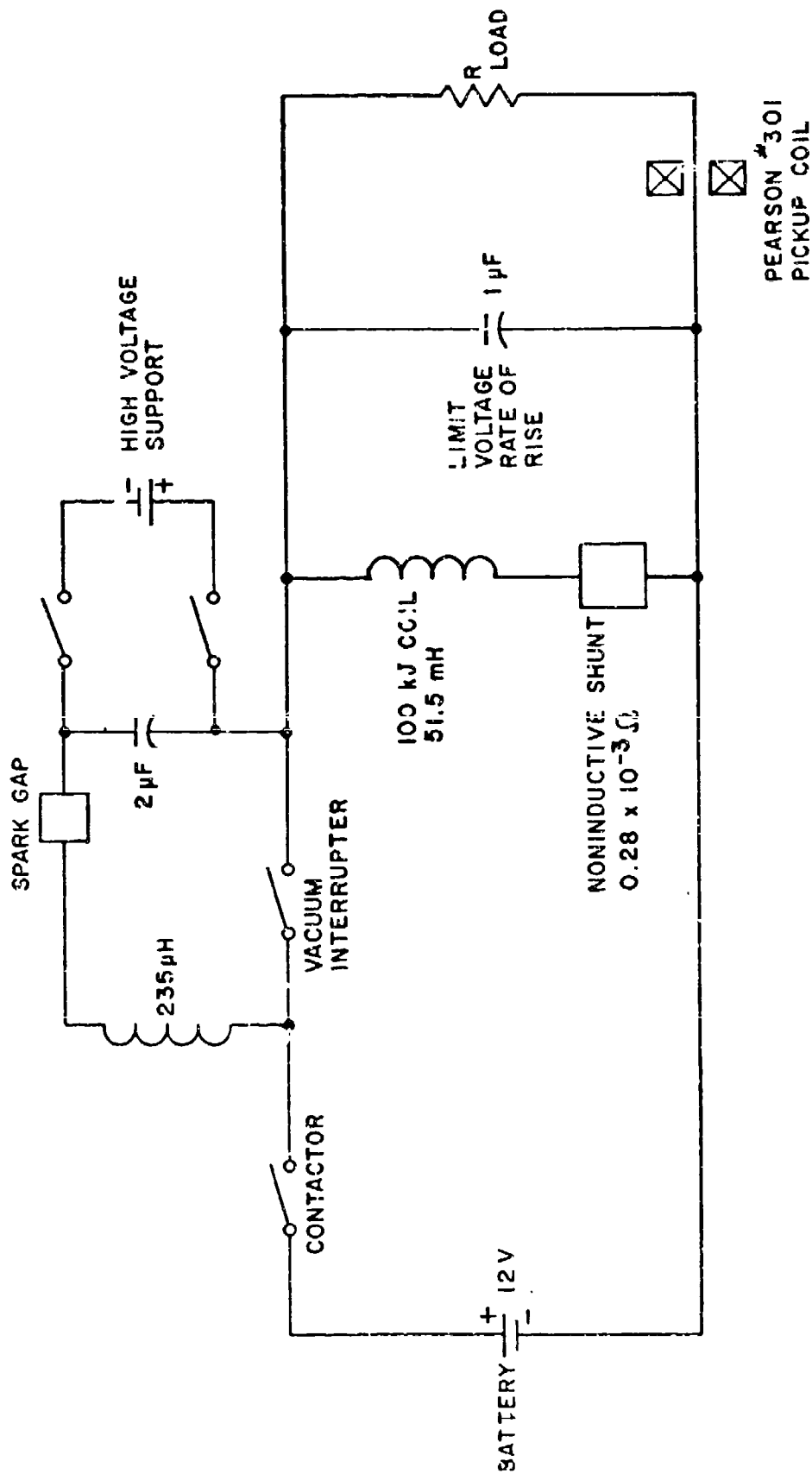


Figure 73: Overall Schematic of Electrical System for 100 kJ Coil

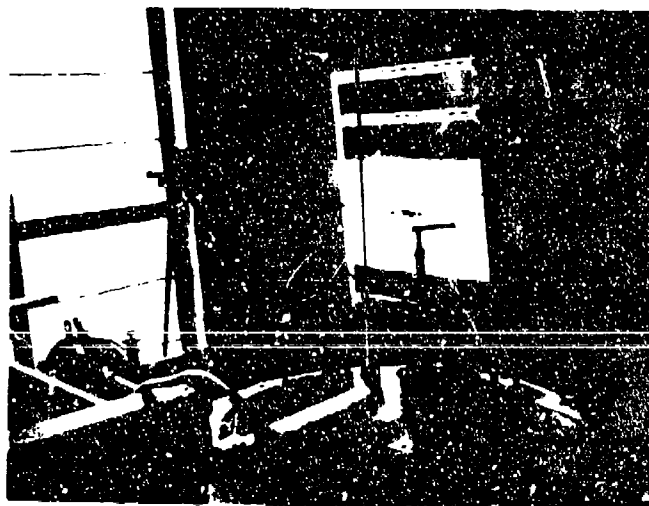
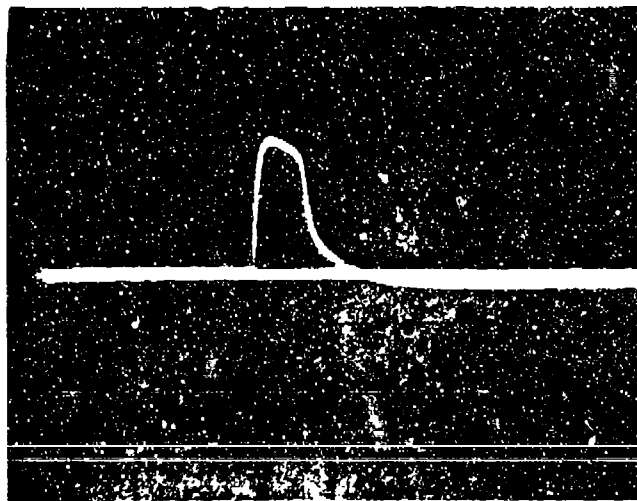


Figure 74

Photograph of top of dewar, power leads for 100 kJ coil, and resistor bank used for switching tests.

Load Current, 500 A/cm



Time 50 ns/cm

Figure 75

Discharge of a 100 kJ coil into 0.6 Ω load.
Peak current - 950 A; Energy - 20 kJ; Parallel
Capacitor - 1,125 μ F.

was exposed. This layer was even more severely damaged than the first layer; some tens of square centimeters were burned and it appeared that the damage had started in this layer and spread into the first layer. The damage seemed to be confined to the first and second layers. The other end of the second layer was not damaged. The second layer too was removed but a sufficient length of conductor was left so that new connections could be made to the current leads should it be decided that the coil be repaired.

The following explanation is given for the cause of this damage. During the first set of experiments to measure losses a capacitor was charged up and then discharged in the coil using a spark gap as the closing switch. The combination of the capacitor and the inductor rings as the charge is transferred backwards and forwards between these two components. Because of dissipative elements in the circuit the amplitude of the oscillatory current decreases. Eventually it becomes so small that the spark gap tries to turn off. When it turns off there are very high rates of change of current and because of the circuit inductance high voltage spikes appear across the energy storage coil. It is thought that these voltage spikes caused a breakdown between adjacent turns in the coil in the region that was damaged to give a shorted turn. Subsequent ringing of the coil caused current to be transferred across this short. This caused local heating in this region which increased the damage. Finally when higher currents were attempted, because of the short, a current greater than the critical current was induced in the shorted turn. This caused a premature quench. Because of the high rate of change of field during discharge very high currents were induced in the shorted turn. This caused insulation to melt and the wire to burn out locally.

3. THEORY OF LOSSES IN PULSED COILS

a. Formulae Used to Predict Losses in Superconductors

The losses in an energy storage coil are of prime importance in designing the system. It is these losses which determine the amount of cryogen required and therefore the size of the cryogenic vessel required. Bean(15, 16) formulated a simple phenomenological model (the critical state model) which allows predictions to be made concerning the magnetic behavior of a high field superconductor in terms of a single empirical parameter, the critical current density, j_c . This model is the starting point for the formulae predicting coil losses which were derived during this program.

According to this model it is assumed that the electric field vector, E , is zero for current densities less than j_c , but rises vertically at j_c with the E and j_c vectors parallel. In other words, any electric field no matter how small will cause this maximum current density j_c to flow locally in the direction of the electric field. Thus a material cooled through the superconducting transition temperature with no current flowing has E and j_c zero everywhere but as soon as the magnetic field is changed (thereby inducing electric fields) current densities of magnitude j_c are induced in portions of the material.

The interaction between the electric field E and the current density j_c gives a local dissipation P per unit volume according to the relation $P = E \times j_c$.

Appendix II of technical report AFAPL-TR-72-38, Vol I derives an expression for the instantaneous power dissipation per unit volume of superconductor in terms of the local conditions of a length of single core superconducting wire carrying a transport current. These local conditions include the ambient field (assumed constant over the diameter of the wire), the rate of change of field, the critical current density (at the local field), and the ratio of the transport current density to the critical current density. The loss per unit volume is proportional to the diameter of the superconductor. It is assumed that the flux fully penetrates the superconductor and so the derivation is not valid for fields so small that only partial penetration exists. An expression for the power dissipation due to currents induced in the normal matrix surrounding the superconductor is also derived. The analysis goes on to derive expressions for power losses in both twisted and untwisted multifilamentary superconducting wire. It is shown that the losses in an untwisted multifilamentary conductor are proportional to the diameter of the bundle of filaments rather than to the diameter of a single filament. It is shown that the effect of twisting is such that the filaments can be made to behave independently provided that the twist pitch can be made small relative to the skin depth of the normal matrix. However, for this particular application at a coil discharge time of 1 ms the required twist pitch for a copper matrix at liquid helium temperature is about 0.1 inch. This is too small for presently available conductors, therefore the minimum loss configuration is one of small individually insulated conductors each consisting of a single strand of superconductor surrounded by copper. The insulation between individual conductors allows the magnetic flux to penetrate each conductor and the losses are thereby minimized.

The expressions derived in technical report AFAPL-TR-72-38, Vol. I, Appendix II, assume a wire of square cross section. For this case, the instantaneous power dissipated per unit volume of conductor due to the superconductor is:

$$P/V = k_1 \frac{w}{4} \frac{dB}{dt} j_c \left[1 + \left(\frac{j_t}{j_c} \right)^2 \right] \frac{1}{w^2} \quad \text{III-3-1}$$

Where:

$$k_1 = 1$$

w = length of the side of the square of superconductor

w_c = length of the side of the square of normal matrix

$\frac{dB}{dt}$ = rate of change of flux density

j_c = critical current density for ambient field conditions

j_t = transport current density

$$W = \frac{w_c}{w}$$

The expression for the instantaneous eddy current power loss in the normal matrix per unit volume of conductor is:

$$P/V = \frac{k_2}{12\rho} w^2 \left(\frac{dB}{dt}\right)^2 \left(\frac{W^4 - 1}{W^2}\right) \quad \text{III-3-2}$$

when the superconductor is in the normal state and:

$$P/V = \frac{k_2}{12\rho} w^2 \left(\frac{dB}{dt}\right)^2 \frac{1}{W^2} \left[(W^4 - 1) + 3(W-1)\left(\frac{j_t}{j_c}\right)^2 \right] \quad \text{III-3-3}$$

when the superconductor is in the superconducting state

Where:

ρ = resistivity of the matrix

$$k_2 = 1$$

the other symbols are as given above.

The analyses which led to the above expressions were extended and expressions were derived for the instantaneous power losses due to a round wire. They differ from the above expressions only in the constant k (a geometry factor). The derivations are given in Appendix I of this report. For a round wire

$$k_1 = \frac{8}{3\pi} \text{ and } k_2 = \frac{3}{4}$$

The above expressions are for instantaneous power loss per unit volume. To obtain the total energy dissipated during a cycle they must be integrated suitably over time and over the volume of the conductor in the coil.

The energy losses in the superconductor are hysteretic type losses and are independent of the time over which the charge or discharge occurs. However, the eddy current energy losses are proportional to the rate of change of flux density in the conductor. The model chosen for the superconductor losses was as follows. It was assumed that critical current density/critical field curve for the material was linear and was defined by j_{c0} (the critical current density at zero field) and B_0 (the flux density at which a linear extrapolation of the B_c - j_c curve from the low field region crosses the $j_c = 0$ line). This is a reasonable approximation to the real curve for restricted sections of the B_c - j_c curve and could be used in the case of the coils built during this program because of their low peak fields at maximum current. It was also assumed that the conductor in the coil at any current experienced a field which

varied linearly from zero to a maximum at the peak field position. In the case of the eddy current losses the magneto resistance of the normal matrix as a function of time and position was also taken into account. A more detailed account of this procedure and the derivations are given in Appendix I of this report. The results of these analyses are as follows. They are given in terms of the average energy loss per unit volume of conductor in a coil which is charged from zero current to a maximum current (or discharged from a maximum current to zero current). The total energy loss for the coil is therefore found by multiplying by the volume of the conductor in the coil.

For the energy dissipated due to the superconductor:

$$E/V = \frac{8}{3\pi} \frac{w}{4} \frac{B_M j_{CO}}{2W^2} \left\{ 1 - \frac{1}{3} \left(\frac{B_M}{B_0} \right) + 2 \left(\frac{j_M/j_{CO}}{B_M/B_0} \right)^2 \left[1 - \frac{1}{2} \left(\frac{B_M}{B_0} \right) + \frac{\left(1 - \frac{B_M}{B_0} \right) \ln \left(1 - \frac{B_M}{B_0} \right)}{\left(\frac{B_M}{B_0} \right)} \right] \right\} \quad \text{III-3-4}$$

Where:

$\left. \begin{matrix} j_{CO} \\ B_0 \end{matrix} \right\}$ = critical current density and flux density which define the B_C - j_C curve for the purposes of this model

B_M = flux density at the peak field position at maximum transport current density

j_M = maximum current density in superconductor

w = diameter of superconducting core

w_C = diameter of normal matrix

$W = w_C/w$

For the energy dissipated due to the normal matrix (assuming an exponential decay of transport current):

$$E/V = \frac{3}{4} w^2 \left(\frac{W^4 - 1}{W^2} \right) \frac{K^2}{12\rho_0 T} \left\{ 1 + \frac{1}{2} \left(\frac{B_M}{K} \right) - \frac{\left(1 + \frac{B_M}{K} \right) \ln \left(1 + \frac{B_M}{K} \right)}{\left(\frac{B_M}{K} \right)} \right\} \quad \text{III-3-5}$$

for when the superconductor is in the normal state and:

$$E/V = \frac{3}{4} w^2 \frac{(w^2-1)}{w^2} \frac{K^2}{12\rho_0\tau} \left\{ 1 + \frac{1}{2} \left(\frac{B_M}{K} \right) - \frac{(1 + \frac{B_M}{K}) \ln(1 + \frac{B_M}{K})}{(\frac{B_M}{K})} \right. \\ \left. + \left(\frac{J_M}{J_{CO}} \right)^2 F \right\} \quad \text{III-3-6}$$

for when the superconductor is in the superconducting state.

Where:

F = a function of B_M , B_0 , w , K

ρ_0 = the zero field resistivity of the material

τ = the exponential decay time constant

K = a factor which defines the magneto-resistance effect

in copper, i.e. $\rho(B) = \rho_0 (1 + \frac{B}{K})$

An expression was also derived for the loss due to a transport current density in the matrix. This would be the situation if the coil were to go normal. For the case where the whole of the coil goes normal at the beginning of the discharge and remains normal throughout the exponential decay period the energy loss per unit volume averaged over the volume of conductor in the coil due to the transport current density is:

$$E/V = \frac{(w^2-1)}{w^2} \frac{J_T^2 \rho_0 \tau}{2} (1 + \frac{B_M}{3K}) \quad \text{III-3-7}$$

Where:

J_T = transport current density in the matrix

and the other symbols are as given above.

Appendix I gives details of these analyses and Table XX summarizes the formulae for energy losses given above. The formulae given above were refined to take account of the actual field distribution in the coil as opposed to an ideal case where the field varied linearly along the length of the wire from zero to a maximum at the peak field position. The formulae instead of having just one field term were written in terms of two field terms. One term defines the lower field experienced by a length of conductor carrying the maximum transport current and the other term defines the upper field. The field distribution in between is again assumed to be linear. The average energy loss per unit volume of the conductor is calculated using these formulae; the total energy loss due

Table XX

ENERGY LOSS FORMULAE (SIMPLIFIED)

These formulae assume that there is a linear variation of ambient field along the length of conductor in the coil from zero to a maximum at the peak field position. It is assumed that the field rises linearly during charge and falls exponentially during discharge. Energies are given in terms of volume of conductor (i.e., copper and superconductor).

1. TRANSPORT CURRENT LOSS

$$\frac{E}{Vol} = \frac{(W^2-1)}{W^2} \frac{j_T^2 \rho_0 \tau}{2} \left(1 + \frac{B_M}{3K}\right) \quad \text{III-3-7}$$

2. EDDY CURRENT LOSS

$$\frac{E}{Vol} = \frac{3}{4} w^2 \frac{(W^2-1)}{W^2} \frac{K^2}{12\rho_0 \tau} \left\{ 1 + \frac{1}{2} \frac{B_M}{K} - \frac{\left(1 + \frac{B_M}{K}\right) \ln \left(1 + \frac{B_M}{K}\right)}{\left(\frac{B_M}{K}\right)} \right\} \quad \text{III-3-5}$$

3. MAGNETIZATION LOSS

$$\frac{E}{Vol} = \frac{8}{3\pi} \frac{w}{4W^2} \frac{j_{co} B_M}{2} \left\{ 1 - \frac{1}{3} \frac{B_M}{B_0} + 2 \left(\frac{j_M}{B_M}\right)^2 \left(\frac{B_0}{j_{co}}\right)^2 \left[1 - \frac{1}{2} \frac{B_M}{B_0} + \frac{\left(1 - \frac{B_M}{B_0}\right) \ln \left(1 - \frac{B_M}{B_0}\right)}{\left(\frac{B_M}{B_0}\right)} \right] \right\} \quad \text{III-3-4}$$

j_T = Maximum transport current density in copper

j_M = Maximum transport current density in superconductor

B_M = Maximum flux density in conductor

B_0 { Flux density and critical current density which define B_c - j_c curve of material over region of interest.

j_{co}

ρ_0 = Resistivity of copper at zero flux density.

K = A factor which defines magneto resistance effect in copper, i.e.,

$$\rho(B) = \rho_0 \left(1 + \frac{B}{K}\right)$$

w = Diameter of superconducting core

W = Ratio of diameters of conductor and superconducting core

τ = Discharge time constant for an exponential decay

to this length of conductor is found by multiplying the average energy loss by the actual volume of the length of conductor in the coil which experiences these upper and lower field limits.

To use these formulae it is of course necessary to know the distribution of field within the windings. The distribution was found by taking a field plot within the windings and calculating the volumes between various field limits. Figures 76 and 77 are such distribution curves for the 1 kJ coil and 7 kJ coil, respectively. They are in the form of histograms. The coil was divided into 10 regions such that the field limits of each region were 0 to 0.1 of the peak field, 0.1 to 0.2 of the peak field, 0.2 to 0.3 of the peak field, etc. The volume of conductor in each region is represented in terms of the ratio of the volume in the region to the volume of the coil. The fractions of volume in the lowest and highest field regions are lowest and the volume fraction peaks in intermediate regions. This is as would be expected since there is only one point in the coil where the field is zero and only one point where it is a maximum whereas intermediate fields extend over large fractions of the volume. Thus with the refined formulae described above and with a knowledge of the actual field distribution in the energy storage coils, predictions could be made as to the energy losses which would be incurred over a charge-discharge cycle under various assumptions as to the state of the conductor as a function of position and time.

b. Models Concerning the State of the Superconductor in a Coil

The simplest two models are shown in Table XXI. Both models assume that the whole of the energy storage coil is superconducting throughout the charge period. The losses on charge are then the sum of a magnetization loss due to the superconductor and an eddy current loss due to the normal matrix. The models differ however on the assumptions made for the state of the coil during discharge. Model 1 assumes that the whole of the coil remains superconducting during the whole of the discharge period. The losses then are the sum of a magnetization loss and an eddy current loss, as on charge. Model 2 assumes that the whole of the coil goes normal as soon as the discharge starts and remains normal throughout the whole of the discharge period. The losses then are the sum of a transport current loss in the normal matrix and an eddy current loss. These two models are two extreme cases and since the losses due to various fractions of the coil can be calculated separately it is possible to have models where a fraction of the windings (in the higher field regions) go normal and the remainder stays superconducting. In Sections III-5, 6 and 7 a comparison is made between the results of the loss experiments and various models. In view of the simplicity of these models, a reasonable agreement between theory and experiment was found.

It has been tacitly assumed that the critical current density j_c is only field dependent. This is not true of course since it is also dependent on temperature. At a constant field strength the critical current density decreases with increasing temperature. Since, as has been pointed out previously, the temperature of the windings rises during a rapid discharge the critical current density at a given field

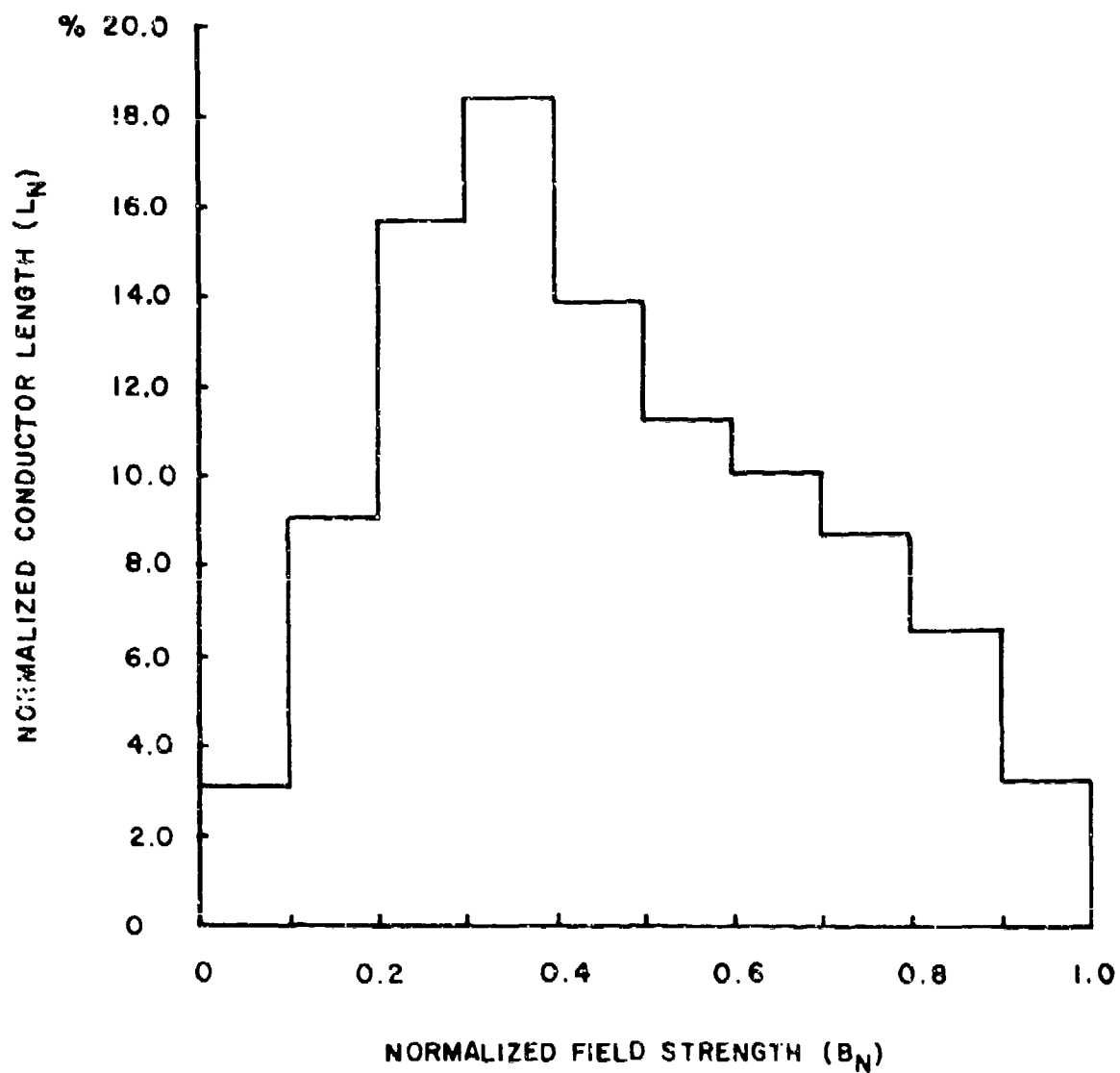


Figure 76: Distribution of Conductor Length with Field Strength for 1 kJ Coil

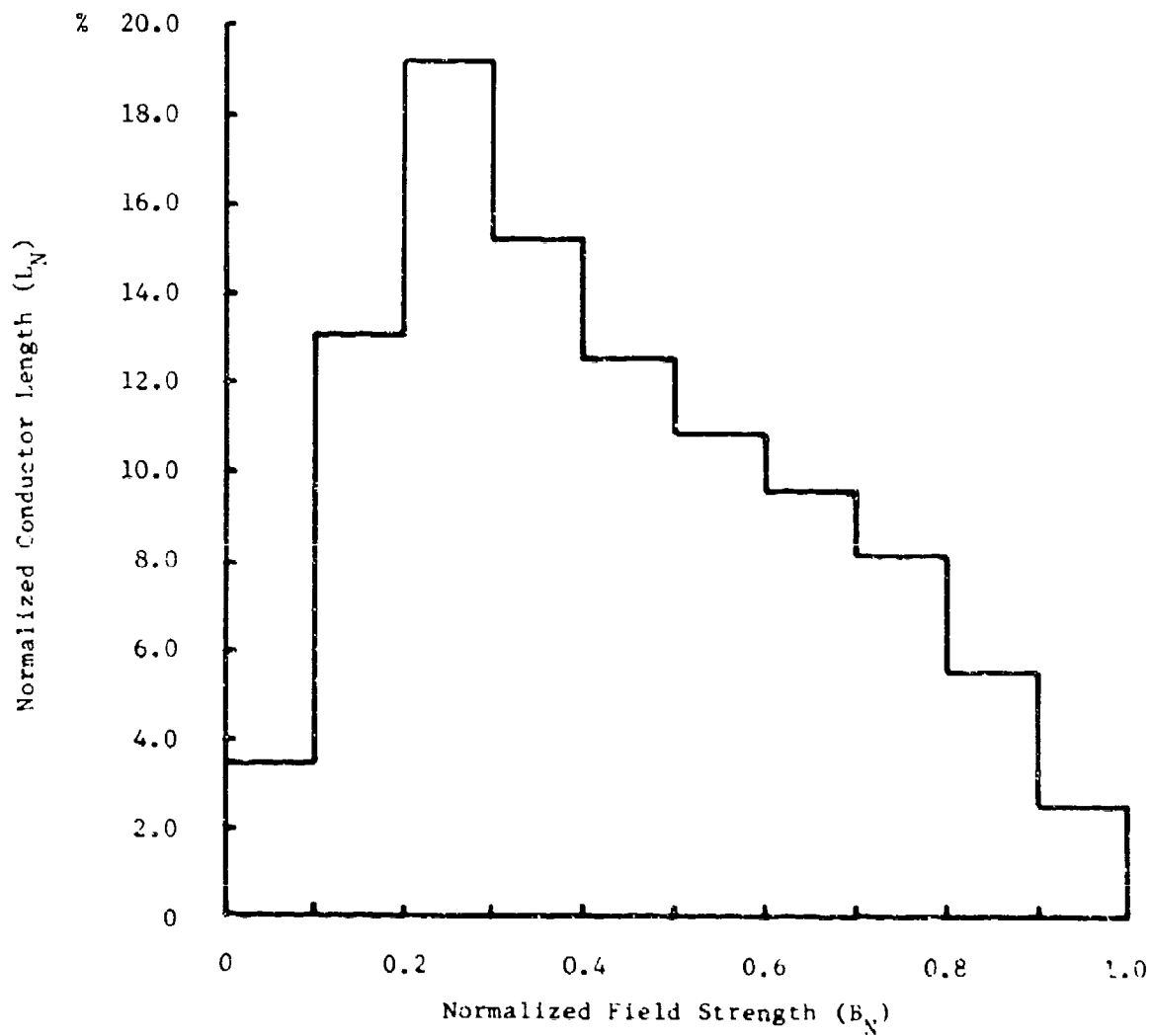


Figure 77 Distribution of Conductor Length with Field Strength for 7 kJ Coil

Table XXI
SIMPLE ENERGY LOSS MODELS

<u>MODEL 1</u>	<u>STATE</u>	<u>LOSS</u>
<u>Charge</u>	Superconducting	Magnetization (M) Eddy (E ₁)
<u>Discharge</u>	Superconducting	Magnetization (M) Eddy (E ₁)
Total Loss/Pulse = 2M + E ₁ + E ₂		

<u>MODEL 2</u>	<u>STATE</u>	<u>LOSS</u>
<u>Charge</u>	Superconducting	Magnetization (M) Eddy (E ₁)
<u>Discharge</u>	Normal	Transport (T) Eddy (E ₂)
Total Loss/Pulse = M + T + E ₁ + E ₂		

NOTE: More complicated models have been used whereby it is assumed that certain fractions (f) of the coil go normal during discharge giving:

$$\text{TOTAL LOSS/PULSE} = M + f_1 M + f_2 T + E_1 + E_2$$

strength can be expected to be less during discharge than during charge. This decrease in current density will result in a lower power loss due to superconductor magnetization. The models used do not take account of this effect and therefore the predicted magnetization losses can be expected to be higher than the real losses. The model also assumes that the critical current density flows throughout the whole of the area of cross-section of the superconductor. This is only true if the field penetrates to the center of the superconductor. In reality, at low fields only partial penetration occurs. Since all of the coil is at low fields for part of the cycle and part of the coil is at low fields for the whole of the cycle, the models described above will again overestimate the size of the magnetization energy loss.

The derivation of the loss due to eddy currents in the matrix assumes that the induced flux fully penetrates the matrix. While this is true at long charge or discharge times it can be expected that at short discharge times the penetration will be skin depth limited so that there will be discharge times below which the eddy current loss is overestimated.

The results of the experiments to measure losses (which will be described in detail in Sections III-5, 6 and 7) suggest that the three possible causes for error described above are significant since the loss measurements are consistently lower than those which would be expected from predictions made according to the models described in this section. This is particularly so for measurements made on the 1 kJ coil at short discharge times.

As far as improving the models is concerned, in light of the limitations described above, it would be relatively easy to take into account the incomplete penetrations of field into both the matrix and the superconductor. However, taking account of the change in critical current density according to temperature is likely to be intractable because of the difficulty of predicting the temperature of the windings as a function of time and position.

4. LOSS MEASUREMENT METHODS

a. Introduction

In order to properly evaluate the performance of an energy storage coil, it is of fundamental importance to measure the energy losses as a function of current and of frequency. The most straightforward method for doing this is the measurement of the rate of boiloff of cryogen (helium) as a function of the operating mode of the coil. While this method is in principle very straightforward, it is in practice restricted to fairly long-term (minutes) repetitive experiments as is discussed in Section III-4-b, Helium Boiloff Method below. An alternative technique (17), which is capable of measuring the losses during a single charge-discharge cycle of the coil, consists of displaying the hysteresis loop for the superconducting coil on an oscilloscope by means of appropriate electronic equipment; the area inside this loop is proportional to the energy loss in the coil. The theoretical and the practical aspects of this electronic loss measurement technique are discussed in Section III-4-c, Electronic

Method below. Of these two methods for measuring losses, the electronic technique is the more practical for experimental purposes because it makes possible the evaluation of a coil by means of a number of single cycles instead of by repetitive operation.

b. Helium Boiloff Method

The heat generated within the windings of a coil when pulsed converts a quantity of liquid helium into helium gas. The mass of gas boiled off is proportional to the quantity of heat dissipated. Thus if the volume of gas evolved can be measured at a known temperature and pressure, the rate of heat generation within the windings can be calculated. Since the quantity of heat generated in energy storage coils is of necessity small, this usually implies that the gas evolved during a number of charge/discharge cycles must be measured. It was possible to carry out this procedure when testing the 1 kJ model coil and the 7 kJ model coil because the electrical circuitry was designed for repetitive pulsing. However, because of limitations in the electrical circuitry of the 100 kJ coil system it was not possible to repetitively pulse it.

Unfortunately the helium evolved from the dewar is due not only to the heat generated in the coil but also to heat conduction down the neck of the dewar, down the support structure and down the leads. Furthermore, the heat conducted down the leads is a function of the current which is passing through the leads and the heat due to all sources other than the coil itself is a function of the liquid level in the dewar. If a metallic dewar is used then there are additional losses when the coil is being pulsed because of eddy currents induced in the walls of the helium container. The gas evolved due to these other sources provides a background boiloff which must be measured and subtracted from the total boiloff measured while pulsing the coil. The accuracy of this method depends to a large extent on whether the boiloff due to these extraneous sources can be accurately measured or estimated and obviously the smaller they are relative to the boiloff due to heat generation within the coil the better is the measurement.

Provided that the liquid level does not change appreciably during the course of a run, the static boiloff due to conduction from room temperature down the walls of the dewar, the current leads, and the support structure can be measured by monitoring the boiloff for a period of time before coil pulsing is started. However the effects of heat generation in the walls of the dewar due to eddy currents and heat generation in the current leads cannot be measured by this method. The first tests were carried out on the 1 kJ coil where the heat generation due to eddy currents in the dewar walls was much higher than the heat generation in the coil itself over the whole of the range of discharge times used. At the smallest discharge times (~ 0.2 ms) it was almost an order of magnitude greater. Clearly the boiloff due to eddy currents in the dewar walls had to be separated from the boiloff due to the coil. This was achieved by building a container around the coil and measuring only the boiloff coming from inside the container. This also helped to reduce the static boiloff. The boiloff due to the dewar walls and one current lead were completely excluded. However because of the high

voltages appearing across the coil terminals and space limitations it was not possible to remove the other current lead from inside the container. Therefore, there was a residual background boiloff due to one current lead and to the structure which was supporting the coil.

The boiloff gas was passed through a long tube (to allow it to warm up to room temperature) to an integrating gas meter. Volume readings were taken before, during and after a run that involved charging and discharging the coil a known number of times. The readings taken before gave a reference rate of background boiloff. Readings were taken after the run until the system had settled down to the same rate of background boiloff as was evident before the start of the run. The quantity of gas evolved due to background was estimated by taking the product of the background rate and the time from the start of the run to the time of the last reading. This was subtracted from the total quantity evolved to give the quantity evolved due to the losses in the coil. This procedure overestimates the coil loss by a quantity which depends on the additional boiloff due to passing current through the one current lead which is inside the container around the coil. However, in view of the experimental difficulties and limitations on the model used to predict the losses, there was reasonable agreement between the experiment and theory.

This method of measuring losses is both time consuming and costly because of the time taken to complete a run. In making measurements on the model coils a run lasted typically one hour. The electronic method described in the next section is to be preferred because since only one pulse is required a greater amount of data can be gathered in a given time and at lower cost because much less helium is consumed. It also has the potential of providing more information since from the shape of the hysteresis loop obtained conclusions can be drawn as to the mechanism of losses within the coil.

c. Electronic Method

To understand the electronic technique for measuring coil losses, it is perhaps simplest to begin by noting that the voltage appearing across the terminals of the coil consists of an inductive part, $L \frac{di}{dt}$, and a resistive part, Ri . The product of the inductive component of $\frac{dV}{dt}$ voltage and the current is the rate at which energy is being stored or removed from the magnetic field of the coil. The product of the resistive component of voltage and the current is the rate at which energy is being dissipated by whatever loss mechanisms are present. If the resistive loss is integrated over the time required for one charge-discharge cycle of the coil, the result must be the energy dissipated during that cycle, which is the desired quantity.

In practice it is helpful to remove the inductive component of voltage before performing the integration because it is 1,000 to 10,000 times larger than the resistive voltage and can be large enough to destroy electronic equipment. This task can be accomplished by producing a purely inductive voltage by means of a secondary winding on the coil or by means of a Rogowski coil around a current lead to the coil and subtracting it from an appropriate fraction of the voltage on the terminals of the coil. If the inductive component of the coil voltage is

nulled in this fashion, the remaining voltage is purely resistive. If this voltage is integrated and fed to the vertical input of an oscilloscope while a voltage proportional to the coil current is fed to the horizontal input of the oscilloscope, the result is a figure which bounds an area that is proportional to the energy dissipated in the coil during a cycle. A mathematical derivation of the theory of this technique is presented in Appendix II. It is proved rigorously that the area bounded by the figure on the oscilloscope is indeed proportional to the energy loss in the coil. A schematic of an appropriate experimental setup is given in Figure 78.

In order to perform a reliable loss measurement by using the technique discussed above, it is necessary to examine the specifications that must be met by the components of the basic electric circuit shown in Figure 78 in order to insure an accurate result. In the analysis of component errors presented in Appendix III, it is shown that the error in the loss loop measurement depends upon integrator drift and on the product of the uncancelled inductive voltage with the phase shift error of the integrator. It is necessary that both the equivalent drift voltage (input DC voltage that would produce the observed drift with an ideal integrator) and the product of the uncancelled inductive voltage with phase shift error of the integrator be small compared with the loss voltage which can, in some cases, be as small as one millivolt. It should be noted that it is also necessary to have an accurate current measurement which is free of phase shift errors.

Because the inductive voltage is typically 10^4 times larger than the loss voltage, it is necessary that the resistive divider pictured in Figure 78 have a resolution of at least one part in 10^4 in order to produce a useful loss loop. If it is assumed that the uncancelled inductive voltage is about the same magnitude as the loss voltage, then it is necessary that the phase shift error of the integrator be no greater than 10^{-2} radian in order to make the phase shift contribution to the measurement error negligible. This restriction on the phase error of the integrator requires that the operational amplifier contained in the integrator (Figure 79) have an upper frequency limit at least an order of magnitude (18) above the highest operating frequency contemplated for the experiment (about 2 kHz in our application), an open loop gain of at least 10^4 to allow an integration time (18) of 10 seconds with a time constant of 33 milliseconds and a maximum phase shift of 10^{-2} radians and have an input impedance large (18) compared to the input resistor of 330 k Ω (Figure 79). The performance requirements of the current shunt, the voltage divider, the integrator, and the overall circuitry layout are summarized in Table XXII.

The design of the current shunt, which is constrained by the requirements for low inductance and for resistance stability as a function of frequency and current is discussed in detail in Appendix IV. A schematic is given in Figure 80 and a summary of electrical characteristics is given in Table XXIII. From Table XXIII it is clear that this current shunt easily fulfills the requirements summarized in Table XXII.

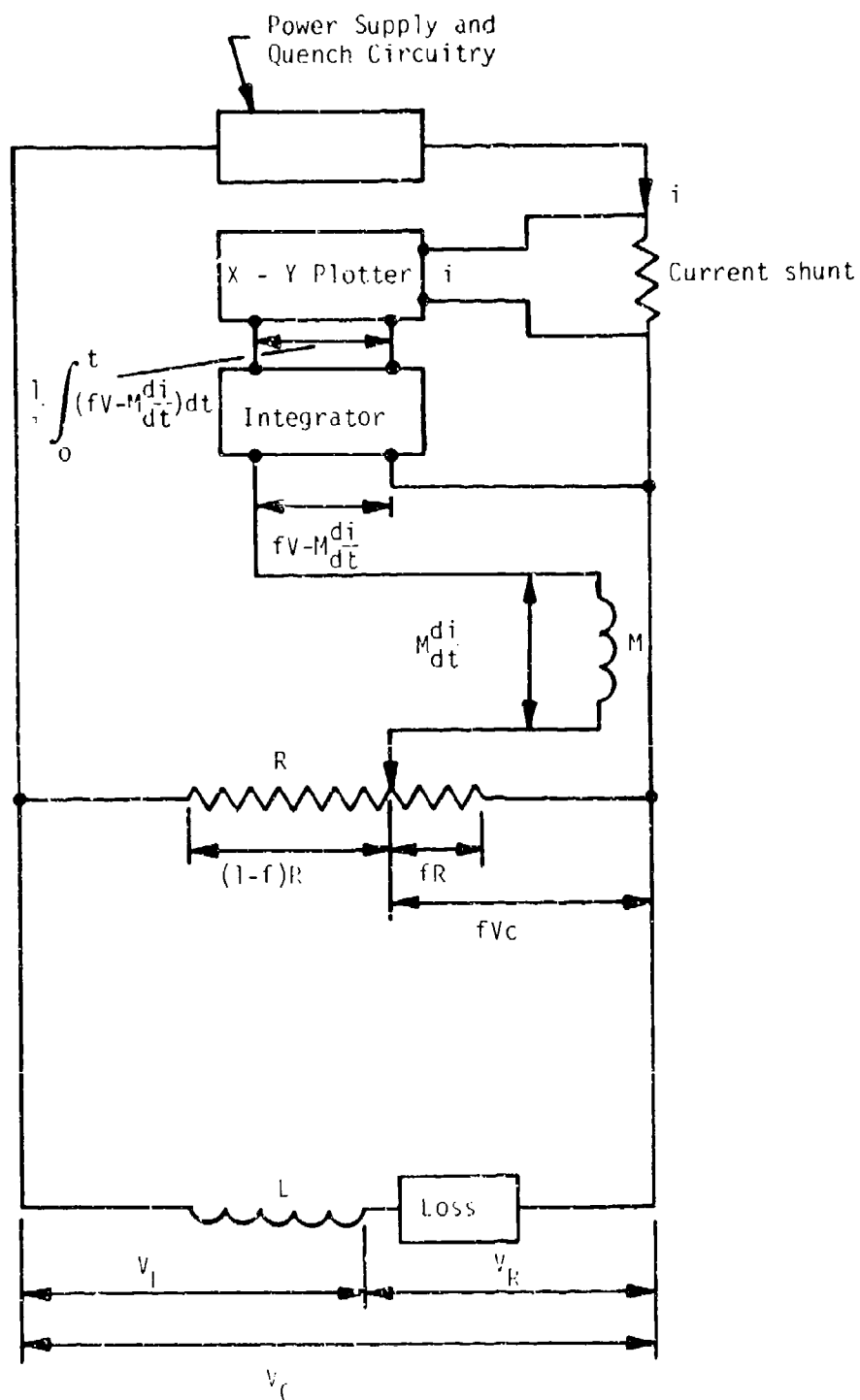


Figure 78 Schematic of Loss Measurement Device Circuit

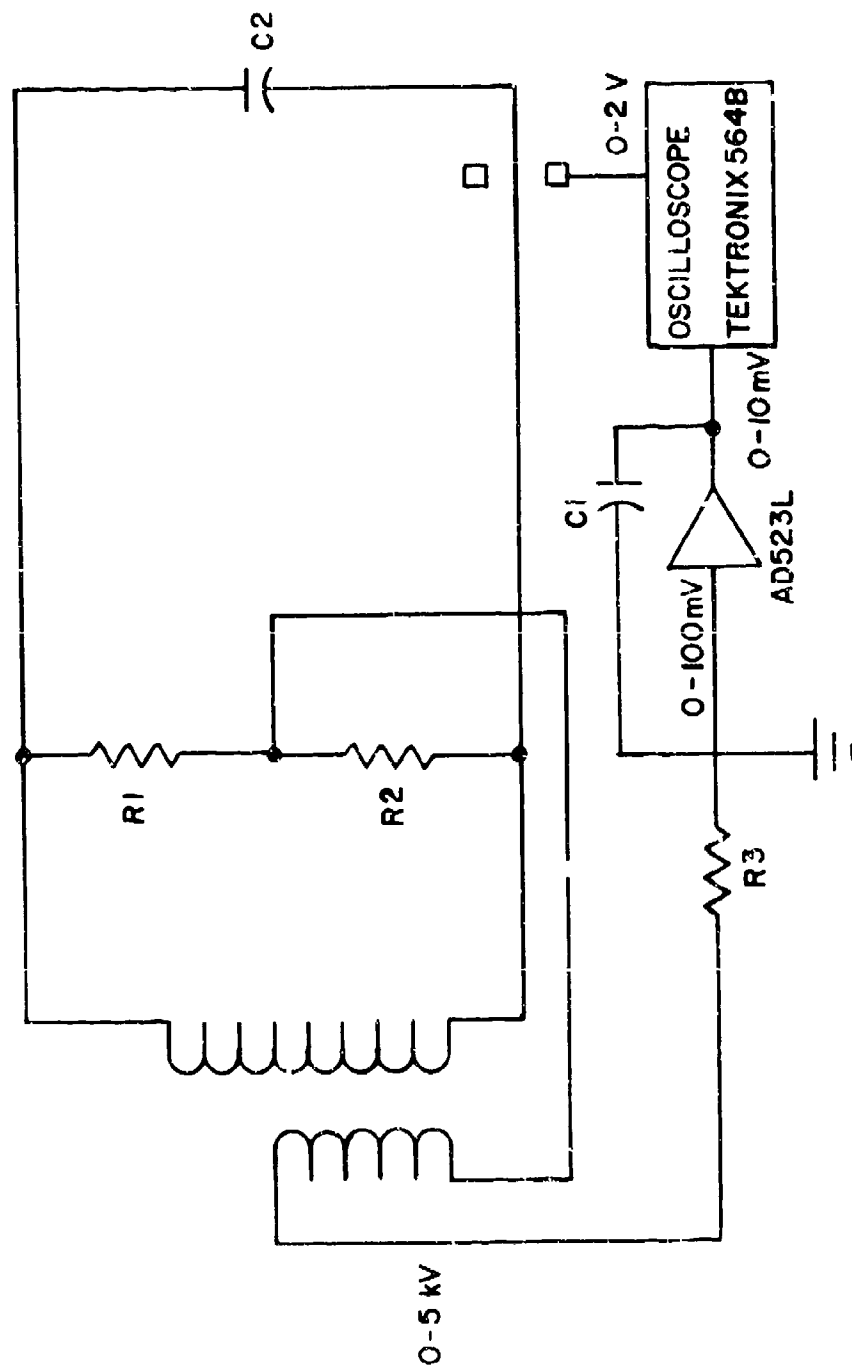


Figure 79 Block Diagram of Loss Measurement Circuit

Table XXII

COMPONENT REQUIREMENTS FOR ACCURATE LOSS MEASUREMENT

Current Shunt:

Must have phase shift of less than 10^{-2} radians up through 2 kHz. Resistance must be independent of current up to 2,000 amps (i.e., no significant heating).

Voltage Divider:

Must be able to stand up to 50 kV (pulsed) without arcing. Must have resolution of at least 1 part in 10^4 , 1 part in 10^5 preferred.

Integrator:

Must be protected against input voltage transients. Must have phase shift error of less than 10^{-2} radian for integration times from 10 seconds to .5 millisecond; this requires an open loop gain greater than 10^4 and a frequency response greater than 20 kHz (at least 100 kHz preferred). Must have equivalent DC input voltage (drift) no greater than a few tens of microvolts. Must have high input impedance.

Circuitry:

Isolation techniques selected must preclude any fraction of the voltage drop in the cables between the coil and the current shunt from entering the integrator.

Dimensions in inches

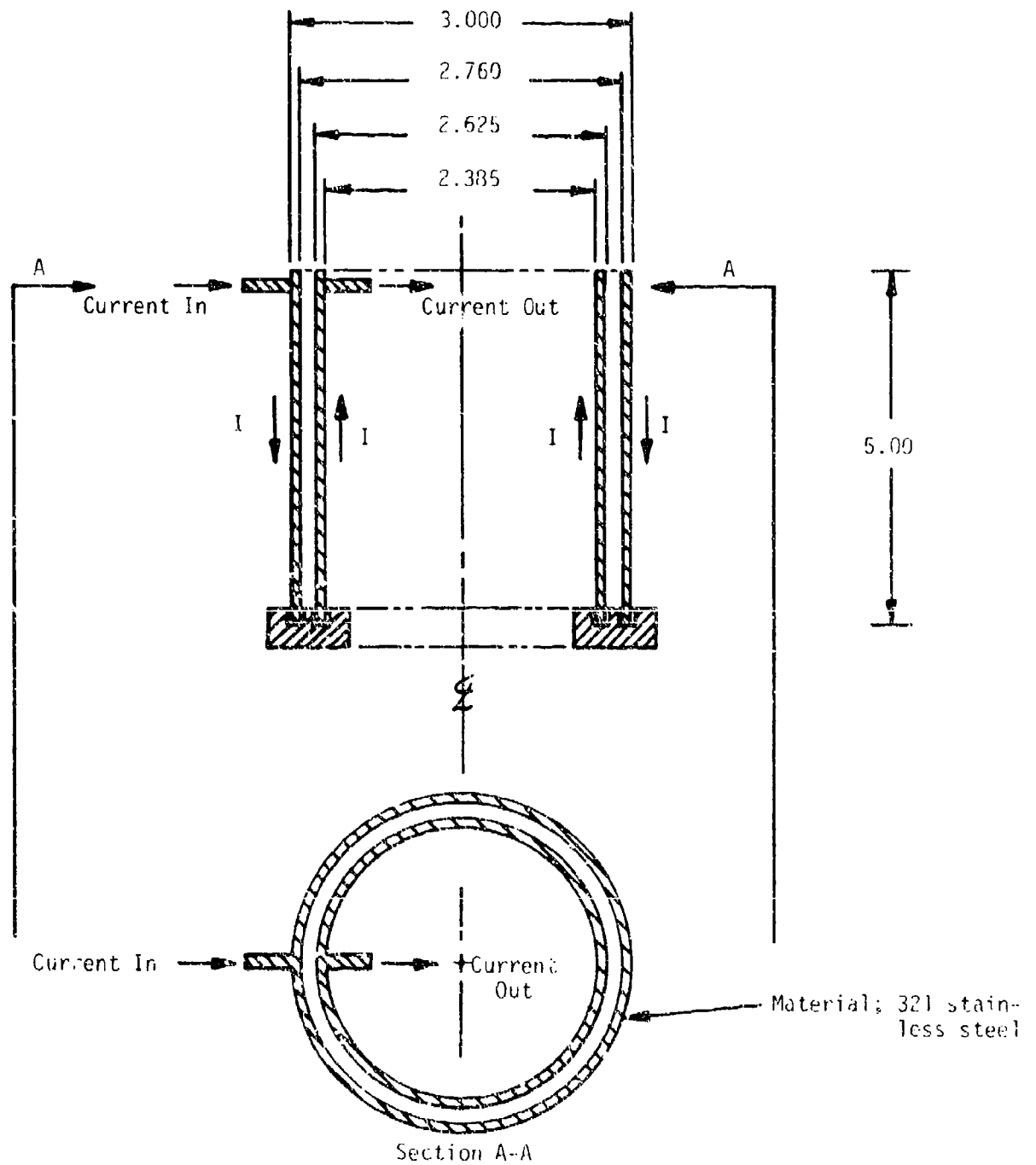


Figure 89 Schematic Illustrating Non-Inductive Current Shunt

Table XXIII
CURRENT SHUNT CHARACTERISTICS

Material:	321 stainless steel
Dimensions:	Inner cylinder - 2.625" OD, 0.120" wall Outer cylinder - 3.000" OD, 0.120" wall Length 5"
dc Resistance:	$R_{dc} = 0.28 \text{ m}\Omega$
dc Voltage:	$V_{dc} = 560 \text{ mV}$ at 2,000 A
Skin Depth:	$\delta = 0.78 \text{ inch}$ for 2 ms discharge $\delta = 0.25 \text{ inch}$ for 0.2 ms discharge
High Frequency Resistance:	$\frac{R_{hf}}{R_{dc}} - 1 = 5.1 \times 10^{-5}$ (0.0051%) for 0.2 ms discharge $\frac{R_{hf}}{R_{dc}} - 1 = 5.1 \times 10^{-3}$ (0.51%) for 0.2 ms discharge

<u>Inductance</u>	$\tau = 2 \text{ ms}, I = 2,000 \text{ A}$	
	<u>$V_{\text{inductive}}$</u>	$\frac{V_{\text{inductive}}}{V_{\text{resistive}}}$
Low Frequency ($\omega=0$) $L=3.09 \times 10^{-9} \text{ H}$	3.09 mV	0.70%
High Frequency ($\omega=\infty$) $L = 1.42 \times 10^{-9} \text{ H}$	1.42 mV	0.32%

(for comparison, if the cylinders were not coaxial then the inductance would be $92.4 \times 10^{-9} \text{ H}$ and $V_{\text{inductive}} = 92.4 \text{ mV}$ and $\frac{V_{\text{inductive}}}{V_{\text{resistive}}} = 21\%$)

Temperature Rise - $\Delta T = 18 \text{ K}$ and $\frac{\Delta R}{R} \approx 1.9\%$ for 20 s charge.

The design of the resistive divider, which is constrained by the requirements for high resolution, compatibility with the input impedance of the integrator, and resistance stability as a function of coil output voltage, is discussed in detail in Appendix V. A schematic of the version of this divider that was used with the 7 kJ coil is given in Figure 81. The overall divider resistance of 59,000 ohms was determined by a tradeoff between compatibility with the integrator and thermal stability; the selection of a large number of discrete components was dictated by the high voltage requirement as is explained in Appendix V. With this two-stage design, a maximum resolution of one part in 10^4 is available (one part in 10^2 from the resistor string and one part in 10^3 from the ten turn pot). It is clear that this fulfills the resolution requirements set forth in Table XXII.

The rather severe requirements that must be satisfied by the integrator in order to ensure an accurate loss measurement led to the selection of a circuit with the minimum number of components, as shown in Figure 82. Protection against high voltage transients, such as might occur during a quench (i.e., the coupling ratio between the storage coil and the sense coil might change thus disturbing the null of inductive voltage by a large amount), was accomplished by the use of a set of zener diodes as shown in Figure 82 (a). On examination of the entire instrumentation circuit (Figure 78) it is clear that the maximum current that can flow through the protection circuit is limited by the resistance of the voltage divider; for a 60 kV transient, the maximum current through the 59,000 ohm divider (Figure 81) is one amp, a level which is well within the capabilities of the components selected. It was determined by experiment (obtaining a loss loop with and without the protection circuit installed) that the insertion of these zener diodes did not introduce significant phase shift or amplitude errors into the integrator circuit. Resetting of the integrator was accomplished by means of a single pole, single throw mechanical (toggle) switch as shown in Figure 82(a). In order to minimize drift, polycarbonate capacitors were used, these are among the lowest leakage ($<10^{-10}$ amps) and most stable types commercially available. In addition, a two-stage design was selected for the amplifier balance circuit (Figure 82 (b)) which provides a resolution of at least one part in 10^5 . The input resistance of 330k ohms was the smallest value that could be used with the largest readily available polycarbonate capacitors (3 microfarads) to produce an integrating time constant of one second (the largest needed for our experiments). It is necessary that this input resistor be as small as possible in order to minimize the long-term drift of the integrator. The operational amplifier selected for this circuit has an open loop gain of 75,000 or more, an input impedance greater than 10^{11} ohms, a frequency limit of 500 kHz, low leakage currents, and moderate cost (Table XXIV). It was found that this integrator fulfilled the phase shift, frequency response, and gain requirements of Table XXII easily. It met the drift requirements (equivalent input voltage of about 30 microvolt,) provided that the balance circuit (Figure 82 (b)) was carefully adjusted for minimum drift every 15-20 minutes. This integrator provides adequate performance for making accurate loss loop measurements if used carefully.

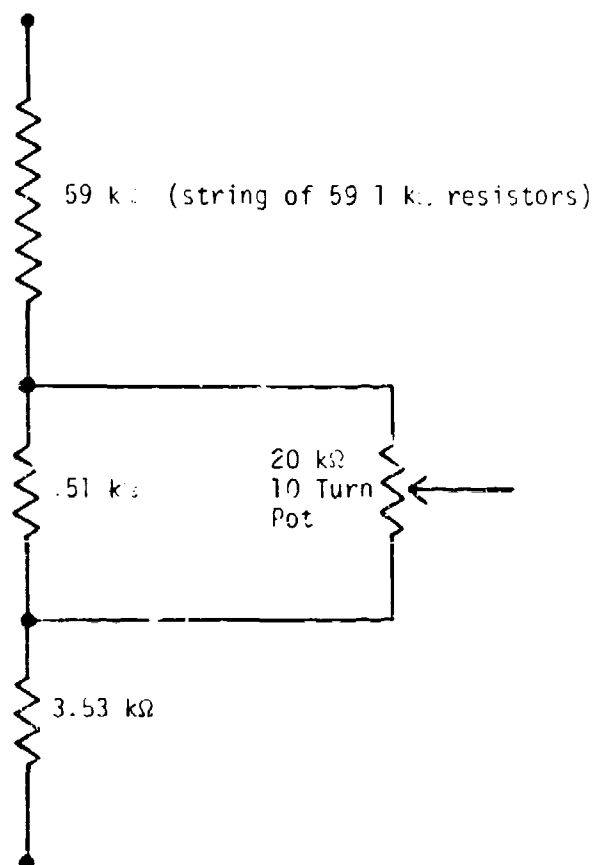


Figure 81 Voltage divider to provide accurate null of the inductive voltage. The voltage applied to the 10 turn pot is 1.5 percent of the total inductive voltage.

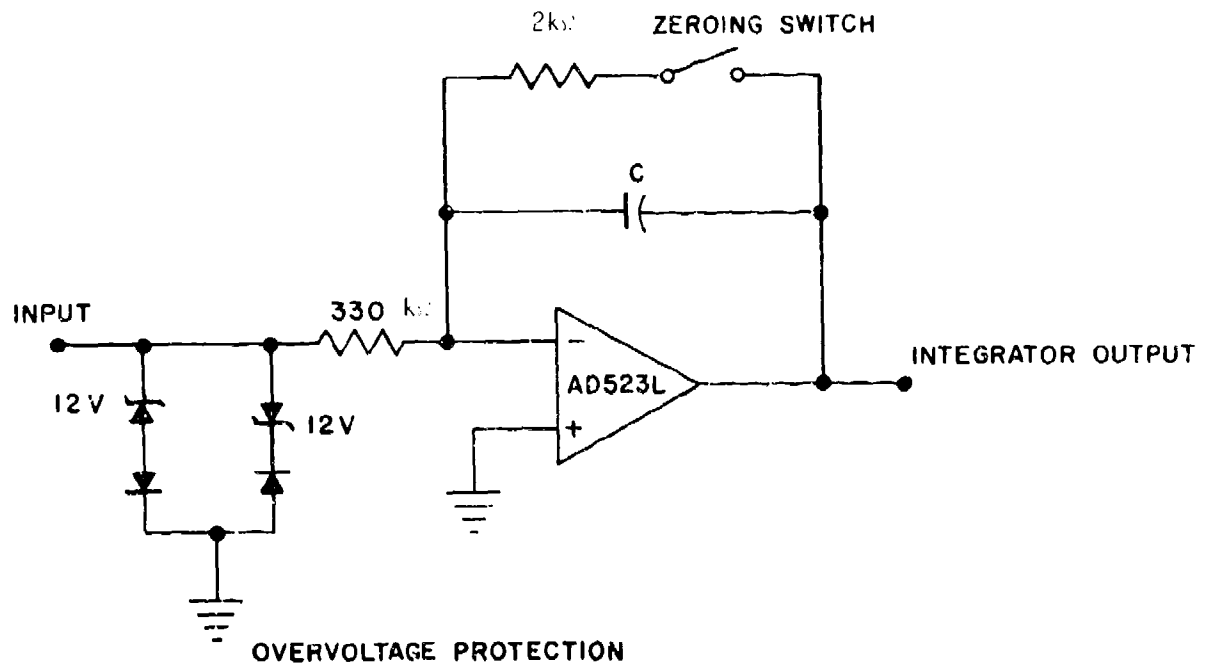


Figure 92(a) Final Version of Integrator Used for Loss Loop Measurements. Capacitor selected by 12 position switch; drift minimized by circuit shown below.

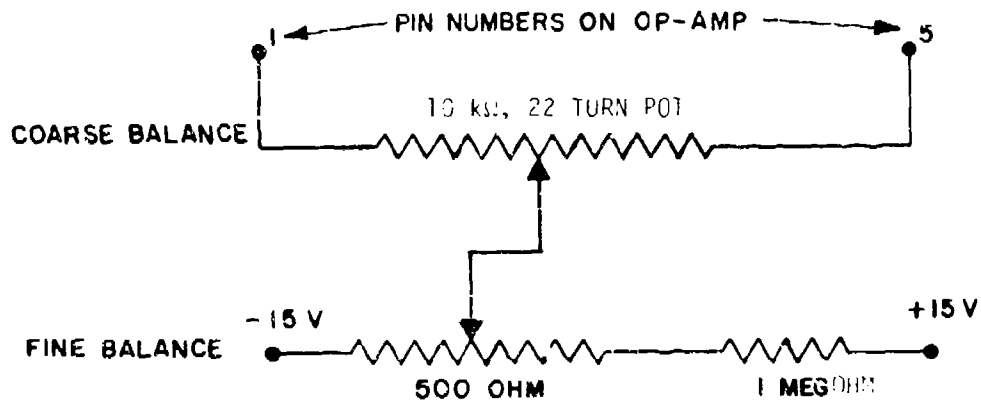


Figure 92(b) DC Balance Circuit Used with Integrator. Best balance available corresponds to DC input voltage (to integrator) of 30 microvolts.

OPERATIONAL AMPLIFIER USED IN INTEGRATOR FOR LOSS MEASUREMENT DEVICE

CENTRAL DESCRIPTION

The AD523J, AD523K, and 523L are internally compensated 11.1 input voltage operational amplifiers that feature self-compensating bias current, potentionance, low drift, high common mode rejection, and high gain. Maximum bias current is as low as 0.25 pA under a warmed up operating conditions are achieved by combining matched small geometry 11.1 chips with a specially designed monolithic chip within a low leakage 109-99 package. The package is manufactured with high resistivity glass insulation and a gold pin connected to the pin to minimize surface leakage currents, power supply induced input noise, and capacitive pickup. The AD523 is fully short circuit protected and offers voltage nullable, and offers maximum voltage drift of 3 μ V/°C, minimum CMRR of 80dB, and minimum gain of 40,000 V/V. The AD523J, K, and L are specified for operation over the 0°C to +70°C temperature range.

[illegible]

Parameter	AD521J	AD521K	AD521L
Open Loop Gain			
$V_{OS} = 0, R_F = 2k\Omega$	20,000 min (50,000 typ)	40,000 min (75,000 typ)	40,000 min (75,000 typ)
$\Delta I_A = 0$ to $+20^\circ\text{C}$	15,000 min	25,000 min	25,000 min
Output Characteristics			
Voltage $R_F = 2k\Omega, I_A = 0$ to $+20^\circ\text{C}$	$\pm 10\text{V max}, \pm 12\text{V typ}$	•	•
Current $I_A = 0$ to $+20^\circ\text{C}$	$\pm 5\text{mA max}$	•	•
Load Capacitance	1,000pF	•	•
Short Circuit Current	25mA	•	•
Frequency Response			
Unity Gain Small Signal	50kHz	•	•
Full Power Response	50kHz	•	•
Slew Rate, Unity Gain	3V μs^{-1} min (5V μs^{-1} typ)	•	•
Input Offset Voltage			
Initial	500V $\mu\text{V max}$ (250V $\mu\text{V typ}$)	200V $\mu\text{V max}$ (100V $\mu\text{V typ}$)	200V $\mu\text{V max}$ (100V $\mu\text{V typ}$)
vs. Temp $I_A = 0$ to $+20^\circ\text{C}$	500V $\mu\text{V max}$ (250V $\mu\text{V typ}$)	300V $\mu\text{V max}$ (150V $\mu\text{V typ}$)	600V $\mu\text{V max}$ (250V $\mu\text{V typ}$)
vs. Supply	200V $\mu\text{V max}$	100V $\mu\text{V max}$	100V $\mu\text{V max}$
Input Bias Current			
Initial, each input $V_{OS} = 50\text{mV max}$	10pA max (0.1pA typ)	5pA max (0.2pA typ)	0.25pA max (0.1pA typ)
vs. Temp, Initial	10pA typ	•	•
vs. Supply, Initial	10pA typ	•	•
Input Noise			
$V_{OS} = 0$ to $+20^\circ\text{C}$	200V $\mu\text{V p-p}$	•	•
vs. Supply	150V $\mu\text{V p-p}$	•	•
Input Voltage Range			
Input Voltage, max V_{OS}	$\pm 10\text{V}$	•	•
Common Mode Rejection, $V_{OS} = 0$			
$I_A = 0$ to $+20^\circ\text{C}$	$\pm 48\text{mV max}$ (800Hz f_{in})	0 to $\pm 0.1\text{mV max}$	$\pm 0.1\text{mV max}$ (900Hz f_{in})
Power Supplies			
$R_F = 2k\Omega$ Full Scale	$\pm 15\text{V}$	•	•
vs. Temp	$\pm 15\text{V max}$	•	•
Current, quiescent	10mA max (typical)	•	•
Full Scale, range			
vs. Temp, range	$\pm 5\text{V max}$	•	•
vs. Temp	$\pm 5\text{V max}$	•	•
Linearity, $V_{OS} = 0$			
0.5% max	5,000	5,000	5,000
0.1% max	20,000	20,000	20,000
0.01% max	100,000	100,000	100,000
Temperature Coefficient, $V_{OS} = 0$			
0.5% max	5,000	5,000	5,000
0.1% max	20,000	20,000	20,000
0.01% max	100,000	100,000	100,000

The final set of considerations that affect the loss measurement is the physical arrangement of circuit elements. It is essential that the voltage entering the integrator contain only the resistive component from the coil. In view of this requirement, the voltage across the coil is picked off by a pair of wires attached directly to the coil (down at the bottom of the dewar); the point of this is to avoid the measurement of any portion of the power loss in the non-superconducting leads attached to the coil. For similar reasons, it is necessary to isolate the current shunt by means of a differential amplifier with very high common mode rejection ratio, or by some equivalent technique, in order to avoid picking up a significant fraction of the voltage drop on the power lead between the coil and the shunt (Figure 72). The DC voltage drop across this length of 3/0 cable is one volt for a current of 1,000 amps. The situation is even more difficult during a rapid discharge because of the inductance (4 microhenries) of this cable: for a discharge time of one millisecond with a current of 1,000 amps, the voltage drop is 4 volts. Because the error voltage can be as small as one millivolt, it is important to avoid picking up even 0.1 percent of this cable voltage. This could happen, for example, if the cables from the two sides of the shunt to the differential amplifier (as in Figure 83) were each terminated by 50 ohm resistors (to minimize noise) and the resistance of the electrical lead from the oscilloscope to the ground point in the figure were about .025 ohms. For similar reasons, i.e., the great sensitivity of this measurement to small error voltages, the oscilloscope and the integrator were both operated from isolation transformers and great care was taken to avoid ground loops; the system ground was taken to be the case of the high voltage power supply used to charge the arc quench capacitor.

5. LOSS MEASUREMENTS MADE USING THE 1 kJ COIL

Loss measurements were made by the boiloff method only on the 1 kJ coil made from single core superconducting wire. The coil was charged and discharged repetitively at a rate of 1 pulse/second into a resistive load. The charge time was 155 ms, and the discharge time constant ranged from 4.5 ms to 0.21 ms. The maximum voltage on discharge at the smallest value of the time constant was approximately 14 kV. Figures 64, 65 and 66 show oscilloscope traces of the current and voltage waveforms. Figures 64 and 65 show the current during charge (single and multiple pulse respectively) and Figure 66 shows the voltage during discharge. The magnet showed no sign of quenching even when charged to currents very near to the critical current. The maximum current reached in the series of tests was 425 A, the critical current being 430 A.

Loss measurements were made using the technique described in Section III-4-b, Helium Boiloff Method. The first series of measurements were made without a shroud around the coil. Consequently, the boiloff measured was due to a number of components, e.g., static dewar loss and lead loss, losses due to the coil, and losses due to eddy current heating in the dewar walls. An experiment was performed to determine the static loss and lead loss by measuring the boiloff with different levels of helium in the dewar and different steady currents in the leads. The range of steady currents was chosen so that it would correspond to the range of rms values of the currents expected in

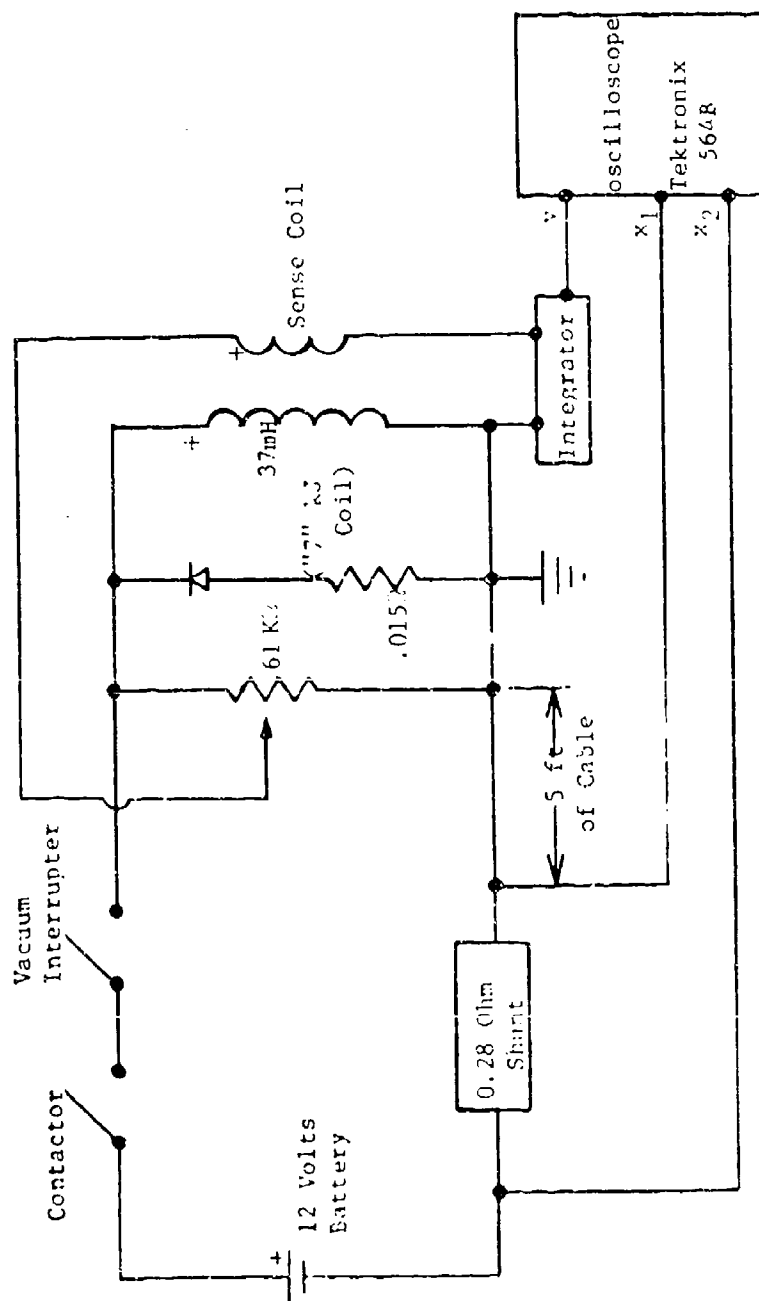


Figure 83 Schematic of low speed experiment for loss loop measurements. Current shunt is attached to differential input amplifier on the oscilloscope.

the pulsed coil tests. However, at those currents it happened that the additional boiloff due to ohmic losses in the leads was small and the static boiloff predominated.

The coil was tested in a metallic dewar with no provisions made to separate the helium boiloff due to losses in the coil from those losses due to eddy currents in the dewar walls. The total measured losses proved to be much higher than the predicted coil losses when the coil was discharged rapidly, even when the background static boiloff was subtracted out.

This was assumed to be because of the losses due to eddy currents in the dewar walls. An analysis was conducted to estimate the magnitude of the eddy current losses in the dewar walls. This is described in detail in Appendix VI, Losses in Conducting Dewar Walls, of technical report AFAPL-TR-72-38, Vol. I. The results indicated that at the shorter discharge times at which the coil was operated these losses would indeed be much greater than the losses due to the coil.

A container was therefore built around the coil to separate the losses due to the dewar from those due to the coil and the coil was again tested over the same range of operation conditions. The container was filled by opening a valve connecting the liquid helium storage volume of the dewar with the volume inside the container surrounding the test coil. This valve was closed prior to taking loss measurements. Under these conditions, only the helium boiloff from the container was measured. The helium boiled off by the eddy current heating in the dewar walls was released directly to the atmosphere. In all experiments, the coil was charged in a time compatible with a pulse repetition rate of five per second, i.e., between 130 ms and 160 ms. In this series of tests the measured losses more nearly coincided with the losses predicted for the coil.

The accuracy of the analysis concerning the losses due to eddy currents in the dewar walls was checked by comparing the predicted and measured eddy current losses. The measured losses were obtained by subtracting the losses due to the coil (as measured in the second series of runs) from the total losses (as measured in the first series of runs). This comparison is shown in Figure 84. It can be seen that there is excellent agreement at the larger discharge times but that the measured losses are smaller than the predicted losses at the shorter discharge times. This can be explained by the following reasoning. The model used for predicting the losses in the dewar walls assumes that the flux fully penetrates the dewar walls so that heat is generated throughout the whole volume of the walls. This is true only over a certain range of rate of change of field since the flux will in fact penetrate only as far as the skin depth. When the skin depth is greater than the wall thickness, the whole of the volume of the walls is available for heat generation but when the skin depth is less than the wall thickness heat is generated only in a volume determined by the skin depth. The skin depth decreases with increasing frequency (decreasing discharge time) and so the model used can be expected to overestimate the losses at shorter discharge times. This is what is observed.

A third series of loss measurements were made this time at a pulse repetition rate of 5 per second. These measurements which were made over a similar range of discharge times agreed well with the measurements made at a

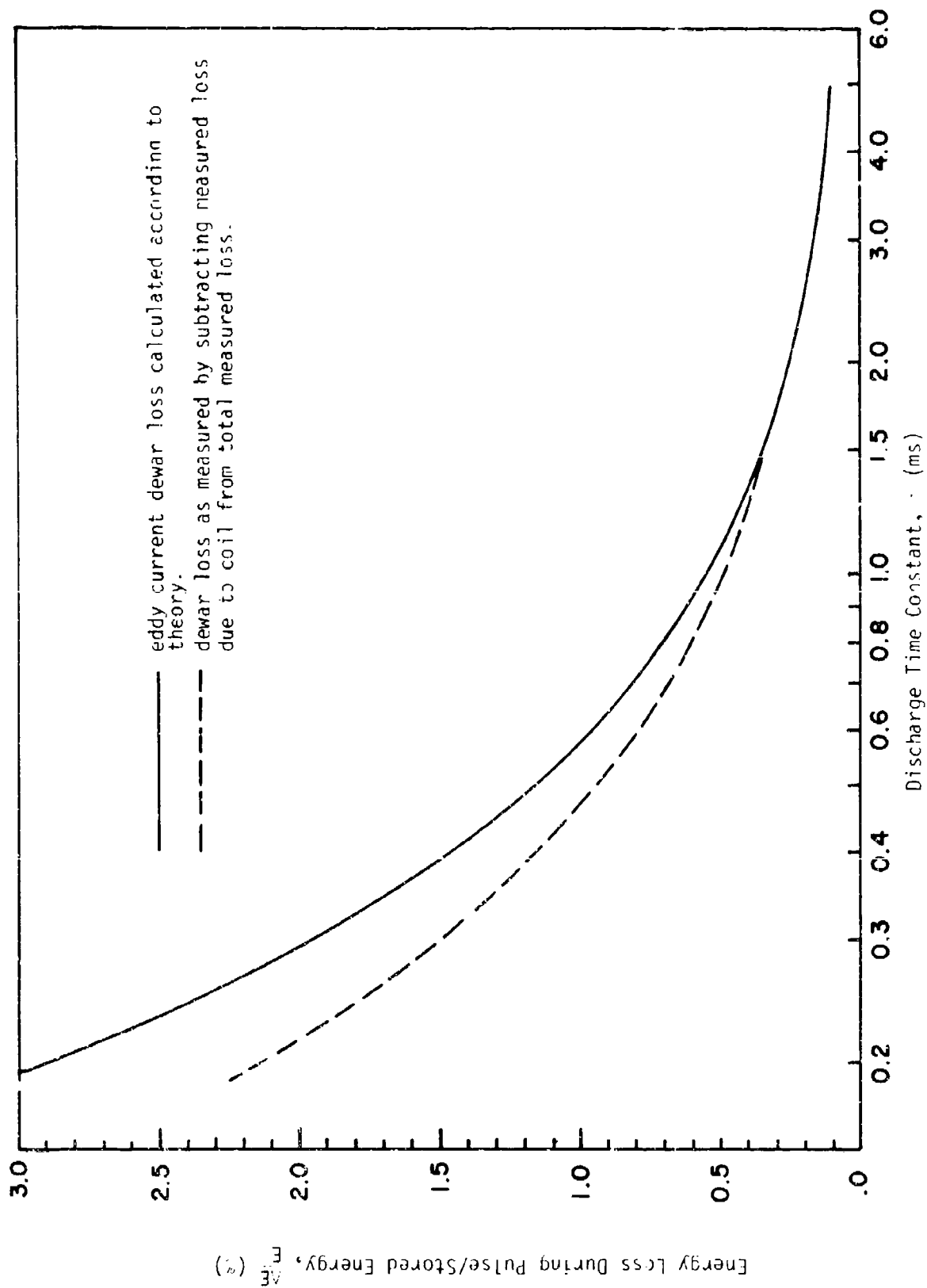


Figure 84: Comparison of Dewar Eddy Current Loss Calculated by Theory and Measured Dewar Loss.

repetition rate of 1 pulse per second. Figures 67, 68 and 69 are oscilloscope traces taken during this series of experiments. Figure 67 shows the detail of the current during charge; Figure 68 shows the current during charge of a long pulse train; and Figure 69 shows a detail of the voltage across the coil during discharge.

Figure 85 shows the measured losses as a function of discharge time constant and the theoretical losses as predicted according to various models. The significance of the various theoretical models is explained in Section III-3, Theory of Losses in Pulsed Coils.

It can be seen that the losses are comparable with or less than the losses predicted according to any of the models shown in the figure. However the trend of the experimental curve as a function of discharge times does not correspond with any of the models. The explanation offered for this is as follows. At the longer discharge times (1 ms to 4 ms) the slope of the experimental curve is such that it follows the slope of the model where it is assumed that the conductor having fields in the range 0.9 to 1.0 of the peak field goes normal during discharge. In this range of discharge times according to the theory derived the dominant losses are the magnetization loss and the transport current loss; the eddy current loss is insignificant. A better fit in this range would result from a reduction in the theoretical magnetization losses. It was indicated in Section III-3, Theory of Losses in Pulsed Coils, that the model used for magnetization losses overestimated them because: complete penetration of flux into the superconductor was assumed whereas in fact at the beginning of the charge period all of the coil is at low fields; and parts of the coil are always at low fields. At low fields only partial penetration exists. Furthermore, the model assumes that the critical current density in the conductor is the critical current density at 4.2 K. This is likely to be true during charge because the coil comes into a steady state situation whereby the heat generated within the windings is dissipated in the helium bath at a low temperature difference between the coolant and the coil. However, on discharge the heat is generated so quickly that it is more realistic to assume adiabatic heating. Thus, some parts of the coil go normal and the temperature of other parts rises an appreciable amount above 4.2 K. Thus the critical current density is lower over certain regions of the coil. This effect too tends to reduce the losses below those predicted by the theory used.

At discharge times of less than about 1 ms the theory predicts that losses due to eddy currents become significant. It is because of the eddy currents that the theoretical curves turn up at low discharge times. The experimental curve however shows no indication of turning up even down to the lowest discharge times used. This indicates that the model used to predict eddy currents in the matrix overestimates them. As was indicated in Section III-3, Theory of Losses in Pulsed Coils, this may be due to the fact that the model does not take account of skin depth effects. Neglecting the skin depth will have the effect of overestimating eddy current losses since the model assumes that full penetration of the matrix exists.

If it is assumed that eddy currents are insignificant even down to the lowest discharge times used, then the theoretical curves can be redrawn. Figure 86 shows the same experimental data presented in Figure 85 together with two new theoretical curves. Both curves assume that the coil is

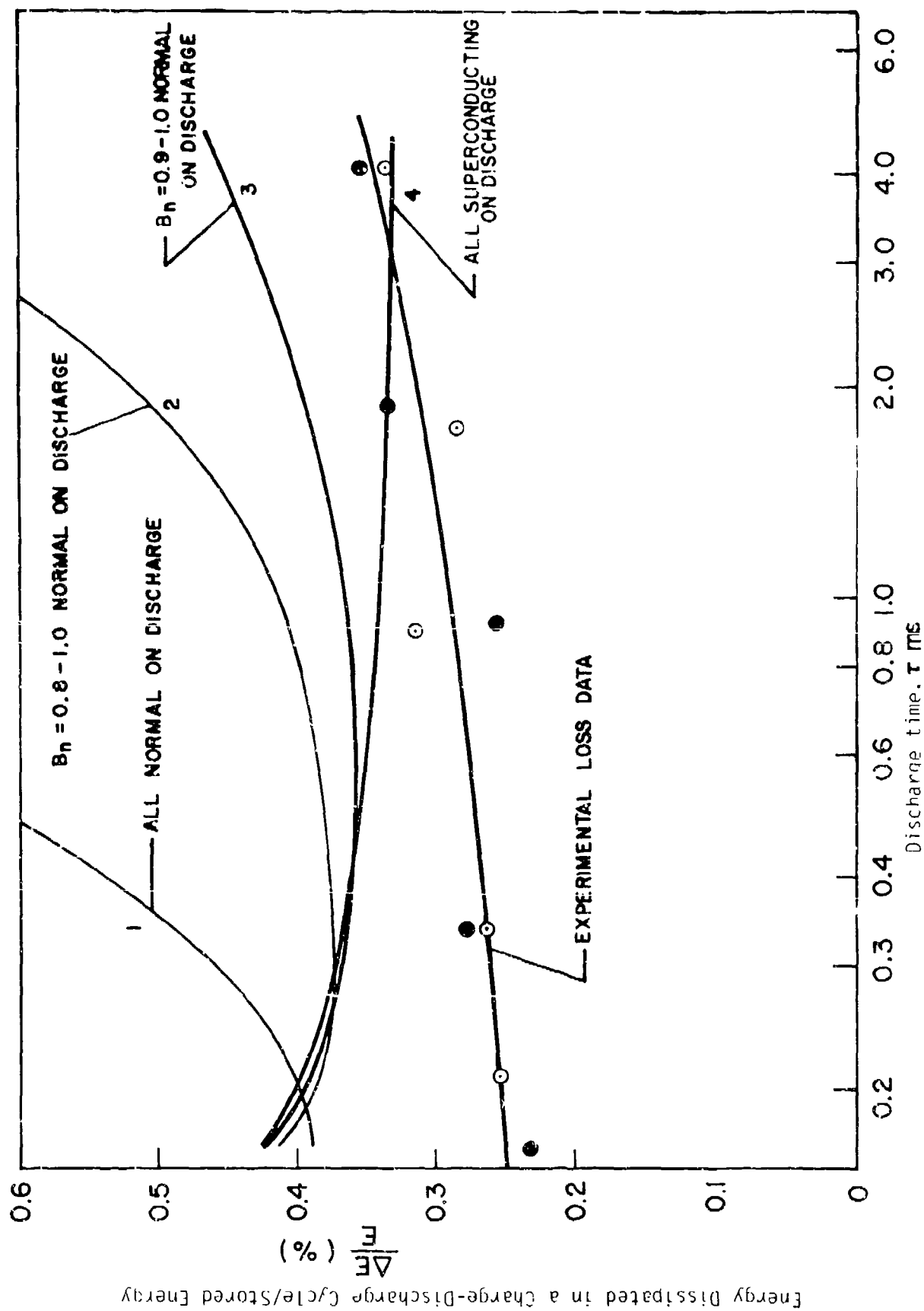


Figure 85 Comparison of Losses Predicted by the Revised Loss Formulae with the Experimental Losses Found Using the 1 Kilojoule Coil.

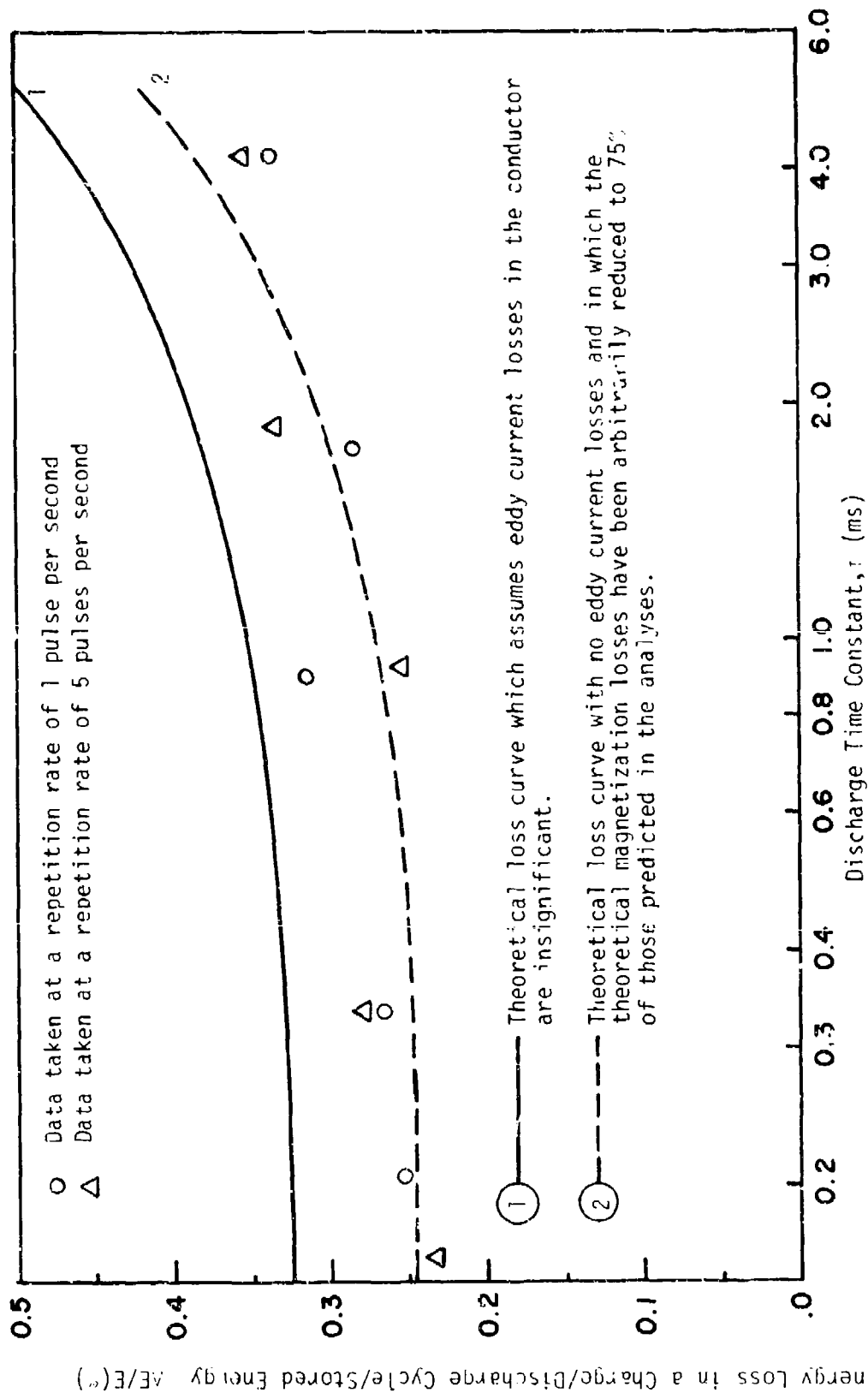


Figure 86: Energy Dissipated in the 1 kJ Coil in a Charge/Discharge Cycle v Discharge Time Constant. Both curves are for the situation where the whole of the coil is superconducting on charge and where the conductor in the region having fields in the range 0.2 to 1.0 of the peak field is normal during discharge.

completely superconducting on charge and that the conductor in the region which experiences fields between 0.9 and 1.0 of the peak field goes normal at the beginning of the discharge and remains normal throughout the discharge. Both curves also assume that eddy currents are insignificant. Curve 1 assumes magnetization losses in the superconductor as predicted by the theory derived. It can be seen that now the trend of the theoretical curve follows the trend of the data points. Curve 2 arbitrarily reduces the magnitude of the magnetization losses to 75% of those predicted by the theory. It can be seen that curve 2 is now a reasonable fit to the data points. Because of the large scatter in the data points it was felt that it would not be useful to be more sophisticated in adjusting the model.

In conclusion, it can be said that within the limitations of the model there is reasonable agreement between theory and experiment and that some additional theoretical analyses should be conducted to obtain closer agreement. The results of the experiment suggest that, contrary to the theory developed, eddy current losses are negligible and that the theory overestimates the magnetization loss by 20% or 30%. It appears, as was predicted, that the coil remains completely superconducting during charge but that during discharge some superconductor in the higher field region goes normal.

6. LOSS MEASUREMENTS MADE USING THE 7 KJ COIL

a. Introduction

The purpose of this (the second) series of tests with the 7 kJ coil was to demonstrate the validity of the electronic loss loop measurement by means of a comparison with the previous boiloff measurements. The boiloff measurements are described in Section III-6-b, Boiloff Measurements, below. A sense coil was added to the 7 kJ coil as shown in Figure 87 to be used in loss measurement as indicated in Figure 78 and as discussed in Appendix II; the voltage coupling ratio between the 7 kJ coil and the sense coil is about 0.06. The primary obstacle to the performance of an accurate electronic loss measurement on the 7 kJ coil was the presense of the metallic dewar which, in most operating regions, behaved like a shorted single turn secondary winding of a transformer. In addition, the dewar wall acted like a magnetic shield, causing the self inductances of the 7 kJ coil and of the sense coil (and hence their mutual inductance) to vary with frequency. Unfortunately, the electronic measurement technique records both the coil losses and the energy absorbed by the dewar. Consequently, Section III-6-c, Inductive Effects of the Metallic Dewar with Respect to the Electronic Method, and Section III-6-d, Energy Losses in the Metallic Dewar, below are concerned with identifying an operating regime in which the dewar effects (resistive and inductive) are small compared to the losses in the coil. A suitable regime was found and the desired measurements were accomplished (Section III-6-e, Electronic Loss Measurements on the 7 kJ Coil, below). The losses measured electronically were found to be in good agreement with the previously obtained boiloff data.

b. Boiloff Measurements

Measurements of losses by boiloff were made in a similar way to those made on the 1 kJ coil, a similar container being constructed around the

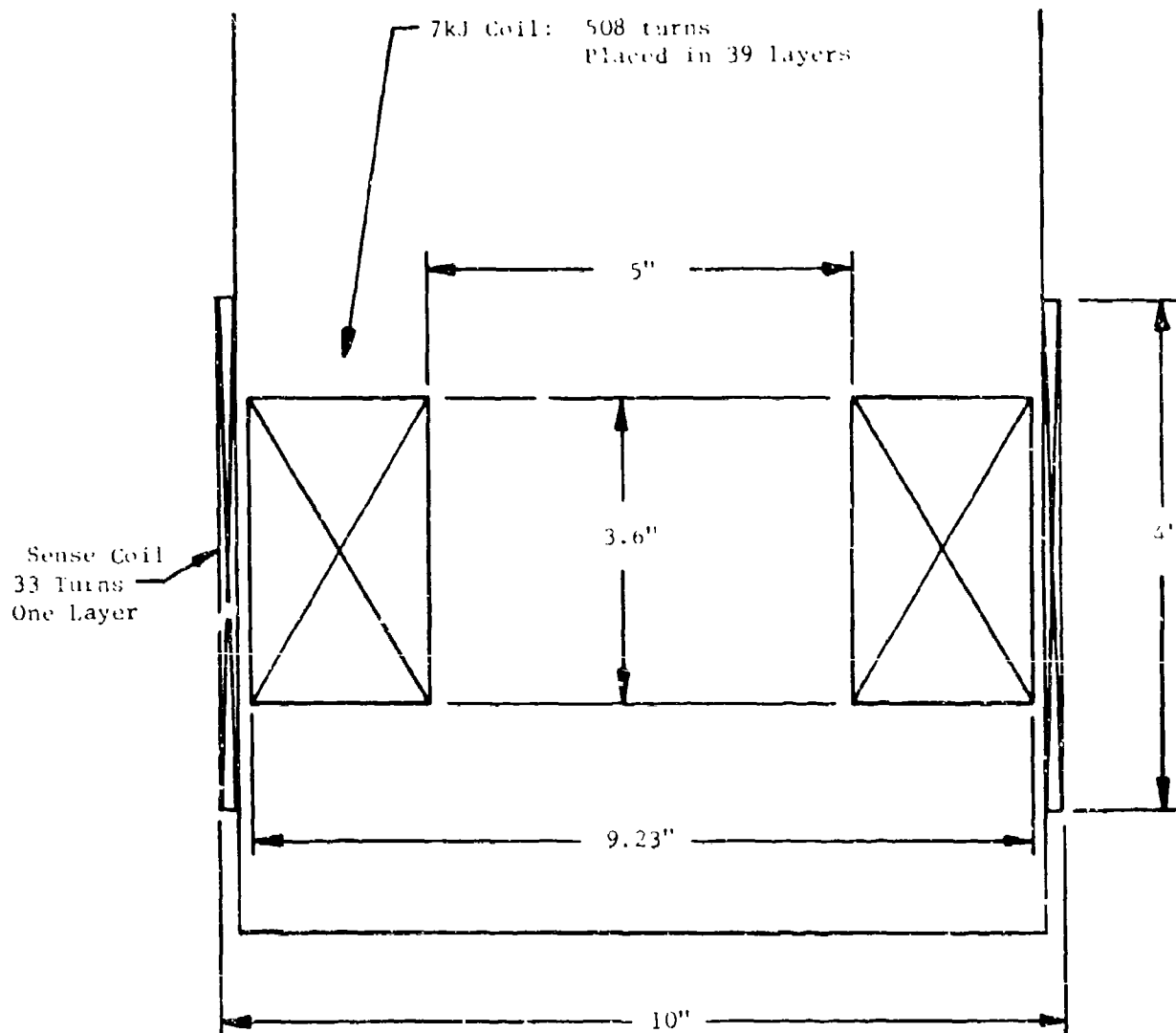


Figure 87 Sketch of 7kJ coil with sense coil added.

7 kJ coil to separate coil losses from losses due to other sources. The results of these measurements are given in Figure 88 together with the predicted losses according to the two extreme theoretical models previously described. As for the 1 kJ coil, for the most part the measured losses tend to agree with a model in which the coil is superconducting during charge and partially normal during discharge. However, the scatter in the experimental data is greater and interpretation is more difficult. It can be seen that there are two very high data points which coincide more than anything with a model according to which the whole of the coil is normal during discharge. It is difficult to believe that this is the case. The only suggestion which can be made is that perhaps these points were taken when part of the coil was above the level of the liquid helium in which case it is possible that part of the coil was normal for part of the charge period. However, it is of course impossible now to confirm this hypothesis.

c. Inductive Effects of the Metallic Dewar with Respect to the Electronic Method

The first problem considered was magnetic shielding by the dewar. In a frequency range where this occurs, the inductance of the storage coil, of the sense coil, and their mutual inductance are all functions of frequency. Figure 89(a) shows the circuit used for measuring inductances at low power levels and Figure 89(b) shows the experimental arrangement for inductance measurements at higher power levels. Figures 90, 91 and 92 show the self inductance of the 7 kJ coil, of the sense coil, and their mutual inductance, as a function of frequency at room temperature both inside and outside the dewar. The measurements were made both at low power levels (using a function generator) and at high power levels (using capacitors charged as high as 20 kV and a spark gap or the vacuum interrupter) in order to check for experimental errors. The technique used is described in Section III-6-d, Energy Losses in the Metallic Dewar. All of these curves show that the dewar causes a significant change in the measurements at frequencies above 10 to 30 Hertz. The apparent increase in mutual inductance (Figure 91) at high frequencies is really caused by capacitive coupling; the frequency at which the capacitive coupling becomes significant is an upper limit to the range in which this sense coil will be useful for making a loss measurement. The inductive effects of the dewar should be more pronounced at lower temperatures because the resistivity of the stainless steel dewar wall will decrease (approximately a factor of three) thus leading to better shielding at a given frequency. Figures 93, 94 and 95 show the results of the corresponding inductance measurements (corresponding to Figures 90, 91 and 92, respectively) at liquid nitrogen temperature (77 K). A plastic dewar was especially constructed for these measurements. As can be seen from the curves, the various inductances are smaller at a given frequency than they were at room temperature. The final set of measurements, Figures 96, 97 and 98 was made at liquid helium temperature in the metallic dewar (there was not a non-metallic dewar of a convenient size available). An examination of all these curves (Figures 90 through 98) indicates that any useful loss measurements must be made at frequencies of less than 10 Hertz in order to avoid changes in coupling to the sense coil caused by the metallic dewar that would disturb the measurement (Appendix II).

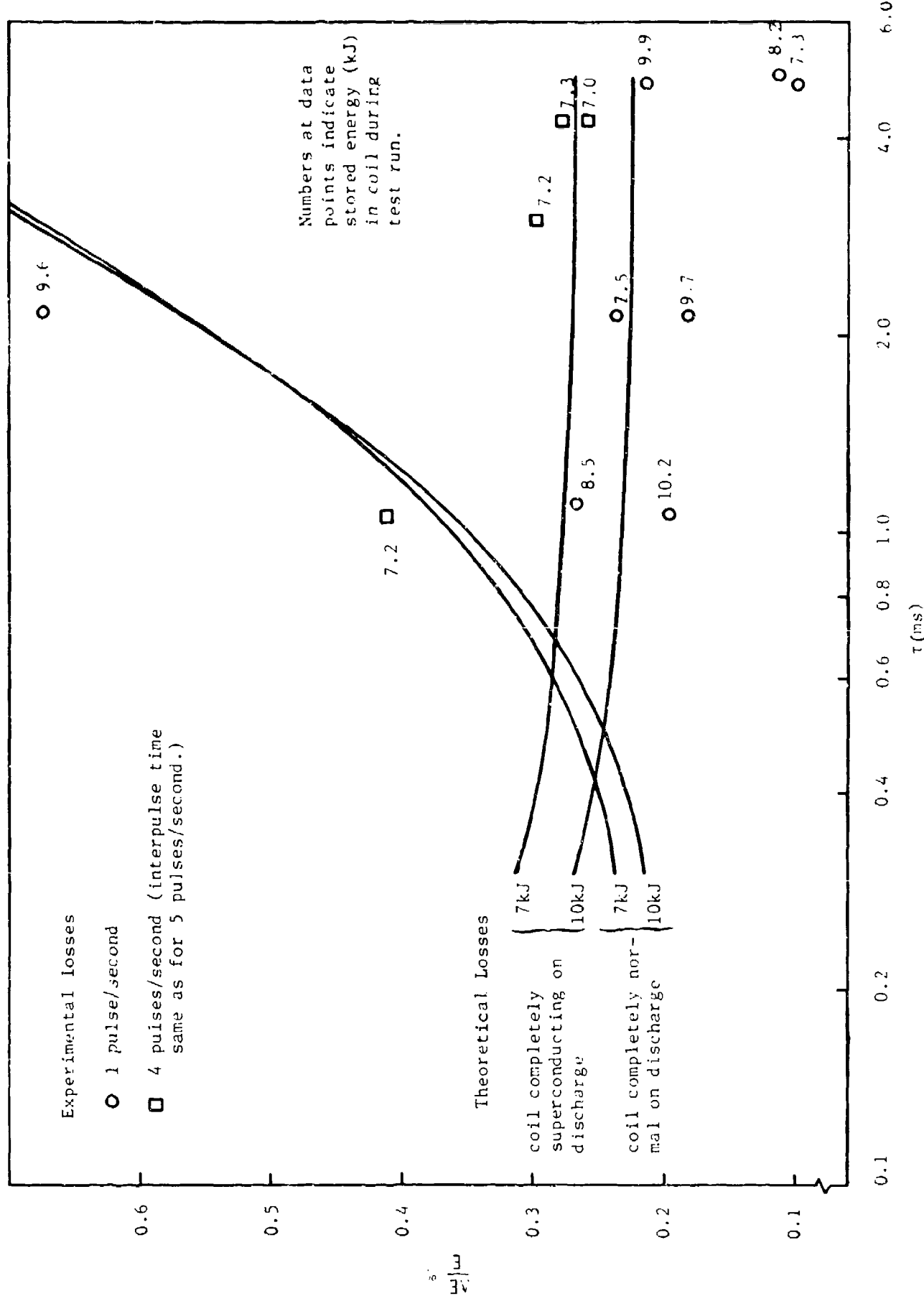


Figure 88 Comparison of Experimental and Theoretical Energy Losses for 7 kJ Model Coil

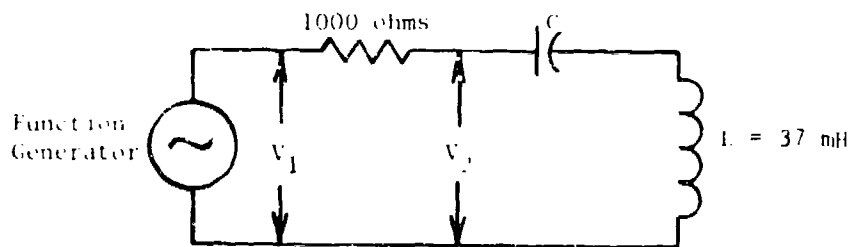


Figure 89(a) Schematic for series resonance experiment. Resistance is given by: $R = 1000 V_2 / (V_1 - V_2)$ where V_1 and V_2 are measured at resonance.

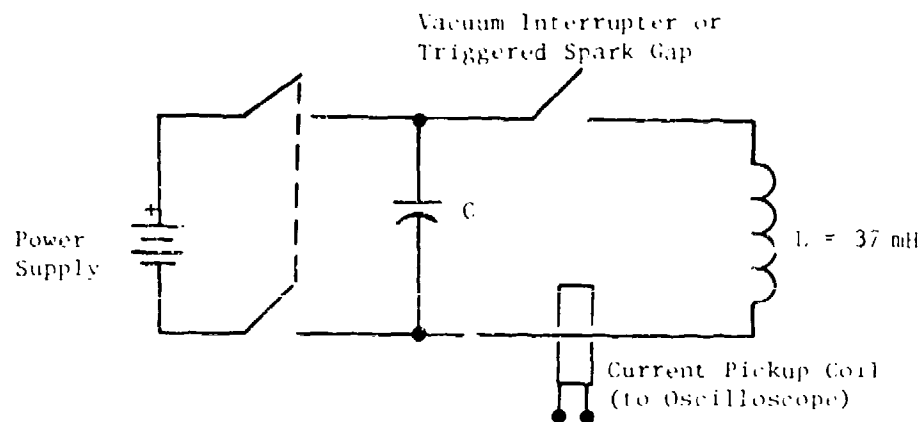


Figure 89(b) Schematic for ringing experiment.

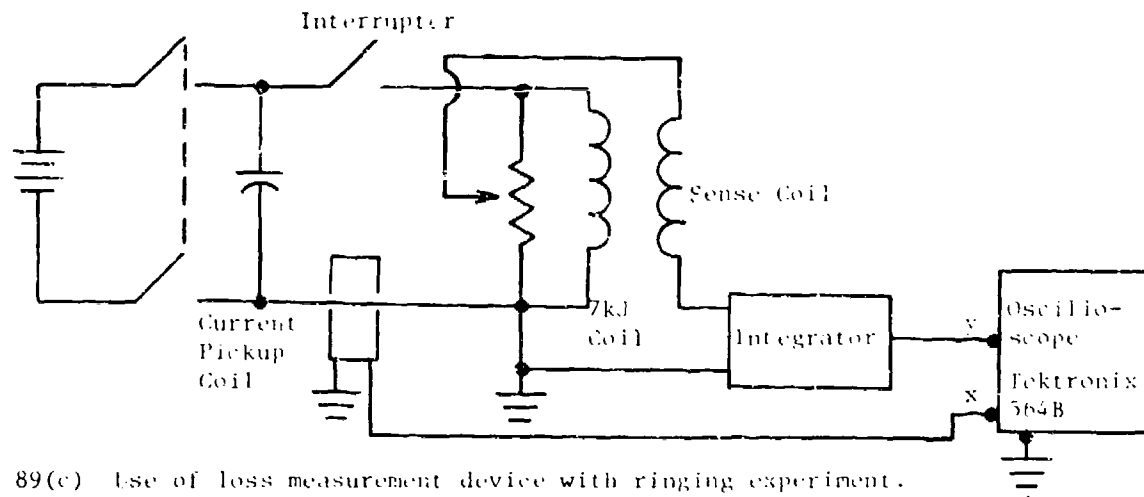


Figure 89(c) Use of loss measurement device with ringing experiment.

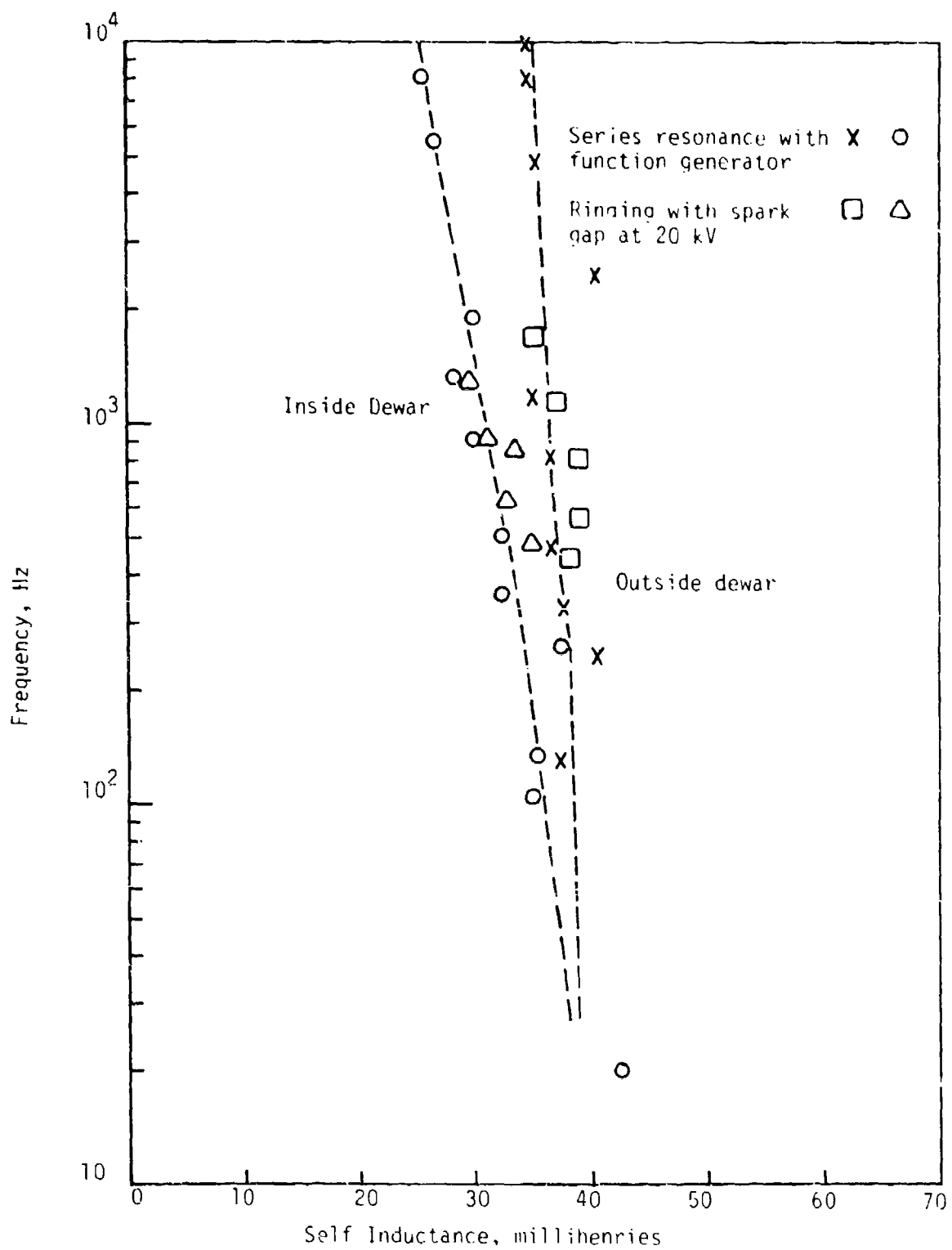


Figure 90: Self Inductance of 7 kJ Coil at Room Temperature.

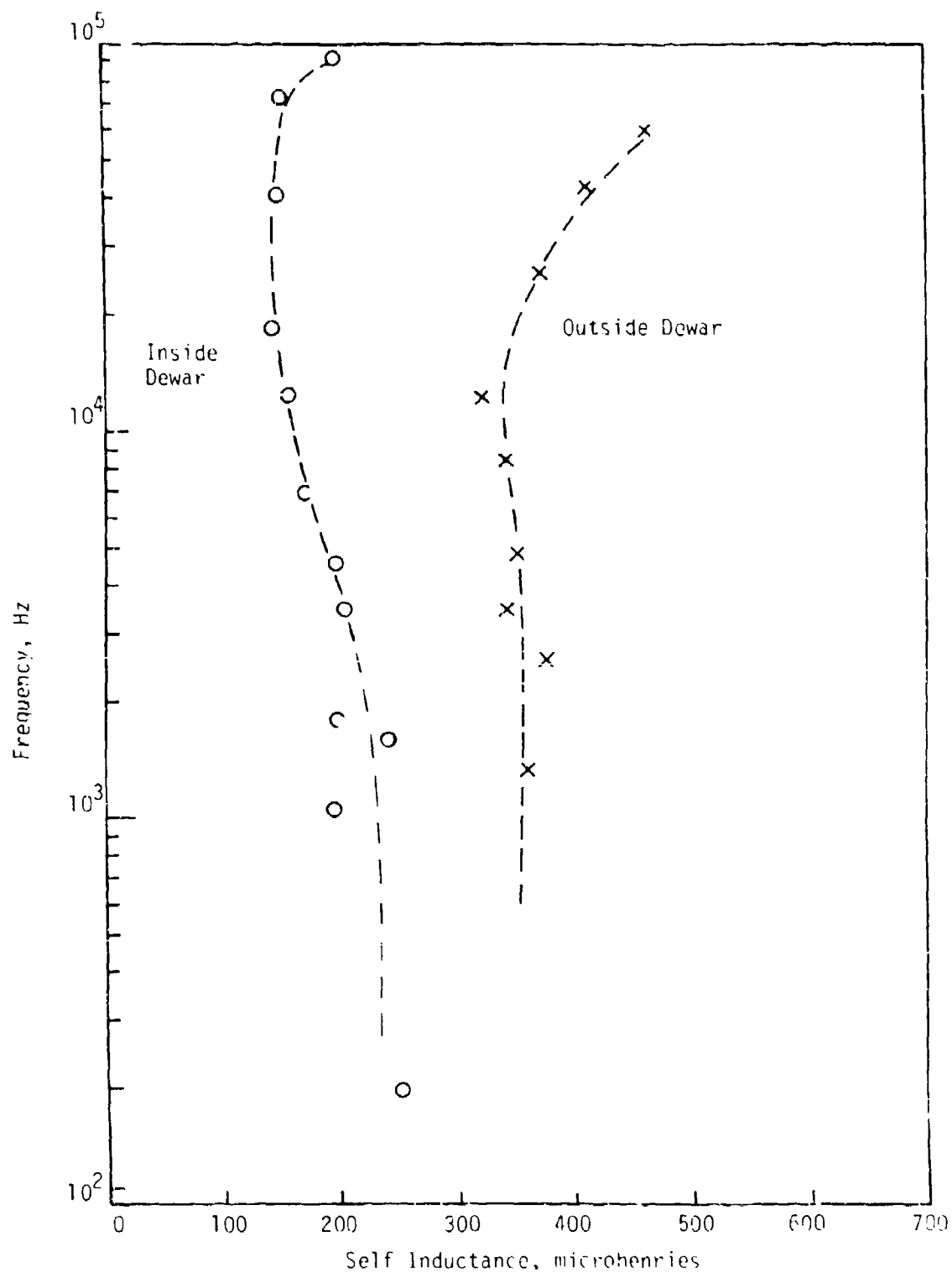


Figure 91: Self Inductance of Sense Coil on 7 kJ Coil at Room Temperature

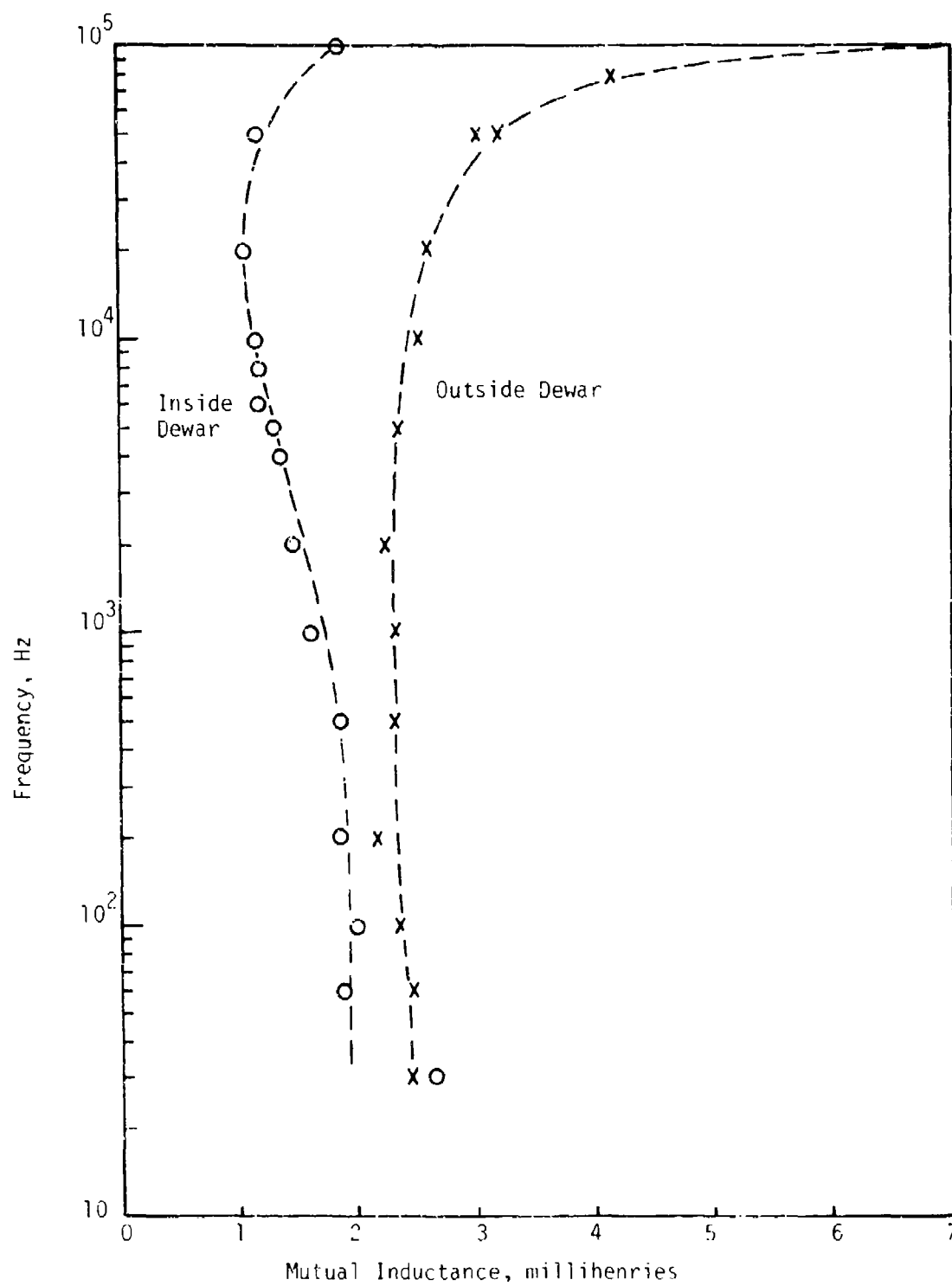


Figure 92: Mutual Inductance Between 7 kJ Coil and Sense Coil at Room Temperature.

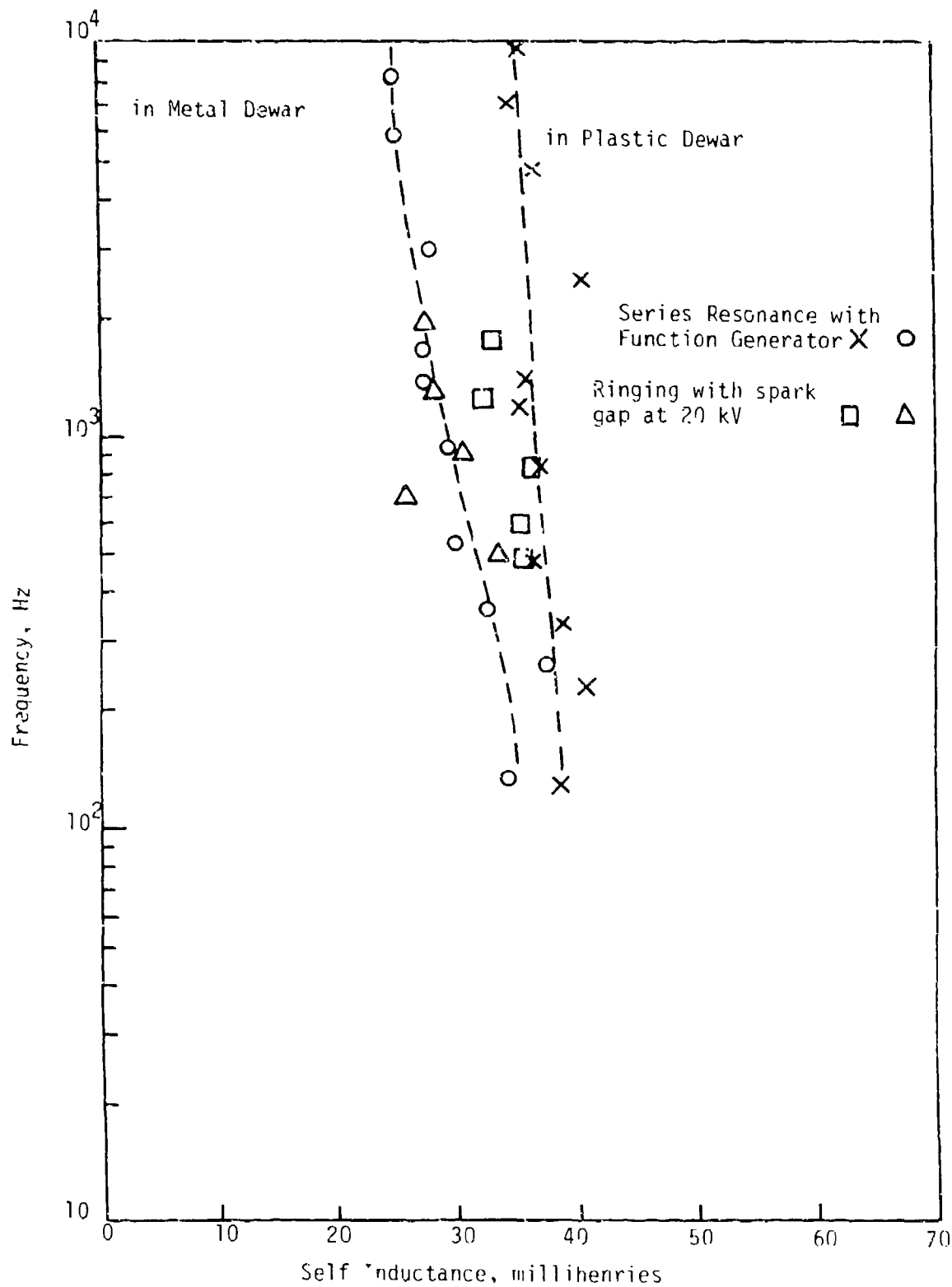


Figure 93: Self Inductance of 7 kJ Coil at 77 K

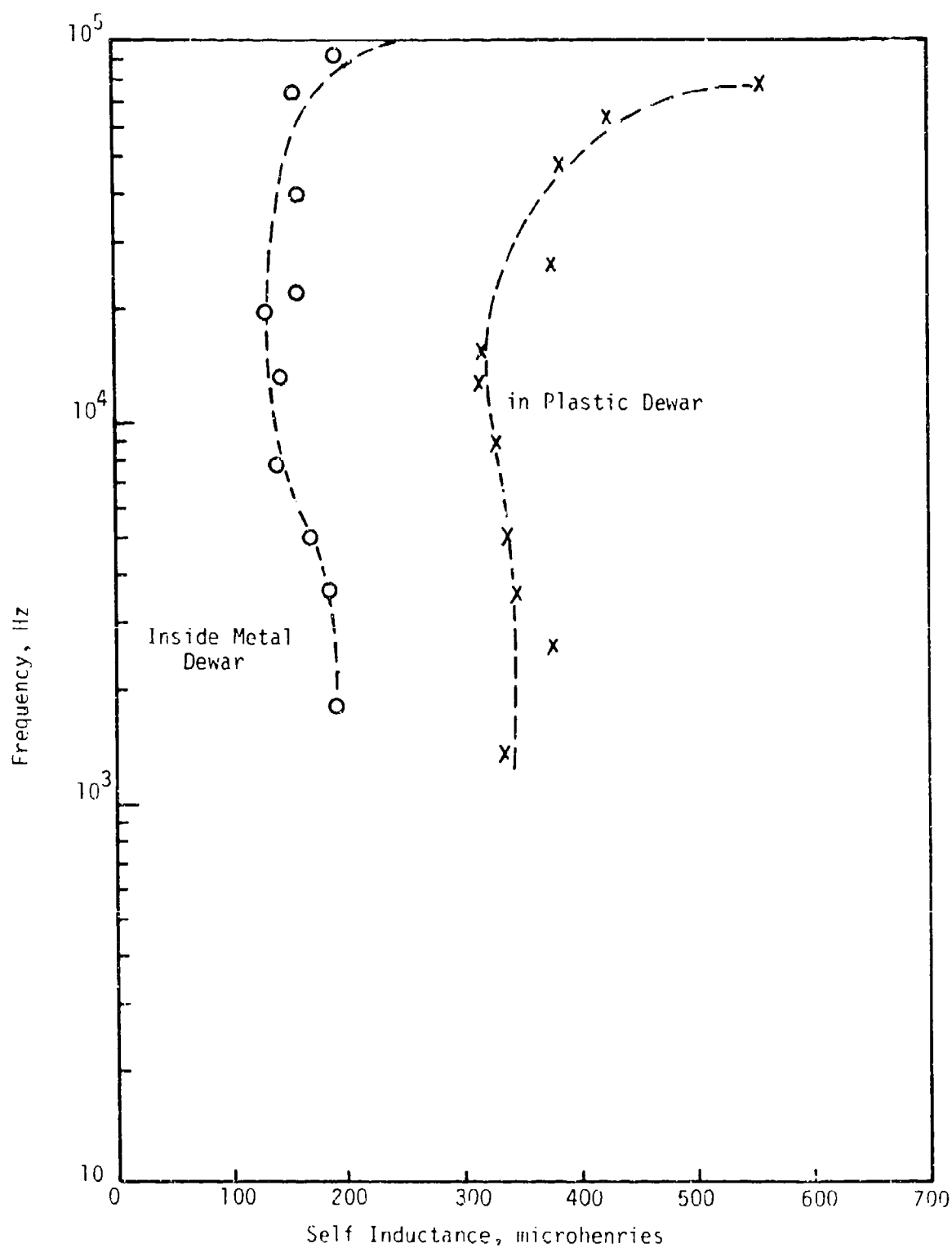


Figure 94: Self Inductance of Sense Coil on 7 kJ Coil at 77 K.

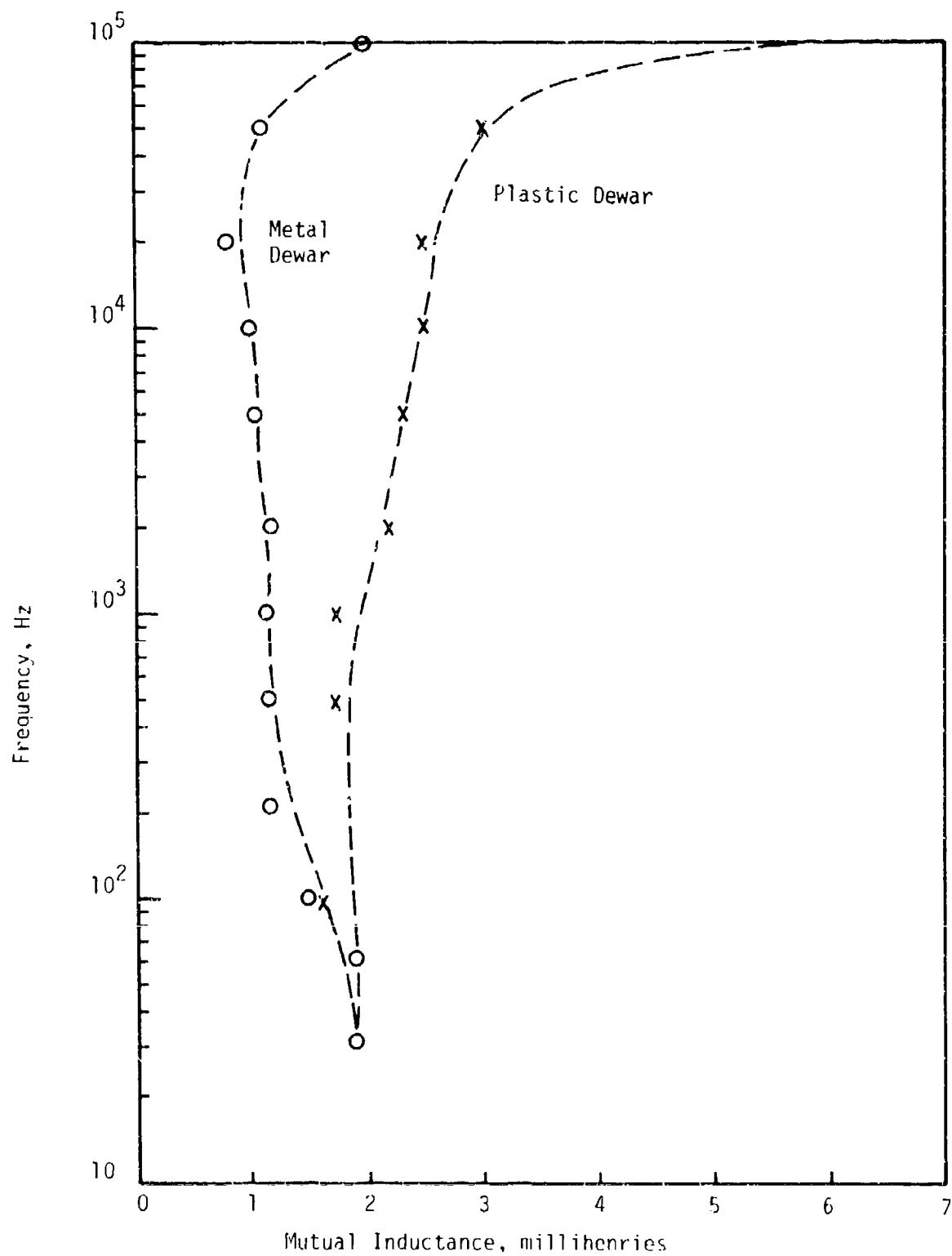


Figure 95: Mutual Inductance Between 7 kJ Coil and Sense Coil at 77 K.

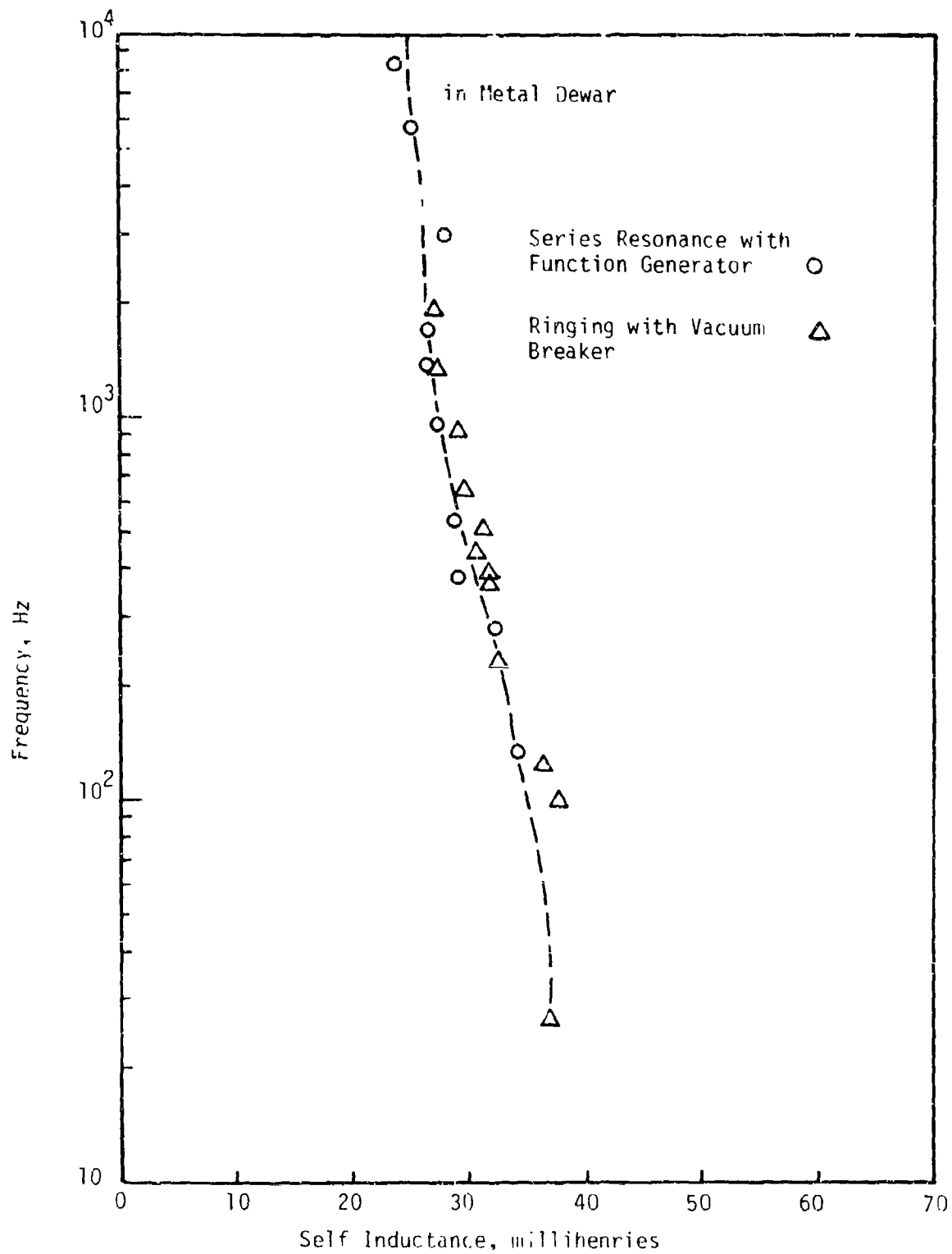


Figure 96: Self Inductance of 7 kJ Coil at 4.2 K.

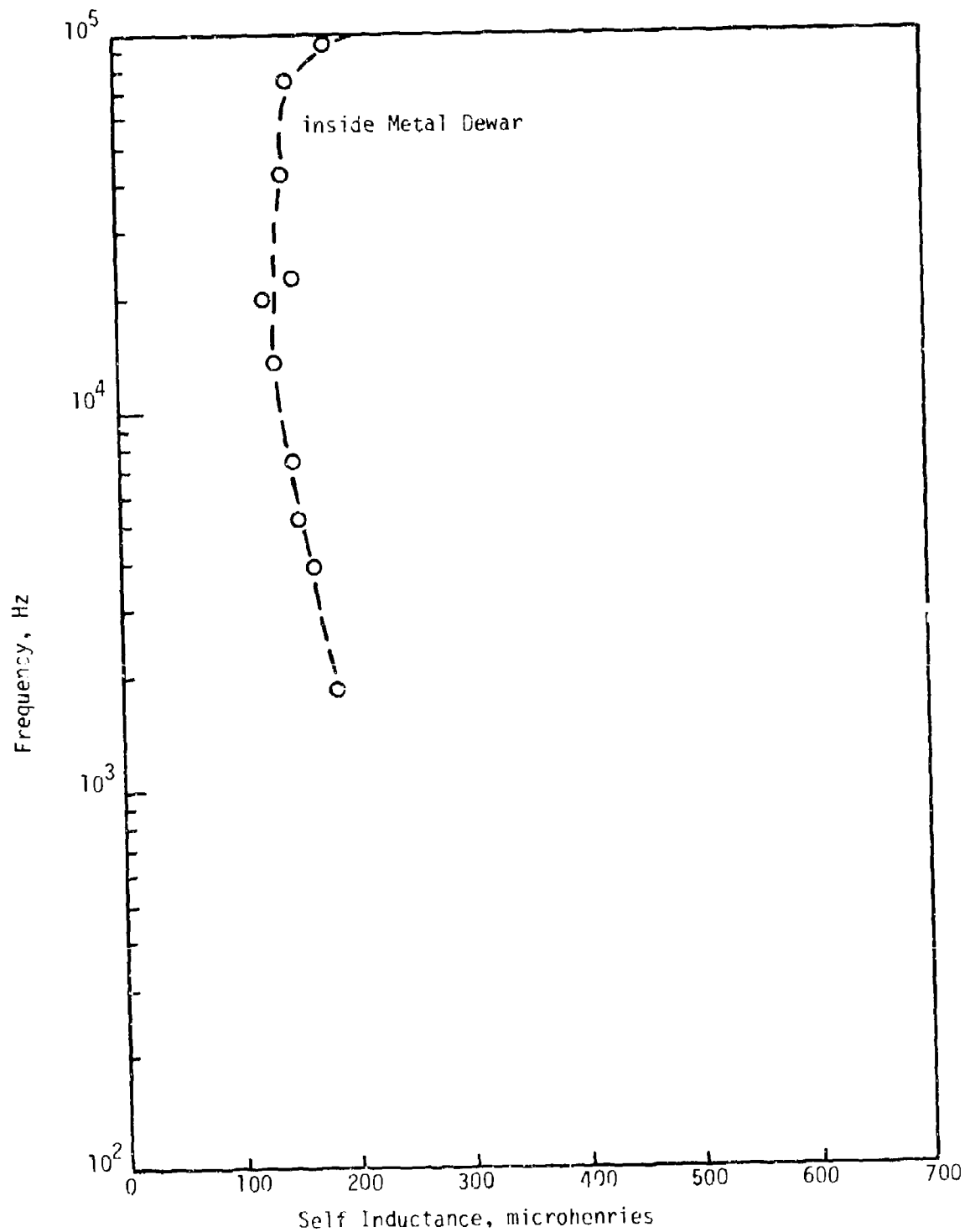


Figure 97: Self Inductance of Sense Coil on 7 kJ Coil at 4.2 K.

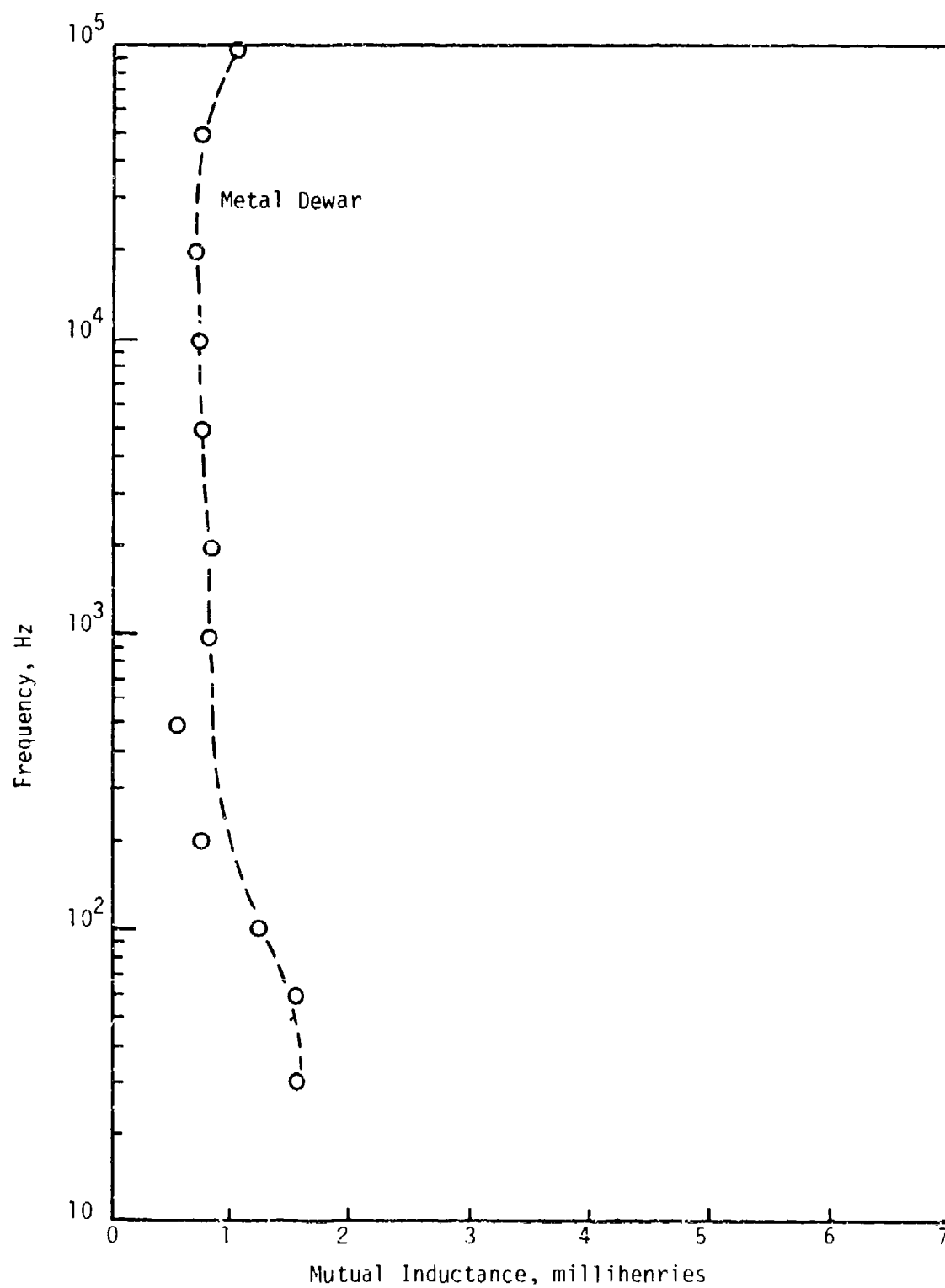


Figure 98: Mutual Inductance Between 7 kJ Coil and Sense Coil at 4.2 K.

d. Energy Losses in the Metallic Dewar

In order to find a range in which the losses in the superconducting coil are larger than the losses in the dewar, it is necessary to make a sufficient number of measurements over a broad enough range of parameters to allow construction of a theoretical model for the dewar losses. The losses were measured as a function of frequency by three techniques: (1) measure the resistance of the 7 kJ coil at series resonance using a function generator in the circuit of Figure 89(a); (2) calculate the effective resistance of the 7 kJ coil by observing the rate at which the oscillations decay in a ringing experiment as in Figure 89(b); (3) use the electronic loss measurement technique (loss loops) to measure the energy loss per cycle during a ringing experiment as in Figure 89(c).

The data taken by measuring the resistance at series resonance were obtained by forming a circuit consisting of the coil (inductor), a capacitor, and a resistor; driving it with a function generator; and observing the voltage across the series L-C components as in Figure 89(a). The resonant frequency is found by adjusting the frequency of the function generator so as to produce a minimum in the observed voltage. Given the resonant frequency for a given capacitor, the coil inductance can be found; given the voltage drop at resonance and the current, the loss resistance can be found. It is necessary to exercise care in interpreting this loss resistance because it includes the resistance of the leads and the ohmic losses in the capacitor; these extraneous resistances were typically less than 0.1 ohm.

The losses and the inductance determined by means of the ringing experiment were obtained by charging a capacitor, switching it onto the coil, and observing the oscillations in current as in Figure 89(b). The current amplitude decays exponentially at a rate that depends on the losses. The equations are:

$$I = I_0 e^{-t/\tau} \sin(\omega t)$$

Where:

$$\tau = \frac{2L}{R}$$

$$\omega^2 = \frac{1}{LC} - \left(\frac{1}{\tau}\right)^2$$

$$I_0 = V \sqrt{\frac{C}{L}}$$

V = the initial voltage on the capacitor

Clearly, an observation of the oscillation frequency and the decay time constant of a ringing circuit will provide the desired measurements of inductance and resistance.

These measurements were made at room temperature, at 77 K, and at 4.2 K, and the results are plotted in Figures 99, 100 and 101, respectively. It is clear, especially from Figure 101, that the dewar losses vary with frequency in a simple way (power law) and hence it should be possible to find a useful theoretical model to describe it.

A simple transformer model for the coupling between the 7 kJ coil and the dewar is pictured in Figure 102 and the appropriate coupling equations are worked out in Appendix VI. As is discussed in the appendix, the dewar acts like a shorted single turn secondary winding for the 7 kJ coil. At lower frequencies (below 10 Hertz), the dewar losses should appear as a resistance whose value varies as the square of frequency. At higher frequencies (near 100 Hertz), the dewar losses should appear as a resistance of constant value; the leveling off of resistance is not observed because in this same frequency range, the resistance in the dewar begins to increase with frequency due to skin effect (i.e., induced currents flow in only a portion of the dewar wall). An analysis of this effect is complicated and is not particularly useful here. Since we need to find a regime in which the dewar losses are smaller than the losses in the 7 kJ coil, the data of Figure 101 was used to obtain estimates of resistance, self-inductance, and mutual inductance for the dewar which could be used in the impedance function derived in the appendix. The estimated values are $R = 0.5 \times 10^{-3}$ ohm, $L = 0.56$ μ H, $M \approx 70.7$ μ H. The predicted loss voltage resulting from the dewar as a function of current and of frequency is shown in Figure 103. An experimentally observed residual coil resistance of 6×10^{-6} ohms is included in this figure.

The aim was to perform an experiment on the 7 kJ coil in which the losses observed are predominantly in the coil. The loss voltage due to the metallic dewar has already been estimated as a function of frequency (Figure 103). The predicted loss voltage due to the superconductor (Appendix VII) is presented in Figure 104 as a function of both frequency and current for sine waves. Note that both Figures 103 and 104 show 5% of the total loss voltage because it is this quantity that is available to the integrator (the coupling ratio of the sense coil is about 0.05). It is desired that the coil loss voltage be much larger than the dewar loss voltage, yet still have as large an amplitude as possible to direct to the integrator. A comparison of Figures 103 and 104 shows that these criteria are best followed at a frequency of about 0.1 Hz and a current of 600 amps or greater. At this point the predicted loss voltage is 6 millivolts, and the predicted dewar voltage is 0.3 millivolts or less.

e. Electronic Loss Measurements on the 7 kJ Coil

An experiment that fits the time scales specified above consists of charging and discharging the 7 kJ coil with rise and fall times of 2 to 3 seconds by means of the arrangement shown in Figure 105 and measuring the losses by the arrangement shown in Figure 83. Loss loops were observed for charging times ranging from 0.5 seconds to 2.5 seconds, which corresponds to a current range of 150 amps to 700 amps and an energy range of 438 Joules to 9,050 Joules. A typical loss loop is given in Figure 106. This loss loop departs from that expected only at

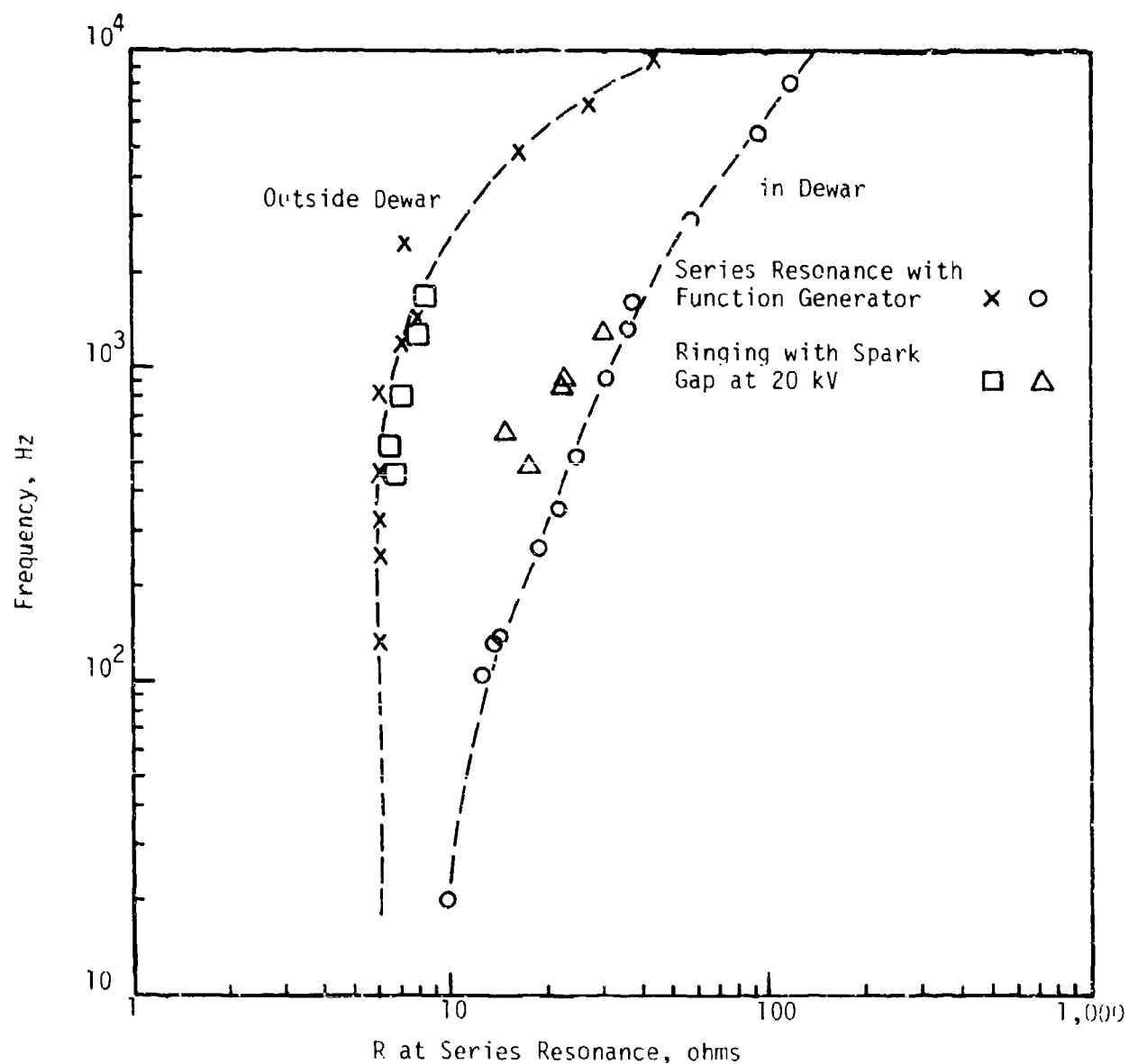


Figure 99: Equivalent Loss Resistance of 7 kJ Coil at Room Temperature.

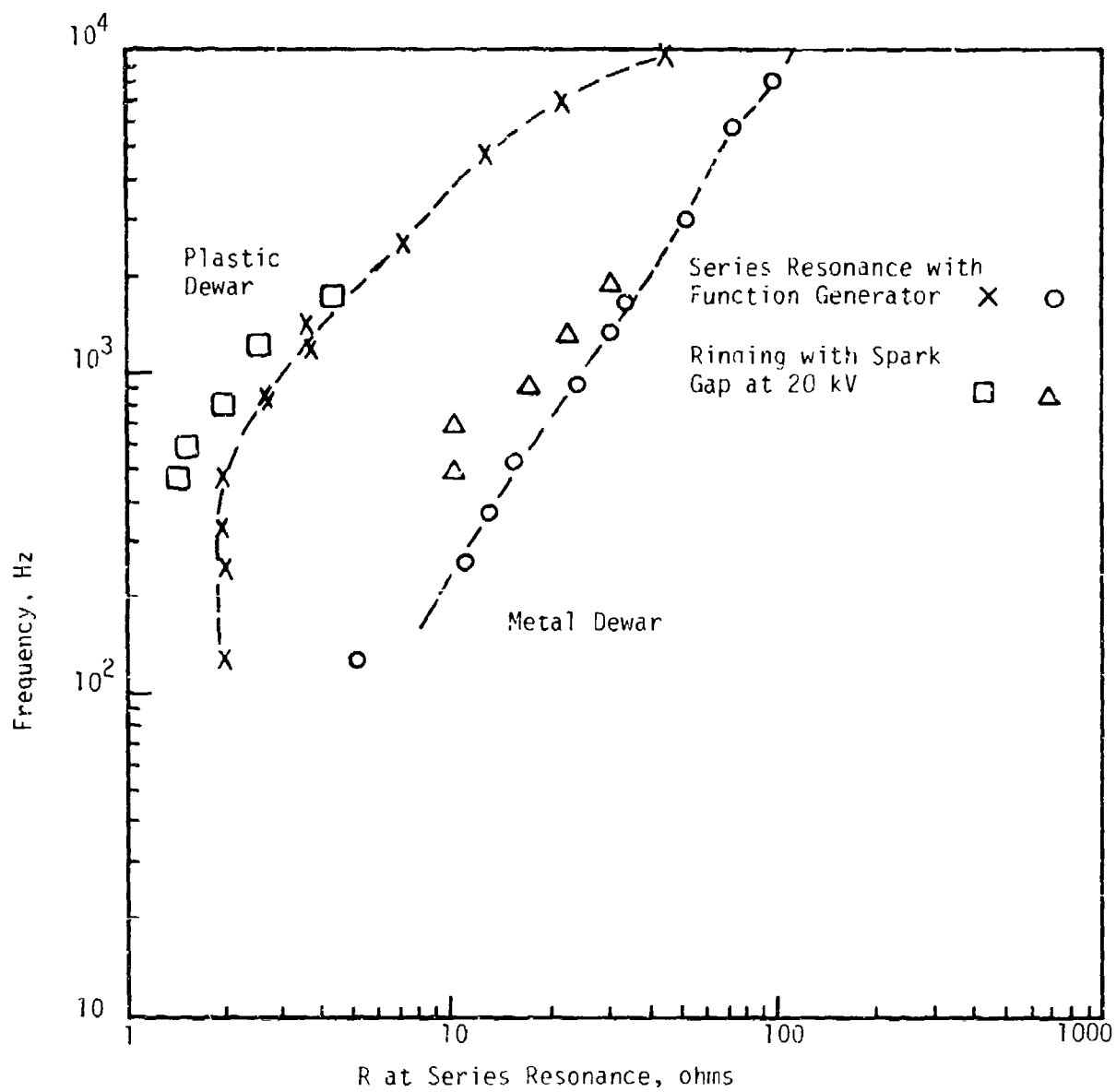


Figure 100: Equivalent Loss Resistance of 7 kJ Coil at 77 K.

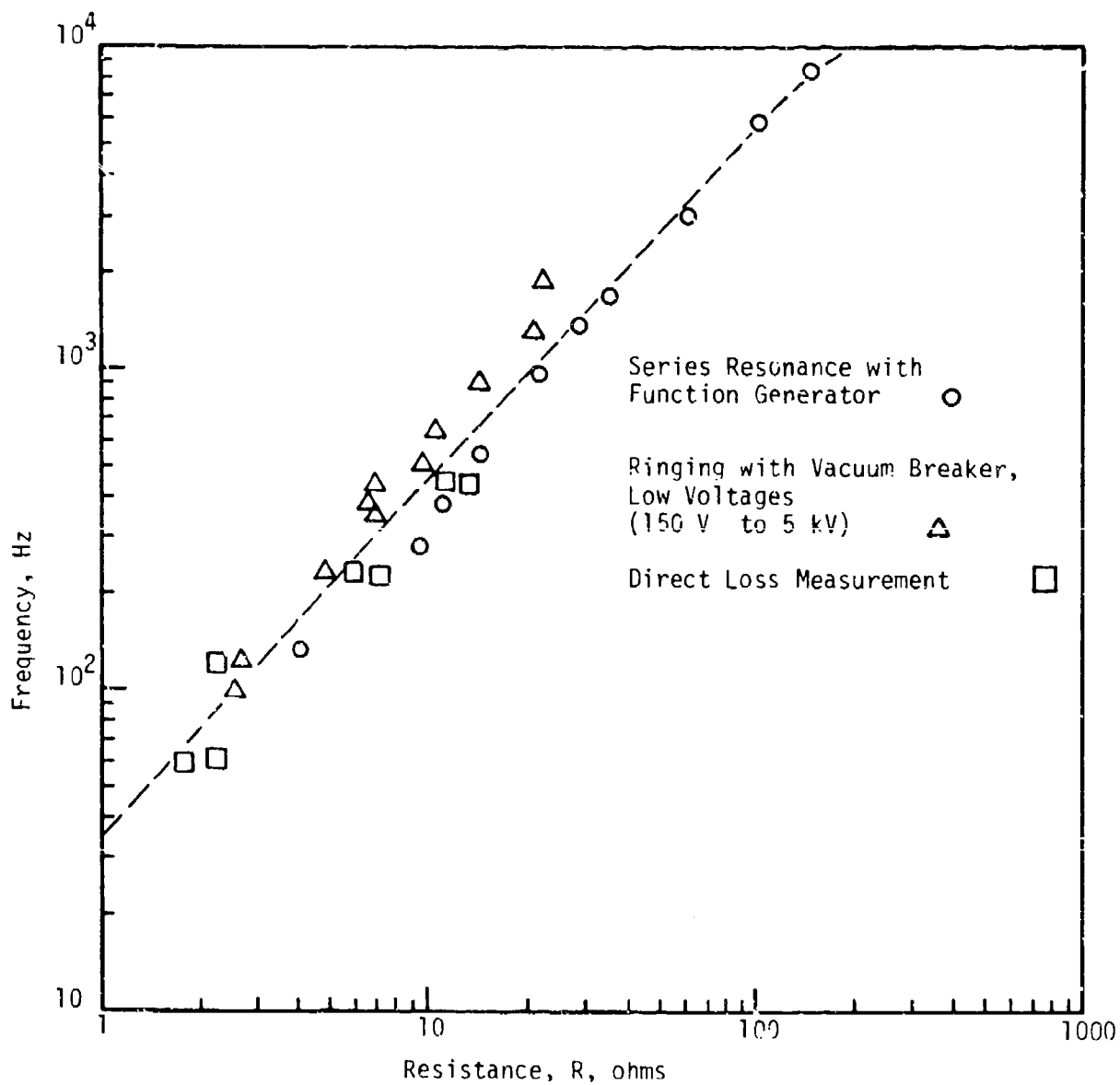


Figure 101: Equivalent Loss Resistance of 7 kJ Coil in a Metallic Dewar at 4.2 K.

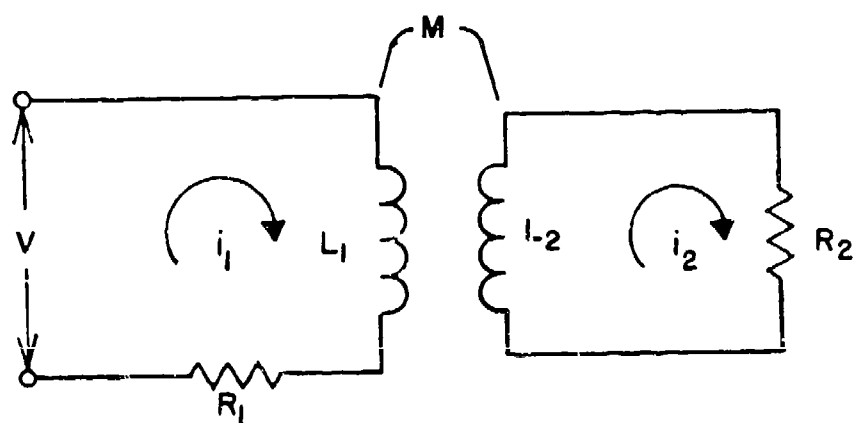


Figure 102: Schematic of model for dewar loss circuit.

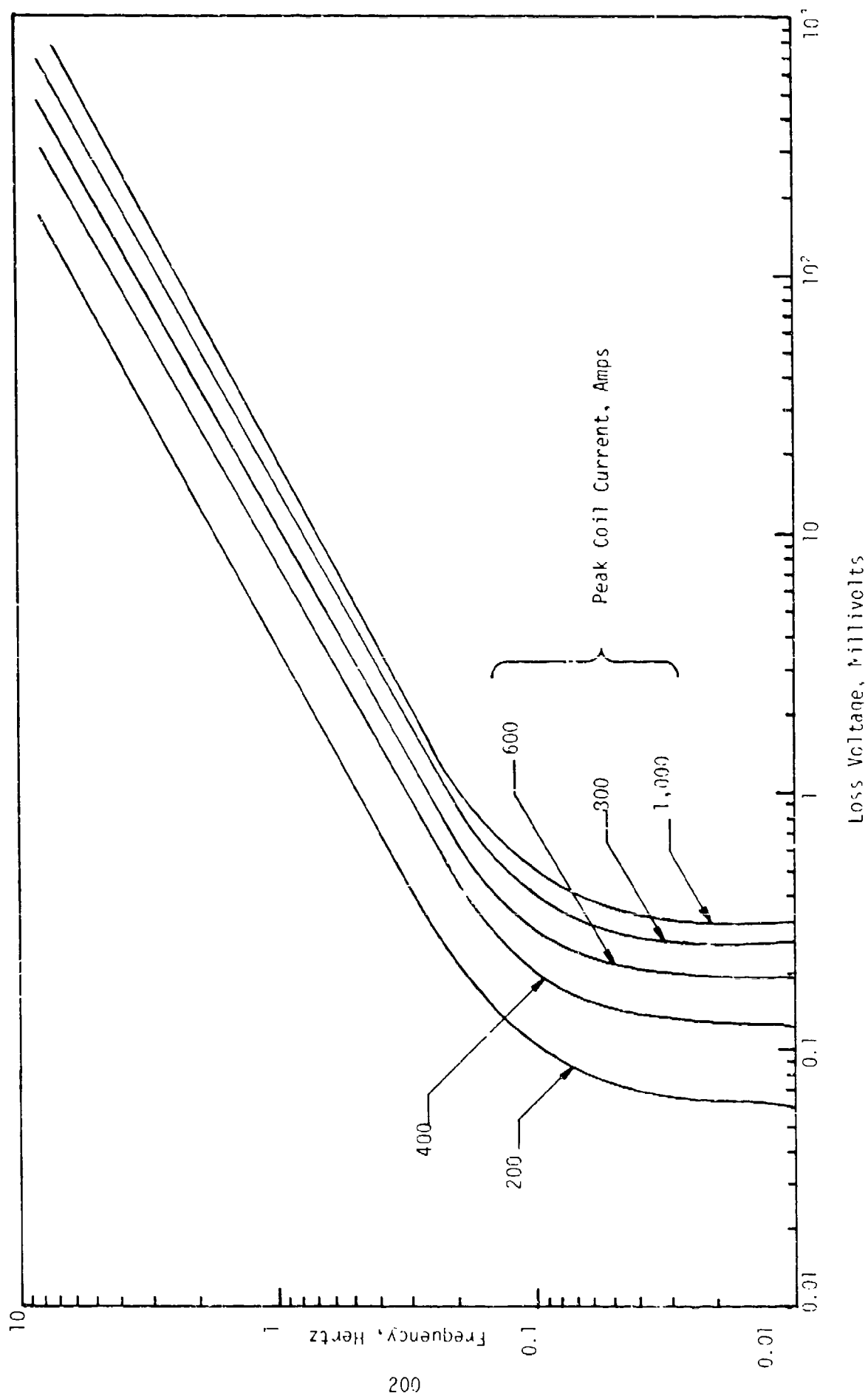


Figure 103: Predicted Loss Voltage Caused by Dewar and by Residual Resistance of Coil after Stepdown by 20:1 Divider.

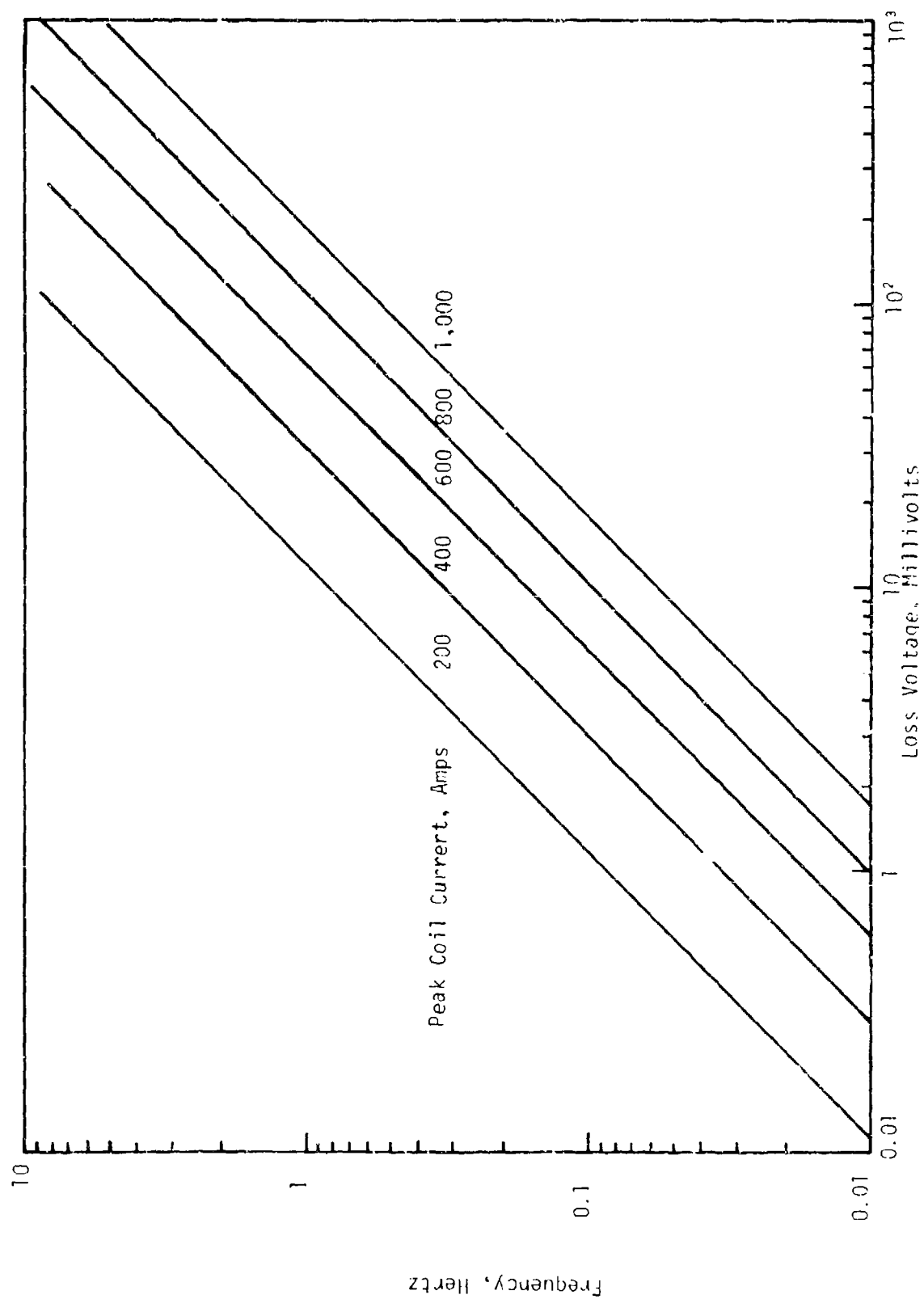


Figure 104: Predicted Voltage Caused by the Superconducting Coil after Stepdown by 20:1 Divider.

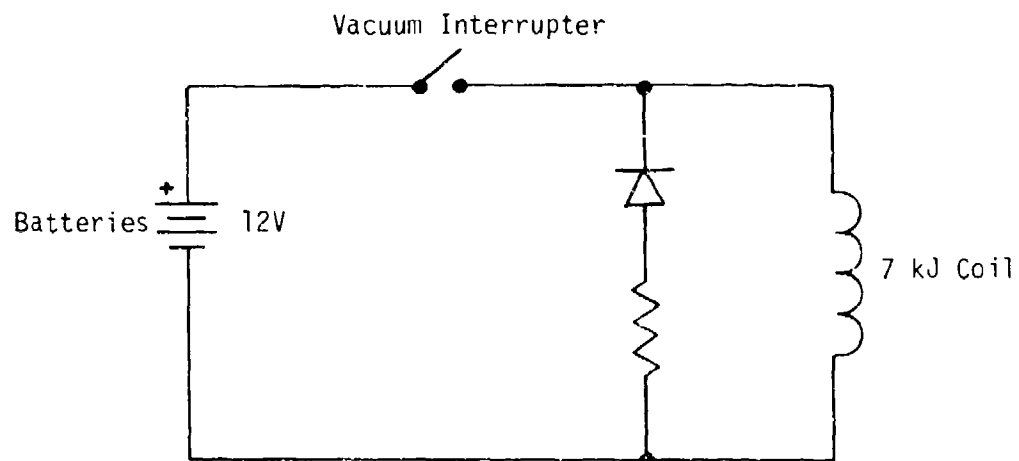
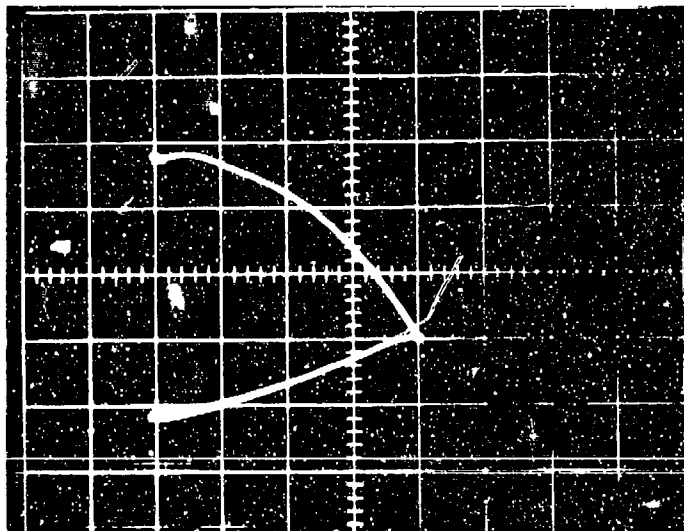


Figure 105: Schematic of Low Speed Loss Measurement Experiment.
Vacuum interrupter is controlled by a mechanical timer.

Integrated Error Voltage 50 mV/cm



Current 179 A/cm

Figure 106

Loss loop for a 7 kJ coil. Divider fraction, 0.059; integrator time constant, 33 ms; total coil energy, 9,600 J.

the time of transition from charge to discharge, i.e., at the time the vacuum interrupter is opened. The electrical noise generated by the arcing in the vacuum interrupter causes the observed loop to show an abrupt change (i.e., the "point" on the right side of the loop) instead of the smoother transition expected. A series of filtering experiments revealed that this effect did not change the area of the loop by more than 10 percent. Because this error is of approximately the same magnitude as the error introduced by the metallic dewar (5 percent) it was not considered worthwhile to pursue this filtering problem further.

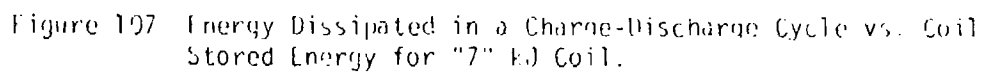
The energy dissipated in the coil during a charge-discharge cycle was calculated from a set of loops similar to that of Figure 106. The results of the electronic measurements are presented in Figure 107 along with the helium boiloff data. From this presentation, it is clear that the two measurement techniques produce similar results.

In Figure 107 it can be seen that at low currents the measured losses tend to be significantly lower than those predicted for magnetization losses only. This situation is to be expected because the model used for the theoretical calculations assumed that the superconductor is fully penetrated whereas in fact only partial penetration occurs at low current levels. The measured losses turn up sharply in the neighborhood of 10 kilojoules stored energy because this operating point is very close to the critical current for the coil; it is likely that some parts of the coil go normal during the cycle, thus adding transport current losses to the magnetization losses.

f. Summary and Conclusions

Loss measurements were made on the 7 kJ energy storage coil by the boiloff method and the electronic method. The scatter in the data obtained by the boiloff method was large and because of this no attempt was made to develop a more sophisticated model (as was done for the 1 kJ coil results) to interpret the data. However, for the most part the boiloff data was not more than about 30% different from predicted values. The electronic data covered the range of energies over which boiloff measurements were made and extended to lower energies. The electronic data was in reasonable agreement with the boiloff data where overlap occurred. At lower energies the electronic loss data deviated (on the low side) from the predicted losses. This is so because the model used for predicting losses overestimates losses for the reasons previously described (see Section III-5, Loss Measurements Made Using the 1 kJ Coil). The theoretical model becomes worse the lower the energies to which the coil is charged.

Thus, in spite of the perturbing effects of the metal dewar, good enough agreement between losses measured by the two methods were obtained to give confidence in the validity of the electronic measurement techniques.



7. LOSS MEASUREMENTS MADE USING THE 100 kJ COIL

a. Introduction

The object of this set of experiments was to determine the losses in the coil as a function of current and frequency and to establish the limits of operation in voltage and current. A mechanical description of the coil has been given previously in this report. In order to make possible an electronic loss measurement, a single layer, 65 turn, $7\frac{1}{2}$ inch high sense coil was placed over the outer layer of the 100 kJ coil; the voltage coupling ratio to this sense coil was observed to be 0.237. In the preliminary set of experiments described in Section III-7-b, Preliminary Measurements below, it was determined that the self inductances of the 100 kJ coil, of the sense coil, and the mutual inductance between them did not change significantly over the range of operating frequencies contemplated; hence it was shown to be feasible to use the electronic technique for measuring losses. In Section III-7-c, Electronic Loss Measurements on the 100 kJ Coil below, is described a set of ringing tests during which losses were measured by the loss loop method and cross checked by observing the decay rate of the oscillating current (for operating regimes in which the coil losses are much greater than losses in the leads).

b. Preliminary Measurements

In order to obtain reliable measurements by the electronic method, it is necessary that the self inductance of the storage coil and the coupling (mutual inductance) between the storage coil and the sense coil remain constant over the range of frequencies contemplated for the experiments. The self inductance of the 100 kJ coil, the self inductance of the sense coil, and the mutual inductance between them were measured by resonance and by ringing (Figure 89(a), (b)) as a function of frequency at room temperature (Figures 108, 109 and 110), at liquid nitrogen temperature, 77 K (Figures 111, 112 and 113) and at liquid helium temperature, 4.2 K (Figures 114, 115 and 116). The self inductance of the 100 kJ coil was found to be stable (52 millihenries) at all temperatures and at frequencies up to 10,000 Hertz (Figures 108, 111, 114). The self inductance of the sense coil was found to be stable (3.7-3.8 millihenries) at all temperatures and at frequencies up to about 5,000 Hertz (Figures 109, 112, 115). The mutual inductance was found to be stable (about 12 millihenries) at frequencies up to about 2,000 to 3,000 Hertz at 77 K and 4.2 K (Figures 113, 116). The difference between the room temperature mutual inductance of 8 millihenries (Figure 110) and the two curves at lower temperatures (12 millihenries) may have been caused by mechanical shrinkage of the coil on exposure to low temperatures or by erroneous measurements at room temperature. The measurements at lower temperatures, especially at 4.2 K, were repeated several times with no observable variations. The apparent increase in the mutual inductance at frequencies above 10,000 Hertz is caused by capacitive coupling between the two coils; the peak at about 20,00 Hertz is a resonance between the self inductance of the storage coil (52 mH) and the capacitance between the storage coil and the sense coil (about 0.01 μ F). The conclusion to be drawn from this set of measurements is that the electronic loss

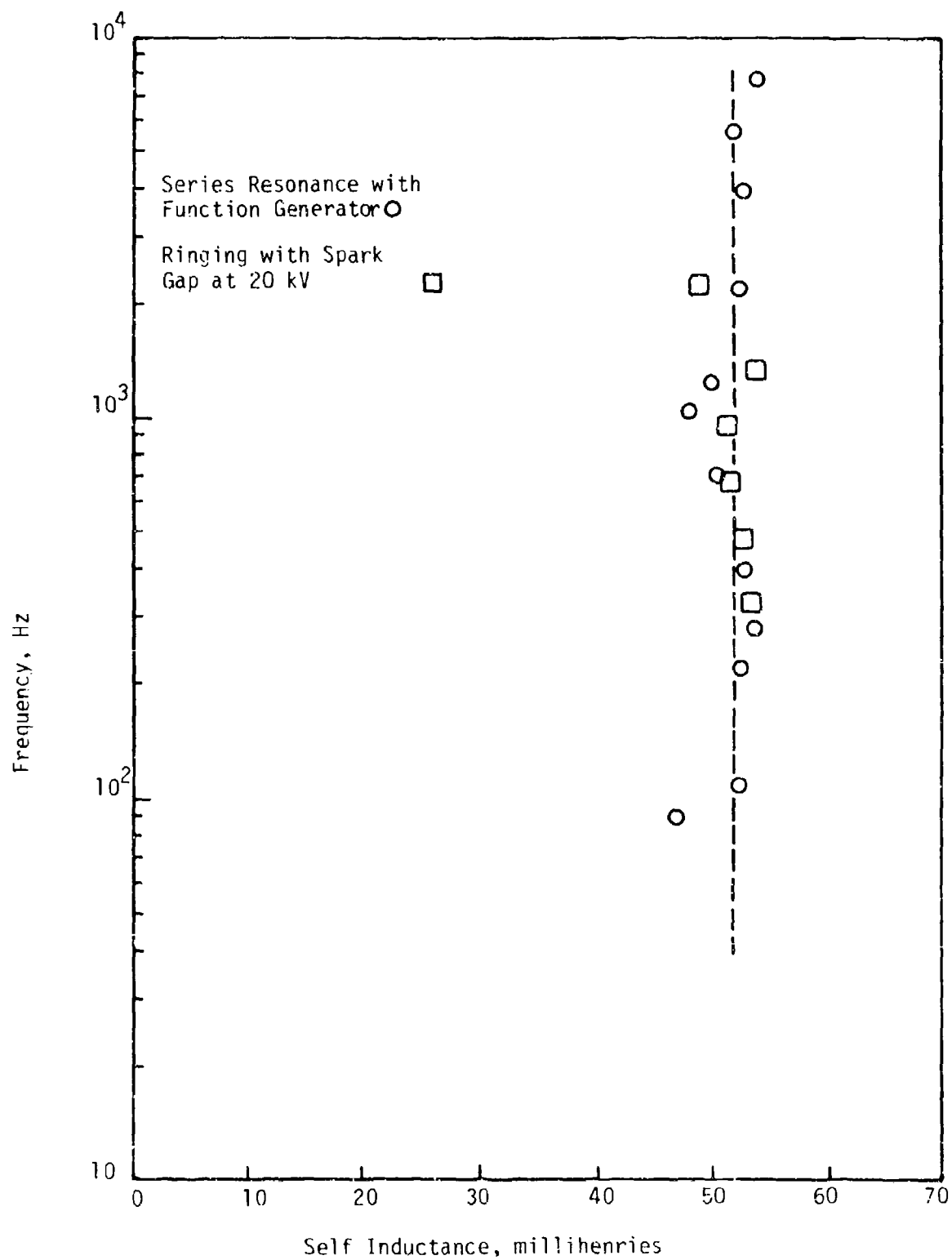


Figure 108 Self Inductance of 100 kJ Coil at Room Temperature.

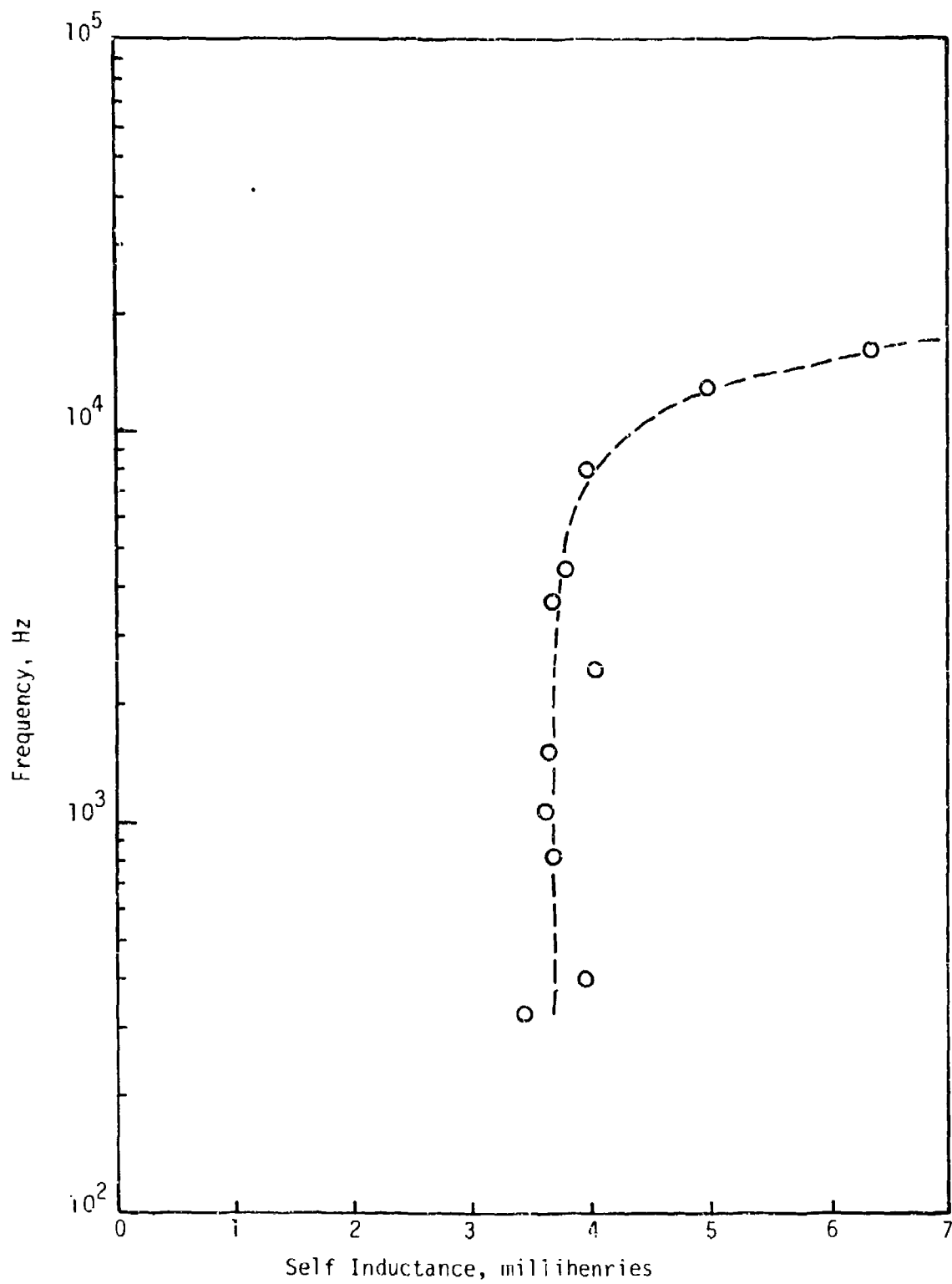


Figure 109 Self Inductance of Sense Coil for 100 kJ Coil at Room Temperature.

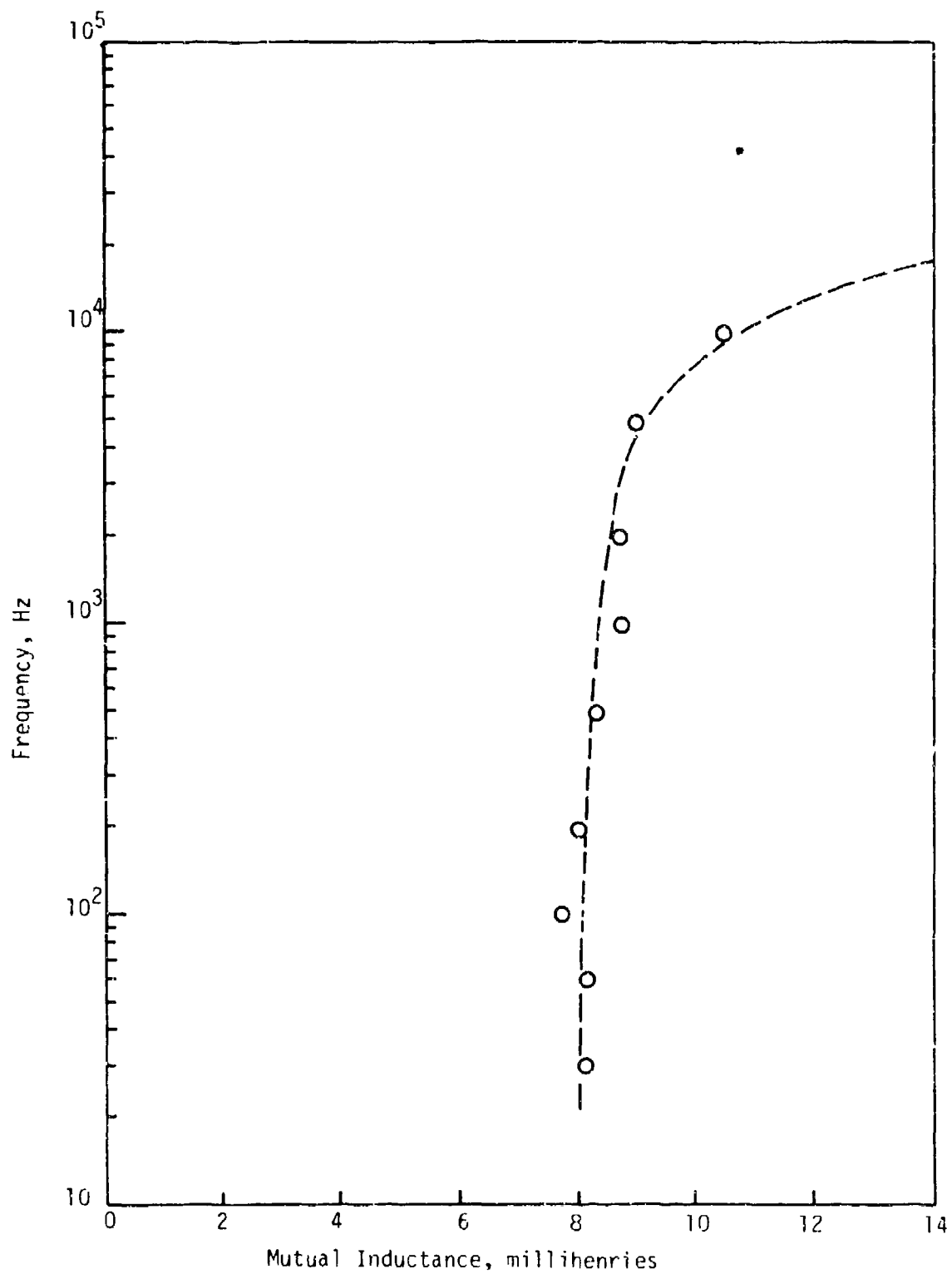


Figure 110 Mutual Inductance Between 100 kJ Coil and Sense Coil at Room Temperature.

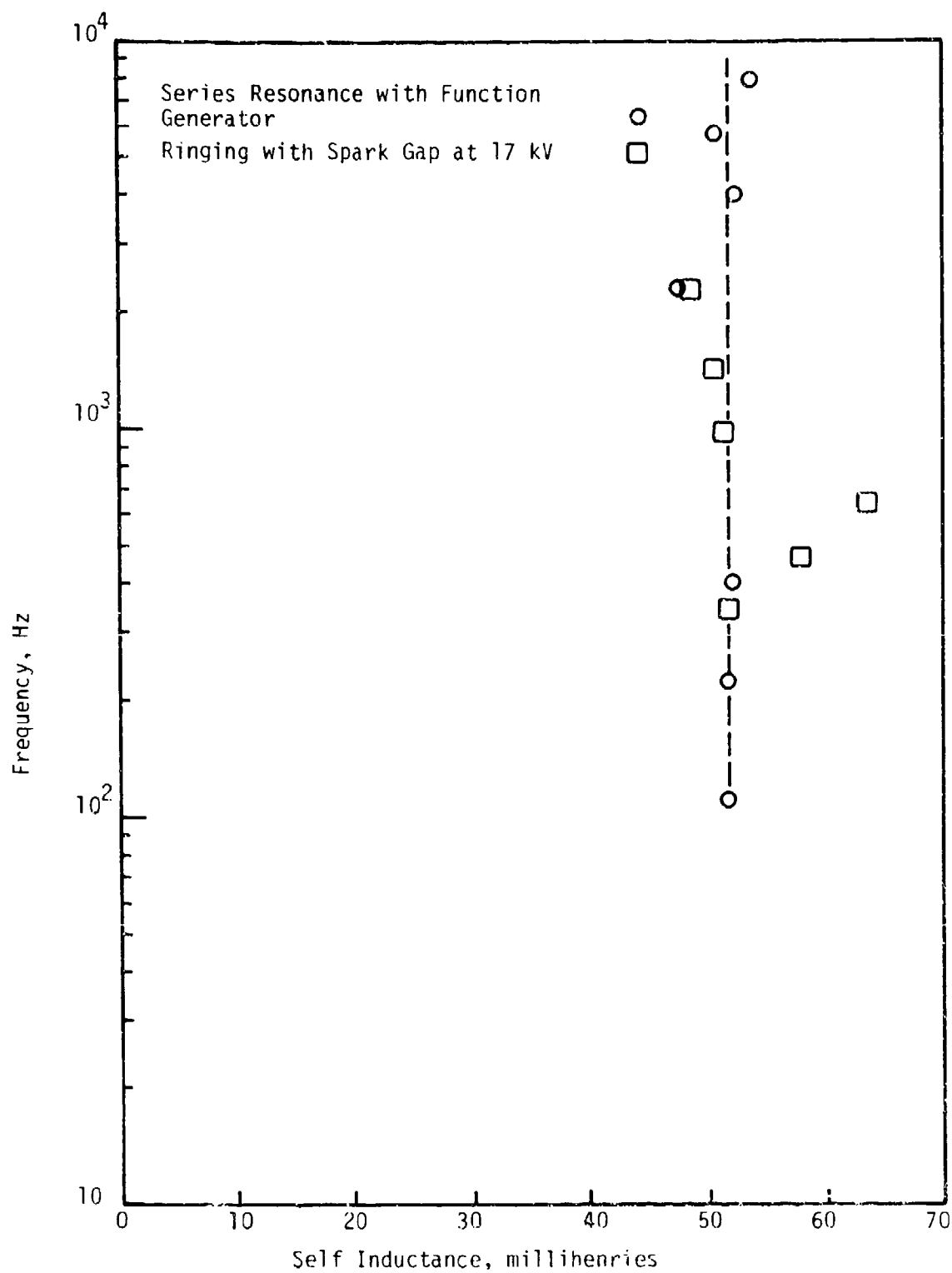


Figure 111 Self Inductance of 100 kJ Coil at 77 K.

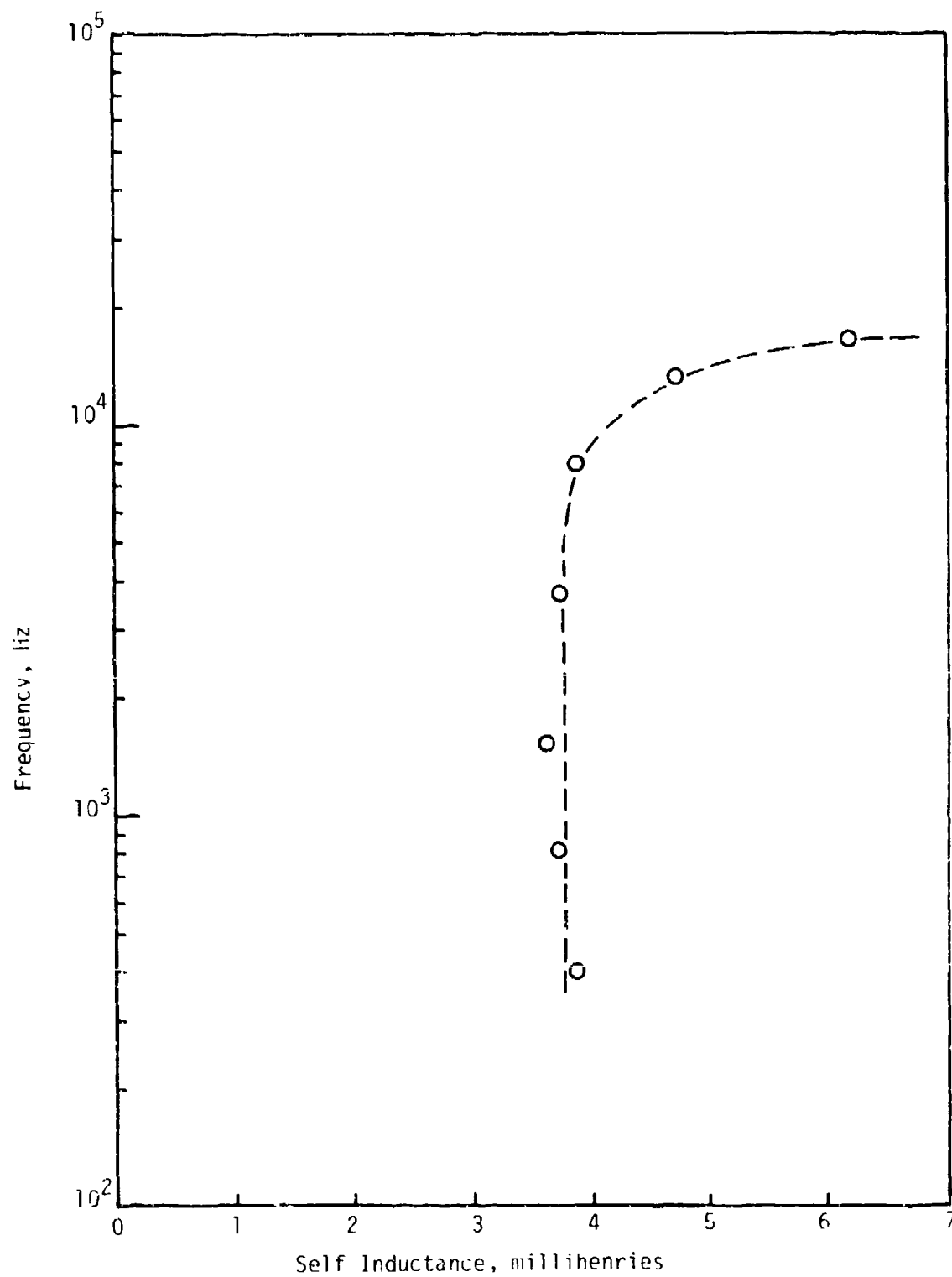


Figure 112 Self Inductance of Sense Coil for 100 kJ Coil at 77 K.

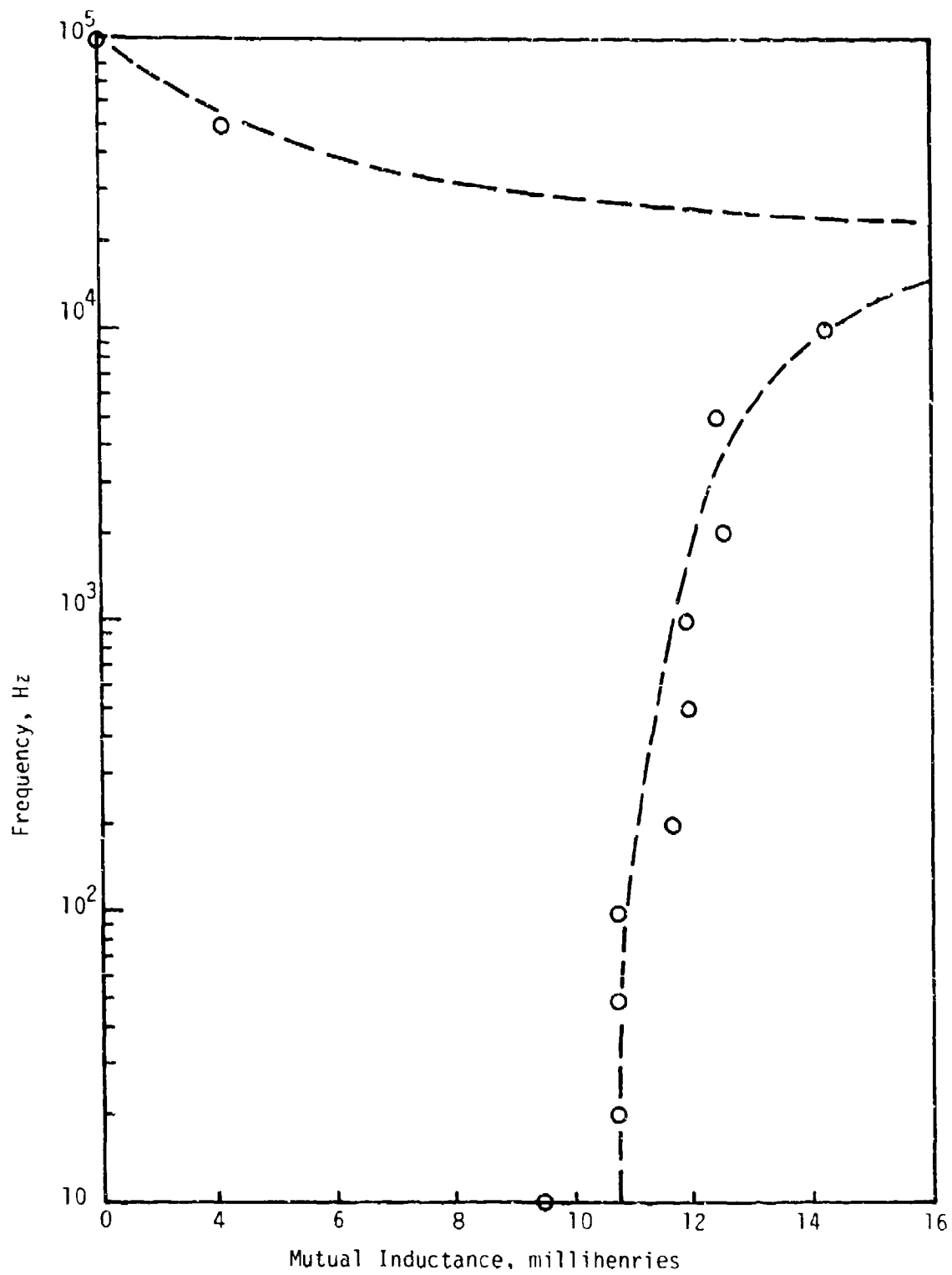


Figure 113 Mutual Inductance Between 100 kJ Coil and Sense Coil at 77 K.

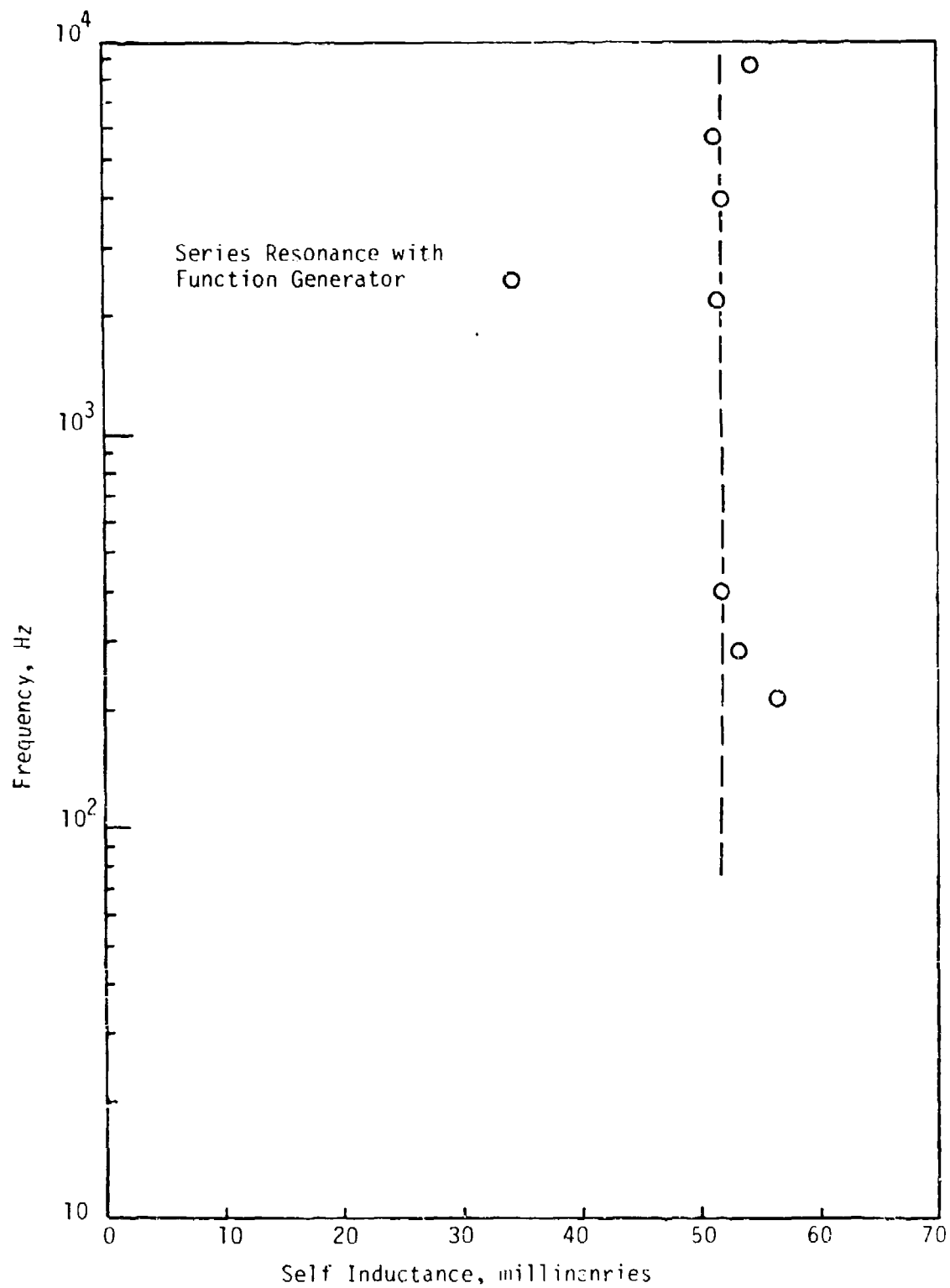


Figure 114 Self Inductance of 100 kJ Coil at 4.2 k.

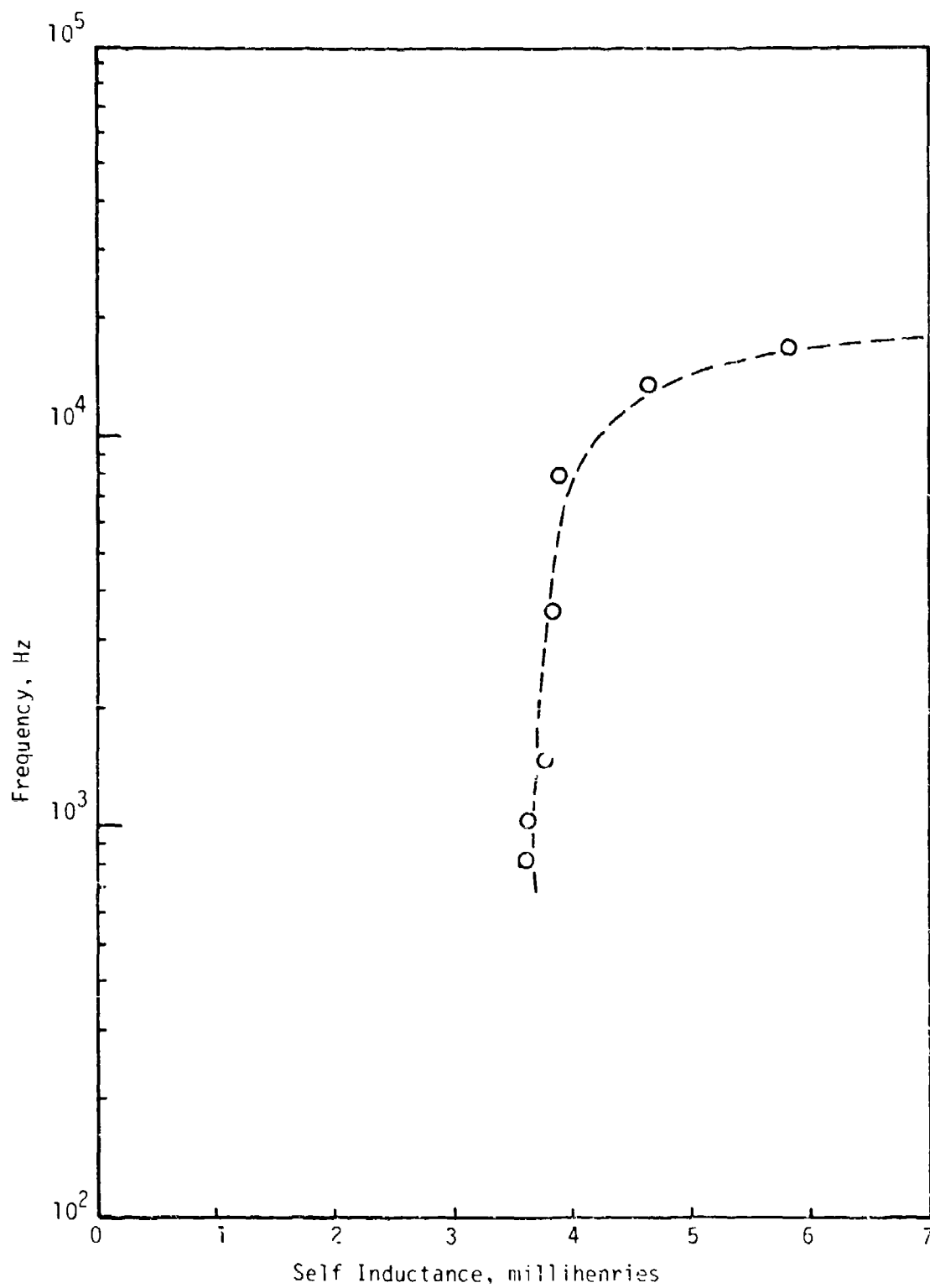


Figure 115 Self Inductance of Sense Coil for 100 kJ Coil at 4.2 k.

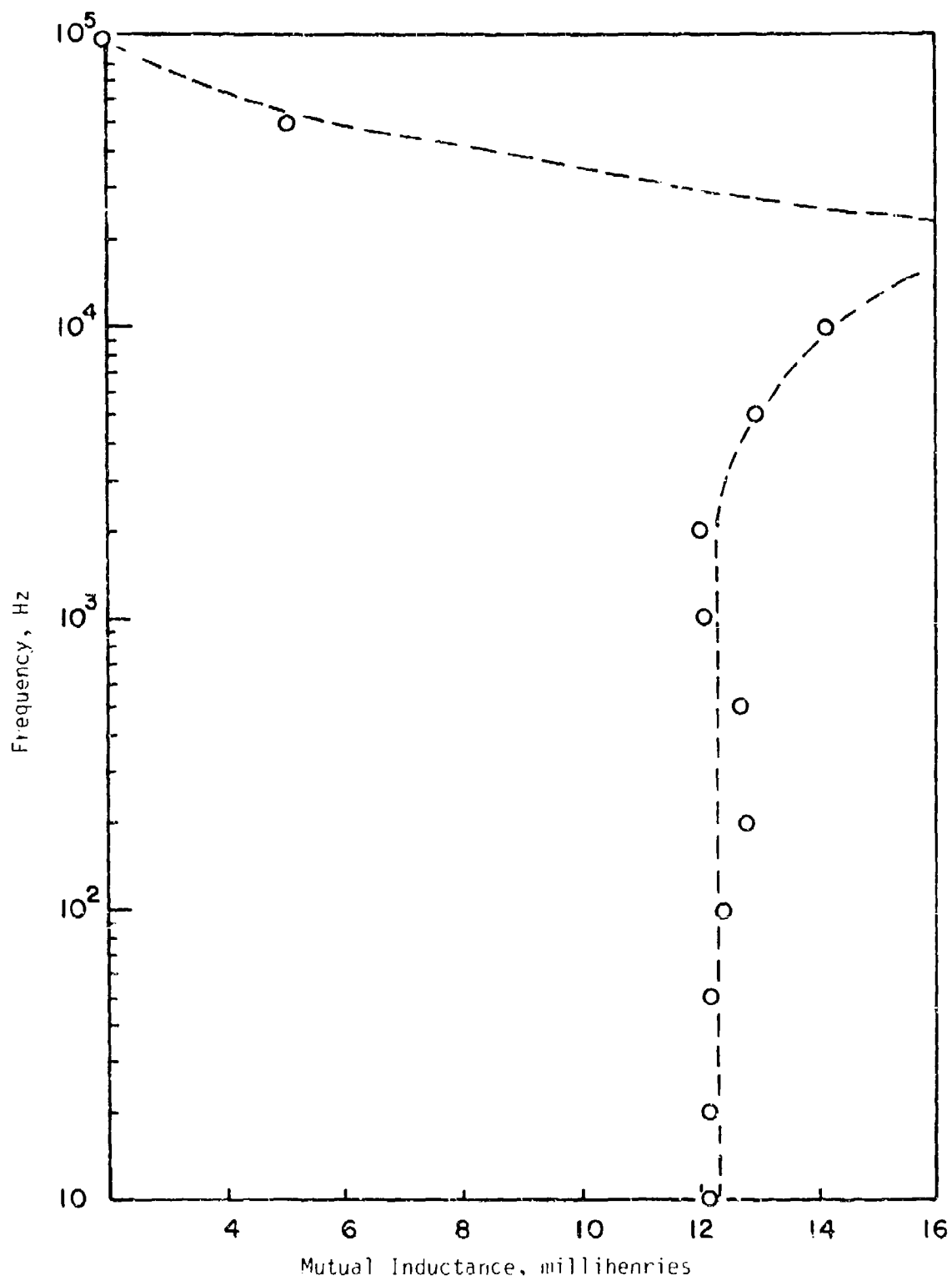


Figure 116 Mutual Inductance Between 100 kJ Coil and Sense Coil at 4.2 K.

measurement technique should be useable without difficulty at frequencies up to at least 2,500 Hertz (and hence switching times as short as 100 microseconds) because of the availability of the non-conducting dewar.

Another preliminary test of the 100 kJ coil consisted of measuring the coil losses by means of resonance (i.e., measure the resistance of the coil at series resonance) and by observing the decay rate of the ringing tests. These are the same techniques that were used to extract the preliminary loss curves for the 7 kJ coil (Figures 99, 100, 101) as was explained in Section III-6-d, Energy Losses in the Metallic Dewar. This loss data, presented as an equivalent loss resistance, was obtained for the 100 kJ coil at room temperature (Figure 117), at liquid nitrogen temperature, 77 K (Figure 118), and at liquid helium temperature, 4.2 K (Figure 119). No significant frequency dependence of losses is observed at room temperature below a frequency of 1,000 Hertz (Figure 117). Without further measurements it is not possible to tell whether the observed frequency dependence of losses at 77 K (Figure 118) is caused predominately by losses in the leads or by losses in the coil. The preliminary loss curve for the 100 kJ coil at 4.2 K (Figure 119) must consist of a sum of coil losses and lead losses. These preliminary curves serve only to give a rough idea of what sort of losses might be expected during actual experimental conditions; because the effects of current amplitude and frequency variation have not yet been separated, no detailed conclusions can be drawn. It is clear that there are no obvious anomalous fluctuations in these energy loss curves, such as were caused by the metallic dewar for the 7 kJ coil.

c. Electronic Loss Measurements on the 100 kJ Coil

The first major task undertaken was the measurement of coil losses at relatively low power levels by means of ringing experiments. These were accomplished by charging a capacitor and switching it onto the coil using either a spark gap or the vacuum interrupter (Figure 89(b)) and using the electronic technique to measure losses. A typical loss loop (actually a nested set of loss loops) is shown in Figure 120. A cross check on the electronic (loss loop) measurements was provided by an observation of the rate of decay of the oscillating coil current because, for these low power measurements, the external (lead) losses were less than one percent of the coil losses. The energy loss per half cycle was obtained from the coil current waveform by calculating the change in energy associated with the change (decay) in current from one cycle to the next

$$\Delta E = \frac{1}{2} L \left[i_{\max-1}^2 - i_{\max-2}^2 \right] \quad \text{III-7-1}$$

and then dividing by two in order to find the energy loss per half cycle (one charge-discharge cycle). A summary of the loss data obtained by all methods is given in Figures 121 and 122; in all cases the agreement between the loss loop method and the current decay method is within experimental error. It should be noted that the losses measured when the spark gap was used as the switch were much higher than those measured when the vacuum interrupter was used. It was found that the spark gap

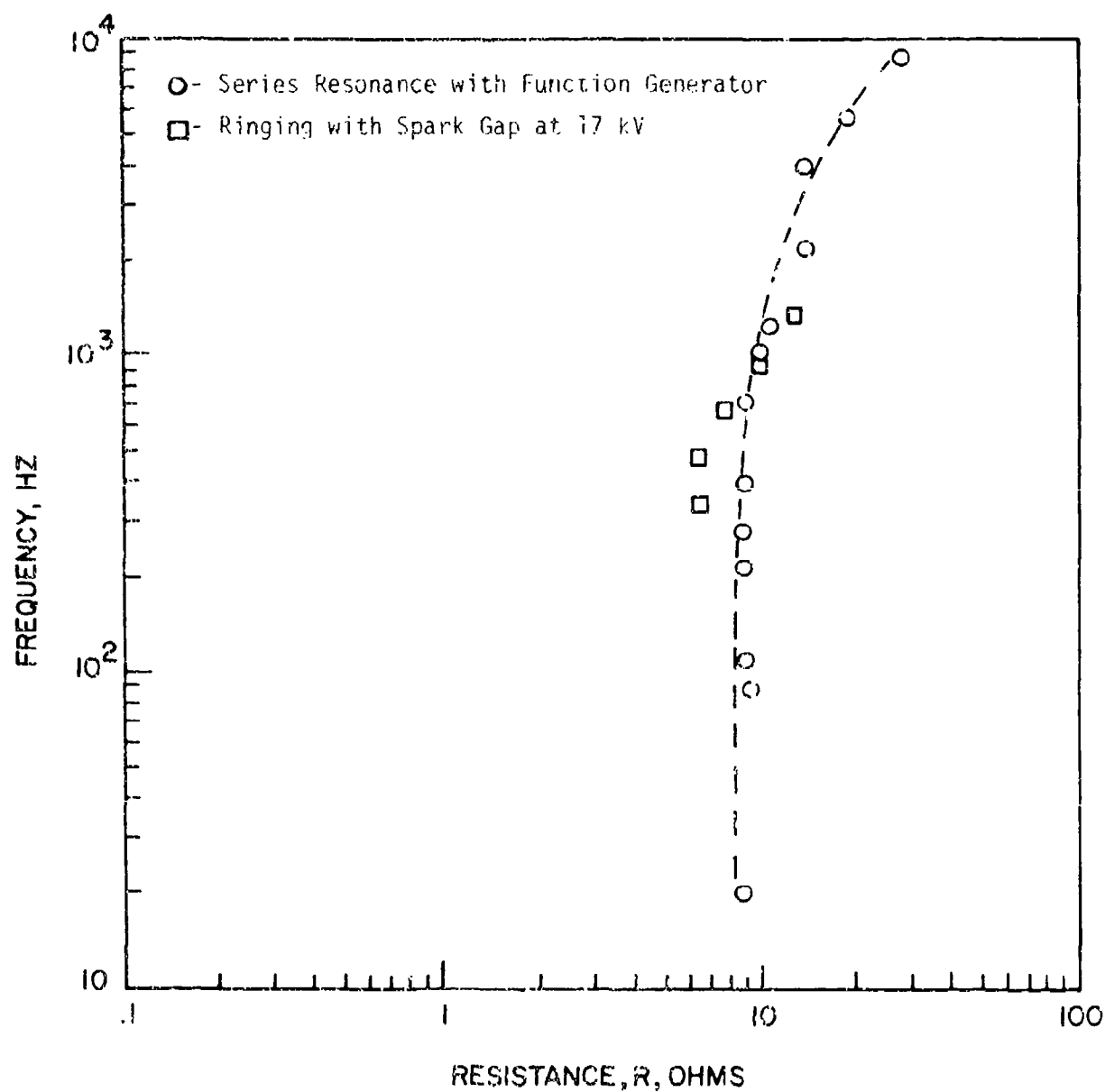


Figure 117 Equivalent Loss Resistance of 100 kJ Coil at Room Temperature.

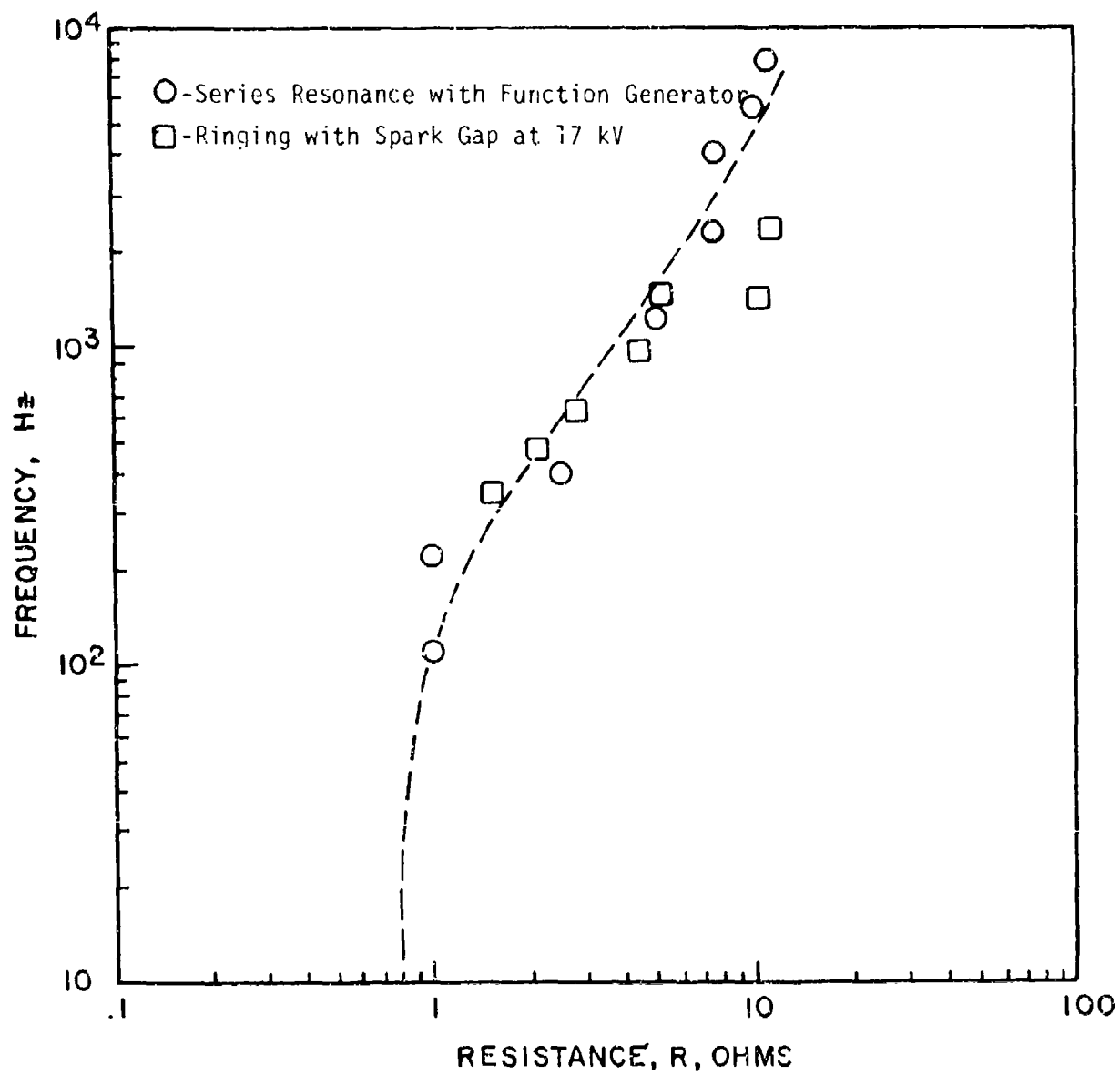


Figure 118 Equivalent Loss Resistance for 100 kJ Coil at 77 K.

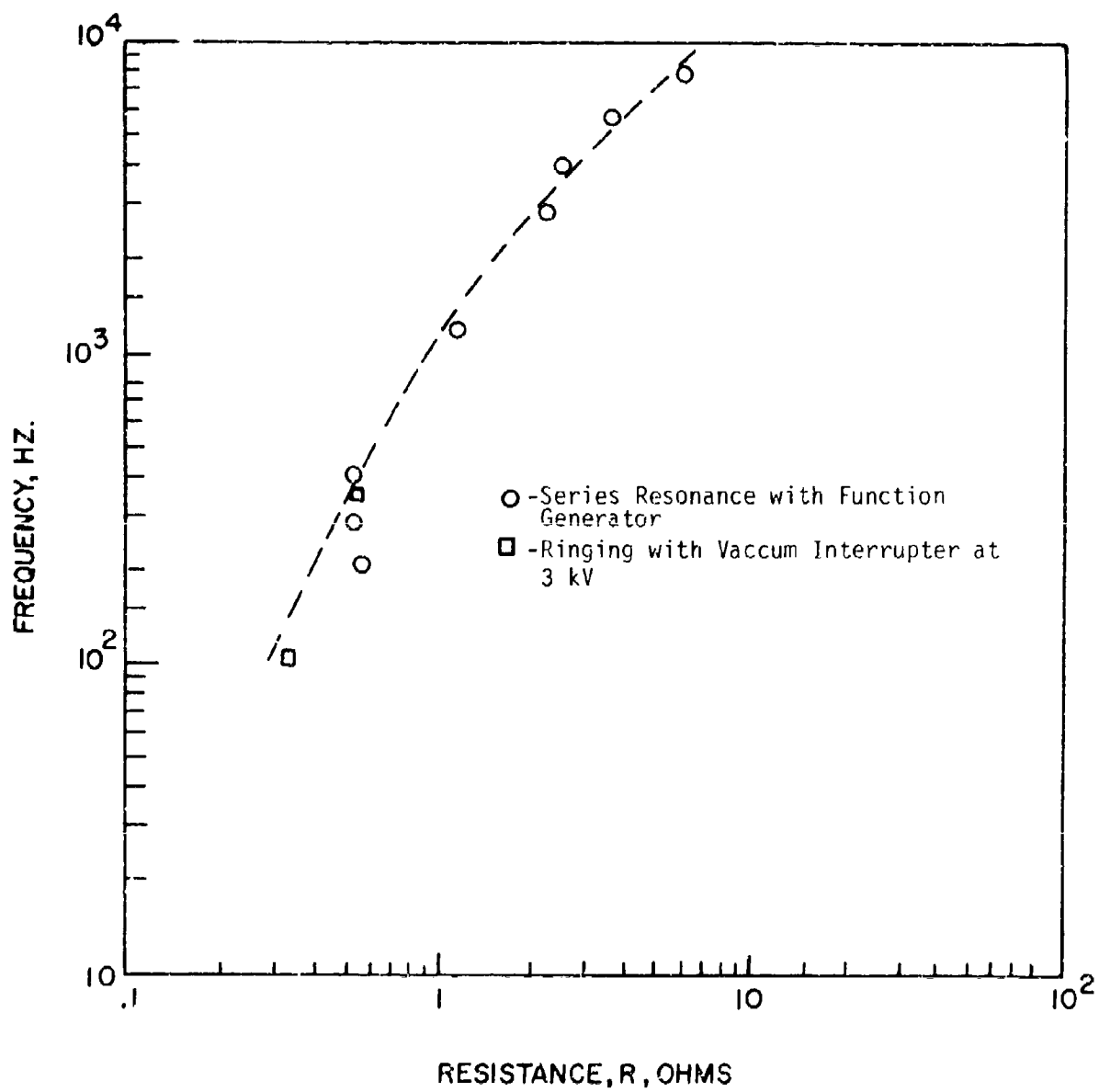
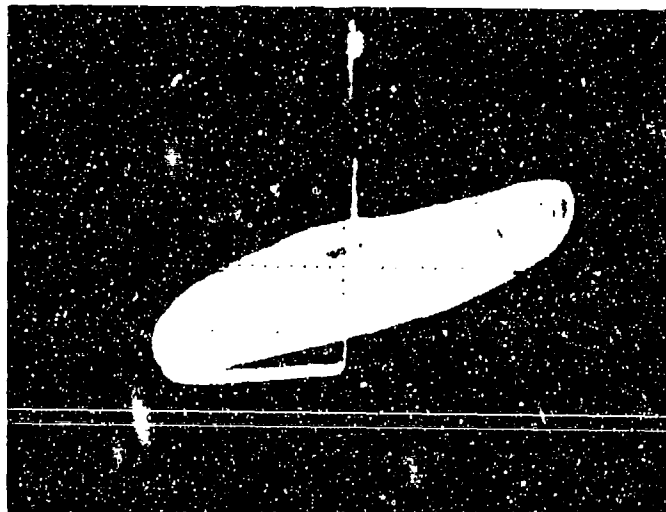


Figure 119 Equivalent Loss Resistance for 100 kJ Coil at 4.2 K.

Integrated Error Voltage 100 mV/cm



Current 200 A/cm

Figure 120

Loss loop for a 100 kJ coil during ringing test. Capacitor, 1,125 μ F; voltage, 4,000 V; divider fraction, 0.237; integrator time constant, 33 ms.

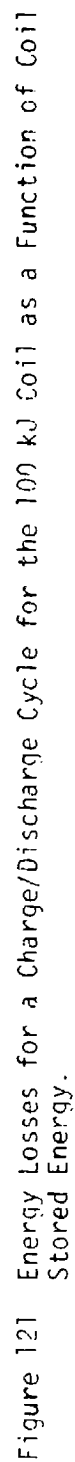


Figure 121 Energy Losses for a Charge/Discharge Cycle for the 100 kJ Coil as a Function of Coil Stored Energy.

Switch	Measurement Method
○ Vacuum Interrupter	Electronic (Loss Loop)
□ Vacuum Interrupter	Decay of Oscillating Coil Current
△ Spark Gap	Electronic (Loss Loop)
◇ Spark Gap	Decay of Oscillating Coil Current

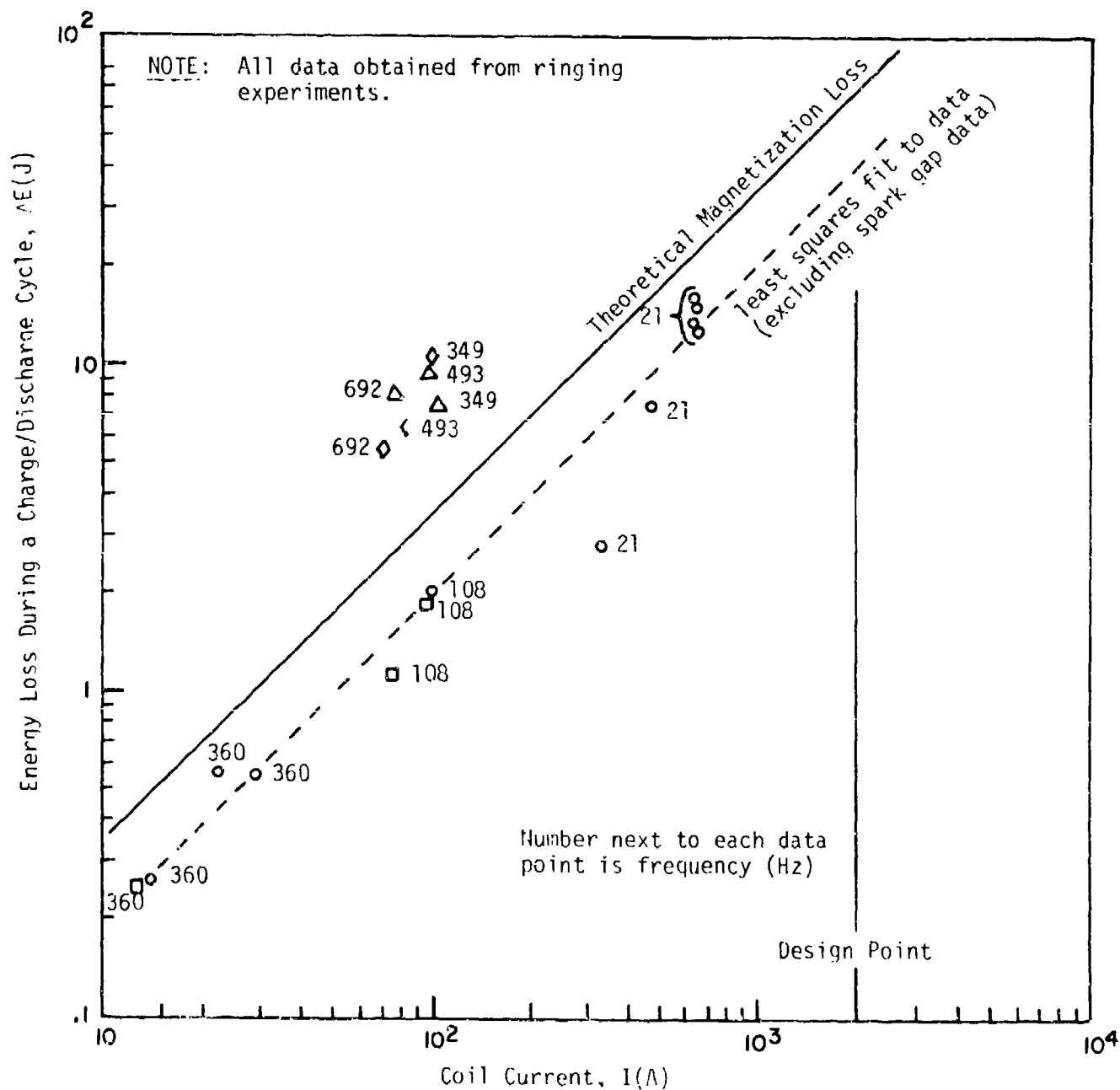


Figure 122 Energy Losses for a Charge/Discharge Cycle for the 100 kJ Coil as a Function of Coil Current.

produced voltage spikes on the coil which made accurate loss measurements difficult to obtain (experimentally); the accurate measurements we did succeed in obtaining (plotted in Figures 121 and 122) gave losses which were much higher than those obtained when operating with the vacuum breaker as a switch. (A possible explanation for this is given in Section III-7-d, Summary and Interpretation.) Because of the difficulty encountered in making measurements using the spark gap, most of the data was obtained with the vacuum interrupter as the switch.

d. Summary and Interpretation

Since it was not possible, because of electrical circuit limitations, to repetitively pulse the 100 kJ coil and make boiloff measurements, loss measurements were made by using the electronic device which had been successfully used in evaluating the 7 kJ coil. Since the 100 kJ coil dewar is non-conducting no complications arose concerning magnetic coupling with the dewar walls. It was therefore possible to discharge capacitors into the coil and obtain hysteresis loops over a range of frequencies and stored energies. At high frequencies the energy losses due to resistive heating in the leads and the external circuitry are small in comparison with the magnetization losses in the coil so it was possible to cross check the losses inferred from the hysteresis loops by observing the rate of decay of current during ringing between the coil and the capacitor. Losses were obtained by both of the above methods by using both a vacuum breaker and a spark gap as the closing switch. While losses as measured by hysteresis loops and ringing with a particular switch were self consistent, the losses measured when the spark gap was used were much higher than the losses measured when the vacuum breaker was used. (An explanation for this initially apparent inconsistency is offered later in this section.) The trend of the data taken using the vacuum breaker was such that it was always less than the losses predicted for magnetization effects. This is consistent with measurements made on the 1 and 7 kJ coils and also with previously suggested reasons as to why the theory predicting magnetization losses overestimate these losses.

There is insufficient data to draw firm conclusions concerning the mechanism of the losses occurring in the coil. However, based on the data taken the following argument is put forward as an interpretation of the results. Figure 123 shows the same data as is shown in Figure 121 except that the trend lines have been drawn through data points representing losses taken at similar frequencies. On this basis the points taken using the spark gap as a switch fall on a line drawn through points taken at similar frequencies using the vacuum breaker as a switch. The trend is such that at the same frequency losses increase with increasing coil current (or coil stored energy) and that at the same coil current (or coil stored energy) losses increase with increasing frequency.

Consider the line through a number of points taken at constant frequency; at low coil energies the measured loss is below that predicted for magnetization alone and the lower the coil stored energy the greater is the difference. The theoretical model as previously indicated assumes full penetration of the conductor by the field. This is valid

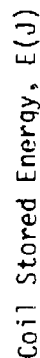


Figure 123 Energy Losses for a Charge/Discharge Cycle for the 100 kJ Coil as a Function of Coil Stored Energy Showing Loss Trend Lines as a Function of Frequency.

at higher fields but becomes less and less accurate as the field is decreased, i.e., at lower currents. This is consistent with the data. As the coil energy increases (again at constant frequency) the measured losses tend to rise above the theoretical curve for magnetization loss alone. This would indicate that parts of the coil are going normal and that the measured loss contains a contribution from a transport current loss.

Consider now a series of loss curves at different frequencies. It can be seen that the higher the frequency then the lower is the coil current at which the loss curves cross the theoretical magnetization loss curve. In other words, on the basis of the hypothesis made above, the transport current losses become significant at higher coil currents as the frequency is decreased. In the limit at very long charge and discharge times they would never become significant because none of the conductor in the coil would go normal. This is because the slower the charge time the lower is the power generation due to magnetization losses and therefore the lower is the heat flux into the liquid helium. As the charge time is decreased (increasing frequency) the conductor in the high field regions generates more power than can be dissipated in the helium on a steady state basis and goes normal. Further decreases in charge time cause conductor in lower field regions to go normal. Thus the shorter the charge time (the higher the frequency) the greater is the proportion of conductor in the coil going normal.

The data points taken by the electronic technique on the 7 kJ coil (see Figure 107) were all taken at the same frequency and these points follow a curve having a similar slope to the constant frequency loss curves shown in Figure 123. The two coils were built using the same conductor and a similar construction technique and so can be expected to behave in a similar way. This data tends to reinforce the argument outlined above concerning the interpretation of the 100 kJ coil data.

Thus the 100 kJ coil loss data is strongly suggestive of the model just described but as was indicated in the remarks prefacing the argument the data upon which the argument was based is scanty. The model can only be confirmed by testing further and obtaining more extensive data.

8. MULTIPLE PULSE TESTS

a. Philosophy

In preparing for pulsed operation with a superconducting coil, it becomes clear very early that the reduction of energy losses in the coil due to magnetization and to eddy currents is of utmost importance. In the design of a light weight system, the energy losses determine the quantity of cryogen that is required for the performance of a given mission and hence determine the amount of weight that must be devoted to the dewar. As has been previously determined (1, 19), the cryogen and the dewar represent the dominant weights of a typical system. The energy losses also determine the practical limits of applicability of a superconducting coil because of the requirement that the energy be removed from the conductor rapidly enough to permit the coil to remain

superconducting. A sizeable fraction of this report has been devoted to the design of a conductor (braided 4.5 mil wire) that would minimize losses, and to the determination of a coil configuration that fulfills the requirements for optimum cooling and for the ability to store 100 kJ at a rather low magnetic field.

In the experiments to be discussed, an alternative procedure for extracting a train of fast pulses from a superconducting energy storage coil is explored. This procedure consists of using the coil as an energy reservoir which is discharged slowly into a capacitor which must store only enough energy for a single output pulse, discharging the capacitor into the load at very high speeds and currents, then repeating the cycle until the energy supply of the coil has been exhausted. In this mode of operation, both the superconducting coil and the capacitor are used to best advantage. The coil becomes a compact reservoir of energy; the capacitor forms a very fast, high power pulse whose rise time is no longer limited by coil losses or by coil switching considerations. Because the coil is cycled slowly, eddy current losses become negligible and magnetization losses are reduced, thus permitting the design of a compact configuration that operates at a higher magnetic field and employs a simplified conductor design. Because the primary task of the coil in this arrangement is to charge a capacitor, the switch design problem is much simplified because both the required coil current and the rate of rise of coil voltage are reduced. With this arrangement, it is also possible to produce output pulses of almost any desired shape because the capacitor can be replaced by a pulse forming network.

The range of applicability for this pulse forming technique has not been evaluated for this report and should be the subject of a separate study. The factors to be considered include a trade off between the potential reductions in coil size and weight, quantity of cryogen, and dewar size and weight, and the additional weight of the capacitors required to form a single pulse. It must also be determined whether it would be necessary to add a pulse transformer to the system to match a load requiring extremely high voltages (several hundred kilovolts). Such a parametric study could be fairly lengthy and as a consequence is not undertaken here; our present purpose is to enumerate the more important factors to be considered in such a study.

During the course of the developmental program that is the principal topic of this report, we recognized an opportunity to test the feasibility of the above described technique for extracting fast pulses from an energy storage coil. The only significant technical problem to be overcome is the realization of a closing switch for connecting the capacitor, which stores sufficient energy for a single pulse, to the load. It is necessary that this switch fire reliably at a prescribed voltage, that it carry at least a few tens of kiloamps, and that it recover its blocking state rapidly enough to permit recharge of the capacitor from the coil for the next pulse. As is explained in Section b below, the particular coil and capacitors available to us established that the switch recovery time must be no greater than 100

microseconds. We developed such a switch and extracted a string of fast (250 microsecond) high energy (2.6 kJ) pulses from the 100 kJ coil at a repetition rate of about 200 Hertz.

b. Design and Testing of Electric Circuit and of Switch for Pulsed Operations

Having established that operation of the 100 kJ coil at a power level of 25 kJ and at moderate voltages (a few kilovolts) was smooth, we tested the technique for producing a series of fast (250 microsecond) high energy (2.6 kJ average) pulses at repetition rates as high as 200 Hertz. This technique consisted of forming a relaxation oscillator using the 100 kJ coil as a current source, a capacitor (1125 μ F) to store the energy for a single pulse, and a helium discharge switch of our own design. A schematic of the electric circuit is given in Figure 124, the basic circuit design is outlined in Appendix VIII, a schematic of the helium switch is given in Figure 125, a photograph is given in Figure 126, and the train of pulses obtained is shown in Figure 127. The repetition rates and amplitudes of the pulses were as predicted except for the first pulse.

The crucial item in this pulse forming experiment is the switch. This must fire reliably at a preset voltage, switch currents of 15,000 amps or more, and recover its blocking ability in not more than ten percent of the 2.4 millisecond interpulse time available (for the first few pulses). In view of these requirements, helium gas was selected because electrical breakdown occurs in helium at the desired voltage (2,000 volts) at easily controllable electrode spacings (of order one centimeter); carbon electrodes were selected to carry the required currents. To minimize recovery time, the helium gas is passed through the switch at a high velocity in order to physically remove the ions from the vicinity of the electrodes. For this "helium blast" to be effective in removing ions, it is necessary to halt ion production by forcing the switch current to zero for a reasonable length of time by means of a suitable arc quench circuit. The design of an appropriate arc quench circuit is outlined in Appendix IX and its position in the overall circuit is shown in Figure 124. Because a pulse repetition rate of 1,000 Hertz was anticipated (for 100 kJ in the coil), it was assumed that the switch could be made to recover in 100 microseconds or less; the arc quench circuit was designed accordingly. While definitive measurements of the recovery time of this switch have not been made, its successful operation in the circuit of Figure 124 shows that the recovery time is less than 100 microseconds. The details of a single pulse are shown in Figures 128 and 129; from these photographs it can be seen that the arc quench circuit forces the switch current to zero and that the switch recovers rapidly.

c. Suggested Future Work

Because the capabilities of the helium switch were not fully evaluated, it is clear that one important task is to complete the evaluation of this switch. In view of its simplicity, it would be worthwhile to explore the operating characteristics of this switch

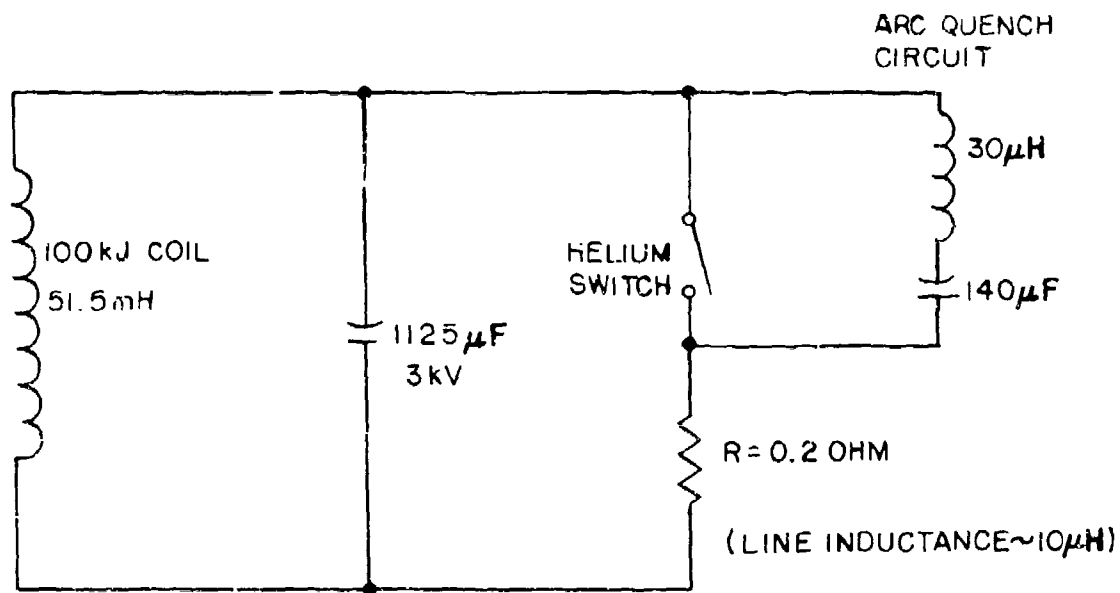


Figure 124 Circuit Used to Extract Train of Pulses from 100 kJ Coil with Helium Switch.

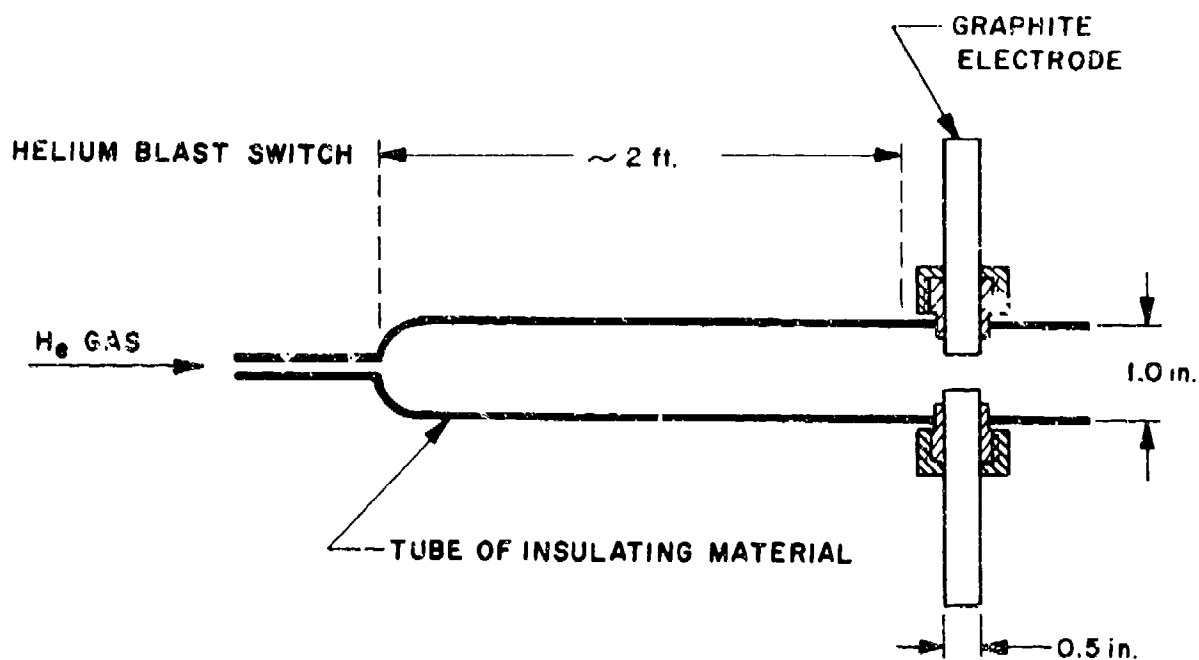


Figure 125(a) Schematic of Helium Blast Switch

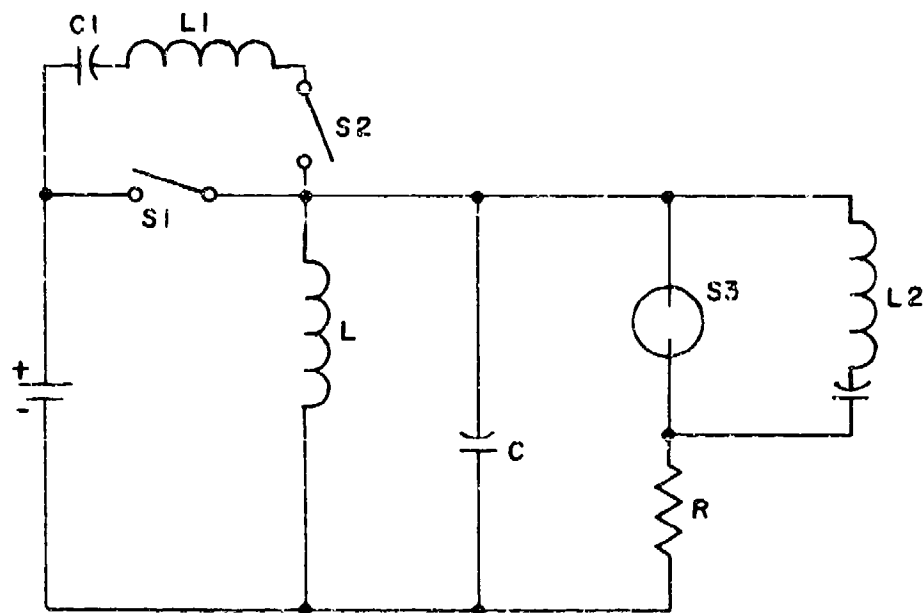


Figure 125(b) High Repetition Rate Pulse Circuit

The vacuum interrupter is denoted by $S1$ and the components of its arc quench circuit are $C1$, $L1$, and $S2$ (spark gap). The Helium Switch is denoted by $S3$ and its arc quench circuit consists of $L2$ and $C2$. The coil has L of 51.5 mH ; C is $1125 \text{ } \mu\text{F}$; $R \approx 0.2 \text{ ohm}$.

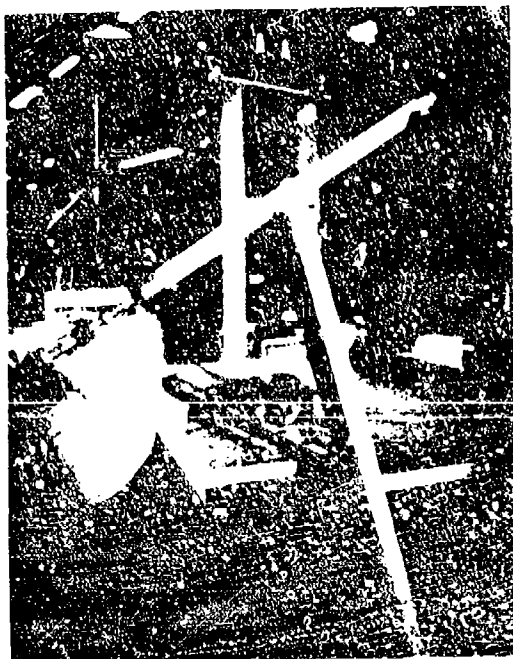
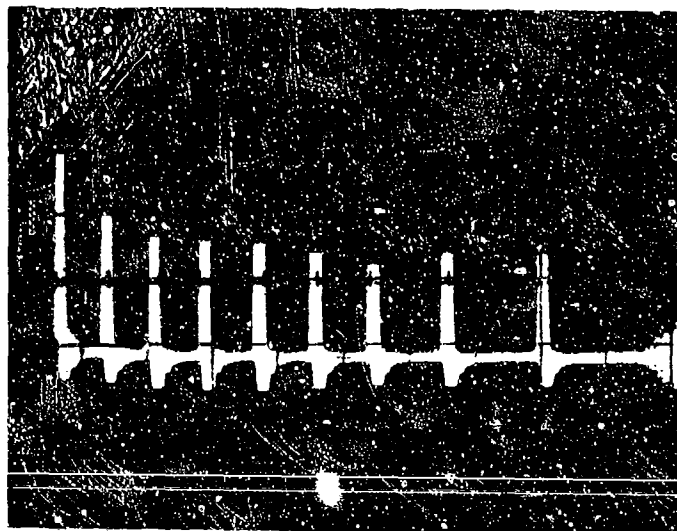


Figure 126 Photograph of Helium Switch.

Load Current 5,000 A/cm

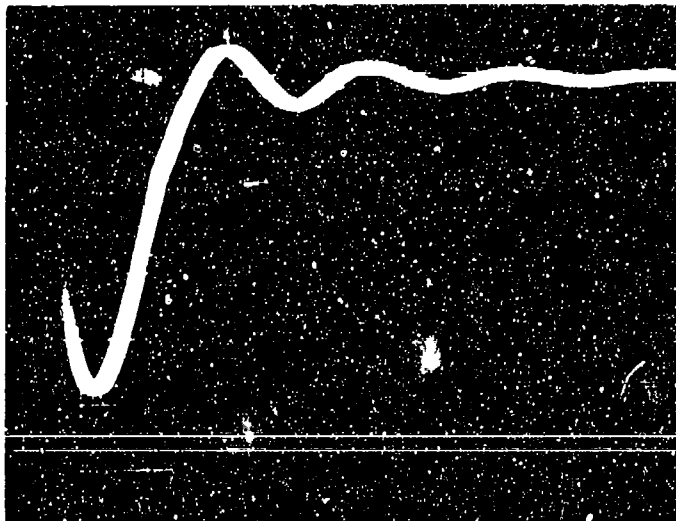


Time 5 nns/cm

Figure 127

Pulses extracted from a 100 kJ coil with helium switch. Total energy - 24 kJ; average pulse energy - 2.67 kJ.

Load Current 2,000 A/cm

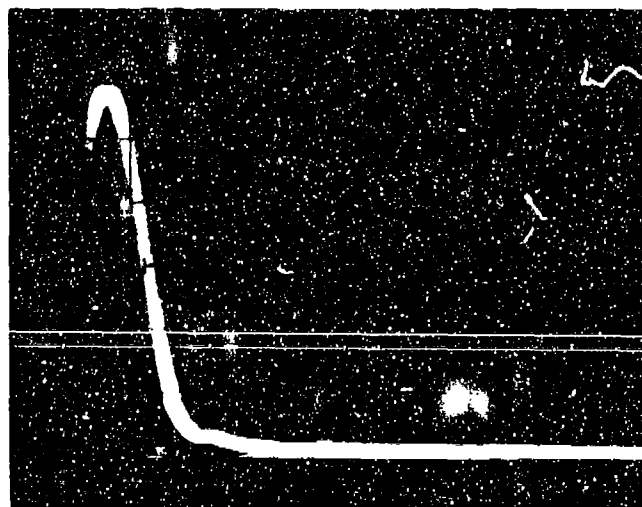


Time 0.2 ms/cm

Figure 128

Single pulse of current to 0.2 Ω load
delivered by helium switch. Firing
voltage - 2,000 V.

Switch Current 2,000 A/cm



Time 0.2 ns/cm

Figure 129

Single pulse of current through the helium switch (includes load current and first half cycle of the arc quench current). Load resistance, 0.2 Ω ; firing voltage, 2,000 V.

with different gases in order to check various ranges of voltage and of recovery speeds. It would be desirable to determine switch recovery rate as a function of current density, total pulse energy, gas flow velocity, and gas species. In addition, it would be useful to evaluate a triggered version of this switch in order to obtain precise control of the firing voltage. Finally, it would be of interest to perform the parametric systems study outlined in Section III-8-a, Philosophy, in order to establish the type of application for which this pulse forming technique is best suited.

REFERENCES

1. Lucas, E. J., Punchard, W. F. B., Thome, R. J., Development of Pulsed High Energy Inductive Storage System, Technical Report AFAPL-TR-72-38, Vol. I (December 1972).
2. Stekly, Z. J. J., Lucas, E. J., Thome, R. J., de Winter, T. A., Inductive Energy Storage System Study, Technical Report AFAPL-TR-69-101 (December 1969).
3. Gareis, P. J., Stern, S. A., Bull. l'Inst. Intern. du Froid, Annex 1966-65, p. 429.
4. Powers, R. J., Chambers, R. M., J. Vac. Sci. Technol., 8, 1, p. 319 (1971).
5. Scott, J. P., "Current Leads for Use in Liquid Helium Cryostats", Proc. ICEC3, p. 176, Berlin (May 1970).
6. Cobine, J. D., Gaseous Conductors, Theory and Engineering Applications, "Section 7.8, The Sparking Potential", Dover Publications, Inc., New York, 1958.
7. Gerhold, J., "Dielectric Breakdown of Helium at Low Temperatures", Cryogenics, October 1972.
8. Alston, L. L., High Voltage Technology, Oxford University Press.
9. Kantrowitz, A. R., Stekly, Z. J. J., Appl. Phys. Lett., 6, 56 (1965).
10. Wilson, M. N., Walters, C. R., Lewin, J. D., Smith, P. F., J. Phys. D. (Appl. Phys.), 3, 1518 (1970).
11. Grover, F. W., Inductance Calculations: Working Formulas and Tables, Chapter 13, Dover Publications, Inc., New York.
12. Carslaw, H. S., Jaeger, J. C., Conduction of Heat in Solids, 2nd ed., pp. 124, 132, Oxford University Press, 1959.
13. Smith, R. V., "Review of Heat Transfer to Helium I", Proc. 1968 Summer Study on Superconducting Devices and Accelerators, p. 249, Brookhaven National Laboratory.
14. Johannes, C., "Recent Advances in Heat Transfer to Helium I", Proc. ICEC3, p. 97, Berlin (May 1970).
15. Bean, C. P., Phys. Rev. Lett., 8, 250 (1962).
16. Bean, C. P., et al., A Research Investigation of the Factors that Affect The Superconducting Properties of Materials, Technical Report AFML-TR-65-431, (March 1966).

REFERENCES (Continued)

17. Wilson, M. N., "An Improved Technique for Measuring Hysteresis Loss in Superconducting Magnets," *Cryogenics*, June 1972.
18. Greene, J. D., Tobey, G. E., Huelsman, L. P., Operational Amplifiers, Design and Application, McGraw Hill Book Company, New York, 1971.
19. Lucas, E. J., Punchard, W. F. B., Thome, R. J., Development of Pulsed High Energy Inductive Energy Storage System, Vol. III, Weight Optimization for Energy Storage Coil, Cryogen and Dewar, Technical Report AFAPL-TR-72-38, Vol. III (December 1972).
20. Williams, J. E. C., Superconductivity and Its Applications, Chapter 8, Hard Superconductors, p. 66, Pion Limited, London 1970.
21. Wilson, M. N., Walters, C. R., Lewin, J. D., Smith, P. F., Spurway, A. H., Experimental and Theoretical Studies of Filamentary Superconducting Composites, Rutherford Laboratory Preprint, RPP/A73, Nov. 1969, Paper II, Walters, C. R., "Stability and Flux Penetration in Multifilament Systems."

APPENDIX I

PREDICTED LOSSES IN SUPERCONDUCTORS

The basic model used as a starting point for the analysis of losses in a superconductor is a simple phenomenological model due to Bean (15, 16). This model allows predictions to be made concerning the magnetic behavior of a high field superconductor in terms of a single empirical parameter, the critical current density, j_c .

A superconductor cooled through the superconducting transition temperature with no current flowing through it in the absence of a magnetic field has j_c zero everywhere. However, as soon as a magnetic field is applied (either by applying a background field or by forcing a current through the wire), an electric field E is generated according to the Maxwell relation $\nabla \times E = -\dot{B}$. This electric field induces a current flow in the superconductor. The critical state model assumes that any electric field E no matter how small causes the critical current density j_c to flow in the direction of the E vector in regions of the superconductor. In other words, the model assumes a non-linear E, j relationship such that E is zero for current densities less than j_c but rises vertically at j_c with the E and j vectors parallel, as shown in Figure 130. The interaction between the electric field E and the critical current density j_c gives a local power dissipation $P = E \cdot j_c$. The computation of the energy losses therefore reduces to the problem of calculating the electric field and the critical current density locally and then integrating suitably over space and time.

To estimate the magnetization losses in a superconductor let us first consider a layer of superconductors of rectangular shape as shown in Figure 131. The thickness of each is $2a$ and the length h . The analysis will be performed for the situation where the magnetic field is parallel to the long dimension h (i.e. parallel to the layer). This is the situation which would exist near the median plane of a long solenoid or in a toroidal winding, and is an approximation for other geometries.

First consider the situation when the layer of superconductors carrying no transport current is immersed in a uniform magnetic field. When the field is at zero no currents flow in the superconductor but as soon as the field increases currents are induced in the superconductor in such a direction as to shield the interior of the conductor from the applied field. This situation is depicted in Figure 132.

The magnitude of the induced current density is (according to the critical state model) j_c , and j_c is determined only by the local ambient field. We make the simplifying assumption that the variation of B across the specimen is small and can be characterized by the external applied field, B_e . This is a good approximation in situations of practical interest e.g. a small diameter wire which is part of a coil consisting of many layers. In this case, 1) the contribution of the wire to the total field is small and 2) because of its small diameter the conductor is fully penetrated for small differences in field between the center of the wire and the outer diameter of the wire.

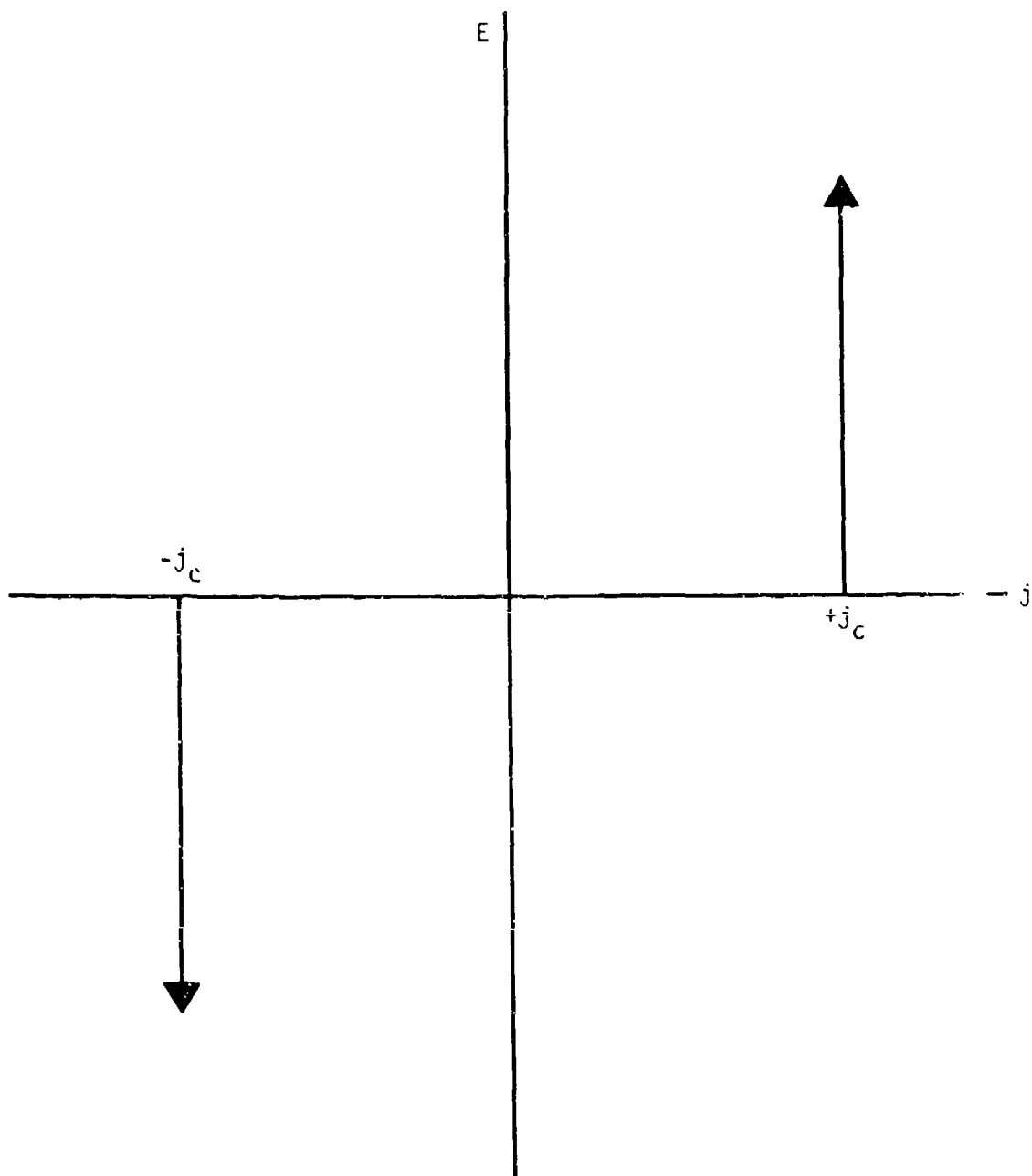


Figure 130. Schematic Illustrating the Non-Linear Electric Field-Current Density Characteristic of the Critical State Model of a Superconductor.

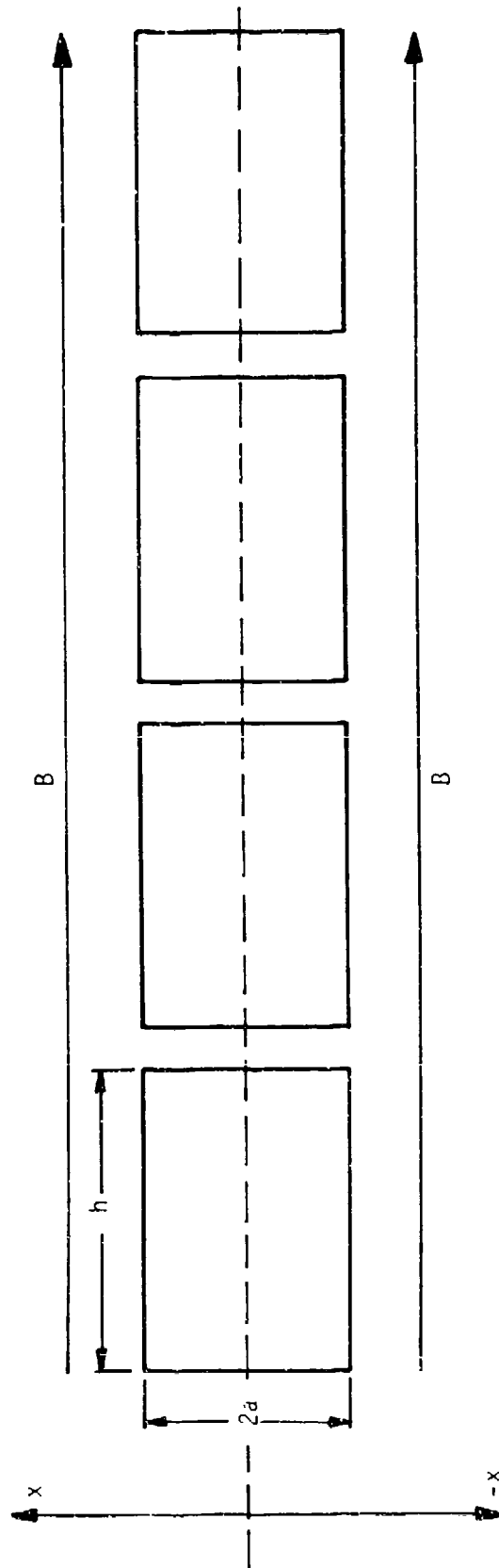


Figure 131. Schematic Showing a Layer of Rectangular Superconductors Immersed in a Background Field B which is Parallel to the Layer.

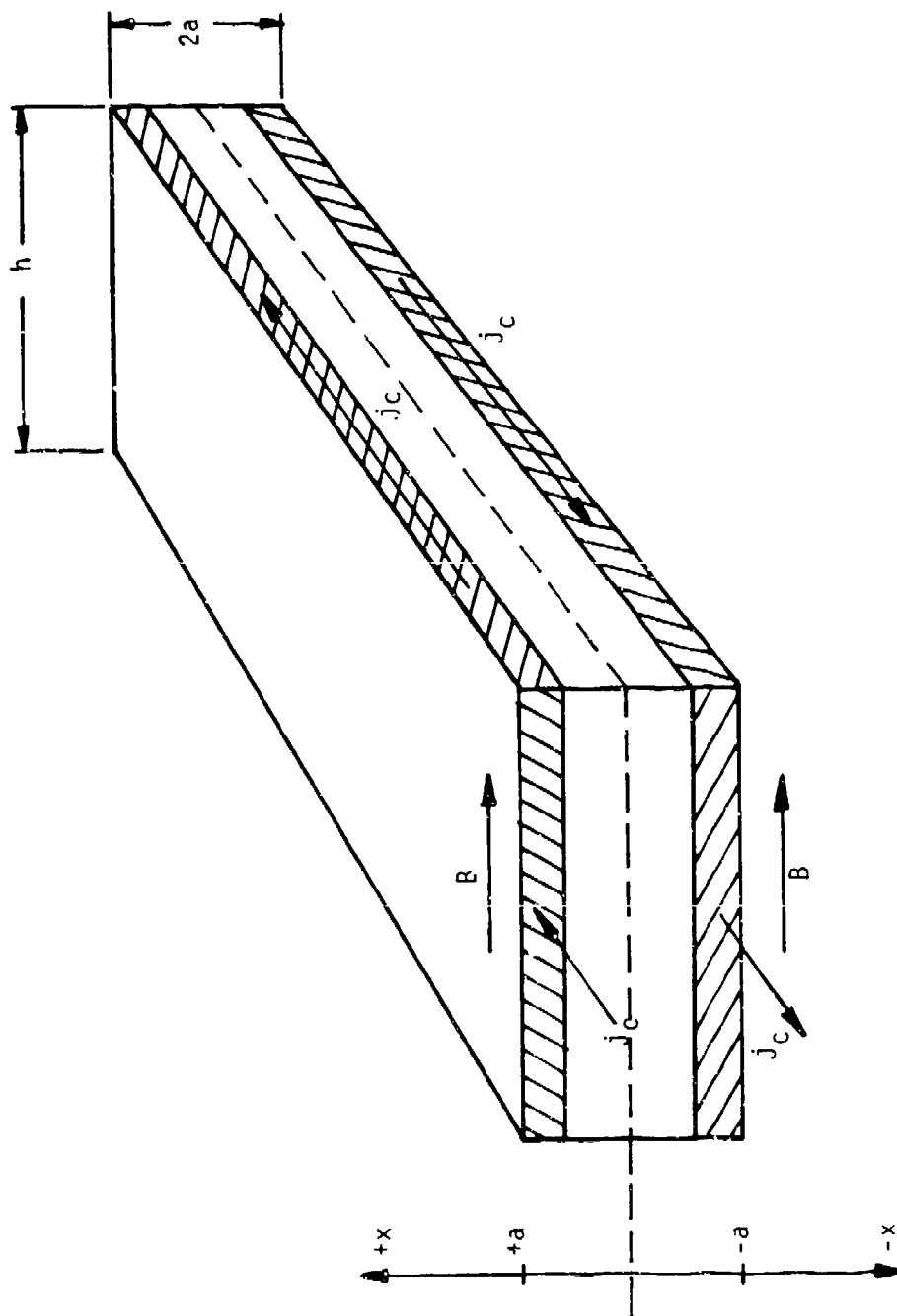


Figure 132. Schematic Illustrating the Shielding Currents Induced on the Surfaces of a Superconductor Immersed in a Field which Rises from Zero to B .

As the external field rises, flux penetrates from the outside of the wire, and the region occupied by the critical current density extends farther and farther into the wire from the outside edge. The profile of flux density in the wire is given by the Maxwell relation $\nabla \times \mathbf{B} = -\mu_0 \mathbf{j}_c$.

Initially the critical currents occupy a region near the outside edge but eventually as the applied field is increased more and more they extend to the center of the wire. Until this point is reached the external flux is completely shielded from the inside of the wire. However, after this point is reached, the external field is incompletely shielded. In fact after this point the shielded field becomes smaller and smaller because as the ambient field is increased the magnitude of the critical current density decreases (see Figure 133 which is a typical $B - j_c$ curve for a superconductor). Eventually at the upper critical field B_c the critical current density is zero, and the external field is not shielded at all. At this point no superelectrons are left to carry current and the specimen reverts to the normal state. The sequence of events described in the above paragraph is depicted schematically in Figure 134. The upper half of the figure shows the profiles of flux density and the lower half the regions occupied by the critical currents and their magnitudes as the external field is increased from zero to the upper critical field B_c . The reference numbers in this figure refer to the points shown on the $B - j_c$ curve in Figure 133. It should be noted that this model ignores the fact that at fields below H_{c1} (the lower critical field) critical currents flow on the surface of superconductor and no flux penetration occurs (20). However, for niobium titanium, H_{c1} is of the order of a few hundred gauss and therefore the model is valid for cases of practical interest.

We will now derive an expression for the electric field as a function of position in the superconductor using the Maxwell relationship

$$\nabla \times \mathbf{E} = -\dot{\mathbf{B}}$$

Since we are considering a one-dimensional case, i.e., that of a slab of superconductor with the applied field parallel to one face as shown in Figure 131 this reduces to

$$\frac{dE}{dx} = -\dot{B}$$

We assume that the variation of field across the conductor is small and that therefore each part of the superconductor is characterized by one value of magnetic field and to a first order the rate of change of magnetic field can be considered constant across the specimen. Then, integrating we obtain

$$E(x) = -Bx + C$$

where C is a constant.

The electric field vector, according to the critical state model, is always parallel to the direction of the critical current density. Since the critical current density changes sign in crossing from one side of the superconductor to the other, the electric field must also change sign. The point where it changes sign is therefore the line which separates regions of critical currents flowing in opposite directions. This concept of an electric

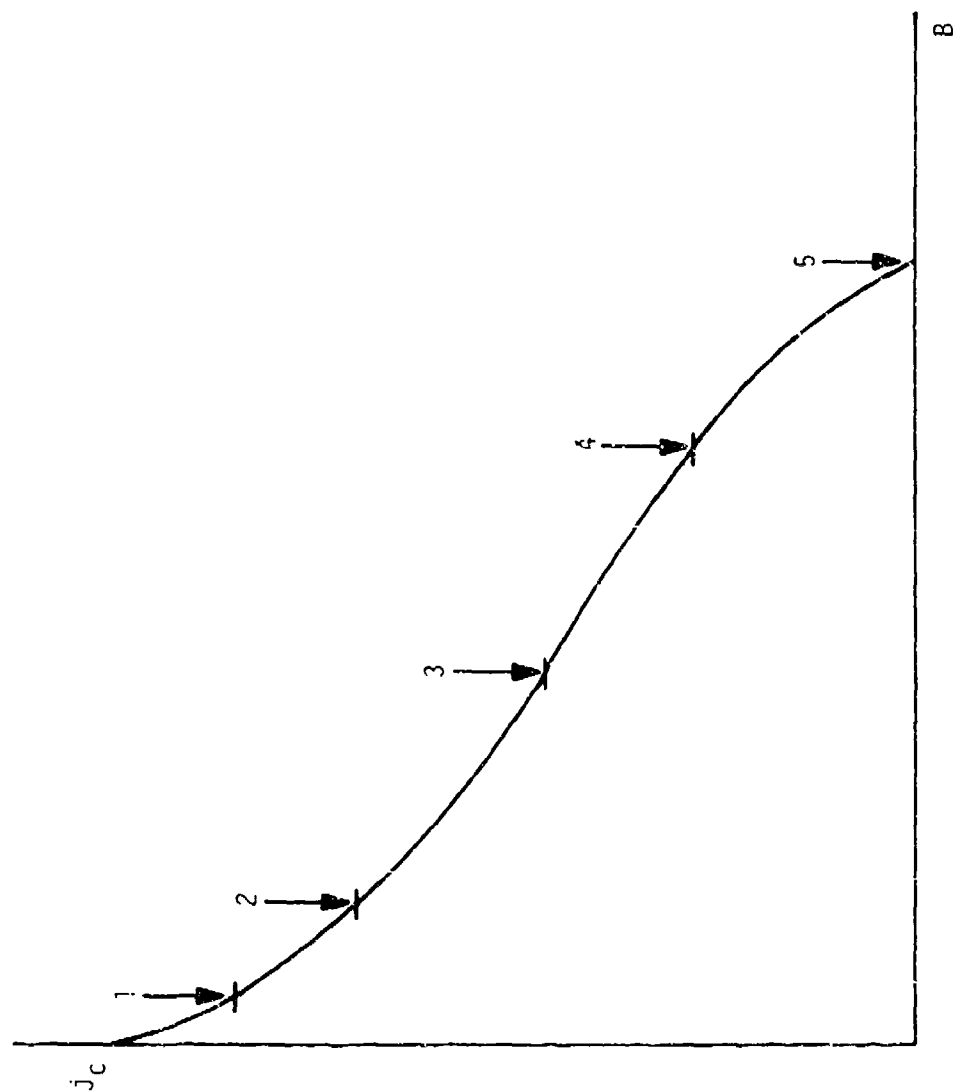


Figure 133. Schematic illustrating a Typical $B - j_c$ Curve for a Superconductor. The field penetration and current density profiles in a slab of superconductor corresponding to the points indicated can be seen in Figure 134.

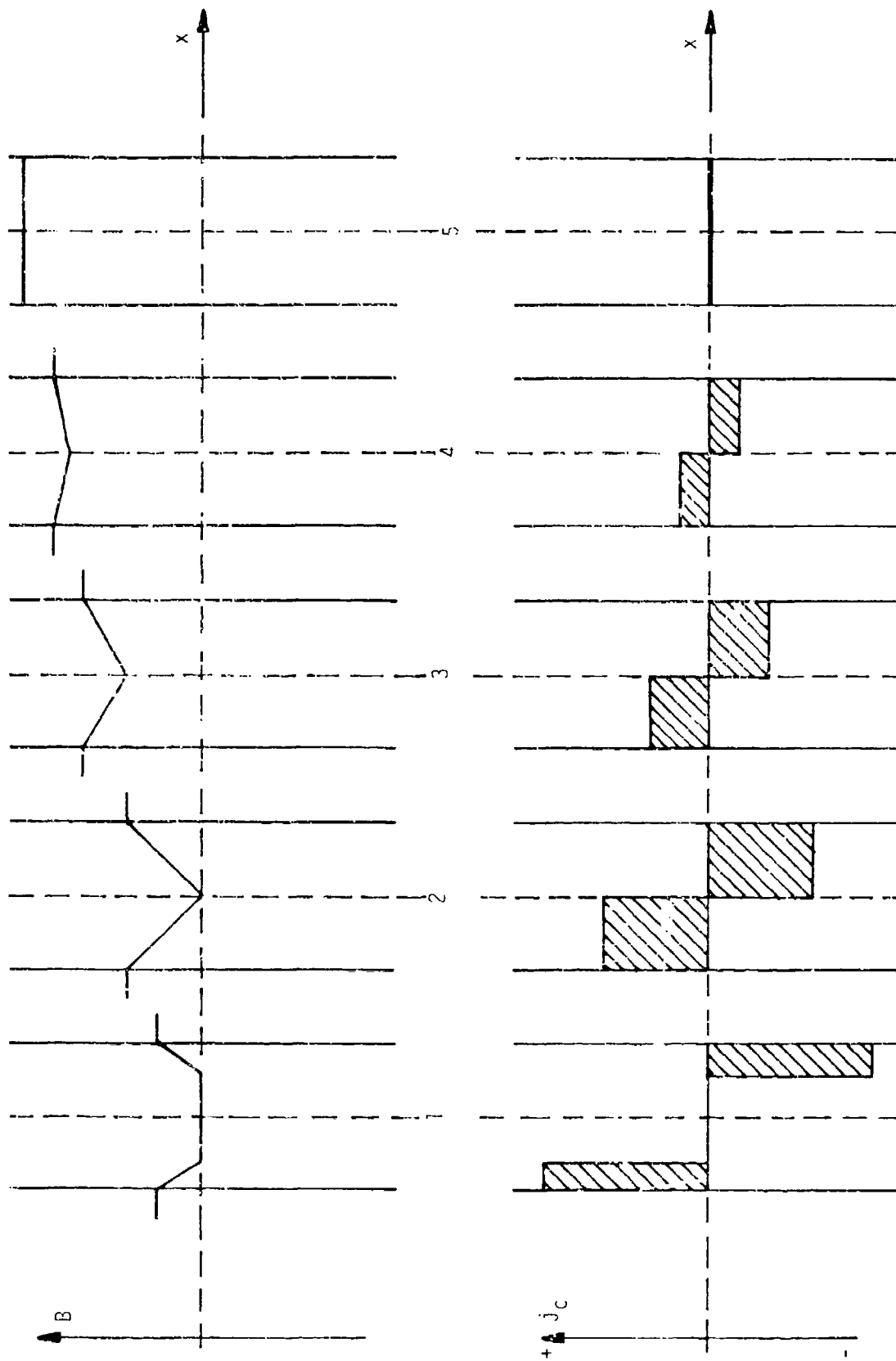


Figure i34. Schematic illustrating the field penetration profiles and critical current density distributions in a flat slab of superconductor as the field is raised from zero to the critical field. See also Figure i33 for points on the $B - j_c$ curve corresponding to the reference numbers above.

center along which the electric field is zero and across which no flux crosses is a useful one and is treated in more detail by Walters (21).

In the situation under consideration here this electric center, where $E = 0$, occurs at the center of the wire ($x = 0$) for applied fields high enough that full penetration has occurred. Therefore, the boundary condition is:

$$E = 0 \text{ at } x = 0$$

then,

$$C = 0$$

and

$$E(x) = -Bx$$

Then, the local power dissipation at a position x in the specimen is:

$$p(x) = E(x)j_c$$

$$p(x) = -Bj_c x$$

This expression could be integrated over the width of the specimen and over time to give the energy dissipated in the specimen. However, this would be of limited usefulness in a practical situation since the case considered so far is one in which no transport current is flowing. It has been dealt with at length only to serve as an introduction to the concepts involved and to outline, using a simple model, the procedure used to arrive at the local power dissipation.

Since eventually we intend to apply the results of the analysis to a coil carrying a transport current, we must modify the analysis to include the effects of a transport current on the distribution of critical current density, the distribution of flux density and on the position of the electric center.

We shall now consider the situation in which the superconductor carries a transport current in addition to being exposed to a background field. These are the conditions to which a wire in a coil is exposed. The presence of a transport current creates a difference in field strength between one side of the conductor and the other so that in contrast to the case treated above the field strengths on each side of the wire are different. Flux still penetrates from each side of the wire and therefore shielding currents are set up in a way similar to that previously described. The flux profiles are again given by the Maxwell relationship $\nabla \times B = -\mu_0 j_c$ and since we again assume that the flux density within the conductor is characterized by the value of the applied field, the rate of change of flux density with respect to distance within the specimen is the same as that given before. However, since now the boundary conditions are different on each side of the wire (the surface fields are different), the point of minimum field is no longer at the midplane of the coil and the shielding currents are no longer symmetrical about the midplane of the wire. Thus, the electric center is also shifted from the midplane.

Figure 135 shows the $B-j_c$ curve for a typical superconductor and also the load line ($B-j_t$ curve) for a conductor which is part of a coil. As the transport current density j_t is increased (points 1 to 5) the background field due to the rest of the coil seen by the specimen increases (points 1 to 5) and the critical current density (which is a function of the ambient field only) decreases. A sequence of flux density and current density profiles corresponding to the reference numbers in Figure 135 is shown in Figure 136.

Initially (point 1), the background field is zero and the transport current is zero. There is no field difference across the wire because of the zero transport current and the electric center is at the median plane. (Case 1 of Figure 136 shows a reverse field in the superconductor and a symmetrical critical current distribution. This is the situation that would exist if the specimen had been cycled from zero to a full reverse field and back to zero and illustrates the hysteretic nature of the properties of superconductors.)

Case 2 (Figures 135 and 136) shows the situation after some transport current is passed through the specimen. The background field due to the rest of the coil has risen. The transport current through the specimen creates fields which add to the background field on one side of the wire and subtract from it on the other side thereby giving a net field difference across the wire. The critical current density has decreased from Case 1 because the background field has risen. Because in our simplification the magnetic field in the wire is assumed to be characterized by the value of the external field (i.e., $\Delta B_{\text{wire}} \ll B_{\text{external}}$), the absolute value of the critical current density is constant across the wire and therefore the modulus of the rate of change of field with respect to distance within the wire

$$\left(\frac{dB}{dx}\right)$$

is also constant each side of the wire. Thus the electric center is shifted towards one side of the wire. The critical current density profile is now such that more critical current is flowing in one direction than in the other. The difference between these critical currents is merely the net transport current flowing. Also shown in Figure 136 is a representation of the transport current density j_t . The transport current density is defined as the transport current divided by the area of cross-section of the wire and is represented as filling the entire area of cross-section uniformly although, as explained above, the true current density distribution is as shown in the sketches representing the critical current density. However, as will become apparent later in the exposition, the transport current density so defined is a useful concept.

As the transport current is increased (points 3 and 4) of Figures 135 and 136 the magnitudes of the critical currents decrease (because of the increasing ambient fields), the electric center is further displaced and the transport current density increases.

Eventually (point 5 of Figures 135 and 136) the electric center reaches the edge of the specimen and the critical currents flow only in one direction (that of the transport current). At this point the magnitude of the transport current density is equal to that of the critical current density. This is

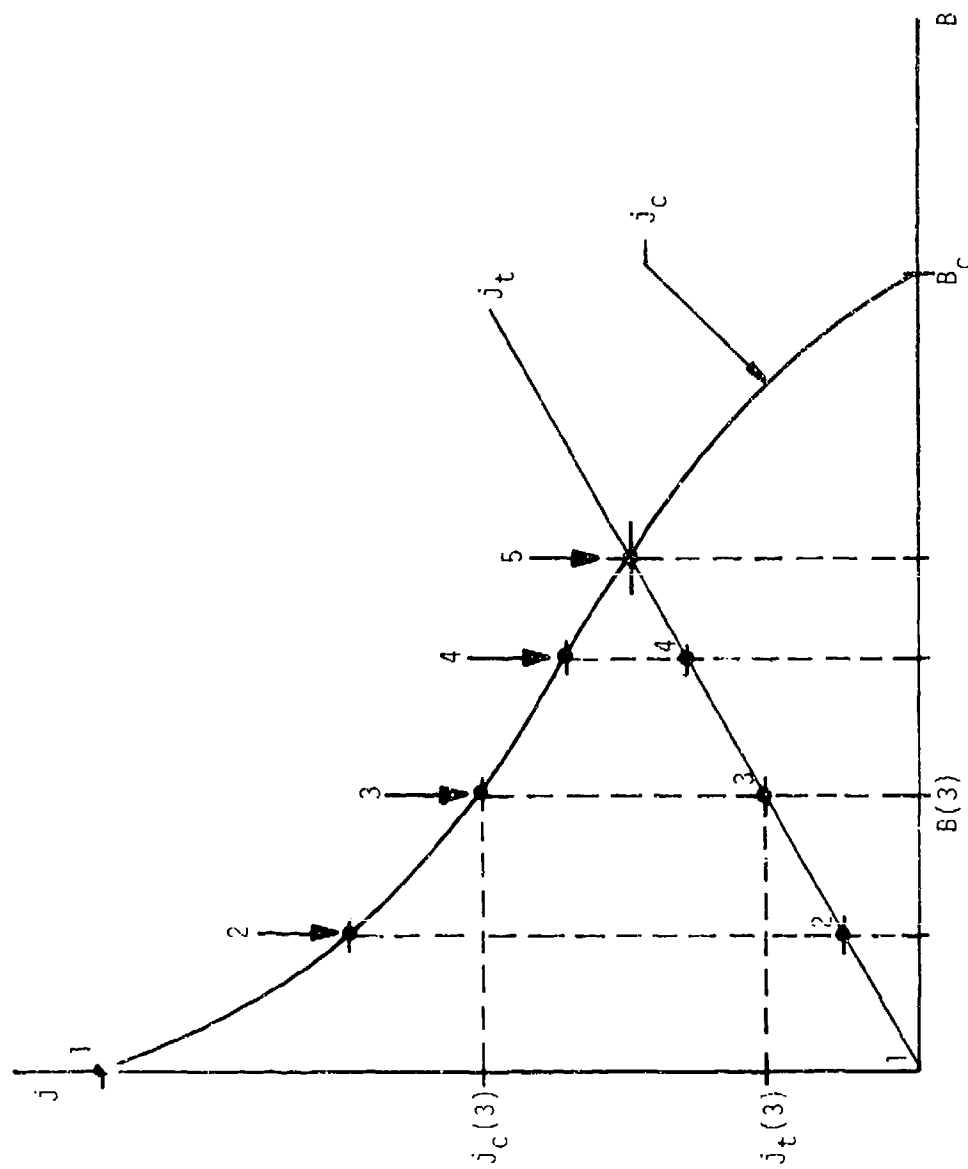


Figure 135. Schematic Showing $B - j_c$ Curve for a Typical Superconductor and the $B - j_t$ Load Line for a Superconductor Carrying a Transport Current. The field penetration, current density and electric field profiles for a slab of superconductor corresponding to the points indicated above can be seen in Figure 136.

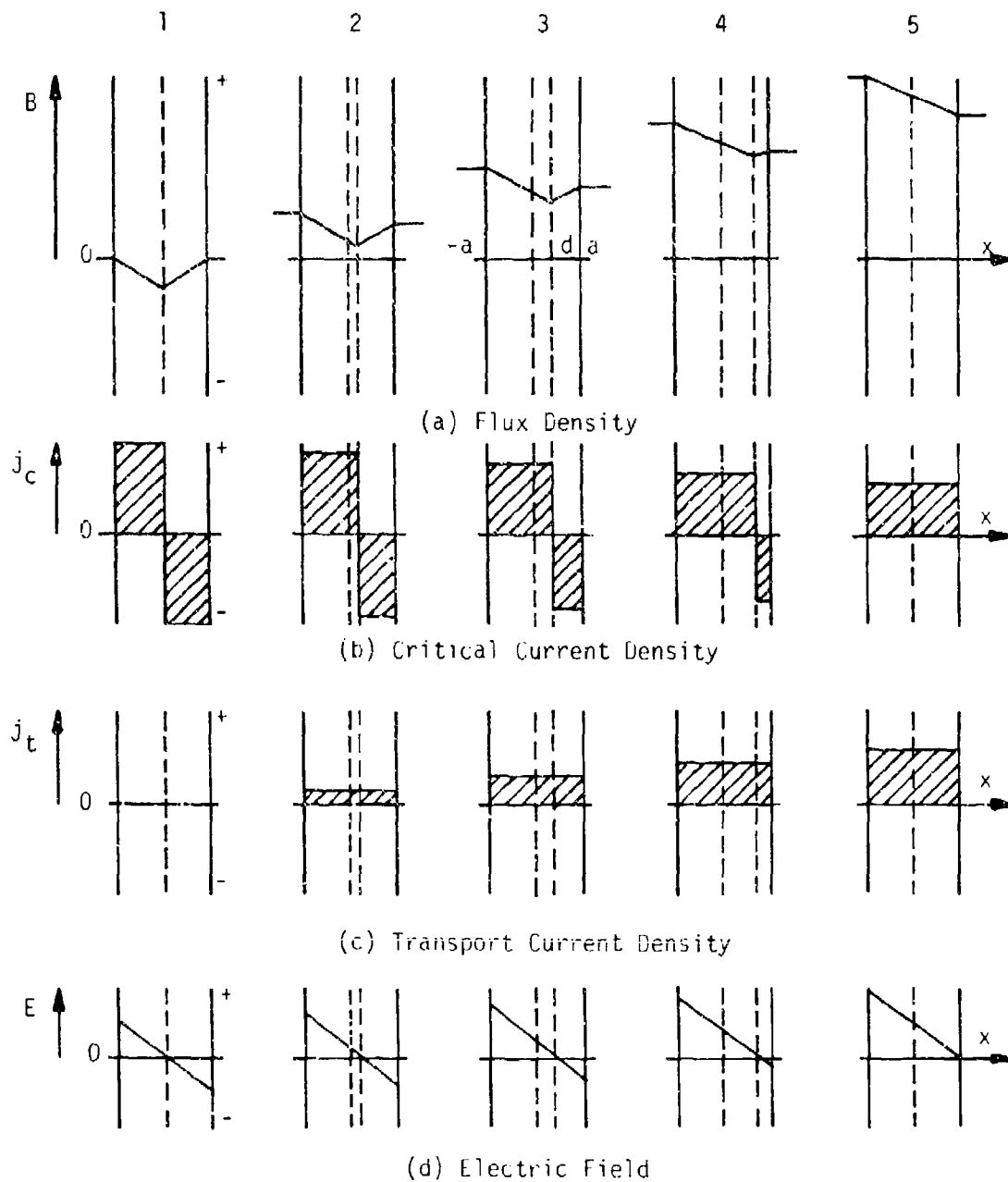


Figure 136. Schematic Showing the Profiles of Flux Density, Current Density and Electric Field Across a Slab of Superconductor Carrying a Transport Current and Subjected to a Background Field Proportional to the Transport Current. The numbers refer to the positions shown on the $B - j_c$ curve in Figure 135.

the saturation current density. If attempts are made to increase the transport current density beyond this point the specimen reverts to the normal state.

We shall now quantify the above description with a view to calculating the local power dissipation in a rectangular wire. Consider Figure 137. This depicts a conductor (height h , width $2a$) carrying a transport current I_t in a background field B (Figure 137(a)). As explained above the transport current creates a difference in flux density across the specimen (Figure 137(b)). This creates an asymmetry in the critical current density distribution (Figure 137(c)). The difference in the critical currents is equal to the net transport current (I_t) flowing. Figure 137(d) shows the equivalent transport current density j_t defined as

$$j_t = \frac{I_t}{2ah}$$

Figure 137(e) shows the electric field E across the specimen. Note that the direction of the electric field is the same as that of the critical currents and that the electric center is at the point ($x = d$) where the critical currents change sign.

We first calculate the position of the electric center. The relevant Maxwell relationship in one-dimensional form is:

$$\frac{dB}{dx} = -\mu_0 j_c$$

which when integrated gives

$$B(x) = -\mu_0 j_c x + C \quad I-1$$

In the region $-a < x < d$ the critical current density is positive. Let this critical current density be j_c^+ . At $x = -a$, $B = B(-a)$ and substitution in equation I-1 gives:

$$C = B(-a) - \mu_0 j_c^+ a$$

$$\therefore -a < x < d \quad B(x) = B(-a) - \mu_0 j_c^+ (x+a) \quad I-2$$

In the region $d < x < a$ the critical current density is negative. Let this critical density be j_c^- . At $x = a$, $B = B(a)$ and substitution in equation I-1 gives

$$C = B(a) + \mu_0 j_c^- a$$

$$\therefore d < x < a \quad B(x) = B(a) - \mu_0 j_c^- (x-a) \quad I-3$$

At point d , the electric center, equations I-2 and I-3 must give the same value for $B(d)$.

$$\therefore B(a) - \mu_0 j_c^- (d-a) = B(-a) - \mu_0 j_c^+ (d+a)$$

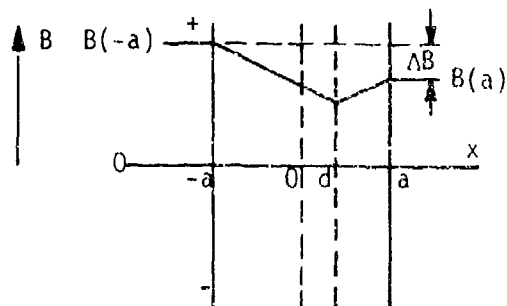


Figure 137(b) Flux Density

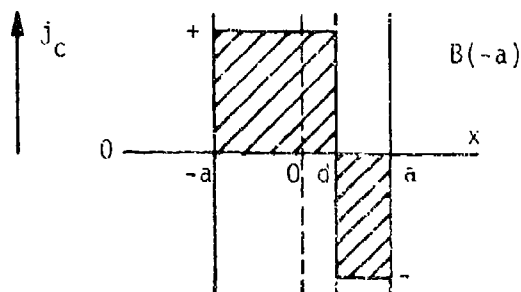


Figure 137(c) Critical Current Density

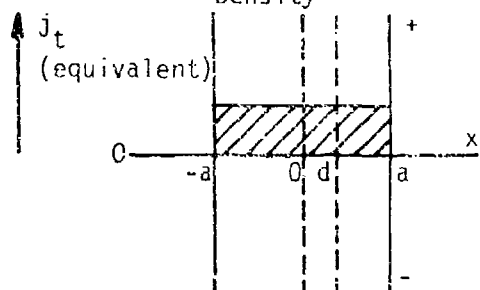


Figure 137(d) Equivalent Transport Current Density

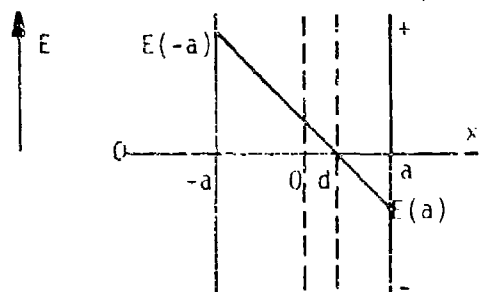


Figure 137(e) Electric Field

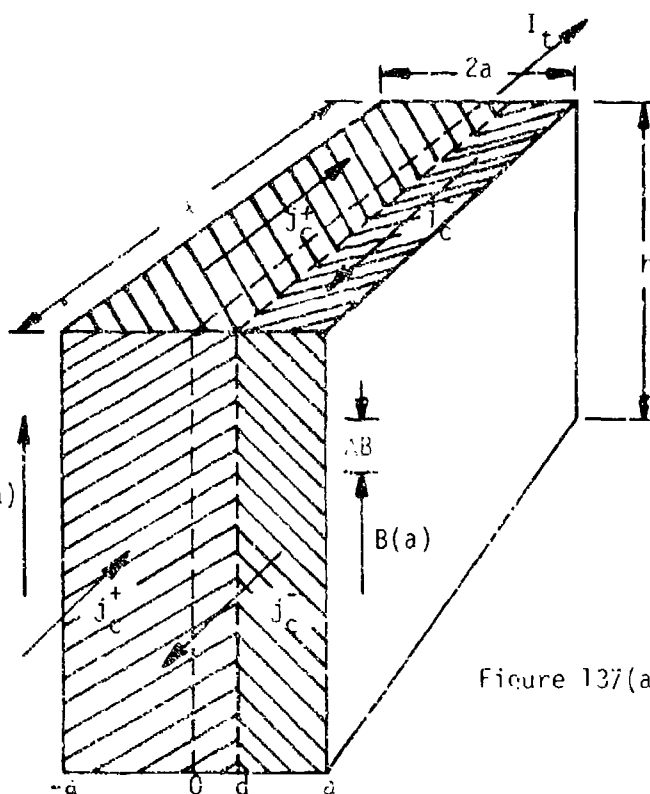


Figure 137(a)

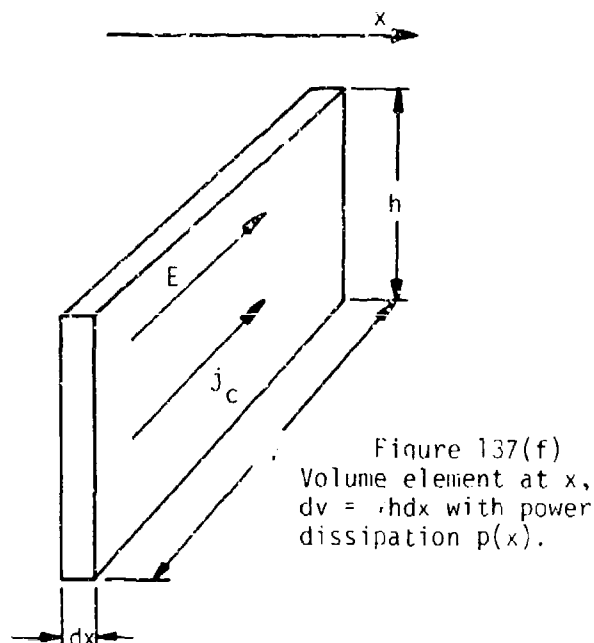


Figure 137(f)
Volume element at x ,
 $dv = hdx$ with power
dissipation $p(x)$.

Figure 137. Model Used for Calculating the Local Power Dissipation $p(x)$ in a Rectangular Slab of Superconductor Carrying a Transport Current Density. Also shown are the flux density, current density and electric field profiles.

and

$$\begin{aligned} B(-a) - B(a) &= \mu_0 j_c^+ (d+a) - \mu_0 j_c^- (d-a) \\ &= \mu_0 d (j_c^+ - j_c^-) + \mu_0 a (j_c^+ + j_c^-) \end{aligned}$$

but $j_c^- = -j_c^+$

$$\therefore B(a) - B(-a) = \mu_0 2d j_c^+ \quad \text{I-4}$$

However $B(a) - B(-a)$ is merely the difference in field ΔB between the two sides of the wire and this difference is due to the transport current I_t . If we define j_t by the relationship:

$$I_t = 2ah j_t \quad (\text{see Figure 137(a)})$$

then

$$\Delta B = \mu_0 2a j_t$$

and from I - 4 $\Delta B = \mu_0 2d j_c^+$

$$\therefore d = \frac{a j_t}{j_c^+}$$

The electric center therefore is given by

$$x = d = a \frac{j_t}{j_c^+}$$

Now using the Maxwell relationship $\nabla \times \mathbf{E} = -\dot{\mathbf{B}}$ in one-dimensional form:

$$\frac{dE}{dx} = -\dot{B}$$

and integrating:

$$E = -Bx + C \quad \text{I-5}$$

$E = 0$ at the electric center $x = d = a \frac{j_t}{j_c^+}$

which when substituted into equation I - 5 gives

$$C = B a \frac{j_t}{j_c^+}$$

and $E = -\dot{B}(x - \frac{j_t}{j_c^+} a)$

I-6

The local power dissipation per unit volume is given by:

$$\frac{p(x)}{\ell h dx} = E j_c \quad (\text{see Figure 137(f)})$$

In the region $-a < x < d$ $j_c = j_c^+$

$$\therefore \frac{p(x)}{\ell h dx} = -\dot{B}(x - \frac{j_t}{j_c^+} a) j_c^+$$

and the local power dissipation per unit length is given:

$$\frac{p(x)}{\ell} = -\dot{B} j_c^+ h (x - \frac{j_t}{j_c^+} a) dx.$$

The total power dissipated per unit length in the region $-a < x < d$ is given:

$$\begin{aligned} \frac{P}{\ell} (-a \rightarrow d) &= -\dot{B} j_c^+ h \int_{x=-a}^{\frac{j_t}{j_c^+} a} (x - \frac{j_t}{j_c^+} a) dx \\ &= -\dot{B} j_c^+ h \left[\frac{x^2}{2} - \frac{j_t}{j_c^+} ax \right]_{-a}^{\frac{j_t}{j_c^+} a} \\ &= -\dot{B} j_c^+ h \left\{ \left(\frac{j_t^2}{j_c^{+2}} \frac{a^2}{2} - \frac{j_t^2 a^2}{j_c^{+2}} \right) - \left(\frac{a^2}{2} + \frac{j_t a^2}{j_c^+} \right) \right\} \\ &= -\dot{B} j_c^+ h a^2 \left\{ -\frac{1}{2} \frac{j_t^2}{j_c^{+2}} - \frac{1}{2} \left(1 + 2 \frac{j_t}{j_c^+} \right) \right\} \\ \frac{P}{\ell} (-a \rightarrow d) &= \frac{\dot{B} j_c^+ h a^2}{2} \left(\frac{j_t^2}{j_c^{+2}} + 2 \frac{j_t}{j_c^+} + 1 \right) \end{aligned}$$

In the region $d < x < a$ $j_c = j_c^-$ and the local power dissipation per unit length is given:

$$\frac{P(x)}{\lambda} = -\dot{B}j_c^- h \left(x - \frac{j_t}{j_c^+} \right) dx$$

The total power dissipated per unit length in the region $d < x < a$ is given:

$$\begin{aligned} \frac{P}{\lambda} (d \rightarrow a) &= -\dot{B}j_c^- h \int_{x = \frac{j_t}{j_c^+} a}^a \left(x - \frac{j_t}{j_c^+} a \right) dx \\ &= -\dot{B}j_c^- h \left[\frac{x^2}{2} - \frac{j_t}{j_c^+} ax \right]_{\frac{j_t}{j_c^+} a}^a \\ &= -\dot{B}j_c^- h \left\{ \left(\frac{a^2}{2} - \frac{j_t a^2}{j_c^+} \right) - \left(\frac{j_t^2}{j_c^{+2}} \frac{a^2}{2} - \frac{j_t^2 a^2}{j_c^{+2}} \right) \right\} \\ &= -\dot{B}j_c^- h a^2 \left\{ \frac{1}{2} \left(1 - \frac{2j_t}{j_c^+} \right) + \frac{1}{2} \frac{j_t^2}{j_c^{+2}} \right\} \\ \frac{P}{\lambda} (d \rightarrow a) &= \frac{-\dot{B}j_c^- h a^2}{2} \left(\frac{j_t^2}{j_c^{+2}} - \frac{2j_t}{j_c^+} + 1 \right) \end{aligned}$$

but $j_c^- = -j_c^+$

$$\therefore \frac{P}{\lambda} (d \rightarrow a) = \frac{\dot{B}j_c^+ h a^2}{2} \left(\frac{j_t^2}{j_c^{+2}} - \frac{2j_t}{j_c^+} + 1 \right)$$

The total power dissipated per unit length is given by:

$$\begin{aligned} \frac{P}{\lambda} (-a \rightarrow a) &= \frac{P}{\lambda} (-a \rightarrow d) + \frac{P}{\lambda} (d \rightarrow a) \\ &= \frac{\dot{B}j_c^+ h a^2}{2} \left\{ \left(\frac{j_t^2}{j_c^{+2}} + \frac{2j_t}{j_c^+} + 1 \right) + \left(\frac{j_t^2}{j_c^{+2}} - \frac{2j_t}{j_c^+} + 1 \right) \right\} \end{aligned}$$

$$= \frac{\dot{B} j_c^+ h a^2}{2} \left\{ \frac{j_t^2}{j_c^2} + 2 \right\}$$

$$\frac{P(-a+a)}{x} = \dot{B} j_c^+ a^2 \left(1 + \frac{j_t^2}{j_c^2} \right) h$$

The average power per unit volume over the cross section of the wire is given:

$$\left. \frac{P}{V} \right|_{\text{average}} = \frac{P(-a+a)}{x h 2a} = \frac{\dot{B} j_c^+}{2} \left(1 + \frac{j_t^2}{j_c^2} \right)$$

or written in terms of the diameter of the wire $w = 2a$

$$\left. \frac{P}{V} \right|_{\text{average}} = \frac{w \dot{B} j_c^+}{4} \left(1 + \frac{j_t^2}{j_c^2} \right) \quad \text{I-7}$$

Thus the power dissipation per unit volume is proportional to the diameter of the wire, to the instantaneous value of the rate of change of applied field and to the instantaneous value of the critical current density which is determined by the instantaneous local field B . The maximum value of the ratio of transport current density to critical current density

$$\left(\frac{j_t}{j_c} \right)$$

is 1. Therefore the effect of transport current is to increase the losses by a factor of between 1 and 2.

Before proceeding to calculate the energy losses over a cycle in a coil we will refine the formula for instantaneous power loss by considering the case of a round wire as opposed to a rectangular wire.

Figure 138 illustrates the model which is a round wire of radius "a." We will use the formula just derived for the average power per unit length for a rectangular wire of dimensions $2a$ by h and apply it to the volume element $2xh$ shown shaded in Figure 138. The average power dissipated per unit length for this element is therefore:

$$\frac{P}{V} (h, -x+x) = \dot{B} j_c^+ x^2 \left(1 + \frac{j_t^2}{j_c^2} \right) dh$$

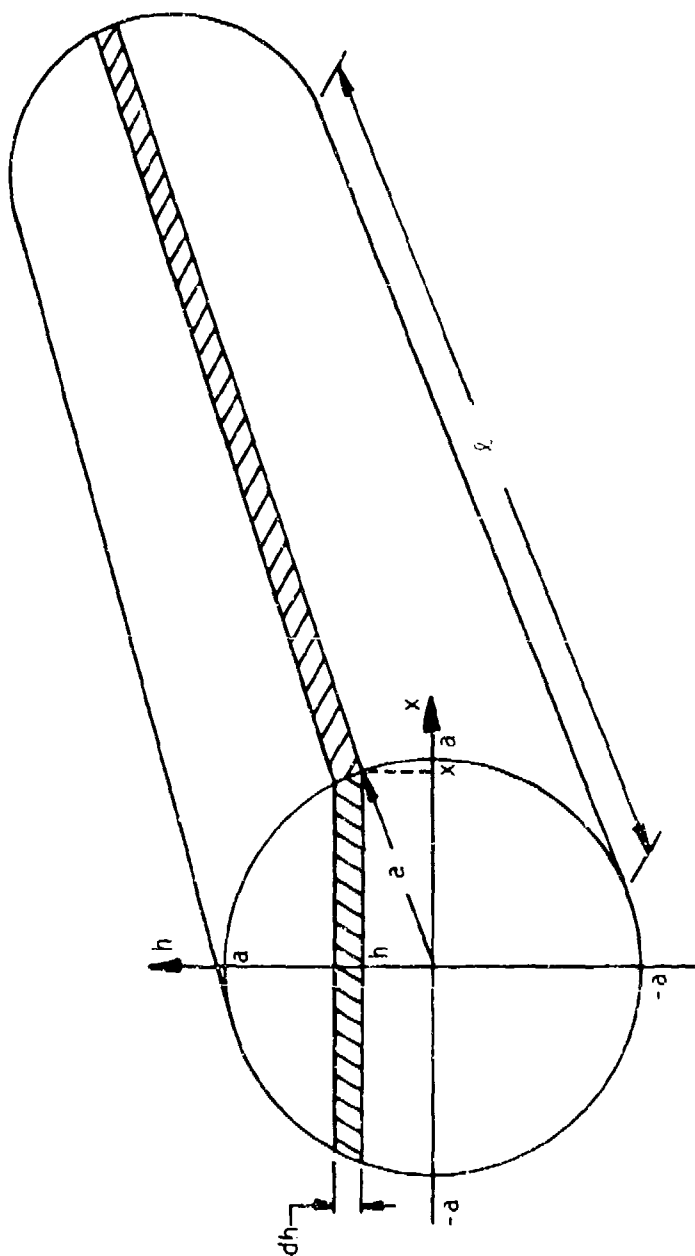


Figure 138. Schematic Illustrating Model Used for Calculating the Power Dissipation in a Wire of Circular Cross Section Carrying a Transport Current.

and the average power dissipated per unit length over the whole of the circular cross section is:

$$\left. \frac{P}{\ell} \right|_{\text{cross section}} = k \int_{h=-a}^a x^2 dh$$

where

$$k = B j_c^+ \left(1 + \frac{j_t^2}{j_c^+{}^2} \right)$$

but $x^2 + h^2 = a^2$

$$\begin{aligned} \therefore \left. \frac{P}{\ell} \right|_{\text{cross section}} &= k \int_{h=-a}^a (a^2 - h^2) dh \\ &= k \left[a^2 h - \frac{h^3}{3} \right]_{-a}^a \\ &= k \left\{ \left(a^3 - \frac{a^3}{3} \right) - \left(-a^3 + \frac{a^3}{3} \right) \right\} \\ &= \frac{4a^3}{3} k \end{aligned}$$

and the average power per unit volume of superconductor is given

$$\begin{aligned} \left. \frac{P}{V} \right|_{\text{average}} &= \frac{P}{\ell} \times \frac{1}{V} = \frac{4a^3}{3} k \times \frac{1}{\pi a^2} \\ &= \frac{4}{3\pi} a B j_c^+ \left(1 + \frac{j_t^2}{j_c^+{}^2} \right) \end{aligned}$$

or written in terms of the wire diameter $w = 2a$

$$\left. \frac{P}{V} \right|_{\text{average}} = \frac{2}{3\pi} w B j_c^+ \left(1 + \frac{j_t^2}{j_c^+{}^2} \right) \quad 1-8$$

Comparing this with the expression for a rectangular wire of width w (equation 1-7) we see that the ratio of the geometry factors is:

$$4 \times \frac{2}{3} = 0.849$$

It should be noted that, in contrast to the formula for the rectangular wire (1-7), because of the circular symmetry of the round wire this formula (1-5) can be used for conductor occupying any position in a coil; the limitation of field parallel to one face no longer applies.

We are now in a position to calculate the energy loss in a magnet which is exposed to a transient field. Consider Figure 139. This shows a typical $B - j_c$ curve for a superconductor and a linear approximation to it in the region over which the coil operates. The linear approximation is defined by the intersections of the straight line with the current density and flux density axes, defined as j_{c0} and B_0 respectively. Also shown is the load line (transport current density j_t versus flux density B) for conductor at a general point within the coil. This load line is defined by j_M which is the maximum transport current density in the coil during a charge/discharge cycle, and B_m which is the flux density seen by the conductor at the moment of maximum current density. The critical current density which corresponds to the maximum flux density is defined as j_{cm} . Furthermore we assume that the coil is charged to its maximum current density in time T_1 .

From 1-8 we have

$$\frac{P}{V} = \frac{2}{3} w j_c \left(1 + \frac{j_t^2}{j_c^2} \right)$$

The linear $B - j_c$ curve gives

$$j_c = j_{c0} \left(1 - \frac{B}{B_0} \right)$$

The load line is

$$j_t = \frac{j_M}{B_m} B$$

The linear rate of change of field gives

$$\frac{dB}{dt} = \frac{B_m}{T_1}$$

Combining the above equations we obtain:

$$\frac{P}{V} = \frac{2w}{3} \frac{B_m}{T_1} j_{c0} \left(1 - \frac{B}{B_0} \right) \left\{ 1 + \frac{j_M^2}{j_{c0}^2} \frac{B^2}{B_m^2} \frac{1}{\left(1 - \frac{B}{B_0} \right)^2} \right\}$$

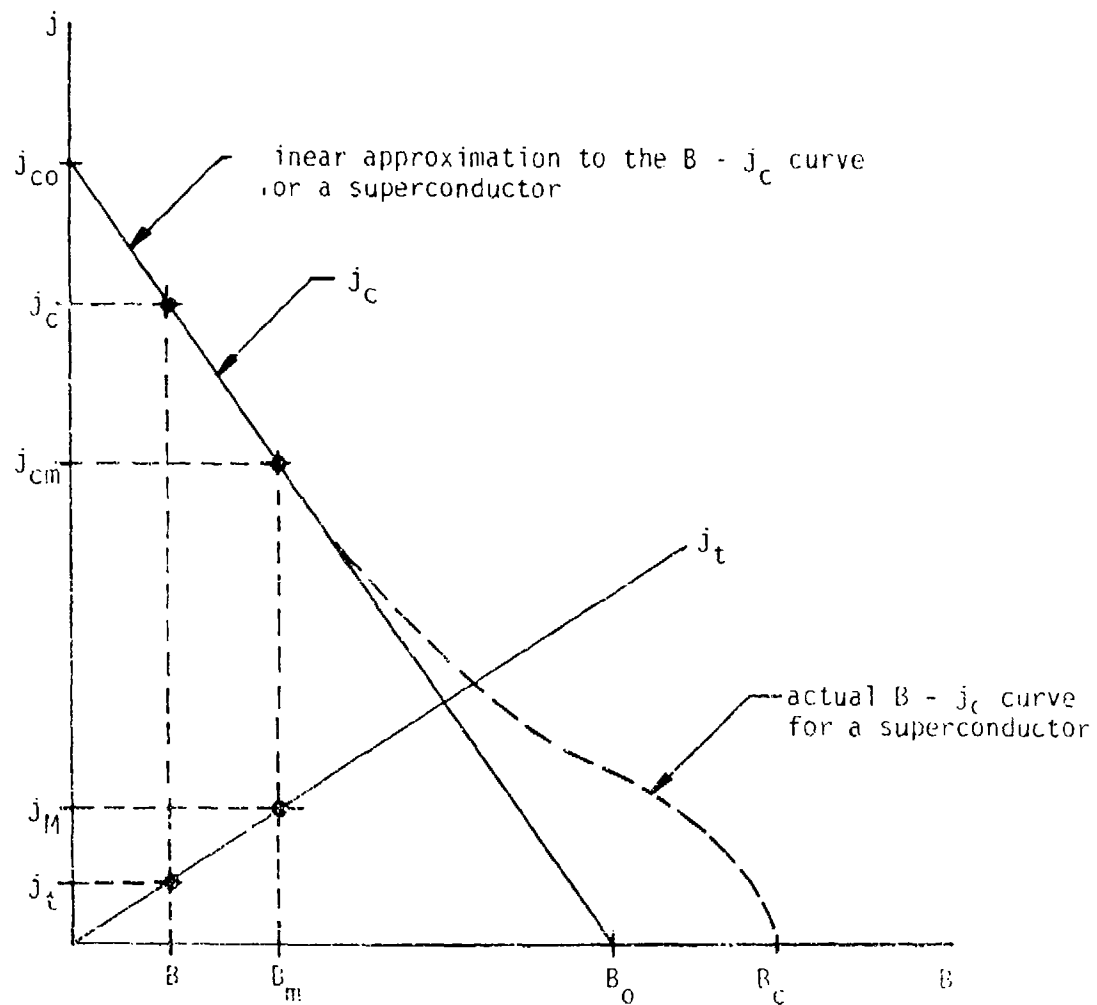


Figure 139. Schematic Illustrating the Model Used to Calculate the Energy Loss in a Coil Carrying a Transport Current.

Normalizing this equation thus:

$$\frac{B}{B_0} = B^*, \quad \frac{B_m}{B_0} = B_m^*, \quad \frac{j_M}{j_{co}} = j^*$$

we obtain

$$\frac{P}{V} = \frac{2W}{3\pi} j_{co} B_0 \frac{B_m^*}{T_1} (1 - B^*) \left\{ 1 + \frac{j^{*2}}{B_m^{*2}} \frac{B^{*2}}{(1 - B^*)^2} \right\}$$

Let $k_1 = \frac{2W}{3\pi} j_{co} B_0$, $k_2 = \frac{j^{*2}}{B_m^{*2}}$

then

$$\frac{P}{V} = k_1 \frac{B_m^*}{T_1} (1 - B^*) \left\{ 1 + \frac{k_2 B^{*2}}{(1 - B^*)^2} \right\}$$

$$\frac{P}{V} = k_1 \frac{B_m^*}{T_1} \left\{ 1 - B^* + \frac{k_2 B^{*2}}{(1 - B^*)^2} \right\}$$

I-9

The energy per unit volume dissipated at this point in the coil in going from $B = 0$ to $B = B_m$ is given:

$$\frac{E}{V} = \int_{B=0}^{B_m} \frac{P}{V} dt$$

but

$$B = \frac{B_m}{T_1} t$$

$$dB = \frac{B_m}{T_1} dt$$

$$\frac{E}{V} = \frac{T_1}{B_m} \int_{B=0}^{B_m} \frac{P}{V} dB$$

or in normalized form:

$$\frac{E}{V} = \frac{T_1}{(B_m/B_0)} \int_{B/B_0 = 0}^{B_m/B_0} \frac{P}{V} d(B/B_0)$$

$$\frac{E}{V} = \frac{T_1}{B_m^*} \int_{B^* = 0}^{B_m^*} \frac{P}{V} dB^*$$

Therefore from I-9

$$\frac{E}{V} = k_1 \int_{B^* = 0}^{B_m^*} \left\{ 1 - B^* + \frac{k_2 B^{*2}}{(1 - B^*)^2} \right\} dB^*$$

$$\frac{E}{V} = k_1 \left[B^* - \frac{B^{*2}}{2} - k_2 \left(B^* + \frac{B^{*2}}{2} + \ln(1 - B^*) \right) \right]_0^{B_m^*}$$

$$\frac{E}{V} = k_1 \left\{ B_m^* - \frac{B_m^{*2}}{2} - k_2 \left[B_m^* + \frac{B_m^{*2}}{2} + \ln(1 - B_m^*) \right] \right\} \text{ ---- I-10}$$

Thus the energy per unit volume dissipated in a region of the coil cycled from zero field to a maximum field B_m is:

$$\frac{E}{V} = \frac{2w}{3} j_{co} B_m \left\{ 1 - \frac{B_m}{2B_0} - \frac{j_M^2}{j_{co}^2} \frac{B_0^2}{B_m^2} \left[\frac{B_m}{2B_0} + \frac{\ln(1 - \frac{B_m}{B_0})}{\frac{B_m}{B_0}} + 1 \right] \right\} \text{ ---- I-11}$$

Note that this is independent of the charge time T_1 ; this same energy loss will be incurred whatever the rate of change of flux density.

We will now proceed to calculate the total energy dissipated in a coil subjected to a cycle from zero transport current density to a maximum current density j_M . A coil is made up of an infinite number of points such as the one for which the above derivation was performed and to accurately predict the loss for the coil as a whole we must have a knowledge of how the field varies throughout the coil volume.

In practice this is achieved by carrying out a field plot within the windings of the coil in question. We can then calculate the fraction of the

volume of the coil which lies between conductor exposed to two maximum fields B_{m1} and B_{m2} when the coil is carrying its maximum transport current density j_M . If we further assume that within this range the maximum field B_m varies linearly along the length of the conductor we can derive an expression for the average energy loss per unit volume of the conductor within that field range. Thus we have for a length of wire (L) having a distribution of maximum field

$$B_m = B_{m1} \text{ at } \ell = 0$$

$$B_m = B_{m2} \text{ at } \ell = L$$

$$B_m = B_{m1} + (B_{m2} - B_{m1}) \frac{\ell}{L}$$

or in normalized form where

$$B_m^* = \frac{B_m}{B_0}, \quad \ell^* = \frac{\ell}{L}$$

$$B_m^* = B_{m1}^* + (B_{m2}^* - B_{m1}^*) \ell^*$$

The average energy dissipated per unit volume for conductor in the region $\ell = 0$ to L is:

$$\begin{aligned} \left. \frac{E}{V} \right|_{\text{average}} &= \frac{1}{L} \int_{\ell=0}^L \frac{E}{V} d\ell \\ &= \int_{\ell^*=0}^1 \frac{E}{V} d\ell^* \end{aligned}$$

but

$$d\ell^* = \frac{dB_m^*}{(B_{m2}^* - B_{m1}^*)}$$

and at $\ell^* = 0$ $B_m^* = B_{m1}^*$

$\ell^* = 1$ $B_m^* = B_{m2}^*$

$$\therefore \left. \frac{E}{V} \right|_{\text{average}} = \int_{B_m^* = B_{m1}^*}^{B_m^* = B_{m2}^*} \frac{E}{V} \frac{dB_m^*}{(B_{m2}^* - B_{m1}^*)}$$

Substituting from equation I-10 gives:

$$\left. \frac{E}{V} \right|_{\text{average}} = \frac{2w}{3\pi} \frac{j_{co} B_o}{(B_{m2}^* - B_{m1}^*)} \int_{B_{m1}^*}^{B_{m2}^*} \left\{ B_m^* - \frac{B_m^{*2}}{2} - \frac{j^{*2}}{B_m^{*2}} \left[B_m^* + \frac{B_m^*}{2} + \ln(1-B_m^*) \right] \right\} dB_m^*$$

or letting $k_3 = \frac{2w}{3\pi} \frac{j_{co} B_o}{(B_{m2}^* - B_{m1}^*)}$

$$\left. \frac{E}{V} \right|_{\text{average}} = k_3 \int_{B_{m1}^*}^{B_{m2}^*} \left\{ B_m^* - \frac{B_m^{*2}}{2} - j^{*2} \left[\frac{1}{B_m^*} + \frac{1}{2} + \frac{\ln(1-B_m^*)}{B_m^{*2}} \right] \right\} dB_m^*$$

$$\left. \frac{E}{V} \right|_{\text{average}} = k_3 \left[\frac{B_m^{*2}}{2} - \frac{B_m^{*3}}{6} - j^{*2} \left\{ \ln B_m^* + \frac{B_m^*}{2} - \ln B_m^* - \frac{(1-B_m^*)}{B_m^*} \ln(1-B_m^*) \right\} \right]_{B_{m1}^*}^{B_{m2}^*}$$

$$\left. \frac{E}{V} \right|_{\text{average}} = k_3 \left[\frac{B_m^{*2}}{2} - \frac{B_m^{*3}}{6} - j^{*2} \left\{ \frac{B_m^*}{2} - \frac{(1-B_m^*)}{B_m^*} \ln(1-B_m^*) \right\} \right]_{B_{m1}^*}^{B_{m2}^*}$$

$$\left. \frac{E}{V} \right|_{\text{average}} = k_3 \left[\frac{(B_{m2}^{*2} - B_{m1}^{*2})}{2} - \frac{(B_{m2}^{*3} - B_{m1}^{*3})}{6} - j^{*2} \left\{ \frac{(B_{m2}^* - B_{m1}^*)}{2} - \left[\frac{(1-B_{m2}^*)}{B_{m2}^*} \ln(1-B_{m2}^*) - \frac{(1-B_{m1}^*)}{B_{m1}^*} \ln(1-B_{m1}^*) \right] \right\} \right] \text{--- I-12}$$

where

$$k_3 = \frac{2w}{3\pi} \frac{j_{co} B_o}{(B_{m2}^* - B_{m1}^*)}, \quad B^* = \frac{B}{B_o}, \quad j^* = \frac{j_M}{j_{co}}$$

In a practical situation this average energy per unit volume is multiplied by the volume of that section of the coil to give the total energy dissipated in that section. A similar calculation is carried out for other sections of the coil and the total energy dissipated in the coil is found by taking the summation of the energy dissipated in the various sections.

It happens in many real situations that the distribution of field through the whole of the windings is quite linear with respect to position along the length of the conductor. In other words, if L is the total length of conductor in the coil and B_M is the field at the peak field position of the coil at the moment of maximum transport current density j_M then:

$$B_m = \frac{\ell}{L} B_M$$

In this case equation 1-12 can be simplified to:

$$\frac{E}{V} \Big|_{\text{average overcoil}} = \frac{2w}{3\pi} j_{co} B_M \left\{ \frac{1}{2} - \frac{B_M}{6B_0} - \frac{j_M^2}{j_{co}^2} \frac{B_0^2}{B_M^2} \left[\frac{B_M}{2B_0} - \frac{(1 - \frac{B_M}{B_0}) \ln(1 - \frac{B_M}{B_0})}{\frac{B_M}{B_0}} - 1 \right] \right\}$$

This formula is simple to use and is more than adequate for obtaining an estimate of the losses incurred in most coils. In this formula j_{co} and B_0 are properties of the superconducting material used, w is a property of the wire, and B_M and j_M are properties of the coil.

APPENDIX II

DERIVATION OF RELATIONSHIP BETWEEN HYSTERESIS LOOP AND LOSS DURING CYCLE

The voltage which appears across the coil terminals consists of an inductive component associated with the rate of change of field in the energy storage coil and dissipative component associated with the loss mechanism.

$$\text{If } V_L = \text{inductive component} = L \frac{di}{dt}$$

$$V_R = \text{dissipative component}$$

$$V_C = V_L + V_R = \text{total voltage measured across coil terminals}$$

A fraction f of the terminal voltage is tapped from a voltage divider R placed across the terminals and from this fraction fV_C is subtracted a voltage $M \frac{di}{dt}$ produced by the mutual inductance between an auxiliary coil and a current lead. The resulting voltage is fed to the input of an integrator.

$$\begin{aligned} \text{Thus input voltage to integrator} &= fV_C - M \frac{di}{dt} \\ &= fV_R + fV_L - M \frac{di}{dt} \\ &= fV_R + (fL - M) \frac{di}{dt} \end{aligned}$$

By suitably adjusting f and M , $fL - M$ can be made as small as is desirable. It should be noted that (as the following analysis will show) it is not essential for the method to be valid that $fL - M$ be made exactly zero. Making it small merely allows the range over which the integrator must work to be greatly reduced.

The output from the integrator is:

$$\frac{1}{\tau} \int_0^t [fV_R + (fL - M) \frac{di}{dt}] dt$$

where τ is the time constant of the integrator.

This signal is fed to the Y axis of an X-Y plotter. In reality because of the rapid discharge times this will be an oscilloscope. A voltage proportional to the current through the coil is fed to the X axis. This signal is derived from the non-inductive shunt described in the text of this report and in Appendix IV.

The combination of signals produces a hysteresis loop whose area is given:

$$A = \int_0^i \left\{ \int_0^t \left[fV_L + (fL - M) \frac{di}{dt} \right] \frac{dt}{\tau} \right\} di$$

$$A = \int_0^i \left\{ \int_0^t \frac{fV_L}{\tau} dt \right\} di + \int_0^i \left\{ \int_0^t \frac{(fL-M)}{\tau} \frac{di}{dt} dt \right\} di$$

$$A = \frac{f}{\tau} \int_0^i \left\{ \int_0^t V_L dt \right\} di + \frac{(fL-M)}{\tau} \int_0^i \left\{ \int_0^t \frac{di}{dt} dt \right\} di$$

at $t = 0$ $i = 0$

$t = t$ $i = i$

$$A = \frac{f}{\tau} \int_0^i \left\{ \int_0^t V_L dt \right\} di + \frac{(fL-M)}{\tau} \int_0^i \left\{ \int_{i=0}^i di \right\} di$$

$$A = \frac{f}{\tau} \int_0^i \left\{ \int_0^t V_L dt \right\} di + \frac{(fL-M)}{\tau} \int_0^i i di$$

$$A = \frac{f}{\tau} \int_0^i \left\{ \int_0^t V_L dt \right\} di + \frac{(fL-M)}{\tau} \frac{i^2}{2}$$

let $\int_0^t V_L dt = x$

$$V_L dt = dx$$

$$A = \frac{f}{\tau} \int_0^i x di + \frac{(fL-M)}{2\tau} i^2$$

integrate by parts

$$\int_{i=0}^i A = \frac{f}{\tau} \left\{ x i - \int_0^i i dx \right\} + \frac{(fL-M)}{2\tau} i^2$$

$$\int_{i=0}^i A = \frac{f}{\tau} \left\{ i \int_0^t V_L dt - \int_0^i i V_L dt \right\} + \frac{(fL-M)}{2\tau} i^2$$

$$\int_{i=0}^i A = \underbrace{\frac{f i}{\tau} \int_0^t V_L dt}_{[1]} + \underbrace{\frac{(fL-M)}{2\tau} i^2}_{[2]} - \underbrace{\frac{f}{\tau} \int_0^i i V_L dt}_{[3]}$$

If we take cycle $i = 0$ to i_{\max} to $i = 0$

$$\begin{matrix} t = 0 & \text{to} & t = t_{\text{cycle}} \\ \text{then terms } [1] \text{ and } [2] = 0 & \text{and} & A_{\text{cycle}} = - \frac{f}{\tau} \oint i V_L di \end{matrix}$$

$$\text{but } i V_L \text{ is power loss} = P \quad \text{and } A_{\text{cycle}} = - \frac{f}{\tau} \oint P_L dt = - \frac{f}{\tau} E_{\text{cycle}}$$

where E_{cycle} is the energy dissipated in a cycle. Thus $E_{\text{cycle}} = - \frac{\tau}{f} A_{\text{cycle}}$

APPENDIX III

EFFECT OF PHASE SHIFT AND DRIFT VOLTAGE ON LOSS LOOP MEASUREMENT

We measure the losses by taking:

$$E_A = \left[\frac{1}{\tau_I} \int dI \int dt \left(fV - L_m \frac{dI}{dt} \right) \right] \left(\frac{I}{f} \right)$$

where:

E_A is the apparent energy described by the loss loop

τ_I is the integrator time constant

$\int dI$ means to calculate the area inside the loss loop

f is the divider fraction

L_m is the mutual inductance to the sense coil

V and I are voltage and current, respectively.

for the sake of simplicity, we use sinusoidal quantities:

$$I = I_0 \cos \omega t$$

$$V = RI + L \frac{dI}{dt}$$

$$= I_0 \left[R \cos \omega t - \omega L \sin \omega t \right]$$

where:

R represents the superconductor loss at a given current and frequency

L is the self inductance of the coil

Assuming the existence of a DC error voltage, v , and a phase shift error, ϕ , it is possible to write:

$$E_A = \left\{ \frac{1}{\tau_I} \int dI \int dt \left[\left(fV - L_m \frac{dI}{dt} \right) + v \right] \right\} \left(\frac{I}{f} \right)$$

error \neq

$$\frac{1}{\omega \tau_I} \int dI \left\{ \cos \phi \left[a \sin \omega t - b \omega \cos \omega t \right] \right. \\ \left. + \sin \phi \left[a \cos \omega t + b \omega \sin \omega t \right] + V \omega t \right\} \frac{\tau_I}{f}$$

where:

$$A = fR$$

$$b = Lm - fL$$

The observed energy is calculated by noting that

$$dI = -I_0 \omega \sin \omega t dt$$

and integrating over a complete cycle. The result of this calculation is:

$$E_A = \frac{1}{2} I_0 \left(\frac{2\pi}{\omega} \right) \left[fRI_0 \cos \phi - 2v + I_0 (\omega Lm - fL) \sin \phi \right] \left(\frac{\tau_I}{f} \right)$$

Typical Values for Actual System:

Loss Voltage (fRI_0): 1mv or greater

DC Error Voltage (v): 30 microvolts or less

Phase shift, ϕ : less than 10^{-3} radian

Resolution of Null Circuit: less than 1 part in 10^5

APPENDIX IV

NON-INDUCTIVE CURRENT SHUNT

For the electronic loss measurement technique to work properly, the coil current must be monitored accurately. A current shunt essentially is a resistor whose current is accurately known so that when the voltage developed across it is measured the current may be calculated. As long as the voltage measured is due only to the resistance of the shunt an accurate reading of the current may be obtained. However, strictly the voltage measured across the shunt is due to the sum of a voltage due to the shunt resistance and a voltage due to the shunt inductance. The former is proportional to the current and the latter is proportional to the rate of change of current. As long as the rate of change of current is small the inductive component of voltage will be small and the measured voltage will be due only to the resistance of the shunt. This situation occurs at long discharge times. However at short discharge times unless special precautions are taken the inductive component becomes large and erroneous readings of current are obtained. Therefore a shunt must be designed in which the inductance is low enough so that at the shortest discharge times likely to be encountered, the inductive component of voltage is small compared with the resistive component of voltage. This is achieved by designing a shunt which consists of two concentric cylinders as shown schematically in Figure 80. The current flows down one cylinder and back up the other one. The cylinders are made so that they are as close together as is practically possible. In this way the current paths are as close together as possible but in opposite directions. The magnetic fields due to each therefore almost cancel and the inductance is much reduced.

Other considerations also enter into the design. The above coaxial arrangement takes care of the inductive problems but changes in resistance during a cycle must also be eliminated. These changes are due to two effects. Firstly, there may be a resistance change due to a temperature rise caused by ohmic heating and secondly at fast discharge times the resistance may change due to a skin effect.

The former may be eliminated by making the shunt sufficiently massive so that changes in temperature are small and have a negligible effect on the resistivity of the material.

The latter must be eliminated by suitably sizing the thickness of the coaxial cylinders. The skin effect is caused by a rapidly changing magnetic field causing an induced voltage which alters the current distribution in the cylinders. Under conditions of fast discharge the current tends to flow preferentially in the outer layers of the cylinder. The faster the discharge the more current "crowds" to the outside of the cylinders. This means that the material on the inside is not available for carrying current and therefore the resistance of the cylinders increases. Calculations indicated that at the discharge times to be encountered a wall thickness of 0.12 inch would be thin enough to eliminate any problems due to the skin effect. Table XXIII is a summary of the results of the analysis carried out to design the shunt.

APPENDIX V

HIGH RESOLUTION VOLTAGE DIVIDER

The primary specification for the voltage divider is high resolution. This requirement is met by means of the two-stage design shown in Figure 81. Because the divider fraction must match the voltage ratio between the energy storage coil and a sense coil (in this case a secondary winding placed around the storage coil), it is sufficient to measure this ratio to one percent accuracy and set up a resistor string such that the difference in divider fraction across the terminals of a single resistor brackets the measured coupling ratio to the sense coil. In other words, the divider fraction can be adjusted to within one percent of the desired value by making one straightforward measurement and constructing a string of discrete resistors accordingly. If a ten turn potentiometer, which has a resolution of 1 part in 1,000, is placed across the terminals of the specified resistor (as in Figure 81), then the total resolution available in the divider fraction is one part in 10^5 .

The other requirements that must be fulfilled by the voltage divider are: (1) ability to withstand 60 kV without arcing, (2) the resistance must be high enough that the components do not suffer excessive heating during a high voltage pulse, and (3) the resistance must be low enough to preclude disturbance of the divider ratio by connection of an integrator with realistic input impedance (300k ohms in our case). The first condition led to the selection of a string of about 60 two-watt resistors (each capable of supporting 1,000 volts) which is mounted on a sheet of plastic (18" x 20"); the terminals of this resistor string are separated by approximately 15 inches. The best compromise between the second and third conditions led to the selection of an overall resistance for the divider of about 60,000 ohms. This is five times smaller than the input impedance of the integrator; a practical upper limit on the input impedance of the integrator is set by the drift requirements as will be discussed later. The heating of this resistor string can be checked by noting that the energy dissipated in the divider string, E_s , is given by:

$$E_s = \left(\frac{1}{2} L I_C^2 \right) \frac{R_l}{R_d} \quad \text{V-1}$$

where L is the coil inductance, I_C is the coil current, R_d is resistance of the divider, and R_l is the load resistance for the coil and is specified by:

$$R_l = \frac{V_{\max}}{I_C} \quad \text{V-2}$$

With the help of equation V-2, the expression for energy lost in the divider string can be converted to the form:

$$E_s = \left(\frac{1}{2} L I_C \right) \frac{V_{\max}}{R_d} \quad \text{V-3}$$

from which it is clear that the worst case (greatest loss) occurs for the highest values of V_{\max} (60,000 volts) and of I_C (1,000 amps) for which R_l

is 30 ohms. If the coil is charged to its rated energy (10J kilojoules), the energy dissipated in the divider is given by equation V-1:

$$E_s = (100,000)(30/60,000) = 50 \text{ Joules}$$

which is about one Joule per resistor. Under these conditions, the maximum increase in divider temperature is only one or two kelvins, a negligible amount.

APPENDIX VI

ELECTRIC CIRCUIT MODEL FOR DEWAR LOSSES

The dewar is regarded as a one-turn secondary winding of a transformer whose primary is the 7 kJ coil, as shown in the schematic of Figure 102. In this diagram, R_2 is the resistance of the dewar, L_2 is the self-inductance of the dewar, L_1 is the self-inductance of the primary, R_1 is the resistance of the primary, and M is the mutual inductance between the primary and secondary. The appropriate loop equations are:

$$(1) \quad V = i_1 R_1 - M \frac{di_2}{dt} + L_1 \frac{di_1}{dt}$$

$$(2) \quad 0 = L_2 \frac{di_2}{dt} - M \frac{di_1}{dt} + i_2 R_2$$

For sine waves these become:

$$(1) \quad V = i_1 R_1 - Mj \cdot i_2 + j \cdot L_1 i_1$$

$$(2) \quad 0 = L_2 j \omega i_2 - Mj \cdot L_1 + i_2 R_2$$

These can be solved for the input impedance:

$$Z = \frac{V}{i_1} = R_1 + \frac{\omega^2 M^2 R_2}{R_2^2 + (\omega L_2)^2} + j \cdot \left[L_1 - L_2 \frac{\omega^2 M^2}{R_2^2 + (\omega L_2)^2} \right]$$

where: $R_1 \cong 6 \times 10^{-6}$ ohms (measured)

$R_2 \cong 0.5 \times 10^{-3}$ ohms (calculated and inferred from Figure 101)

$M \cong 70.7$ μ H (estimated by dividing M to sense coil by 33)

$L_2 \cong 0.56$ μ H (estimated from L of the sense coil and calculated)

$L_1 \cong 37$ mH (measured)

For frequencies below about 10 Hertz, the resistive part of this becomes:

$$Z = R_1 + \frac{\omega^2 M^2}{R_2} \cong 6 \times 10^{-6} + 3.95 \times 10^{-4} f^2$$

APPENDIX VII

PREDICTED LOSS VOLTAGE FOR THE 7 kJ COIL DUE TO MAGNETIZATION LOSSES

Figure 104 (predicted coil loss voltage) was prepared from an expression derived earlier in this report which is:

$$V = -f \left(\frac{\pi}{4}\right)^2 \frac{w}{4} L_c \frac{B_0}{I_{co}} \left\{ 1 - \frac{1}{3} \left(\frac{B_M I_{co}}{B_0 I_M} \right)^2 - \frac{1}{\left(1 - \frac{B_M I_t}{B_0 I_M} \right)} \right\} \frac{dI_t}{dt}$$

where, for the 7 kJ coil, the parameters are:

$I_{co} = 2000 \text{ A}$ $B_0 = 7.36 \text{ Wb/m}^2$	}	$\frac{B_0}{I_{co}}$ defines short sample characteristics of the material
$w = 7.37 \times 10^{-5} \text{ m}$		diameter of the Nb-Ti core
$L_c = 2.96 \times 10^2 \text{ m}$		length of conductor in the coil
$I_M = 1000 \text{ A}$ $B_M = 3.99 \text{ Wb/m}^2$	}	$\frac{B_M}{I_M}$ defines coil load line
$f = 0.05$ (resistive divider fraction)		
$I_t =$ coil current (amps), operating current		

Hence the expression for the 7 kJ coil is:

$$V = -17.8 \times 10^{-6} \left\{ 0.608 - \frac{1}{(1 - 0.542 \times 10^{-3} I_t)} \right\} \frac{dI_t}{dt}$$

This is plotted for sine waves, for which

$$\frac{dI_t}{dt} = \omega I_t$$

APPENDIX VIII

DESIGN OF RELAXATION OSCILLATOR TO PRODUCE A SERIES OF PULSES FROM AN ENERGY STORAGE COIL

Initial Energy in Coil: $E = \frac{1}{2} Li^2$ $i = \sqrt{\frac{2E}{L}}$

Energy in One Small Pulse: $E_p = \frac{1}{2} CV^2$ $V = \sqrt{\frac{2E_p}{C}}$

Charge on Capacitor: $Q = i\tau = CV$ τ = charging time for first pulse

If we specify E_p and E , we get:

$$\tau = \frac{CV}{i} = \sqrt{LC} \sqrt{\frac{E_p}{E}}$$

If we also specify L and C , then τ is given as above.

EXAMPLE: $L = 51.5 \text{ mH}$, $C = 1,125 \text{ }\mu\text{F}$, $E = 25 \text{ kJ}$ or 100 kJ , $E_p = 2.6 \text{ kJ}$

(a) $\tau = 2.4 \text{ ms}$ (25 kJ), 1.2 ms (100 kJ)

(b) $V = 2,100 \text{ volts}$

(c) $i = 985 \text{ A}$ (25 kJ), $1,950 \text{ A}$ (100 kJ)

If we specify V instead of C , we get $C = \frac{2E_p}{V^2}$, hence:

$$L = \frac{1}{2} \tau^2 E \frac{V^2}{E_p^2}$$

EXAMPLE: $\tau = 0.02 \text{ s}$, $V = 2,000 \text{ volts}$, $E = 100 \text{ kJ}$, $E_p = 2 \text{ kJ}$

(a) $L = 20 \text{ H}$

(b) $C = 1,000 \text{ }\mu\text{F}$

(c) $i = 100 \text{ A}$

Note that the decay of coil current with time has not been considered, hence the time between pulses, τ , is correct only for the first few pulses. In practice, the time between pulses will increase as coil current decays.

APPENDIX IX

DESIGN OF ARC QUENCH CIRCUIT FOR HELIUM SWITCH

REQUIREMENTS:

- (a) Negative peak in arc quench circuit current occurs at time t to shut off the switch current. This happens after $3/4$ cycle.
- (b) Peak current of arc quench circuit is greater than the switch current at time t .
- (c) Time for current zero (about $1/4$ cycle of arc quench circuit) must be greater than recovery time for switch.
- (d) Initial voltage on the arc quench capacitor is the switch firing voltage, V .
- (e) Arc quench capacitor must recharge properly between shots, hence ringing must damp out rapidly through the load resistance.

EQUATIONS:

$$\text{Condition (a) demands: } \tau_{\text{off}} = \frac{3}{2} \pi \sqrt{LC} \quad (1)$$

$$\text{Conditions (b) and (d) demand: } V/I_0 \geq \sqrt{L/C} \quad (2)$$

$$\text{Condition (c) demands: } 2\pi \sqrt{LC} \gtrsim 4\tau_{\text{recovery}} \quad (3)$$

$$\text{Condition (e) demands: } \sqrt{L/C} \sim 2R_{\text{Load}} \quad (4)$$

EXAMPLE: Choose $\tau_{\text{off}} = 300 \mu\text{s}$, $V = 1800$ volts, $I_0 = 3600$ A
(Coil current plus residual discharge current from large capacitor).

EQUATIONS (1) and (2) completely specify L and C :

$$L = (2/3\pi) (V/I_0) \tau_{\text{off}} = 31.8 \mu\text{H}$$

$$C = (2/3\pi) \tau_{\text{off}} (I_0/V) = 127 \mu\text{F}$$

These values will be effective if: $\tau_{\text{recovery}} \sim 100 \mu\text{s}$ (recovery of switch)

$$\text{and } R_{\text{Load}} \sim \frac{1}{2} \sqrt{L/C} = 0.25 \Omega$$

In addition, we need the time between pulses to be long enough for 3 or 4 arc quench oscillations to take place -- we have at least enough time for 3 oscillations. Actual circuit used is shown in Figure 124.